Fault zone architecture, microstructures, deformation mechanisms and frictional behaviour of seismogenic, shallow-crustal, lithologically heterogeneous faults

RACHAEL JANE BULLOCK

Fault zone architecture, microstructures, deformation mechanisms and frictional behaviour of seismogenic, shallow-crustal, lithologically heterogeneous faults

Rachael Jane Bullock

A thesis submitted in partial fulfilment of the requirements for the degree of Doctor of Philosophy at Durham University

Department of Earth Sciences, Durham University, UK

July 2015

Abstract

Earthquakes that rupture the Earth's surface are typically the most damaging and highlight the need for us to better constrain the style of deformation and frictional behaviour of fault zones in the shallow crust. This thesis presents two studies of natural, seismogenic, shallow crustal fault zones: 1) the Gubbio fault zone, which has been exhumed from 2.5-3 km depth and deforms a mixture of limestone and phyllosilicate-rich marly limestone; and 2) the Masada fault zone, which deforms near-surface, poorly lithified lake sediments. Field studies were complemented by low- and high-velocity rotary shear experiments to constrain the frictional behaviours of the naturally observed fault gouges under representative conditions. In addition, microstructural analyses of both naturally- and experimentally-produced fault rocks were performed in order to constrain the deformation mechanisms operating during fault slip.

Our results show that the dominant deformation mechanisms operating within a fault zone, which are highly variable depending on environmental conditions such as depth, fault rock composition, fluid presence and composition, and strain-rate, will control: 1) fault zone architecture and therefore the distribution of seismicity; and 2) slip zone processes, which can subsequently affect the frictional behaviour of a fault, and also determine whether or not signatures of seismic slip are produced during rupture propagation. These are useful tools for geologists when trying to decipher the seismic history of natural faults. Frictional behaviour, in terms of the likelihood of rupture propagation through the shallow crust, is also found to vary significantly as a function of the aforementioned environmental conditions. A fuller knowledge of spatial, and possible temporal, variations in fault zone properties is therefore essential if more accurate earthquake forecasting models and assessments of their associated hazards are to be produced.

Declaration

I declare that this thesis, which I submit for the degree of Doctor of Philosophy at Durham University, is my own work and not substantially the same as any which has previously been submitted at this or any other university.

Rachael J. Bullock
Durham University
July 2015

Acknowledgements

First and foremost I would like to thank Nic, for being a fantastic supervisor. It was Nic's lectures during my 3rd year of undergraduate studies at Durham which first got me interested in fault mechanics and inspired me to do my MSci research project and subsequently my PhD with him on the subject. Nic has been an incredibly dedicated and supportive supervisor throughout. Admittedly, his high standards have occasionally left me pulling my hair out, but I have appreciated every single piece of 'constructive criticism' that I have received over the years, in the knowledge that, collectively, they have undoubtedly improved my skills and thought processes as a researcher. I surely would not be where I am today, or have enjoyed some of the successes that I have, without his guidance.

Second, my thanks go to Bob, who has been an equally helpful, supportive and enthusiastic supervisor. Both Nic and Bob have seemingly had much faith in me when I sometimes have had very little in myself, and have provided me with opportunities and the means to travel to several international conferences which have helped me to mature both personally and academically, and provided me with much inspiration for my work.

I also cannot thank my third supervisor, Shmulik, enough, first for taking care of much of the logistical side of things during my time in Israel, thus ensuring that my fieldwork went smoothly and to plan, and second for his generosity, both in kind and with his time, during my visits to Israel. I would also like to thank Ran, Ofir, and Sagea for their gracious assistance in the field; my fieldwork literally would not have been possible without their help, or their field coffee-making skills.

Thank you to Ian Chaplin for always being a friendly face and not complaining (too much) when I brought him horrible samples to make thin sections from, and for often making them in record time. Big thanks to Leon Bowen as well, again for always greeting me with a smile and providing banter, often going out of his way to help me, and for just being an all-round legend when it comes to microscopy. Thanks also to Sam Clark, Gary Oswald and João Trabucho-Alexandre for showing me the ropes of XRD.

Thanks to all my friends in Durham who have helped the days-months-years pass by in a fairly pleasant manner. Special thanks to Siân for putting up with my increasingly regular grumbles and incessantly stupid questions, to Loraine, for being the little ray of sunshine that sits opposite me, and to Fienke, for all the abuse. Thanks also go to baker extraordinaire Davey S for supplying me with copious amounts of cake and bread. It's a small miracle that I have not yet become obese. On

which note I would also like to send a shout-out to all my chums and acquaintances at Elvet Striders (especially Jules, Caroyln and the mudparents) and Durham Tri Club for introducing me to new hobbies. All the exercise has kept me sane and helped me to remember there is far more to life than work!

Of course a final thanks must go to Mum, Dad and Chris for just generally putting up with me and for letting me get on with what I want to do, whilst always being supportive.

Table of contents

List of Figures

Chapter 1

Chapter 2

Chapter 3

Chapter 4

Chapter 5

Chapter 6

List of Tables

Chapter 2

Chapter 3

Chapter 5

Chapter 1

Introduction

1.1 *Background to research*

1.1.1 *Earthquakes and the seismic cycle*

When the Earth's crust is subject to an applied stress, for example, at tectonic plate boundaries, it will break, resulting in the formation of fractures. Fractures along which two adjacent blocks of the crust slide past one another, accumulating displacement, are referred to as faults. Over time, the faults bounding two moving blocks will accumulate stress in the form of elastic strain energy, plus a lesser component of gravitational energy. When stress accumulates to the point at which it reaches the shear strength of the fault, the fault will fail abruptly and the stored strain energy will be released during an earthquake. Under certain conditions, some parts of faults are not able to accumulate large amounts of stress, and in such cases, stress is released more steadily over time via aseismic fault creep.

The seismic cycle of a fault can be split into four periods, characterized by different styles of slip behaviour (Fig. 1.1). During the interseismic period, i.e., between earthquakes, faults are either completely locked, or are creeping at very slow rates of mm/yr. Thus, shear stress gradually accumulates on a fault and at the same time, fault strength increases due to cohesive strengthening (Marone et al., 1995; Muhuri et al., 2003). During the pre-seismic period, or nucleation phase of an earthquake, slip accelerates, creating an instability which triggers the subsequent co-seismic motion on the fault (Scholz, 1998; Sibson, 1989); it is characterized by accelerated fault creep at rates of

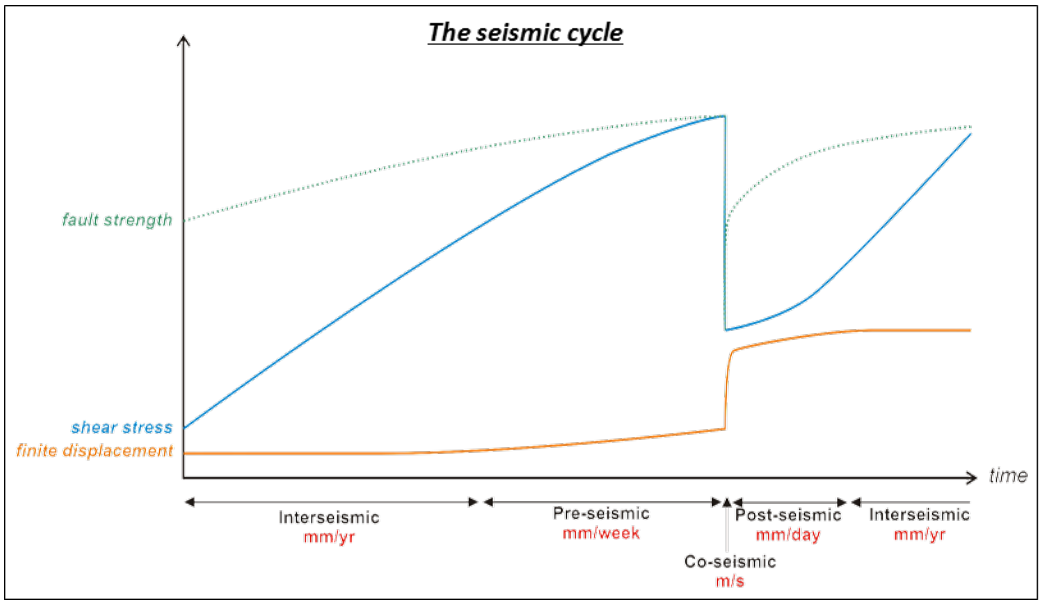

Figure 1.1 Schematic diagram showing the evolution of fault strength, shear stress and finite displacement on a fault with time over the course of the seismic cycle. Modified from (Di Toro et al., 2012).

up to mm/day-week, and/or foreshocks. Accordingly, displacement on the fault starts to increase, and there is a decrease in the rate of shear stress accumulation and fault strengthening. The co-seismic period, or earthquake, occurs when the shear stress acting on the fault reaches the shear strength of the fault. This causes the fault to fail, at which point there is an instantaneous stress drop and decrease in fault strength. Fault slip rates during an earthquake are on the order of m/s and co-seismic displacements may be up to several tens of metres for large-magnitude (M = 8-9) events. Following an earthquake, fault strength starts to recover and shear stress again starts to accumulate. However, any remaining or newly created stress perturbations in certain regions of the fault zone will continue to be relaxed via either aftershocks or aseismic afterslip. Afterslip initially occurs at a rate of mm/day during the days-weeks immediately after a seismic event, but decays exponentially to background interseismic creep rates over a period of months to years following the main event (Marone, 1998; Marone et al., 1991).

1.1.2 *Earthquakes as frictional processes*

1.1.2.1 *The frictional strength of faults*

It is generally accepted that earthquakes occur on pre-existing faults, rather than on new, instantaneously formed surfaces. They are therefore a frictional, rather than a fracture, phenomenon and an understanding of frictional sliding processes between two rock surfaces is fundamental for understanding the mechanics of earthquakes.

It is apparent from Fig. 1.1 that the amount of stress a fault can accumulate depends on the strength of the fault. The strength of a fault is represented by the coefficient of sliding friction, μ, which is the ratio of shear stress to normal stress acting on a plane (Amontons, 1699). In 1978, James Byerlee compiled the results of several frictional sliding experiments and found that, regardless of rock type, the coefficient of sliding friction lies between 0.6 and 0.85 (Byerlee, 1978). The only exceptions are a few clay minerals, for example, montmorillonite, illite and talc, which have much lower frictional coefficients in the approximate range 0.2-0.4, or even as low as 0.1 when they are wet (see Behnsen and Faulkner, 2012 for a review). In-situ stress measurements in boreholes show that these laboratory-derived friction coefficients are consistent with the strength of the brittle intraplate crust (Townend and Zoback, 2000).

1.1.2.2 *Frictional behaviour at sub-seismic slip velocities*

The way in which a fault behaves is determined by the evolution of its frictional strength over the course of the seismic cycle. Experimental studies of fault friction have shown that the time-dependent nature of friction can be described by a rate-and state-variable friction law (Dieterich,

1979; Dieterich, 1981; Ruina, 1983), whereby fault strength is dependent on both velocity (the rate effect) and on the slip history of the fault (the state effect). Within this framework, static friction, μ_s, is found to increase logarithmically with hold time, t (Dieterich, 1972; Fig. 1.2). This effect is attributed to an increase in real contact area (effectively cohesion) between two fault surfaces with time under an applied normal load (Dieterich, 1972). It is this effect that is responsible for the strength recovery of faults after an earthquake.

Second, dynamic friction, μ_d, is found to be dependent upon sliding velocity. Upon an increase in sliding velocity, there is an instantaneous increase in μ_d, referred to as the direct effect and represented by the parameter a (Fig. 1.3). This is followed by a longer-term response as friction evolves towards a steady-state value over a critical slip distance, D_c; this is referred to as the evolution effect and is represented by the parameter b (Fig. 1.3). The value of the combined parameter *(a-b)* determines the frictional stability of a fault. If (a-b) <0 then a material is said to be velocity-weakening (Fig. 1.3a), a condition which is unstable and a pre-requisite for the stick-slip behaviour associated with earthquake nucleation (e.g. Brace and Byerlee, 1966; Dieterich and Kilgore, 1996; Scholz, 1998). If (a-b) >0 a material is said to be velocity-strengthening (Fig. 1.3b), a condition which produces stable sliding and favours fault creep (Scholz, 1998). Earthquakes can only nucleate in regions of the crust that are velocity-weakening. In addition, if an earthquake propagates into a velocity-strengthening region of the crust, it will result in a negative stress drop,

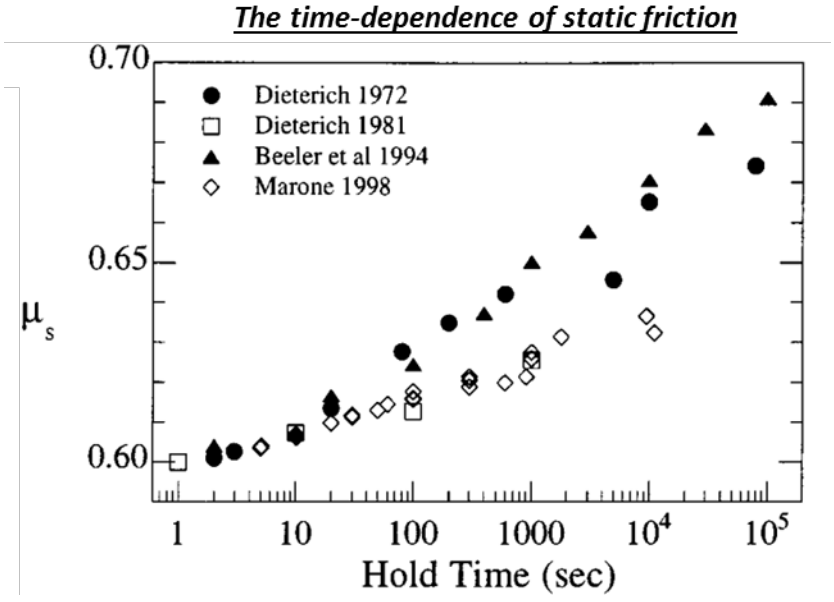

Figure 1.2 Experimental data showing the logarithmic increase in static friction, μ_s, with hold time. Solid symbols are results for initially bare surfaces, open symbols are results for granular gouge layers. Figure taken from (Marone, 1998).

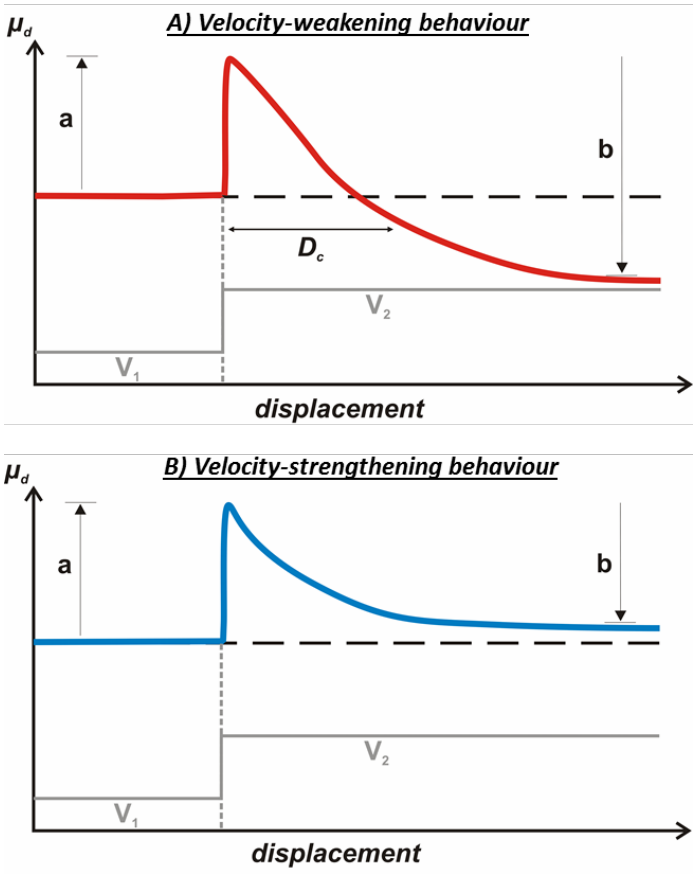

Figure 1.3 Schematic diagrams illustrating the velocity-dependence of dynamic friction, μ_d, when sliding at sub-seismic slip velocities. Fig. **a** depicts velocity-weakening behaviour. Fig. **b** depicts velocity-strengthening behaviour.

which will slow down and maybe even terminate the rupture (Scholz, 1998).

1.1.2.3 *Frictional behaviour at co-seismic velocity*

Although Byerlee's rule and rate and state friction laws describe well the frictional strength and behaviour of faults sliding at sub-seismic velocities (i.e., during the inter-, pre- and post-seismic periods), the development over the past two decades of high-velocity frictional testing apparatuses has revealed that the frictional behaviour of faults sliding at co-seismic velocities is rather different. Fig 1.4, which summarizes the results of frictional sliding experiments performed over a range of slip rates and on both cohesive and non-cohesive rocks typical of seismogenic sources, shows clearly that friction remains in the Byerlee range until slip rates approach 1 m/s (i.e., seismic slip velocity), at which point there is a dramatic decrease in frictional sliding coefficient to values of 0.1-0.2 (see Di Toro et al., 2011 for a review). This behaviour is referred to as 'dynamic weakening'. Dynamic weakening behaviour is attributed to the larger mechanical work rate

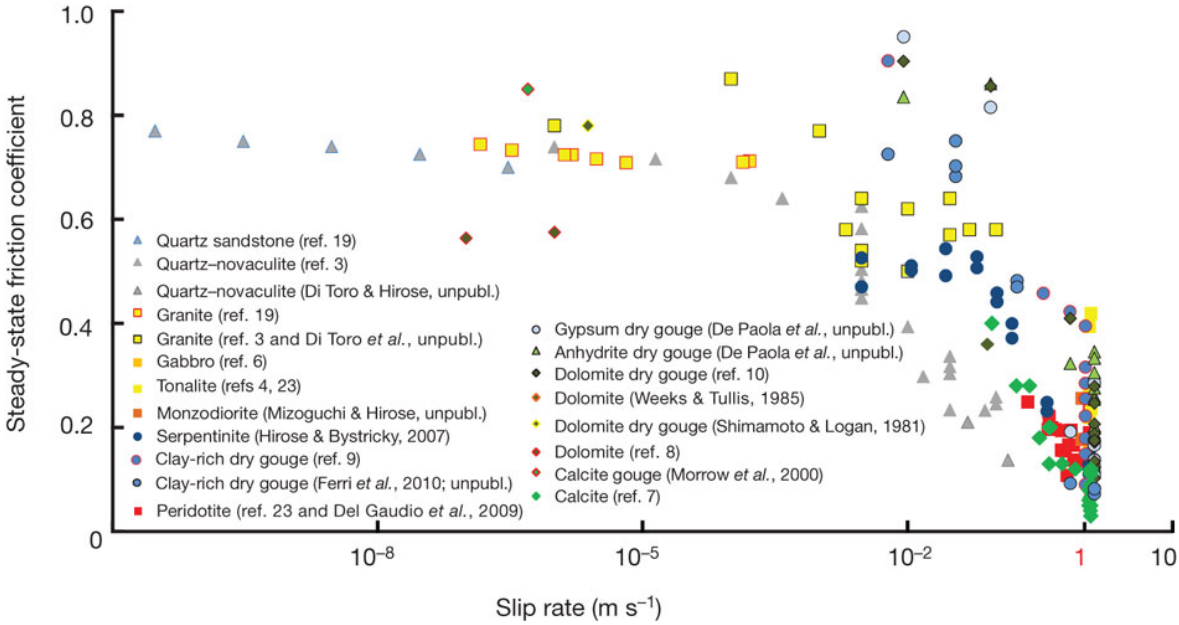

Figure 1.4 Plot showing steady-state sliding friction coefficient as a function of slip rate for friction experiments performed on a wide range of upper-crustal rock types. Figure taken from (Di Toro et al., 2011).

experienced at faster sliding velocities, which can trigger mechanical and thermally-activated chemical reactions within the slipping zone that may act to weaken the fault (Di Toro et al., 2011).

Various dynamic weakening mechanisms have been proposed, dependent upon the rock-type involved, since different rock types have different thermal properties. In the case of silicate rocks, dynamic weakening has been attributed to melt (i.e. pseudotachylyte) generation along the fault surface during slip (Di Toro et al., 2006; Hirose and Shimamoto, 2005; Spray, 2005), or to the formation of a silica gel (Di Toro et al., 2004; Goldsby and Tullis, 2002), both of which would act to lubricate the fault. In the case of carbonate rocks, which will undergo thermal dissociation before they have the chance to melt, dynamic weakening appears to be due to the release of CO_2 into the slip zone, according to the reaction:

$CaCO_3 \leftrightarrow CaO + CO_2$ (1).

This generates a fluid overpressure, P_f, within the slip zone, which reduces the effective normal stress, σ'_n (since $\sigma'_n = \sigma_n - P_f$) and hence the shear strength of the fault (since $\tau_f = \mu.\sigma_n$) (De Paola et al., 2011a; De Paola et al., 2011b; Han et al., 2007). The other product of this decomposition reaction is a layer of sub-rounded and spherical nanoparticles of calcium oxide, coating the slip surface. These nanoparticles, along with nanoparticles produced mechanically by cataclasis, may have a rolling effect on the slip surface, leading to further lubrication (De Paola et al., 2011b; Han

et al., 2010; Han et al., 2011). Similarly, in the case of thermally unstable phyllosilicates, dynamic weakening has been associated with dehydration reactions and subsequent over-pressurization (e.g. Brantut et al., 2008; Ujiie and Tsutsumi, 2010).

1.1.2.4 *The energy budget of an earthquake*

The accumulated elastic and gravitational energy, W, released during an earthquake (represented by the area under the trapezoid in Fig. 1.5) is partitioned into radiated energy, E_R, the energy consumed in overcoming fault friction, E_F, and fracture energy, E_G (i.e., the energy dissipated via fracturing processes) (Fig. 1.5):

$$\Delta W = E_R + E_F + E_G \quad (2)$$

(Kanamori and Rivera, 2006). If the energy released at the front of a propagating rupture tip exceeds the energy dissipated during propagation (represented by the area under the curve labelled σ_f in Fig. 1.5), then slip will be able to accelerate (Griffith, 1920; Kanamori, 2001). The evolution of friction during earthquakes and the dynamic friction coefficient are therefore key parameters in controlling seismic fault slip and radiated energy (Kanamori, 2001).

1.1.3 *Fault zones*

1.1.3.1 *Fault zone architecture*

As two adjacent blocks of crust slide past one another along a fault, the rocks that make up those blocks of crust become deformed. Major seismogenic fault zones are often up to several hundred metres wide, as rocks on either side of the fault become progressively more deformed over time as

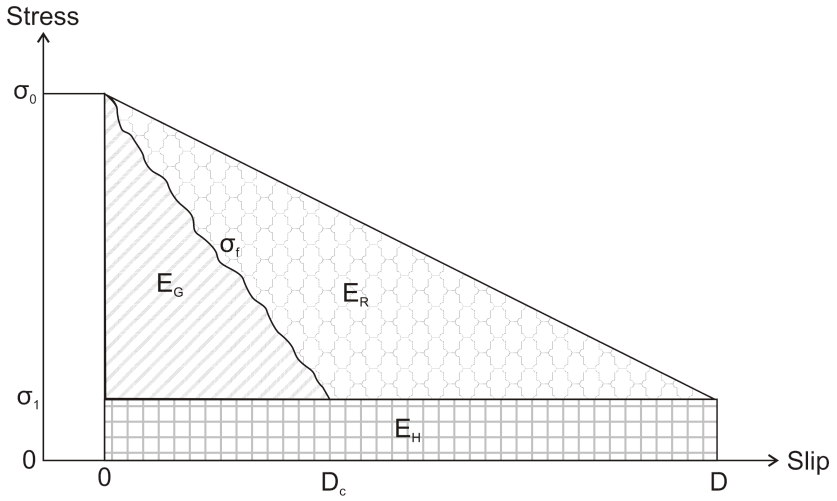

Figure 1.5 Graphical representation of the energy budget of an earthquake. See text for description. Modified from Kanamori and Brodsky (2004).

the fault moves. Within the damaged zone that bounds a fault, there is typically a fault core, ranging from a few metres to a few tens of metres wide, within which most of the fault displacement is accommodated. Further slip localization appears to occur within the fault core, where principal slip zones (PSZs), typically less than a few mm wide, exist. It is thought that slip during individual earthquake events is localized within such PSZs (Sibson, 2003).

1.1.3.2 *Deformation styles and mechanisms*

Deformation styles and mechanisms within fault zones vary according to the environmental conditions during deformation. In the upper ~10 km of the crust, rocks are deformed within the brittle (or frictional) regime (Fossen, 2010). In the brittle regime, the physical conditions, i.e. low temperature and confining pressure, promote brittle deformation mechanisms such as frictional sliding along grain boundaries, grain rotation and grain fracture (Fossen, 2010; Sibson, 1977; Sibson, 1986). In the shallowest part of the crust (1-3 km), where sediments are poorly lithified and thus have high porosity, grains are able to translate and rotate to accommodate frictional grain boundary sliding, without locking up and abrading one another. This process is referred to as granular or particulate flow, and may result in a distributed style of deformation that appears ductile at the meso-scale (Fossen, 2010). At greater confining pressure, and in low-porosity rocks, the limited pore space does not allow grains to shuffle around and so instead grain fracturing and crushing must occur in order to accommodate grain boundary sliding (Fossen, 2010). This process is referred to as cataclasis. Fracturing is a strain-weakening process which leads to the localization of deformation (Reches and Lockner, 1994). Consequently, faults within the brittle part of the crust are often characterized by localized PSZs no more than a few cm thick (e.g. Sibson, 2003 and references therein), within which intense cataclasis occurs and results in the formation of cataclasites and gouges. In the case of wider, perhaps more mature fault zones, a more moderate form of cataclasis may occur, whereby crushed grains flow during shearing – a process referred to as cataclastic flow (Fossen, 2010). Cataclastic flow, like particulate flow, may result in broad shear zones, and the production of structures that appear ductile at the meso-scale (Fossen, 2010). A distributed style of deformation within the upper crust can also result if deformation occurs via pressure-solution, a fluid-assisted form of diffusive mass transfer (DMT) (Rutter et al., 1986). With increasing depth, and hence increasing pressure and temperature, faults pass into the plastic regime, where ductile deformation, governed by crystal-plastic ± DMT mechanisms, is distributed over wide shear zones (Fossen, 2010; Kohlstedt et al., 1995; Sibson, 1977).

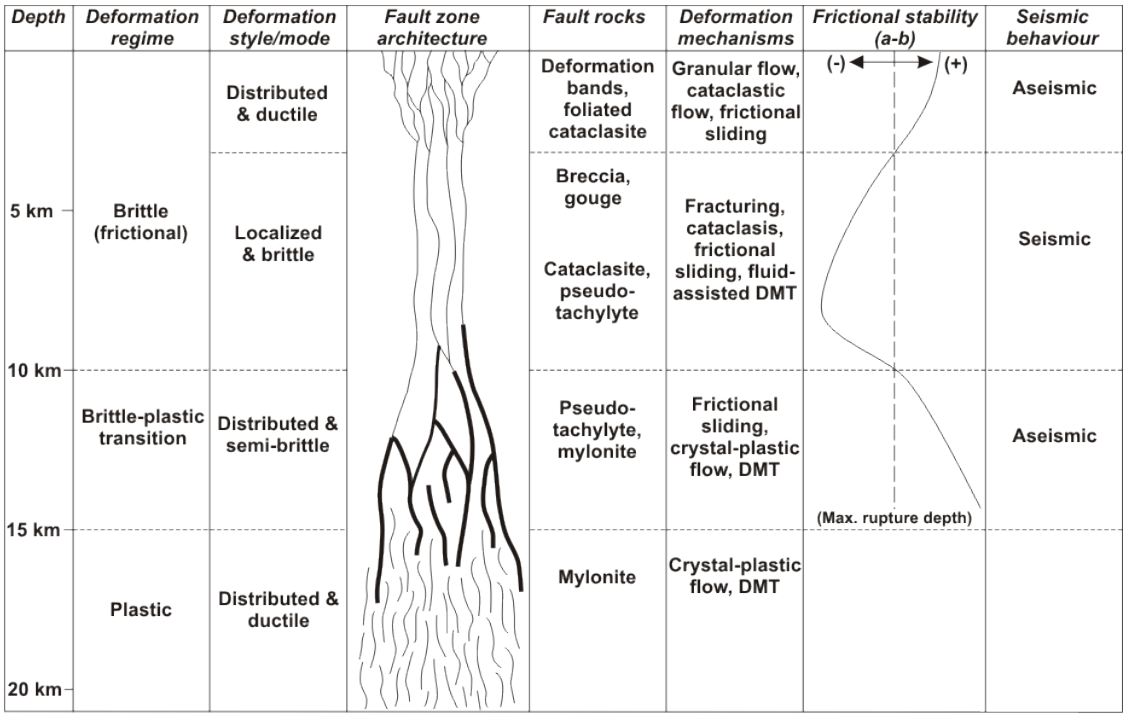

Figure 1.6 The Sibson-Scholz conceptual model of fault zone properties with depth. The case shown is for a continental fault zone. Modified from Scholz (1988).

1.1.3.3 *Conceptual models of fault zone properties*

The depth-dependence of deformation styles and mechanisms has led to the development of conceptual models of fault zone properties, such as that shown in Fig. 1.6. Also shown in Fig. 1.6 is the depth-dependence of frictional stability and seismicity. Earthquake hypocentre data show that the majority of earthquakes nucleate at depths of approximately 5-15 km, in the case of continental earthquakes (Scholz, 1988), or 10-40 km, in the case of subduction zone earthquakes (Byrne et al., 1988; Hyndman et al., 1997). An upper and a lower cut-off in seismicity are then observed above and below these depth ranges. The lower limit in seismicity is attributed to increasing temperature with depth, which brings about a transition from unstable (velocity-weakening) to stable (velocity-strengthening) slip corresponding to the onset of crystal-plastic deformation (Tse and Rice, 1986). The upper cut-off has been attributed to the velocity-strengthening nature of unconsolidated sediments and/or incohesive fault gouges in the shallow portion of the crust, as demonstrated during rate-and-state friction experiments performed at sub-seismic slip velocities (e.g. Blanpied et al., 1987; Byerlee and Summers, 1976; Marone et al., 1990). There is evidently a close correspondence between deformation mechanism, deformation style and frictional stability, suggesting that they are in some way related.

1.2 *Thesis rationale*

The conceptual fault zone model presented in Fig. 1.6 depicts a broad generalization of fault zone properties, based on a compilation of seismological, experimental, and field observations. The truth is that deformation processes and frictional behaviour within fault zones rarely adhere completely to such a model. One of the most significant exceptions is the propagation of seismic ruptures along localized principal slip zones in the shallow crust to generate surface-rupturing earthquakes. Pertinent recent examples of such events include:

- The 2008 M_w = 7.9 Wenchuan, China, earthquake (Xu et al., 2009): 90,000 deaths, 375,000 injured, over 5 million displaced[1].
- The 2009 M_w = 6.3 L'Aquila, Italy, earthquake (Chiarabba et al., 2009): 300 deaths, 1,000 injured, 40,000 displaced[1].
- The 2010 M_w = 8.8 Maule, Chile, earthquake (Delouis et al., 2010): over 500 deaths, 12,000 injured and 800,000 displaced[1].
- The 2011 M_w = 9.0 Tohoku, Japan, earthquake (Ide et al., 2011): 20,000 deaths, over 5,000 injured, 130,000 displaced[1].

Given the damage and destruction caused by such events, there is an evident need to better constrain the style and mechanisms of deformation in, plus the frictional behaviour of, upper-crustal fault zones, particularly in the shallowest portion of the crust (<3 km), where fault zone properties play a crucial role in determining the manner in which seismic energy is either dissipated or transmitted towards the surface. The properties of fault zones in the upper few km of the crust therefore forms the focus of this thesis, with a special focus on carbonate and phyllosilicate-rich host materials.

1.3 *Thesis objectives*

The reason why fault zone processes and behaviours in the shallow crust rarely adhere to a simple conceptual model is that fault zone properties are: 1) spatially heterogeneous, both along-strike and down dip, as a result of changes in depth (confining pressure), lithological variations, the presence and composition of fluids, the effects of previous deformation events and changes in fault zone geometry; and 2) temporally heterogeneous, due to variations in strain-rate over the course of the seismic cycle (of particular importance is the 'dynamic-weakening' of faults when subject to seismic slip velocities (e.g. Di Toro et al., 2011 and references therein) , and due to the progressive accumulation of displacement/fault maturity. The research presented within this thesis aims to

[1] Population effects data taken from http://earthquake.usgs.gov/earthquakes/

better constrain how such heterogeneities may affect the fault zone architecture, deformation mechanisms and frictional behaviour of seismogenic, shallow-crustal fault zones. More specifically, the over-arching aims of this thesis are:

- To characterize the geometry and architecture of shallow-crustal, seismogenic fault zones hosted in different (and heterogeneous) lithologies, with a particular emphasis on the geometries of the principal slip zones.
- To characterize the microstructures, deformation mechanisms and slip zone processes within shallow-crustal, seismogenic fault zones hosted in different (and heterogeneous) lithologies.
- To constrain the frictional properties of experimental, lithologically heterogeneous fault gouges deformed under shallow-crustal conditions during different stages of the seismic cycle.
- To constrain the microstructures, deformation mechanisms and slip zone processes within experimental, lithologically heterogeneous fault gouges, deformed under shallow-crustal conditions, during different stages of the seismic cycle.
- To link the frictional evolution of experimentally deformed fault gouges to their microstructural evolution.
- To relate the mechanical and microstructural results of laboratory friction experiments to the seismic behaviour, microstructures and slip zone processes operating within natural, shallow-crustal fault zones.

1.4 *Methodology*

The above aims have been achieved by:

- Conducting field studies of two seismogenic fault zones hosted in differing lithologies, and deformed at different depths within the shallow crust:
  1) The Gubbio fault zone in the Northern Apennines of Italy, which has been exhumed from 2.5-3 km depth and deforms a mixture of limestone and phyllosilicate-rich marly limestone.
  2) The Masada normal fault zone in Israel, which is associated with the Dead Sea fault zone and deforms near-surface, poorly lithified lake sediments.
- Conducting microstructural analyses of naturally deformed fault rocks collected from the above-mentioned field areas, using both optical and scanning electron microscopy.
- Conducting mineralogical analyses (using X-Ray diffraction) of naturally deformed fault rocks collected from the above-mentioned field areas.

- Performing sub-seismic rate-and-state friction experiments and high-velocity friction experiments on synthetic gouges (derived from material collected from the above-mentioned field areas) using a low to high-velocity rotary shear apparatus.
- Conducting microstructural analyses of experimentally deformed fault rocks from the above-mentioned field areas using optical and scanning electron microscopy.
- Comparing the microstructures of naturally and experimentally deformed fault rocks (produced during our experiments, and previously published experimental studies) in order to make inferences about the frictional behaviour of natural, seismogenic fault zones in the shallow crust.
- Up-scaling the results of laboratory friction experiments to make inferences about the behaviour of lithologically heterogeneous, shallow-crustal faults over the course of the seismic cycle.

Details of field and laboratory methods are presented below.

1.4.1 *Fieldwork*

The fieldwork at Gubbio was conducted during two visits. The first visit to the field (two weeks) was made during the summer of 2010, when I was studying the Gubbio fault as part of my Masters project (*"Slip zone structure and processes in seismogenic carbonate faults"*), which was also completed at Durham University under the supervision of Dr. Nicola De Paola. A second visit to Gubbio (one week) was made during the summer of 2011, prior to commencing my PhD. The fieldwork at Masada was conducted over a four week period during the spring of 2012.

Detailed field observations were made of outcrop- and meso-scale brittle deformation features, with a particular focus on the structures, geometries and fault rocks associated with localized PSZs. Structural orientation data were collected using a compass clinometer and have been plotted using the Stereo32, version 1.0.3, software. Oriented hand specimens were collected, again with a focus on taking samples of PSZs, in order to study hand-sample scale and micro-scale deformation features.

1.4.2 *Microstructural analyses*

1.4.2.1 *Sample preparation*

Thin sections were prepared by Ian Chaplin in the Rock Sectioning Laboratory in the Department of Earth Sciences at Durham University. Selected hand samples from the field were reduced in size using a rock saw and/or a trim saw, before being encapsulated and impregnated with a low

viscosity EPO-FLOW epoxy resin. Experimental gouge samples, due to their small size and delicate nature, were first encapsulated and impregnated before being trimmed. Samples were impregnated under both vacuum (in a vacuum oven) and pressure (in a Technomat® pressure unit) and then left for 3-4 days to post-cure. Once cured, samples were sliced in the desired orientation and then ground to 500 μm using a diamond disk. Particularly in the case of poorly cohesive samples, the impregnation through to grinding stages had to be repeated several times to ensure the retention of material. Samples were then lapped on a glass plate with Al_2O_3 powder (9.5 μm), to produce a flat, damage-free surface. This surface could then be bonded to a frosted glass slide using a bonding jig. After this, the prepared sections were lapped to 45 μm using a using a Logitech LP50 and were subsequently polished with a 0.3 μm Al_2O_3 powder in suspension on a polishing cloth (Plano-cloth), using a Buehler EcoMet 300 grinder-polisher.

1.4.2.2 *Analytical machines*

Thin sections were analysed using both an optical microscope and a scanning electron microscope (Logan and Semeniuk). For SEM analyses, samples were coated with a 20-40 μm thick (depending on sample composition) conductive layer of carbon prior to analysis, using a Cressington 108 Carbon/A coating machine, to reduce sample charging. Samples were then analysed using a Hitachi SU-70 FEG SEM at the G.J. Russell Microscopy Facility at Durham University. This machine was also used for Energy-Dispersive X-ray (EDX) analyses to determine the site-specific elemental composition of sample constituents. Occasional use of an FEI Helios Nanolab 600 focused ion-beam (FIB) microscope (also at the G.J. Russell Microscopy Facility) was employed in order to obtain higher-resolution secondary electron images of nano-scale textures. In these cases samples were coated with platinum, using a Cressington 328 coating machine, which facilitates the production of higher-resolution images compared to carbon coating. All microstructural analyses were performed by the author, after receiving comprehensive training from Leon Bowen (G.J. Russell Microscopy Facility).

1.4.3 *Mineralogical analyses*

The mineral compositions of undeformed (protolith) and deformed fault rocks were analysed using X-Ray Diffraction (XRD). During XRD, the unique crystallographic structure of a mineral phase will produce a unique diffraction pattern, according to Bragg's Law (Bragg and Bragg, 1913):

$$2dsin\theta = n\lambda \quad (3),$$

where d = the spacing between diffracting lattice planes, θ = the incident angle of the X-ray beam, n is a positive integer and λ = the wavelength of the incident X-ray beam. Two types of XRD

analyses were performed. The first is a bulk powder analysis, used to determine the bulk mineralogy of samples. The second is a clay fraction analysis, which is necessary for the identification of individual clay minerals.

1.4.3.1 *Sample preparation*

For bulk powder analysis, samples were prepared by either crushing (when the rock was cohesive) or gently disaggregating (when the rock was incohesive) the rock, and subsequently grinding the sample to a fine powder using an agate pestle and mortar. Samples were then passed through a 60 μm sieve, to remove any remaining larger particles, and packed into a 20 mm diameter well in a Perspex sample holder. The surface of the sample was then roughened using the sharp edge of a spatula. This preparation technique produces a random orientation of grains on the sample surface, which will reduce any biases during the subsequent analysis.

To identify clay minerals via XRD, it is necessary to first separate the clay fraction from the bulk rock and then to produce mounts where clay particles are oriented with their (001) planes parallel to the sample surface, in order for diagnostic basal reflections to be produced (Moore and Reynolds, 1997). For clay fraction analysis, we followed the method outlined in Moore and Reynolds (1997), with slight adaptations following advice from João Trabucho-Alexandre (personal communication). It was again necessary to first gently disaggregate samples, taking care not to cause damage to clay particles. Seeing as the major components of the rocks studied during the work presented here were calcite/aragonite and clay, the clay fraction could be easily separated from the bulk rock by placing the samples in 0.3 molar acetic acid to remove the carbonate. Once all the carbonate had dissolved, the samples were centrifuged at 3300 RPM for 3 minutes, in 45 ml centrifuge tubes, and the acid subsequently poured away. To remove any leftover acid, samples were rinsed with de-ionised (DI) water, centrifuged, and the water poured away, a process which was repeated three times.

The next stage was to separate the particle sizes that remain in the sample, to ensure that only the clay fraction ($0.2 < \phi < 2$ μm) is analysed. This was done by adding 10 ml of peptisation liquid (hydrated sodium pyrophosphate) to the sample remaining in the centrifuge tubes and then shaking well to mix. The centrifuge tubes were then filled to the top with DI water and the sample mixed again. The samples were then centrifuged at 750 RPM for 3 minutes and checked to see if all larger fragments had sunk to the bottom (if not, then the samples were re-centrifuged). The liquid in this sample, which contains clay-sized particles (<2 μm, according to Stokes' law for particle settling (Svedberg and Nichols, 1923)), was decanted into a new centrifuge tube. The new tube containing the liquid was then topped up with DI water and centrifuged at 3300 RPM for 30 minutes, to allow

for settling of particles between 0.2-2 μm. The liquid was then checked to see whether it was cloudy or not; if it was, then the samples were re-centrifuged. Once the liquid was clear, and thus interpreted to contain only particles <0.2 μm, it was discarded. The remaining solid at the bottom of the tube is what was used to create the clay mounts for analysis.

Before preparation of the clay mounts, the peptisation liquid was rinsed from the samples, so as not to produce a signal during analysis. This was done by adding DI water to the tubes, mixing, and centrifuging at 3300 RPM for 30 minutes, a process which was repeated three times. Once the water had been poured away, a gloopy liquid remained in the bottom of the tubes. This was pipetted onto a glass microscope slide and then left to air-dry. This preparation technique produces an oriented clay mount.

In order to differentiate between certain clay minerals, the mounted clays were run after under-going different pre-analysis treatments. First, all samples were run as air-dried. Then samples were run after treatment with ethylene glycol, which allows for the identification of clays within mixed-layers. This treatment involved placing ethylene glycol in the base of a vaporization dish, and placing the samples on a platform above. The covered dish was then left in an oven at 60°C overnight to allow samples to fully glycolate. The second treatment involves heating air-dried samples in a furnace for 24 hours at 550°C. This causes the structures of certain clay minerals to collapse, hence facilitating their identification.

1.4.3.2 *Diffractometer settings*

Samples were analysed in a Bruker D8 Advance Diffractometer (CuKα radiation) housed in the Department of Chemistry at Durham University. For bulk powder analyses, samples were analysed over a 2θ range of 2-90°, with a step-size of 0.02° at 0.3 seconds per step. Clay samples were analysed over a 2θ range of 2-50°, with a step-size of 0.02° at 0.85 seconds per step.

1.4.4 *Friction experiments*

1.4.4.1 *Low to high velocity rotary shear apparatus*

Friction experiments were performed using the low to high velocity rotary shear apparatus (model MIS-233-1-77, built by the Marui & Co., Ltd Company, Osaka, Japan) at the Rock Mechanics Laboratory, Durham University (Fig. 1.7a). The apparatus is housed in a rigid loading frame, made of assembled steel plates, and set up in a vertical configuration, secured to the floor by a base plate (Fig. 1.7a and c).

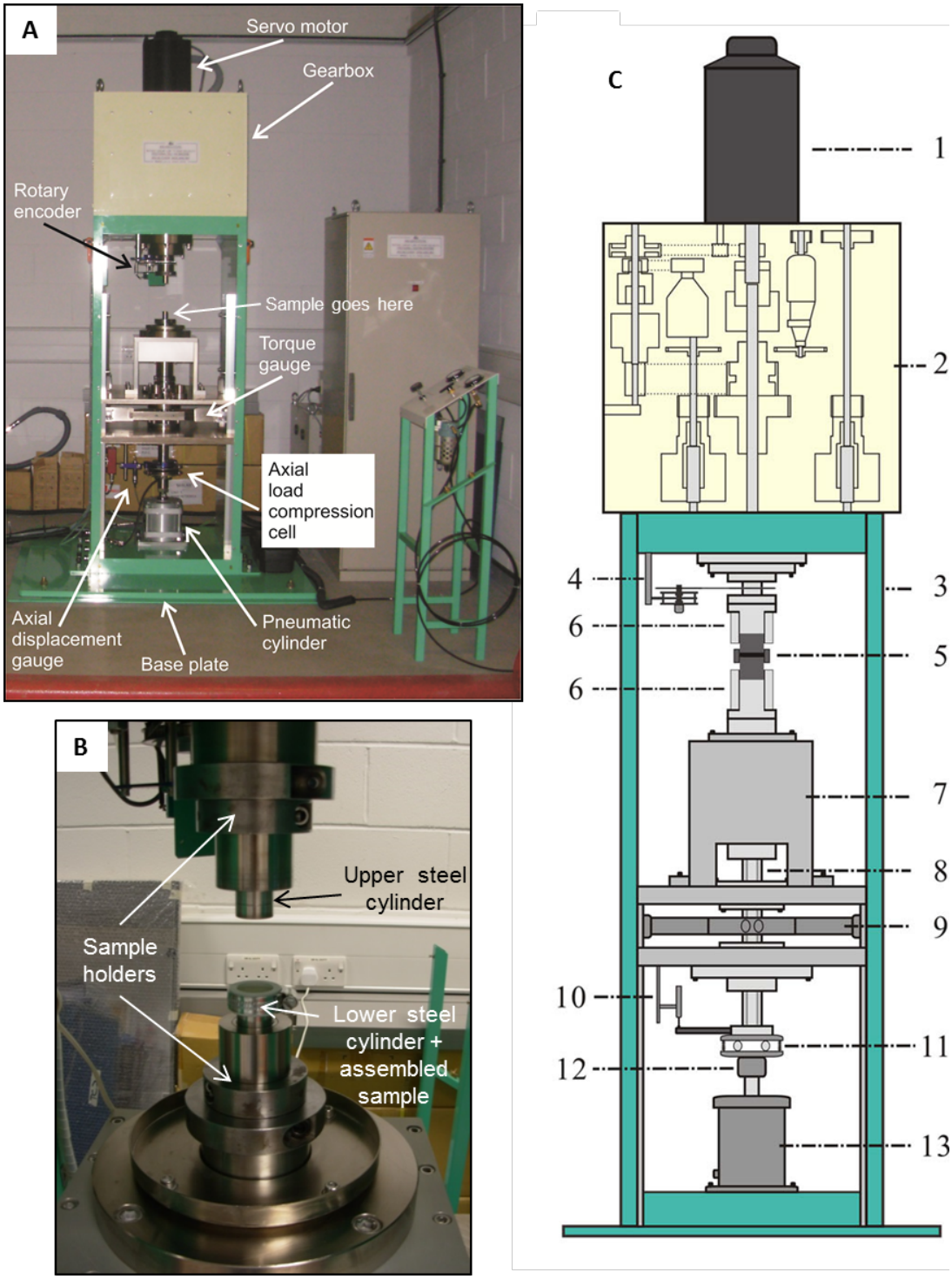

Figure 1.7 a) Photograph of the low to high velocity rotary shear apparatus installed in the Rock Mechanics Laboratory at Durham University. **b)** Close up image showing an assembled sample mounted in the apparatus. **c)** Schematic diagram showing the main units of the apparatus, from Ma et al. (2014). 1 = servo motor, 2 = gear box, 3 = loading frame, 4 = rotary encoder, 5 = specimen assembly, 6 = locking devices holding specimen assembly, 7 = frame for holding the lower loading column, 8 = axial loading column, 9 = torque gauge, 10 = axial displacement transducer, 12 = axial force gauge, 13 = air actuator.

Samples are mounted onto sample holders (Fig. 1.7b), where they are kept fixed to the main shafts and axially aligned during the experiments by a hydraulic mechanical lock (Fig. 1.7c). During the experiments, the upper main shaft rotates, whilst the lower one remains stationary. The upper main shaft of the apparatus is driven by an electric, servo-controlled motor with 11 kW power, 70 Nm rated torque and a maximum rotation speed of 1500 RPM. During the experiments presented herein, the electric servomotor was controlled manually. The revolving speed of the main shaft ranges from $1.5*10^{-6}$-1500 RPM, and is controlled using a system of clutches and reduction gears located in the gearbox (Fig. 1.7a and c). This corresponds to a peripheral slip rate of 6 cm/yr to 2 m/s, when applied to cylindrical samples with an outer diameter of 25 mm. The apparatus can accelerate to the maximum peripheral target speed of 2 m/s in 205-270 ms at normal stresses of 3 and 18 MPa, respectively, with accelerations of 3.7 and 4.9 m/s^2, respectively.

An axial load is applied to the lower main shaft by a pneumatic piston (Bellofram type cylinder) with an 82 mm stroke, and it is able to produce a thrust of 10 kN (Fig. 1.7a and c). The axial load system is equipped with a high-precision air regulator to reduce and automatically correct the load fluctuation during loading. Axial load measurements are performed using a thin compression load cell (strain gauge type, Fig. 1.7a and c) with a 10 kN capacity and a rated output of 2 mV/V ±0.5%. Axial load cell resolution is ±0.005 kN.

Torque values attained during the experiments are measured by two compression load cells (strain gauge type) (Fig. 1.7a and c), which are activated by a torque bar fixed to the lower, main shaft. The load cell capacity is 1 kN, with a rated output of 2 mV/V ±0.5%. Torque cell resolution is ±5*10-4 kN.

The axial displacement values attained during the experiments are measured using a high sensitivity displacement gauge (strain gauge type) with a 10 mm capacity and a rated output of 5 mV/V ±0.1% (Fig. 1.7a and c). Axial displacement resolution is $\pm 2*10^{-3}$ mm.

The revolution speed and the cumulative number of revolutions are measured by a tachometer and a pulse counter, respectively, based on the pulses measured by a rotary encoder with a capacity of 3600 pulses/revolution (Fig. 1.7a and c).

Details of experimental procedures will be presented in the relevant research chapters. Data during the experiments is recorded by a data logger. Data processing was subsequently performed using Matlab and graphs were produced using KaleidaGraph, version 4.1.1, graphing software.

1.4.4.2 *Sample assembly*

A synthetic fault zone was created by sandwiching up to 1.5 g of gouge (details of materials used will be presented in the relevant chapters) between two stainless steel cylinders (25 mm in diameter), whose ends are machined to simulate slip surface roughness and to ensure that slip localizes within the gouge layer, rather than at the boundaries between the gouge and the steel cylinders. During the experiments presented in Chapter 3, the cylinders used had ends which were

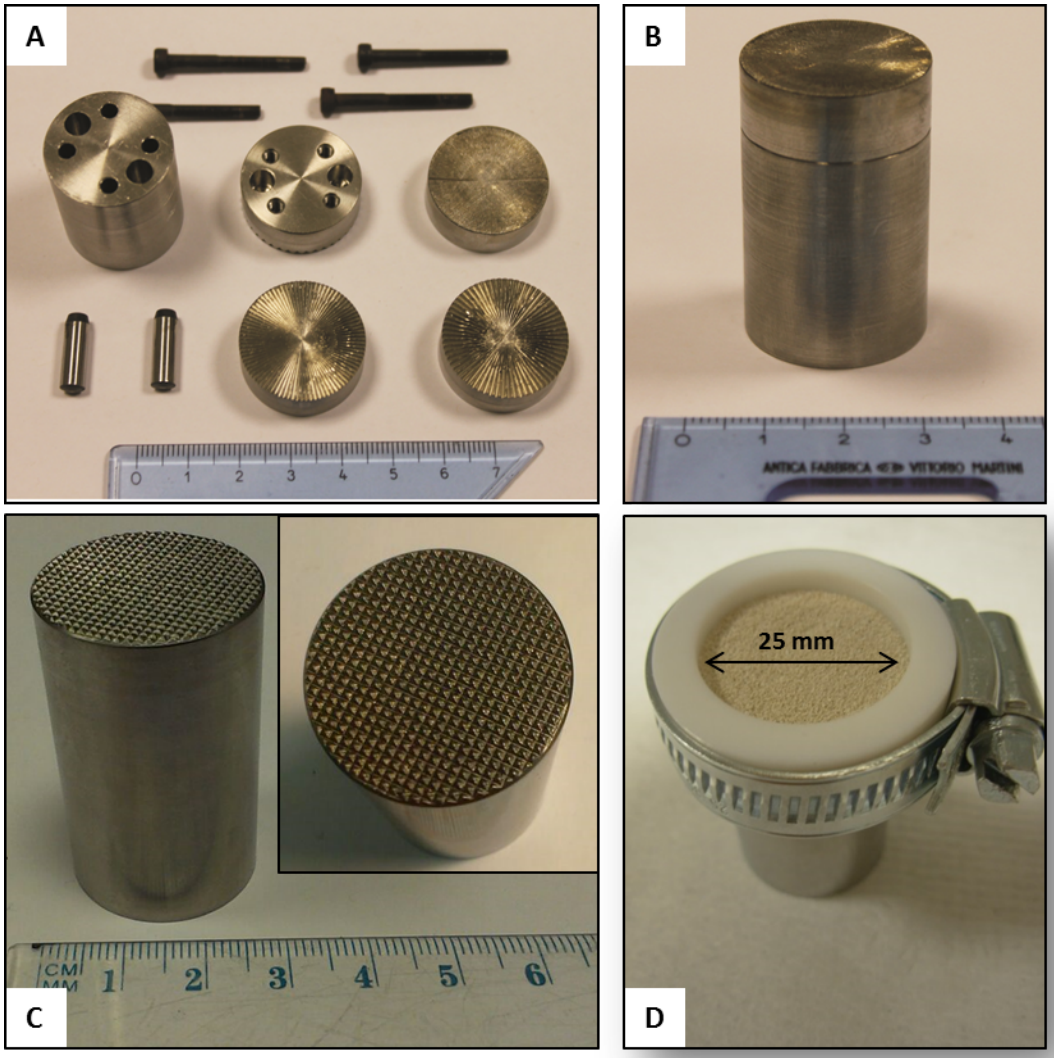

Figure 1.8 a) Disassembled components of the stainless steel cylinders used during the experiments presented in Chapter 3, which have radially grooved ends. **b)** Assembled cylinder used during the experiments presented during Chapter 3. **c)** One of the cylinders used during the experiments presented in Chapter 5, which had ends machined in a gridded fashion. **d)** Assembled gouge sample. A Teflon ring is placed around the upper part of the lower steel cylinder and is tightened in place using a hose clip. This creates a confined well in which the gouge can be placed.

machined with radial grooves of 500 μm height (Fig. 1.8a and b). During the experiments presented in Chapter 5, the cylinders used had ends which were machined to a depth of 500 μm in a gridded fashion (Fig. 1.8c). To limit gouge loss during the experiments, the sample assembly was confined using a Teflon ring (Mizoguchi et al., 2007), which was tightened to the steel cylinder using a hose clip (Fig. 1.8d). The inner edges of the Teflon rings are machined to reduce their sharpness and avoid ring damage and sample contamination by Teflon.

1.4.4.3 *Experimental determination of slip rate and slip for cylindrical samples*

To calculate the slip rate within the gouge layer, it is necessary to convert angular velocity, ω (in rad/s; RPM can be converted to rad/s by multiplying by $2\pi/60$) to linear velocity, v (in m/s). This can be done using the equation:

$$v = \omega r \qquad (4),$$

where r is the sample radius (in metres). Also, given the cylindrical shape of the samples, v increases with sample radius. Thus, the slip rate that we use is an "equivalent slip rate", V_e (Hirose and Shimamoto, 2005; Shimamoto and Tsutsumi, 1994), corresponding to the slip rate within the sample at *2/3r*. Taking into account the above factors, the equation for calculating V_e is:

$$V_e = \frac{4\pi Rr}{3\times 60} \qquad (5),$$

where R is the revolution rate of the motor in RPM. We refer to the equivalent slip rate simply as the slip rate v in this thesis and, as a consequence, the, displacement, d is calculated as

$$d = V_e t \qquad (6),$$

where t is the time.

1.5 *Thesis outline*

This thesis is presented as four "journal-style" research chapters (Chapters 2-5), in addition to this introductory chapter (Chapter 1), which describes the thesis aims, methodology and organization, and a final discussion chapter (Chapter 6), which discusses and compares the main findings and conclusions of the fore-going research chapters. A brief synopsis of each of the research chapters, and details of author contributions, are included below. A number of appendices are also included at the end of this thesis, the contents of which are outlined below.

1.5.1 *Research Chapters*

Chapter 2: **"***Lithological controls on the deformation mechanisms operating within carbonate-hosted faults during the seismic cycle"*

A significant proportion of moderate-large earthquakes, plus aftershocks, nucleate within and propagate through upper-crustal carbonate-dominated sequences, where the effects of lithological variations on fault behaviour are poorly understood. We studied the Gubbio fault, which is an active (1984, Ms = 5.2) (Haessler et al., 1988) normal fault in the Northern Apennines of Italy, hosted in Mesozoic-Cenozoic limestones and interbedded phyllosilicate-rich marls. An intercalation of field, microstructural and mineralogical observations is used to constrain the dominant deformation mechanisms operating within the limestone-hosted fault-core domains, compared to those operating within the marl-hosted domains. A model is subsequently proposed for the distribution of seismicity in lithologically complex carbonate-hosted faults over the course of the seismic cycle.

This chapter has been published in its presented form in the Journal of Structural Geology (Appendix 3): *Bullock, R. J., N. De Paola, R. E. Holdsworth, and J. Trabucho-Alexandre (2014), Lithological controls on the deformation mechanisms operating within carbonate-hosted faults during the seismic cycle, Journal of Structural Geology, 58(0), 22-42, doi:http://dx.doi.org/10.1016/j.jsg.2013.10.008.*

The author conducted the fieldwork (with the help of two field assistants: Eddie Dempsey and Igor Faoro), collated field data, performed microstructural analyses (with the assistance of Leon Bowen at the G.J. Russel microscopy facility, Durham University) and X-Ray diffraction (XRD) analyses (under the guidance of João Trabucho-Alexandre, who also assisted in interpretation of the XRD spectra). The manuscript was written by the author, taking into account supervisory feedback, plus editorial comments and suggestions from the co-authors. In addition, the article was reviewed by Cristiano Collettini, an anonymous reviewer and JSG editor William Dunne, whose thoughtful comments helped to improve the manuscript.

Chapter 3: *"An experimental investigation into the role of phyllosilicate content on earthquake propagation during seismic slip in carbonate faults"*

Upper-crustal carbonate faults commonly contain small amounts of phyllosilicate in their slip zones, due to pressure-solution and/or clay smear processes (Bullock et al., 2014 (Chapter 2); Collettini et al., 2013; Tesei et al., 2013). To assess the effect of phyllosilicate content on

earthquake propagation in carbonate faults, high-velocity friction experiments using a rotary shear apparatus were performed at 1.3 m/s on end-members of calcite, illite-smectite and smectite gouge, and on mixtures of these materials. Experiments were performed at 9 MPa normal load, under room-humidity and water-saturated conditions, and were terminated at distinct stages during their frictional evolution to allow for sample recovery and inspection of gouge microstructures. Distinct stages in the frictional evolution of the gouges are linked to distinct stages in their microstructural evolution, enabling the proposal of a micro-mechanical model which explains the frictional behaviour of dry and water-saturated clay-bearing gouges during seismic slip. Our results have significant implications for the propagation of earthquake ruptures in clay-bearing carbonate faults, and also for the identification of seismic markers in clay-bearing carbonate fault zones.

This chapter has been published in its present form in the Journal of Geophysical Research (Appendix 4): *Bullock, R. J., N. De Paola, and R. E. Holdsworth (2015), An experimental investigation into the role of phyllosilicate content on earthquake propagation during seismic slip in carbonate faults, Journal of Geophysical Research: Solid Earth, 120, 3187-3207, doi:10.1002/2015JB011914.*

The author conducted the experimental work (under the guidance of Nicola De Paola), data processing and microstructural analyses and wrote the manuscript. The author was responsible for the concept development of the paper, which benefited from supervisory feedback, editorial comments and suggestions from the PhD supervisors. Brett Carpenter and Cristiano Collettini provided constructive reviews which helped to clarify and strengthen the manuscript.

Chapter 4: *"Structure and deformation mechanisms of near-surface, seismogenic fault zones in poorly lithified sediments"*

Constraining the structure and deformation mechanisms of faults in the shallow-most portion of the Earth's crust is necessary in order to understand how seismic energy is either dissipated or transmitted during rupture propagation towards the surface. We describe the architecture, geometries and microstructures of seismogenic normal faults within the Masada fault zone, Israel. The faults formed at the surface in poorly lithified, high-porosity (up to 50%), brine-saturated lake sediments of the Pleistocene Lisan Formation, which were deposited in the palaeo-Dead Sea (Schramm et al., 2000). The sediments comprise alternating 1-3 mm thick laminae of ultrafine-grained aragonite and clay-rich clastic detritus. Field and microstructural observations are used to develop a model for fault evolution in near-surface, poorly lithified, clay-bearing, brine-saturated

sediments, and to propose mechanisms by which seismic rupture propagation through such materials may be facilitated. A particular emphasis is placed on how our observations may be used, in part, to explain the occurrence of tsunamigenic earthquakes in subduction zone settings.

The author conducted the fieldwork, with some assistance from PhD supervisors Shmuel Marco and Nicola De Paola, and from students from the Department of Geophysics at Tel Aviv University: Ran Issachar, Ofir Yosifson and Sagea Tahan. The author also collated the field data, conducted the microstructural analyses and wrote the paper. The presented manuscript has benefited from editorial comments and suggestions from PhD supervisors Nicola De Paola, Robert Holdsworth and Shmuel Marco.

Chapter 5: *"The frictional properties and deformation mechanisms of faults in near-surface, poorly lithified sediments: implications for rupture propagation in the shallow crust"*

Earthquakes which rupture the Earth's surface are typically the most damaging: in continental settings they cause vast damage to infrastructure and in marine settings they generate devastating tsunamis. The recent surge of 'great' earthquakes (Lay, 2015), plus observations of localized earthquake-hosting principal slip zones close to the Earth's surface (such as those that will be described in Chapter 4), highlights the need to better constrain the frictional properties of shallow-crustal fault zones in order to improve our understanding of the factors which control the propagation of earthquakes towards the surface. We designed a set of rotary shear friction experiments on synthetic gouges containing ultrafine-grained aragonite and clay-rich clastic detritus, derived from poorly lithified sediments collected from the seismogenic Masada fault zone in Israel (studied in Chapter 4). We performed low-velocity rate-and-state friction experiments and high-velocity friction experiments at normal loads of 1-18 MPa (equivalent to a depth range of 0.05-1 km), and under room-humidity, water-saturated and brine-saturated conditions. We also studied the microstructures of the deformed gouges. Results are discussed in the context of the implications for the seismic behaviour of near-surface faults, and the implications for the identification of seismic markers in natural shallow-crustal fault zones in poorly lithified sediments.

The author conducted the experimental work, with assistance from Nicola De Paola and Shmuel Marco. The author also performed all data processing and microstructural work and wrote the manuscript after supervisory discussions with Nicola De Paola, Robert Holdsworth and Shmuel Marco, who also provided editorial comments and some suggestions on the manuscript.

1.5.2 *Appendices*

Appendix 1 contains additional field observations, experimental data and microstructural observations to complement the data presented in Chapter 3.

Appendix 2 contains details of mineralogical analyses, additional experimental data, and data tables to complement the data presented in Chapter 5.

Appendix 3 is the published version of Chapter 2.

Appendix 4 is the published version of Chapter 3.

Appendix 5 is a paper published in EPSL, on which I am a co-author (my contribution was towards the microstructural analyses and conceptual development):
De Paola, N., Holdsworth, R.E., Viti, C., Collettini, C., Bullock, R.J. (2015) Can grain size sensitive creep lubricate faults during the initial stages of earthquake propagation? Earth and Planetary Science Letters, 431, 48-58.

References

Amontons, G., 1699. De la resistance causee dans les machines. Memories del l'Academie Royale, 206.
Behnsen, J., Faulkner, D.R., 2012. The effect of mineralogy and effective normal stress on frictional strength of sheet silicates. Journal of Structural Geology.
Blanpied, M., Tullis, T., Weeks, J., 1987. Frictional behavior of granite at low and high sliding velocities. Geophysical Research Letters 14, 554-557.
Brace, W.F., Byerlee, J.D., 1966. Stick-Slip as a Mechanism for Earthquakes. Science 153, 990-992.
Bragg, W.H., Bragg, W.L., 1913. The Reflection of X-rays by Crystals.
Brantut, N., Schubnel, A., Rouzaud, J.N., Brunet, F., Shimamoto, T., 2008. High-velocity frictional properties of a clay-bearing fault gouge and implications for earthquake mechanics. Journal of Geophysical Research 113, B10401.
Bullock, R.J., De Paola, N., Holdsworth, R.E., Trabucho-Alexandre, J., 2014. Lithological controls on the deformation mechanisms operating within carbonate-hosted faults during the seismic cycle. Journal of Structural Geology 58, 22-42.
Byerlee, J., 1978. Friction of rocks. Pure and applied Geophysics 116, 615-626.
Byerlee, J., Summers, R., 1976. A note on the effect of fault gouge thickness on fault stability. International Journal of Rock Mechanics and Mining Sciences & Geomechanics Abstracts 13, 35-36.

Byrne, D.E., Davis, D.M., Sykes, L.R., 1988. Loci and maximum size of thrust earthquakes and the mechanics of the shallow region of subduction zones. Tectonics 7, 833-857.
Chiarabba, C., Amato, A., Anselmi, M., Baccheschi, P., Bianchi, I., Cattaneo, M., Cecere, G., Chiaraluce, L., Ciaccio, M., De Gori, P., 2009. The 2009 L'Aquila (central Italy) Mw6. 3 earthquake: Main shock and aftershocks. Geophysical Research Letters 36, L18308.
Collettini, C., Viti, C., Tesei, T., Mollo, S., 2013. Thermal decomposition along natural carbonate faults during earthquakes. Geology 41, 927-930.
De Paola, N., Chiodini, G., Hirose, T., Cardellini, C., Caliro, S., Shimamoto, T., 2011a. The geochemical signature caused by earthquake propagation in carbonate-hosted faults. Earth and Planetary Science Letters 310, 225-232.
De Paola, N., Hirose, T., Mitchell, T., Di Toro, G., Viti, C., Shimamoto, T., 2011b. Fault lubrication and earthquake propagation in thermally unstable rocks. Geology 39, 35-38.
Delouis, B., Nocquet, J.M., Vallée, M., 2010. Slip distribution of the February 27, 2010 Mw= 8.8 Maule earthquake, central Chile, from static and high-rate GPS, InSAR, and broadband teleseismic data. Geophysical Research Letters 37.
Di Toro, G., Goldsby, D.L., Tullis, T.E., 2004. Friction falls towards zero in quartz rock as slip velocity approaches seismic rates. Nature 427, 436-439.
Di Toro, G., Han, R., Hirose, T., De Paola, N., Nielsen, S., Mizoguchi, K., Ferri, F., Cocco, M., Shimamoto, T., 2011. Fault lubrication during earthquakes. Nature 471, 494-498.
Di Toro, G., Hirose, T., Nielsen, S., Pennacchioni, G., Shimamoto, T., 2006. Natural and Experimental Evidence of Melt Lubrication of Faults During Earthquakes. Science 311, 647-649.
Di Toro, G., Mittempergher, S., Ferri, F., Mitchell, T.M., Pennacchioni, G., 2012. The contribution of structural geology, experimental rock deformation and numerical modelling to an improved understanding of the seismic cycle: Preface to the Special Volume "Physico-chemical processes in seismic faults". Journal of Structural Geology 38, 3-10.
Dieterich, J.H., 1972. Time-dependent friction in rocks. Journal of Geophysical Research 77, 3690-3697.
Dieterich, J.H., 1979. Modeling of rock friction: 1. Experimental results and constitutive equations. Journal of Geophysical Research: Solid Earth 84, 2161-2168.
Dieterich, J.H., 1981. Constitutive properties of faults with simulated gouge. Mechanical behavior of crustal rocks: the Handin volume, 103-120.
Dieterich, J.H., Kilgore, B., 1996. Implications of fault constitutive properties for earthquake prediction. Proceedings of the National Academy of Sciences of the United States of America 93, 3787-3794.
Fossen, H., 2010. Structural geology. Cambridge University Press.
Goldsby, D.L., Tullis, T.E., 2002. Low frictional strength of quartz rocks at subseismic slip rates. Geophysical Research Letters 29, 25-21-25-24.
Griffith, A.A., 1920. The phenomena of rupture and flow in solids. Philosophical transactions of the royal society of london. Series A, containing papers of a mathematical or physical character, 163-198.
Haessler, H., Gaulon, R., Rivera, L., Console, R., Frogneux, M., Gasparini, G., Martel, L., Patau, G., Siciliano, M., Cisternas, A., 1988. The Perugia (Italy) earthquake of 29, April 1984: a microearthquake survey. Bulletin of the Seismological Society of America 78, 1948-1964.
Han, R., Hirose, T., Shimamoto, T., 2010. Strong velocity weakening and powder lubrication of simulated carbonate faults at seismic slip rates. Journal of Geophysical Research 115, B03412.
Han, R., Hirose, T., Shimamoto, T., Lee, Y., Ando, J., 2011. Granular nanoparticles lubricate faults during seismic slip. Geology 39, 599-602.
Han, R., Shimamoto, T., Hirose, T., Ree, J.H., Ando, J., 2007. Ultralow friction of carbonate faults caused by thermal decomposition. Science 316, 878-881.
Hirose, T., Shimamoto, T., 2005. Growth of molten zone as a mechanism of slip weakening of simulated faults in gabbro during frictional melting. Journal of Geophysical Research: Solid Earth 110, n/a-n/a.

Hyndman, R., Yamano, M., Oleskevich, D., 1997. The seismogenic zone of subduction thrust faults. The Island Arc 6, 244-260.
Ide, S., Baltay, A., Beroza, G.C., 2011. Shallow Dynamic Overshoot and Energetic Deep Rupture in the 2011 Mw 9.0 Tohoku-Oki Earthquake. Science 332, 1426-1429.
Kanamori, H., 2001. Energy budget of earthquakes and seismic efficiency. Earthquake Thermodynamics and Phase Transformations in the Earth's Interior 76, 293-305.
Kanamori, H., Brodsky, E.E., 2004. The physics of earthquakes. Reports on Progress in Physics 67, 1429.
Kanamori, H., Rivera, L., 2006. Energy partitioning during an earthquake. Earthquakes: Radiated Energy and the Physics of Faulting, 3-13.
Kohlstedt, D.L., Evans, B., Mackwell, S.J., 1995. Strength of the lithosphere: Constraints imposed by laboratory experiments. Journal of Geophysical Research: Solid Earth 100, 17587-17602.
Lay, T., 2015. The surge of great earthquakes from 2004 to 2014. Earth and Planetary Science Letters 409, 133-146.
Logan, B.W., Semeniuk, V., 1976. Dynamic metamorphism: processes and products in Devonian carbonate rocks, Canning Basin, Western Australia. Geological Society of Australia.
Ma, S., Shimamoto, T., Yao, L., Togo, T., Kitajima, H., 2014. A rotary-shear low to high-velocity friction apparatus in Beijing to study rock friction at plate to seismic slip rates. Earthq Sci 27, 469-497.
Marone, C., 1998. Laboratory-derived friction laws and their application to seismic faulting. Annual Review of Earth and Planetary Sciences 26, 643-696.
Marone, C., Raleigh, C.B., Scholz, C., 1990. Frictional behavior and constitutive modeling of simulated fault gouge. J. geophys. Res 95, 7007-7025.
Marone, C., Vidale, J.E., Ellsworth, W.L., 1995. Fault healing inferred from time dependent variations in source properties of repeating earthquakes. Geophysical Research Letters 22, 3095-3098.
Marone, C.J., Scholtz, C., Bilham, R., 1991. On the mechanics of earthquake afterslip. Journal of Geophysical Research: Solid Earth (1978–2012) 96, 8441-8452.
Mizoguchi, K., Hirose, T., Shimamoto, T., Fukuyama, E., 2007. Reconstruction of seismic faulting by high-velocity friction experiments: An example of the 1995 Kobe earthquake. Geophysical Research Letters 34, L01308.
Moore, D.M., Reynolds, R.C., 1997. X-Ray Diffraction and the Identification and Analysis of Clay Minerals. Oxford University Press.
Muhuri, S.K., Dewers, T.A., Scott, T.E., Reches, Z.e., 2003. Interseismic fault strengthening and earthquake-slip instability: Friction or cohesion? Geology 31, 881-884.
Reches, Z.e., Lockner, D.A., 1994. Nucleation and growth of faults in brittle rocks. Journal of Geophysical Research: Solid Earth 99, 18159-18173.
Ruina, A., 1983. Slip instability and state variable friction laws. J. geophys. Res 88, 359-310.
Rutter, E., Maddock, R., Hall, S., White, S., 1986. Comparative microstructures of natural and experimentally produced clay-bearing fault gouges. Pure and Applied Geophysics 124, 3-30.
Scholz, C., 1988. The brittle-plastic transition and the depth of seismic faulting. Geologische Rundschau 77, 319-328.
Scholz, C.H., 1998. Earthquakes and friction laws. Nature 391, 37-42.
Schramm, A., Stein, M., Goldstein, S., 2000. Calibration of the 14 C time scale to 50 kyr by 234 U-230 Th dating of sediments from Lake Lisan (the paleo-Dead Sea): earth Planet. Sci Lett 175, 27-40.
Shimamoto, T., Tsutsumi, A., 1994. A new rotary-shear high-speed frictional testing machine: Its basic design and scope of research (in Japanese with English abstract). Journal of the Tectonic Research group of Japan 39, 65-78.
Sibson, R., 1977. Fault rocks and fault mechanisms. Journal of the Geological Society 133, 191-213.

Sibson, R.H., 1986. Earthquakes and Rock Deformation in Crustal Fault Zones. Annual Review of Earth and Planetary Sciences 14, 149-175.
Sibson, R.H., 1989. Earthquake faulting as a structural process. Journal of Structural Geology 11, 1-14.
Sibson, R.H., 2003. Thickness of the seismic slip zone. Bulletin of the Seismological Society of America 93, 1169-1178.
Spray, J.G., 2005. Evidence for melt lubrication during large earthquakes. Geophysical Research Letters 32, n/a-n/a.
Svedberg, T., Nichols, J.B., 1923. DETERMINATION OF SIZE AND DISTRIBUTION OF SIZE OF PARTICLE BY CENTRIFUGAL METHODS. Journal of the American Chemical Society 45, 2910-2917.
Tesei, T., Collettini, C., Viti, C., Barchi, M.R., 2013. Fault architecture and deformation mechanisms in exhumed analogues of seismogenic carbonate-bearing thrusts. Journal of Structural Geology 55, 167-181.
Townend, J., Zoback, M.D., 2000. How faulting keeps the crust strong. Geology 28, 399-402.
Tse, S.T., Rice, J.R., 1986. Crustal earthquake instability in relation to the depth variation of frictional slip properties. Journal of Geophysical Research: Solid Earth (1978–2012) 91, 9452-9472.
Ujiie, K., Tsutsumi, A., 2010. High-velocity frictional properties of clay-rich fault gouge in a megasplay fault zone, Nankai subduction zone. Geophysical Research Letters 37, L24310.
Xu, X., Wen, X., Yu, G., Chen, G., Klinger, Y., Hubbard, J., Shaw, J., 2009. Coseismic reverse- and oblique-slip surface faulting generated by the 2008 Mw 7.9 Wenchuan earthquake, China. Geology 37, 515-518.

Chapter 2

Lithological controls on the deformation mechanisms operating within carbonate-hosted faults during the seismic cycle

Abstract

A significant proportion of moderate-large earthquakes, plus aftershocks, nucleate within and propagate through upper-crustal carbonate-dominated sequences, where the effects of lithological variations on fault behaviour are poorly understood. The Gubbio fault is an active (1984, Ms = 5.2) normal fault in Italy, hosted in Mesozoic-Cenozoic limestones and interbedded marls. Fault core domains derived from limestone at the studied outcrop are characterised by fractures/hydrofractures and breccias and host a number of localised (<1.5 mm wide) principal slip zones (PSZs). The majority of displacement of up to 230 m is concentrated in these PSZs, which comprise cataclasites, gouges, and calcite veins. Degassing bubbles, 'quenched' calcite, and the transformation of smectite to illite, are also observed within PSZs, implying frictional heating and seismic slip. In contrast, marl-rich domains exhibit distributed shear planes bounding a continuous and pervasive foliation, defined by phyllosilicate-rich pressure-solution seams. Microstructures in the seams include folds/kinks of phyllosilicates and pressure shadows around clasts, consistent with aseismic fault creep. A model is proposed for the behaviour of lithologically complex carbonate-hosted faults during the seismic cycle, whereby limestone-dominated fault core domains behave in a predominantly seismic manner, whereas phyllosilicate-rich domains behave in a predominantly aseismic manner.

2.1 *Introduction*

The large-scale architecture of upper crustal faults at <5 km depth comprises either a single high-strain fault core surrounded by a damage zone (e.g. Chester et al., 1993), or multiple high-strain cores, which bound lenses of damaged material (e.g. Faulkner et al., 2003). The differentiation between fault core and damage zone is generally based on the presence and spatial distribution of deformation products (Chester and Logan, 1986; Chester et al., 1993; Shipton et al., 2006). The fault core, which ranges from a few metres up to a few tens of metres wide, consists of cataclastically deformed fault rocks and typically contains one or more principal slip surfaces (PSSs) (Shipton et al., 2006; Faulkner et al., 2010). Damage zones, which are up to a few hundred metres in width, consist of fractured protolith rocks and smaller displacement subsidiary slip surfaces (Faulkner et al., 2010). The fault core is where most of the displacement is accommodated, and the deformation processes occurring here are the focus of the present paper.

Fault core architectures vary widely between faults and appear to be controlled, in part, by the composition of the protolith. Upper crustal faults derived from carbonates (e.g. Agosta and Aydin, 2006; Micarelli et al., 2006; De Paola et al., 2008; Bastesen and Braathen, 2010; Molli et al., 2010; Smith et al., 2011a; Fondriest et al., 2012) and crystalline rocks (e.g. Chester and Chester, 1998;

Wibberley et al., 2003; Walker et al., 2013) tend to exhibit narrow fault cores that are less than a few metres in width, comprising cohesive and incohesive random-fabric fault rocks such as breccias, cataclasites and gouges (Sibson, 1977). The majority of the displacement within these fault cores is localised along discrete PSSs and within their associated principal slip zones (PSZs).

Numerous field studies of major seismogenic faults suggest that slip during individual earthquake events is localised along these PSZs, which are typically no more than a few cm thick (see Sibson, 2003, for a review). Notable examples include: the PSZ associated with the 1999 Mw 7.6 Chi Chi thrust earthquake in Taiwan, which has been estimated to be just 1 mm thick (Kuo et al., 2013); the Nojima fault, responsible for the 1995 M 7.2 Kobe earthquake in Japan, which contains several gouge and pseudotachylyte layers, each less than a few mm thick (Otsuki et al., 2003); and the PSZ responsible for the 2008 Ms 8.0 Wenchuan earthquake in China, which comprises a ~1 cm thick layer of fault gouge (Li et al., 2013). At the microscale, PSZs are often observed to contain sub-zones, which range from a few hundred microns to a few millimetres in width, composed of variably developed cataclasites and gouges and frequently displaying Riedel shear geometries (e.g. Power and Tullis, 1989; Otsuki et al., 2003; De Paola et al., 2008; Smith et al., 2011a; Fondriest et al., 2012).

In contrast, upper crustal fault zones rich in phyllosilicates typically display much wider fault cores, often adhering to the multiple fault cores model. For example, the exhumed Carboneras fault in SE Spain has a fault core up to 1 km wide (Faulkner et al., 2003), which comprises numerous high-strain gouge zones of a few metres in thickness (Faulkner et al., 2003). Similarly, the SAFOD (San Andreas Fault Observatory at Depth) borehole core and field studies of the Median Tectonic Line in Japan have revealed several phyllosilicate-rich fault core strands, each >1 m wide (Zoback et al., 2010; Holdsworth et al., 2011; Jefferies et al., 2006). Rather than displacement being localised within PSZs, it is uniformly distributed within each gouge band; and rather than random-fabric fault rocks being the dominant deformation products, phyllosilicate-rich fault cores typically display a continuous, highly foliated fabric, though Riedel shear geometries are still conspicuous features (e.g. Rutter et al., 1986; Faulkner et al., 2003; Rutter et al., 2012).

Consequently, in lithologically heterogeneous, upper crustal fault zones, where crystalline/carbonate and phyllosilicate-rich protoliths are interlayered, we might expect to see a complex fault zone architecture with separate domains of localised and distributed deformation. This geometry has been documented along ancient, exhumed examples of presently inactive major strike-slip faults (e.g. the Carboneras fault zone, Faulkner et al., 2003), low-angle normal faults (e.g. the Zuccale fault in Central Italy, Collettini and Holdsworth 2004; Smith et al., 2011b) and in

accretionary complexes (e.g. the Chrystalls Beach Complex mélange, New Zealand, Fagereng and Sibson, 2010). Attention now is turning to active fault zones, in an attempt to understand how lithological heterogeneities within multi-layered sequences cut by a fault may affect not only the fault zone architecture, but also the seismic behaviour of the fault (e.g. Nemser and Cowan, 2009; Chiaraluce, 2012; Gratier et al., 2013; Tesei et al., 2013).

Quartzo-feldspathic and carbonate rocks typically have sliding friction coefficients in the Byerlee range of 0.6-0.85 (Byerlee, 1978) and experimentally exhibit slip-weakening and velocity-weakening behaviour (Logan et al., 1992; Beeler et al., 1996; Marone et al., 1990; Gu and Wong, 1994; Verberne et al., 2010; Collettini et al., 2011), which is necessary for earthquake nucleation and unstable stick-slip behaviour (Dieterich and Kilgore, 1994; Marone, 1998; Scholz, 1998). These lithologies also display dynamic-weakening behaviour during high-velocity rotary shear experiments (see Di Toro et al., 2011, for a review), with the coefficient of friction reducing to sub-Byerlee values (<0.2) at seismic slip velocities, facilitating earthquake propagation.

In contrast, many phyllosilicates (e.g. talc, smectites) are weak, particularly when wet, (sliding friction <<0.3, e.g. Behnsen and Faulkner, 2012) and most types exhibit velocity-strengthening behaviour (e.g. Saffer et al., 2001; Saffer and Marone, 2003; Moore and Lockner, 2004; Ikari et al., 2007; Morrow et al., 2007; Ikari et al., 2009; Tembe et al., 2010; Ikari et al., 2011; Moore and Lockner, 2011; Behnsen and Faulkner, 2012; Sone et al., 2012; Tesei et al., 2012). Velocity-strengthening behaviour does not favour earthquake nucleation and rock units displaying this behaviour are expected to act as barriers to earthquake propagation due to a negative stress drop (Scholz, 1998). Thus, upper crustal fault rocks rich in weak phyllosilicate minerals are thought to deform predominantly aseismically by fault creep. For example, the creeping behaviour of faults such as the San Andreas is attributed to the presence of smectitic phyllosilicates in fault gouges (e.g. Carpenter et al., 2011; Lockner et al., 2011, Holdsworth et al., 2011).

Over the course of the seismic cycle, a fault may experience a broad spectrum of slip rates. These range from mm/yr, during the interseismic period, to mm/day-week during the pre-seismic (earthquake nucleation) and post-seismic (afterslip) periods and, then, to slip rates of m/s during earthquake propagation. It seems reasonable to hypothesise that lithological heterogeneities within the fault core will strongly influence which parts of a fault zone deform seismically or aseismically during the different seismic intervals. To further investigate this proposal, we document here the deformational and microstructural characteristics of the Gubbio normal fault (1984, Ms = 5.2) in the northern Apennines of Italy (Fig. 2.1a). This upper-crustal, seismically active fault deforms a succession of alternating limestone and cm-scale marl beds. Outcrop to microscale deformation

features within the Gubbio fault zone have previously been studied by Bussolotto et al. (2007), who characterised the spatial and temporal relationships of structures in the fault zone, together with a determination of the P/T conditions and fluid behaviour during deformation. Here, we use a combination of microstructural (optical microscopy and field emission scanning electron microscopy, SEM) and mineralogical analyses (Energy-dispersive X-ray spectroscopy, EDX, and X-ray diffraction, XRD) to study the dominant deformation mechanisms active within the fault core, and to assess the likely influence of lithology on deformation style. We use these findings to propose a conceptual model for the long- (inter- and post-seismic period) and short-term (co-seismic) frictional behaviour of the fault zone.

2.2 *Geological setting*

The northern Apennines of Italy have undergone NE-SW shortening since the middle Miocene, resulting in the development of a NE-verging fold and thrust belt (Barchi et al., 1998b). In the Gubbio area, this deformation is represented by the NW-SE striking Gubbio anticline (De Paola et al., 2006 and references therein). An upper Pliocene-Quaternary late-orogenic extensional regime is superimposed upon the folds and thrusts, forming a series of extensional basins bounded by NNW-SSE trending normal faults (Barchi et al., 1998a; Boncio and Lavecchia, 2000) (Fig. 2.1a). This extensional regime currently dominates the tectonics of the northern Apennines, although it has a relatively slow separation rate of 2-3 mm/yr (D'Agostino et al., 2009).

The Gubbio fault is an active segment of a 150 km long fault system known as the Umbria Fault System (Collettini et al., 2003). The surface trace is 22 km long, striking NW-SE (~N130˚) (Figs. 2.1a and 2.2a). Seismic reflection data suggest that it has a listric profile at depth, with average dips of ~60-70˚ to the SW at the surface, decreasing to 10-15˚ at ~6 km, where it reactivates a pre-existing thrust fault (Mirabella et al., 2004) (Fig. 2.1a). At the surface, the fault juxtaposes Jurassic-Oligocene carbonates, belonging to the Umbria-Marche succession, in the footwall against Quaternary fluvio-lacustrine deposits, of the Gubbio Basin, in the hangingwall (Collettini et al., 2003; Bussolotto et al., 2007) (Fig. 2.1b).

A maximum displacement of 3.2 km at the centre of the Gubbio Basin was estimated by Collettini et al. (2003), which accumulated during multiple tectonic phases. Historical and instrumental records of moderate-large earthquakes occurring on the Gubbio fault are limited, since no permanent station coverage exists (Collettini et al., 2003; Pucci et al., 2003). However in 1984, the Gubbio area experienced a Ms 5.2 (Haessler et al., 1988) earthquake, located ~10 km south of the town of Gubbio at 7 km depth (ISC, 2001), and this event was attributed to movement on the Gubbio fault (e.g. Collettini et al., 2003). A temporary seismic network installed three days after

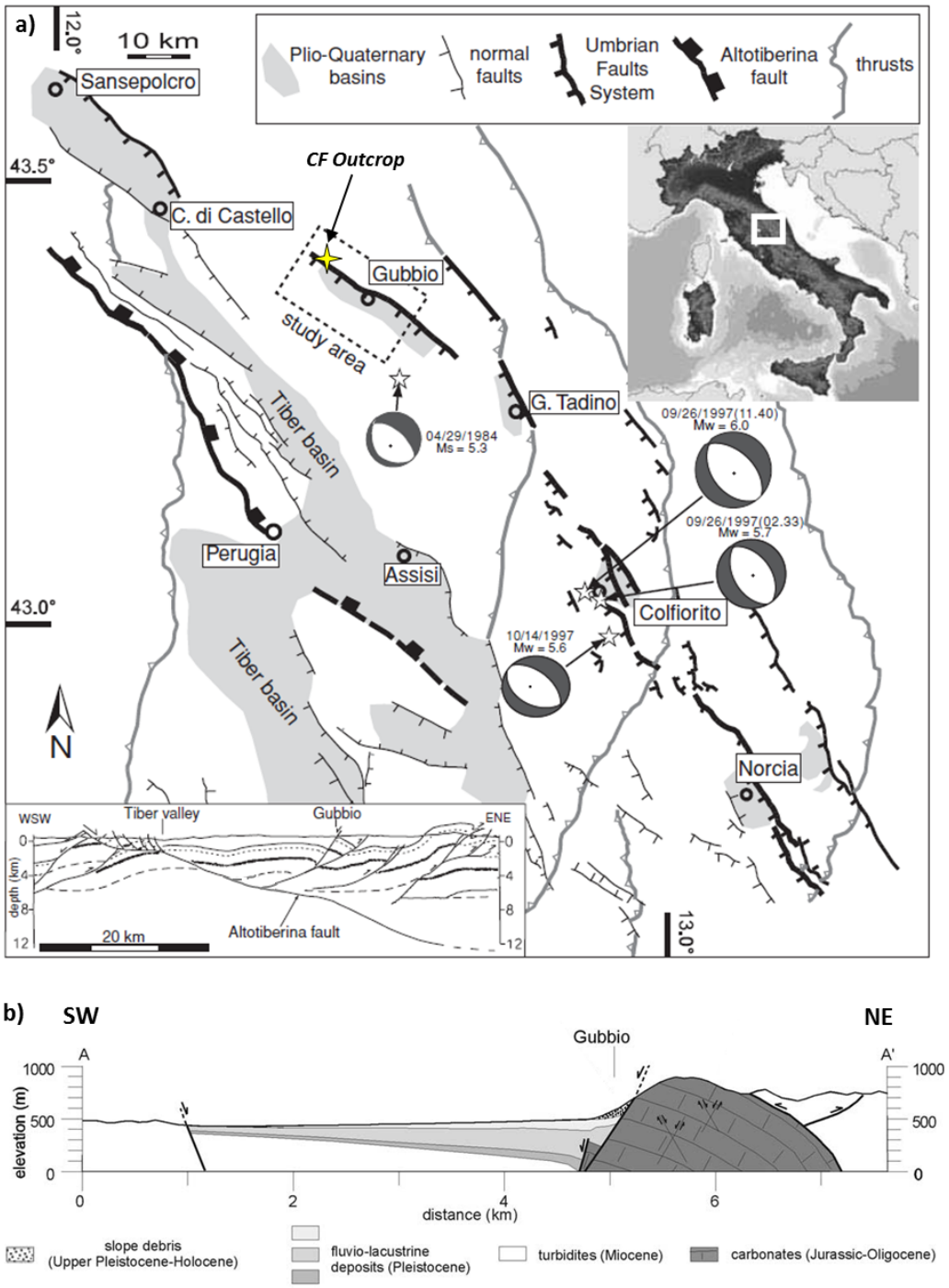

Figure 2.1 a) Schematic structural map of the Umbria region (from Pucci et al., 2003, after Barchi et al., 2001), showing location of study area. Focal mechanisms and magnitudes are for the 1997 Colfiorito sequence (Ekström et al., 1998) and the 1984 Gubbio earthquake (Dziewonski et al., 1985). The location of the Cava Fillippi (CF) outcrop is indicated. Inset is a schematic regional geologic section, constructed with the aid of seismic profile interpretations (modified from Boncio et al., 1998). **b)** Geological cross-section of the Gubbio fault, with the Gubbio basin to the west in the hangingwall and the Gubbio anticline to the east in the footwall (modified from Collettini et al., 2003).

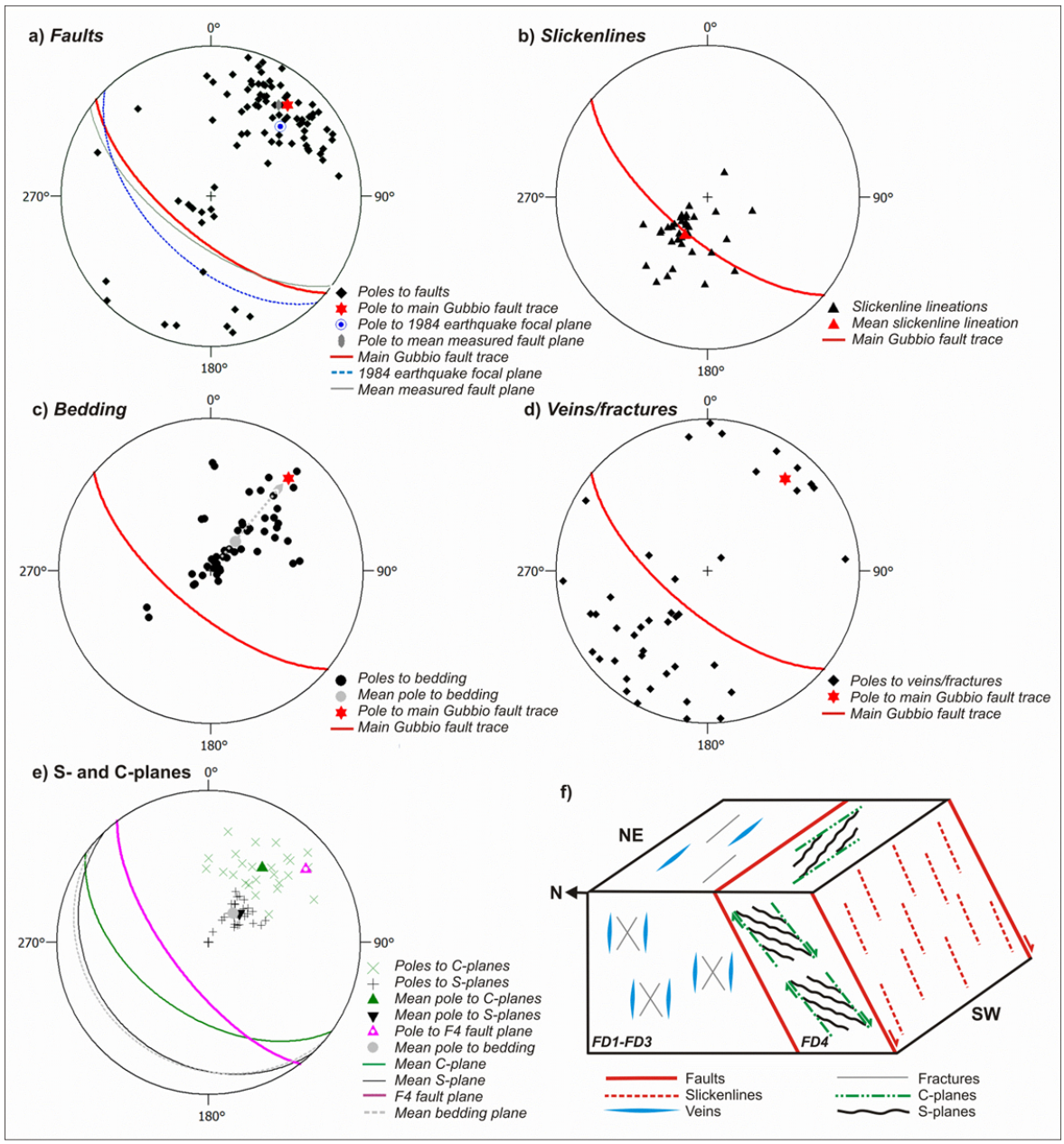

Figure 2.2 a-e are equal area, lower hemisphere stereographic projections of the main structural features related to the Gubbio normal fault. Measurements are taken from both the damage zone (in the case of bedding, veins/fractures and faults) and from within the fault core. The trace of the main Gubbio fault is plotted on projections **a-d** as a reference. **a)** PSSs and subsidiary faults. The mean trend of the measured faults is consistent with the trend of the main Gubbio fault trace (Collettini et al., 2003) and the focal plane of the 1984 Gubbio earthquake (Westaway et al., 1989), which are also plotted. **b)** Slickenlines on fault surfaces, plunging steeply SW in a pure dip-slip geometry. **c)** Bedding: rotation of bedding from the protolith to the fault core is highlighted by the dashed arrow. **d)** Fractures and veins. **e)** C- and S-planes of the S-C fabric in FD4, and also observed within the slip zones of F3 and F4. The plane of F4 and the mean bedding plane are also plotted. **f)** Block diagram summarising the angular relationships between the structures observed at Gubbio, all of which have kinematics consistent with extension related to movement on the Gubbio normal fault.

the main event recorded ~300 aftershocks (M <3.5), arranged in two linear clusters trending sub-parallel to the strike of the Gubbio fault: a northern cluster (10 km long and 3 km wide in map view), where seismicity was limited to depths of 1-4 km, and a denser southern cluster (14 km long and 5 km wide), where seismicity was limited to depths of 4-6 km (Collettini et al., 2003). The aftershocks were located in the hangingwall of the Gubbio fault, rather than on the fault plane itself, and thus were interpreted to represent stress readjustments within the fault hangingwall (Pucci et al., 2003). Microseismicity has been recorded in the Gubbio area during a survey conducted from October 2000-May 2001 (Piccinini et al., 2003), which allowed Chiaraluce et al. (2007) to clearly image the subsurface geometry of the northern portion of the Gubbio fault. The Umbria fault system has hosted two other major normal faulting events during recent decades: the Norcia earthquake in 1979 (Mw = 5.8) (Deschamps et al., 1984), and the Colfiorito seismic sequence from 1997-1998 (Mw < 6.0) (Amato et al., 1998). In addition, the 2009 L'Aquila (Mw = 6.1) (Chiarabba et al., 2009) earthquake was located ~130 km SE of Gubbio on the Paganica fault, also part of the Apennine fault system. Real-time slip analyses using LiDAR-based methods showed that the latter earthquake was succeeded by slow, afterslip deformation in the months following the earthquake (Wilkinson et al., 2010; D'Agostino et al., 2012). All of these seismic events nucleated in and propagated through the Mesozoic-Cenozoic carbonatic multilayer bedrock sequence.

The outcrop that forms the focus of this present study is at Cava Filippi (43°23'21.95"N, 12°29'51.83"E), located ~1.5 km to the N of the village of Mocaiana, which lies near to the NW termination of the Gubbio fault and where the displacement on the fault is ~1.5 km (Mirabella et al., 2004). This outcrop is part of the footwall of the Gubbio fault. The fault rocks at Cava Filippi formed at depths of less than 2.5-3 km within a confined fluid system (Bussolotto et al., 2007).

2.3 *Fault zone architecture*

2.3.1 *Terminology*

Throughout this paper, certain terminologies and abbreviations are used, which we now define. Firstly, the fault core contains a number of *slip zones*, which are zones up to a few 10s of cm wide, containing variably developed brittle fault rocks (breccias, cataclasites; see below). These slip zones each contain a *principal slip zone* (PSZ), which at our study site is never greater than 1.5 mm thick. PSZs typically consist of ultracataclasite or gouge. Each PSZ is associated with a discrete *principal slip surface* (PSS), which sharply cuts the PSZ along one of its margins. The majority of displacement within the fault core is thought to be accommodated collectively along the PSSs and within the associated PSZs (e.g. Sibson, 2003; Smith et al., 2011a).

Secondly, we follow the classifications of Woodcock and Mort (2008) for brittle fault rocks that are defined primarily by grain size. A cohesive fault rock with ≥30% large clasts (≥2 mm in diameter) is classified as a breccia. Anything with <30% large clasts is a cataclasite, and different classes of cataclasite are defined according to the ratio of small clasts (0.1-2 mm in diameter) to cement/matrix (clasts <0.1 mm in diameter). A fault gouge is defined as a fine-grained fault rock that is incohesive (Woodcock and Mort, 2008). The breccias are further subdivided based on how well the clasts fit together. In *crackle breccias,* the clasts are separated by thin seams of cement/matrix and have little evidence for rotation of clasts. In *mosaic breccias,* clasts display greater separations and rotations, but adjacent clasts can fit back to their original configuration. In *chaotic breccias,* clast separation and rotation are so large as to preclude reassembly by visual inspection. In addition to these random-fabric fault rocks, we also describe a number of foliated brittle fault rocks, where the fabrics are a result of pressure-solution processes dominating over brittle processes.

2.3.2 *Protolith*

Here we refer to the protolith as the "relatively undeformed" host rock, where brittle deformation is at a background level. The hangingwall rocks, which are not exposed in the study area, are Quaternary-age lacustrine and fluvial deposits of the Gubbio Basin, which range from clay-rich lignites through to sandstones and conglomerates (GE.MI.NA, 1963). Protolith rocks in the footwall of the Gubbio fault dip gently to the NE (Fig. 2.2c).

The rocks deformed within the fault core of the Gubbio fault belong to the Scaglia Rossa Formation. The Scaglia Rossa Formation is part of a Jurassic to Oligocene carbonate succession in the Umbria-Marche Apennines (Collettini et al., 2003). It consists of Turonian to Danian pale grey-red, micritic limestones with regular marl interbeds up to several cm thick (Bortolotti et al., 1970; Trabucho-Alexandre et al., 2011). The two deformed members in our study area are a "micritic limestone" member (Fig. 2.3a), which consists predominantly of beds (up to 20 cm thick) of micritic limestone (~5 wt. % clay; marl interbeds are infrequent), and the "marly limestone" member (Fig. 2.3b), which is generally more thinly bedded (beds average 5-10 cm thick) and contains frequent marl-rich horizons of up to 2 cm thick. Thus, portions of the fault core derived from the marly limestone have a more significant phyllosilicate content (up to ~20 wt. %) compared to those portions derived from the micritic limestone.

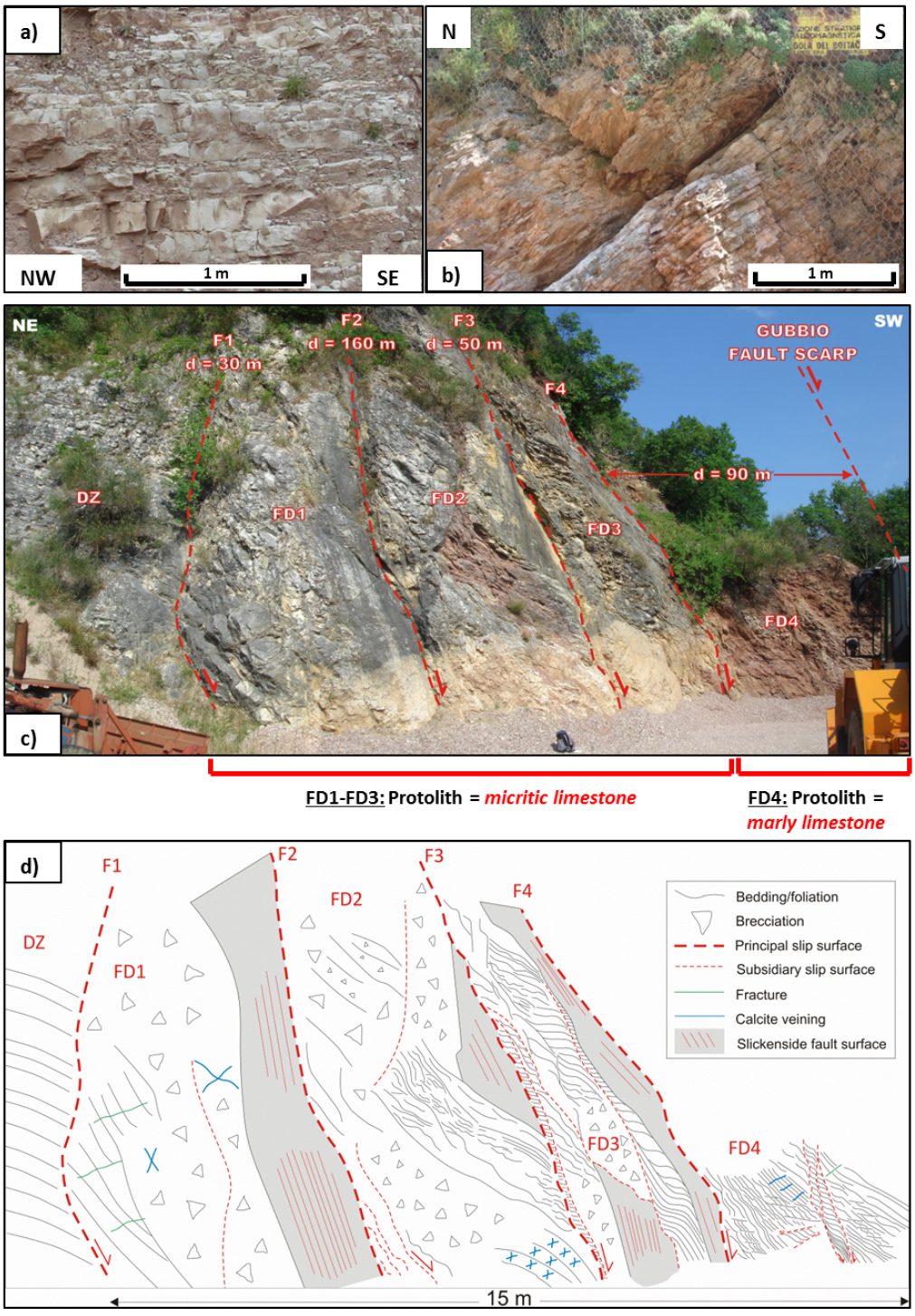

Figure 2.3 a-b show photographs of the undeformed rocks of the Scaglia Rossa Formation, which represent the protolith of the rocks deformed in the core of the Gubbio fault: **a)** The micritic limestone member. **b)** The marly limestone member. **c)** Photograph of the fault core exposed at Cava Filippi, with PSSs (F1-F4) highlighted and the fault core domains (FD1-FD4) labelled. DZ = damage zone. Estimated fault/intradomain displacements, d (from Bussolotto et al., 2007), are also labelled. Colour variations in the outcrop are due to weathering and leaching rather than compositional differences. **d)** Schematic sketch of the outcrop shown in **c**, showing the main structural features. See text for description.

2.3.3 *Damage zone*

We refer to the damage zone as the portion of the fault zone in which the protolith has been variably fractured during fault-related deformation. Several fracture sets are present, some of which emanate from the earlier compressional phase of deformation that resulted in the formation of the Gubbio thrust and anticline (De Paola et al., 2006). Here, we describe only those features that are clearly attributed to the current extensional phase of deformation. The damage zone is ~220 m wide, corresponding to a region measured from the damage zone-fault core boundary, where fracture/vein density values peak at ~15 fractures counted per metre on a 1-D transect (Sagi, 2012), to the protolith, where fracture/vein density decays to background values (<2 fractures/m, Sagi, 2012). The fractures are predominantly pure dilational features (Sagi, 2012) and are often infilled by calcite; calcite mineralisation locally forms up to 75% of the rock volume. A few shear-extensional fractures are present with offsets up to 5 mm (Sagi, 2012), as well as some dip-slip faults with displacements of up to 5 m (Sagi, 2012). All fractures, veins and faults strike sub-parallel to the main Gubbio fault trace, with both synthetic and antithetic dips, often displaying an Andersonian geometry (Fig. 2.2d). Within 2 m of the fault core-damage zone boundary, bedding starts to become highly rotated with beds being dragged into the fault core to dip at steep angles of up to 75˚ to the SW (Fig. 2.2c).

Stylolites are also notable features within the damage zone. Typically, they are either sub-parallel or sub-perpendicular to bedding, and thus are likely a combined product of diagenesis and the prior compressional deformation phase. The stylolites in the damage zone have a high-amplitude, sutured morphology, using the classification scheme of Logan and Semeniuk (1976), with very thin seams of insoluble residue (<100 μm thick) comprising <5% of the total rock volume.

2.3.4 *Fault core*

We refer to the fault core at Cava Filippi as the part of the fault zone where the majority of the normal displacement and associated fault rocks are concentrated (Figs. 2.3c and 2.3d). This outcrop was selected for its excellent exposures in an active quarry, orthogonal to the main PSSs. The damage zone-fault core boundary is marked by a PSS (F1) and thus is very sharp. The fault core has a width across-strike of ~15 m, and is bounded to the SW by a major escarpment that corresponds to the unexposed trace of the Gubbio fault. Following the practice of Bussolotto et al. (2007), we subdivide the fault core in the quarry into four structural domains (FD1-FD4), delimited by four main slip zones, which are bounded by the PSSs, F1-F4 (Figs. 2.3c and 2.3d). FD1-FD3 are derived from the micritic limestone member of the Scaglia Rossa Formation, whereas FD4 is derived from the marly member, creating a marked lithological heterogeneity within the fault core.

Bussolotto et al. (2007) used biostratigraphic controls to estimate the individual fault and intradomain displacements, which are illustrated in Fig. 2.3c and described in Section 2.3.4.1. These estimates suggest that each PSS has several tens of metres of displacement, whereas the displacement within the domains (i.e. within FD1, FD2 and FD3) between the faults is negligible. The exception is domain FD4, which, along with F4, is estimated to have accommodated up to 90 m of displacement. In total, the cumulative displacement at the Cava Filippi outcrop is estimated to be 150-230 m, which equates to ~12% of the total estimated throw of the Gubbio fault (Bussolotto et al., 2007), the remainder of the throw being accommodated by the adjacent main Gubbio fault scarp.

2.3.4.1 *Mesostructural observations*

Domains FD1-FD3 (micritic limestone protolith)

FD1 is characterised by highly rotated bedding planes, which are dipping very steeply compared to the shallowly dipping beds in the adjacent damage zone, at angles of up to 75° towards the SW (Figs. 2.2c and 2.3d). Some bedding surfaces are striated, in an orientation consistent with slickenlines observed on the PSSs (Fig. 2.4a), suggesting that they have been locally reactivated as shear planes. Moving toward F2, the limestones are increasingly fractured so that bedding is almost completely destroyed leading to the development of breccias (Fig. 2.3d). A few relict bedding features remain in FD2. FD2 is characterised by intense fracture and hydrofracture abundance, resulting in heavy brecciation of the rocks (Fig. 2.4b). The exception is a patch of red, marl-rich material, with dimensions of ~1x2.5 m (Fig. 2.3c), which displays characteristics similar to those described for FD4, which will be described later.

We measured fracture densities across the fault core along a 1-D transect. Fracture density in domains FD1-FD2 is ~51 fractures/m, three times greater than observed in the flanking damage zone. Fractures and veins throughout FD1-FD2 are present in two dominant sets, as in the damage zone. Both strike NW-SE (sub-parallel to the principal slip surfaces), with one set dipping SW whereas the other dips antithetically to the NE (Figs. 2.2d and 2.2f). The veins have curviplanar geometry, are up to 2 cm wide, and are filled with calcite (Fig. 2.4a). Several subsidiary slip surfaces occur in FD2 (Fig. 2.3d), and constraining the displacements for each was not possible, but the lack of any well-developed slip zones and associated gouges or cataclasites suggests that displacements are small, probably less than a few mm.

The breccias in FD1-FD2 range in composition from 30-70% limestone clasts, set in a crystalline calcite cement, and range from mosaic to chaotic breccia types (Fig. 2.4c). Limestone clasts are

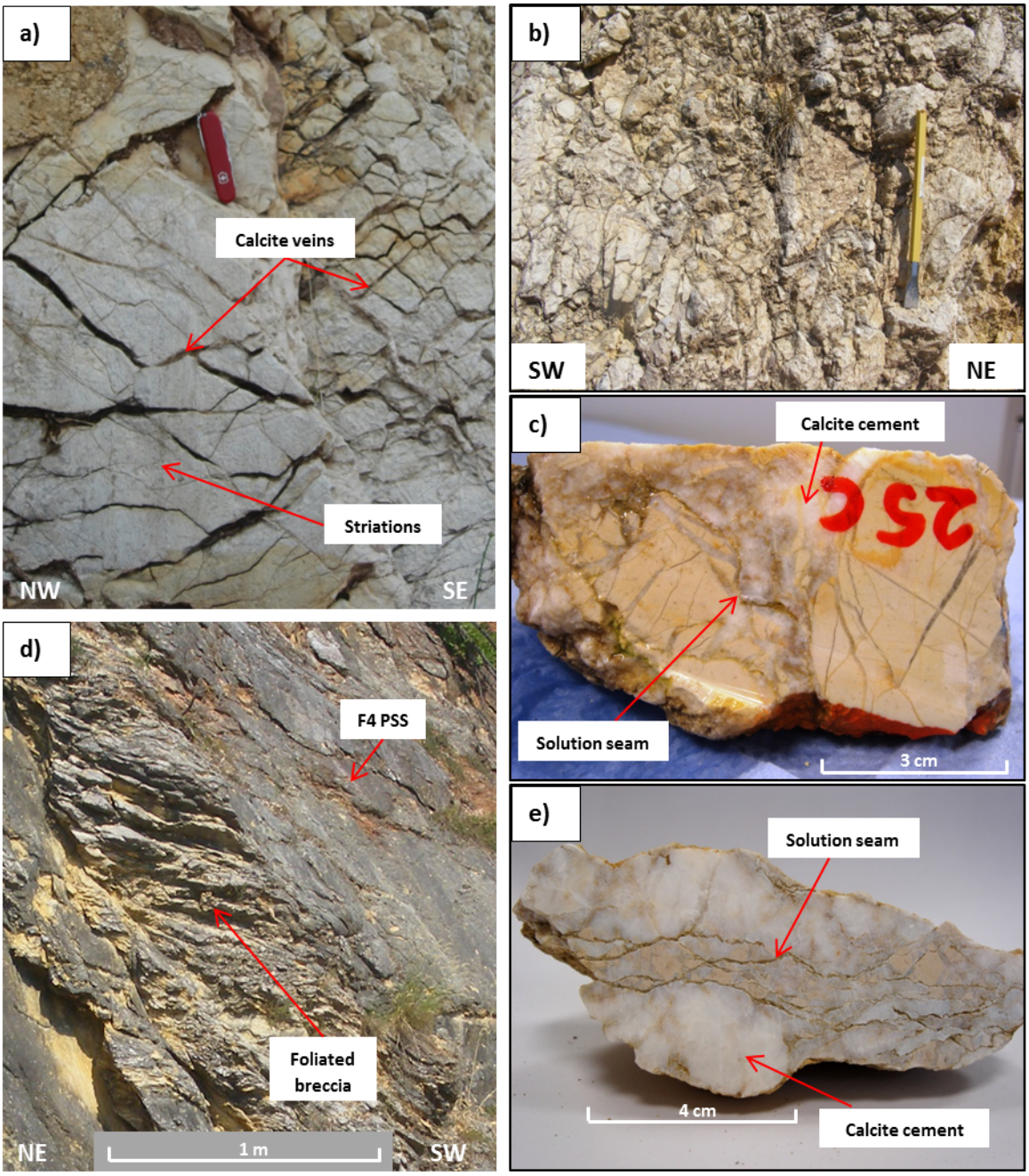

Figure 2.4 Typical mesoscale features in domains FD1-FD3. **a)** FD1: bedding surfaces are striated. They also display several cross-cutting calcite veins, which have curviplanar geometries. **b)** FD2: pervasive fractures and hydrofractures created breccias and destruction of bedding. **c)** Mosaic breccia from FD1, although the large clast on the right hand side displays a crackle breccia texture. Angular clasts of limestone are transected by calcite veins. A solution seam runs across the centre of the sample. **d)** FD3 is characterised by foliated breccias. **e)** Chaotic breccia from FD3 with a large proportion of calcite cement. Clay-rich solution seams define a foliation.

very angular and randomly oriented, ranging from <1 mm up to 10 cm in diameter. Clasts are commonly transected by several very fine calcite veins, which are typically <<1 mm thick. This geometry creates a crackle breccia texture in certain clasts within the host mosaic/chaotic breccias (Fig. 2.4c). Individual crystals within the calcite cement may be visible with the naked eye and are up to 5 mm in diameter. At the mesoscale, it is difficult to differentiate between what may be clasts of calcite and the calcite cement. Intermittent clay-rich pressure-solution seams are also present, constituting ~5% of the rock volume (Fig. 2.4c). Where bedding features are still present, the solution-seams are sub-parallel and sub-perpendicular to the bedding, consistent with the geometries observed in the protolith. However, where bedding surfaces have been reactivated as shear planes, solution seams are at angles of ~40° to the plane.

Domain FD3 is characterised by coarsely foliated breccias (Fig. 2.4d). They range from mosaic- to chaotic-type and the foliation is defined by anastomosing pressure-solution seams (Fig. 2.4e), which dip at angles ranging from ~20-40° to the SW, thus creating an angle of 30-50° to the dip of the PSSs (Fig. 2.4d). Calcite mineralisation in veins and breccia cements represents 25-85% of the rock volume and limestone clasts range from 10-65%. Again, clasts are angular and display a wide range of sizes from <1 mm up to 5 cm. The solution seams have a spacing of ~5 cm and locally comprise up to 10% of the bulk rock volume. Solution seams within FD1-FD3 (Figs. 2.4c and 2.4e) typically have lower amplitude to wavelength ratio compared to those in the damage zone, and hence have a smoother, less sutured morphology. They are also noticeably thicker, being up to 3 mm wide, and occasionally contain visible fragments of calcite and limestone (< 1 mm in size). Fracture density in FD3 is ~0.3 fractures/m, slightly lower than in domains FD1-FD2.

Slip zones and PSSs, F1-F4 (micritic limestone protolith)

F1-F4 are discrete shear planes, and >10 m in length based on available exposure, which cut sharply through the outcrop (Fig. 2.5a). F1 (displacement = 3±27 m, Bussolotto et al., 2007) lacks a well-developed slip zone, but a PSZ is present, consisting of a clay-rich gouge, up to 2 mm thick and containing sub-mm clasts (~25%) of calcite and limestone, coats the slip surface. F2 (displacement = 130±30 m, Bussolotto et al., 2007) also lacks a well-defined slip zone, although in hand specimen, a zone up to 1 cm thick of chaotic breccia is observed immediately underlying the PSS (Fig. 2.5b). This brecciated zone comprises clasts of chert (20%), limestone (15%) and calcite (10%), averaging 1 mm in size, set in a calcite cement (55%). Again, the PSZ consists of a clay-rich gouge layer up to a few mm thick, which coats the PSS.

F3 (displacement ≤ 50 m, Bussolotto et al., 2007) has a slip zone up to 35 cm wide, which has a foliated S-C fabric (Fig. 2.5c). The C-planes are defined by shear planes running sub-parallel to F3,

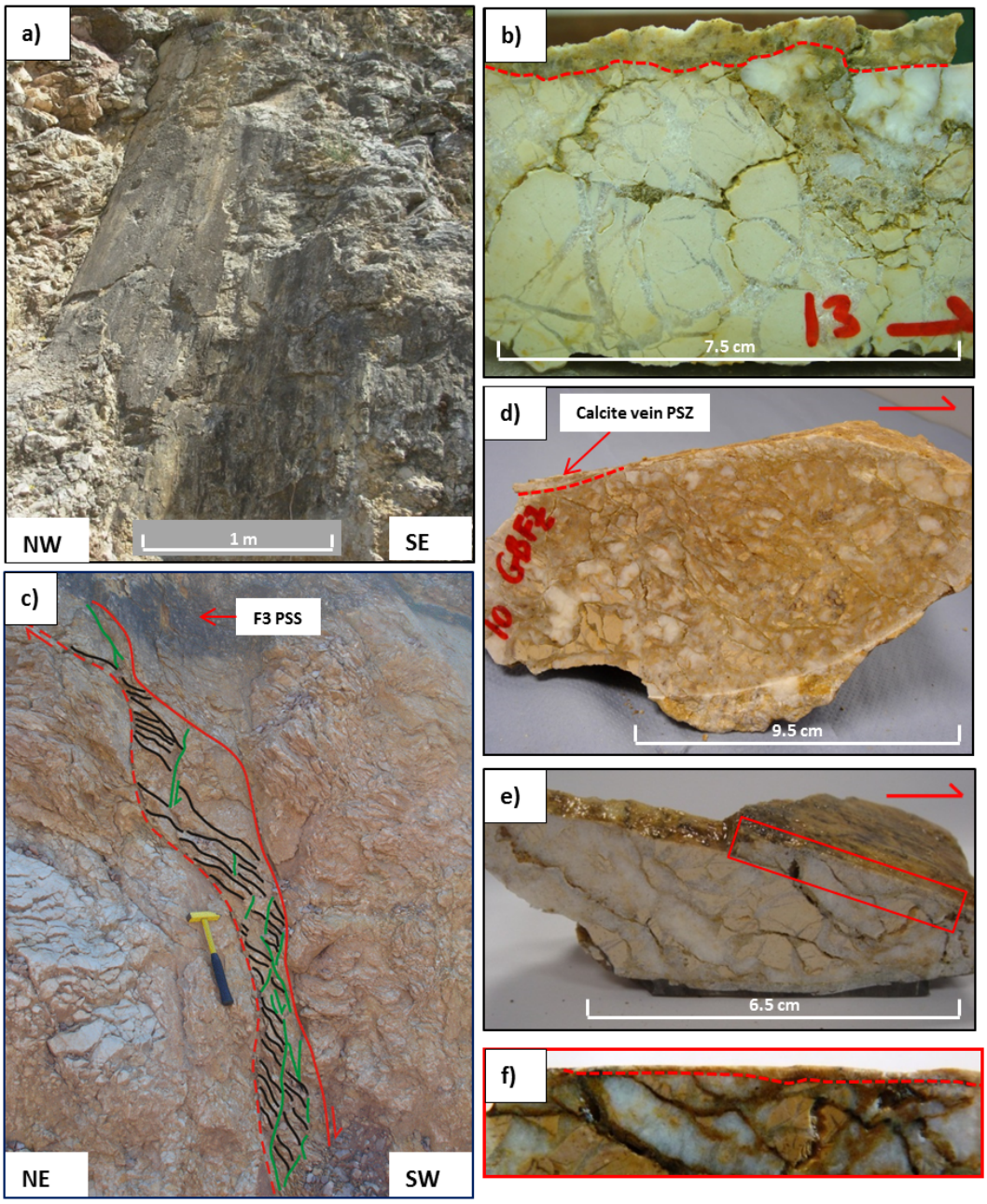

Figure 2.5 Mesoscale features associated with the PSSs F1-F4. **a)** Fault surface of F2. **b)** A zone of chaotic breccia, up to 1 cm thick, underlies the PSS of F2 (PSS lies at top of sample). A layer of gouge also lay on top of the PSS but was lost during sample cutting. The remainder of the rock comprises a mosaic breccia. **c)** The slip zone of F3, which is up to 35 cm wide and displays a foliated S-C fabric (C-planes are shown in green, S-planes in black). **d)** A chaotic breccia from the slip zone of F3. A PSS lies along the top of the sample, and just beneath is a calcite vein-dominated PSZ, up to 5 mm wide. Clay-rich pressure-solution seams are formed at angles of up to 50° from the dip direction of the PSS and create a foliated fabric. **e)** Chaotic breccia and PSZ from F4. Boxed area is shown in **f**, to show the location of the PSZ. The PSZ is up to 1.5 mm wide and consists of ultracataclasite. Note that the pressure-solution seams displayed in **d** and **e** have a smoother morphology, and smaller amplitude to wavelength ratios, than observed in domains FD1-FD2 (see Fig. 2.4).

and the S-planes are defined by phyllosilicate-rich pressure solution seams that constitute up to 10% of the rock volume. They form at angles of up to 50° from the dip of F3 and have average spacings of ~1.5 cm (Fig. 2.5d). Within the lithons bounded by the foliation, the rock is composed of angular clasts of limestone (15%) and calcite (30%) formed from fragmented calcite veins and/or cement, typically < 5 mm in size, set in a calcite cement (55%). Given that 30% of the clasts are fragmented veins or cement, then this rock can be classified as a chaotic breccia. F3 has a PSZ up to 1 mm wide, defined by a layer of calcite veining (up to 0.5 mm wide) (Fig. 2.5d), plus a ~0.5 mm thick gouge layer.

F4 (displacement of 60±30 m along with FD4) also has a slip zone up to 50 cm wide, associated with an S-C foliated chaotic breccia (Fig. 2.5e). Here, angular limestone and calcite clasts comprise up to 30% each and the calcite cement comprises ~40% by volume. Clasts range from <1 mm to 3.5 cm diameter, averaging ~5 mm in size. Some clasts can still be fitted back together in a jigsaw geometry. The phyllosilicate-rich pressure solution seams are oriented at angles of up to 30° from the dip of F4 (Fig. 2.5e), and are often very closely spaced (average spacing ~5 mm). This high density means that the clay seams locally form up to 15% of the rock volume. In addition, the least-weathered parts of the fault exhibit a PSZ up to 1.5 mm wide composed of ultracataclasite (Fig. 2.5f). The PSSs of F1-F4 are often heavily mineralized, displaying calcite slickenfibres in addition to slickenlines that both indicate predominantly dip-slip fault movement (Figs. 2.3b and 2.5a).

Domain FD4 (marly protolith)

In FD4, which is derived from the marly limestone, the deformation style is very different. Compared to other parts of the fault core, fractures are not abundant and shear localisation along through-going faults is rare. Instead, the deformation is represented by a continuous and pervasive S-C fabric (Fig. 2.6a). The C-planes have an average strike direction that is sub-parallel to the domain-bounding PSSs (Figs. 2.2e-f and 2.6a-b), but they dip at a shallower angle, which is explained by the fact that they appear to have re-activated the pre-existing bedding planes that rotated during deformation. The C-planes are defined by an anastomosing network of clay-rich pressure-solution seams (Fig. 2.6d). Individual seams are up to a few mm thick. Many C-planes have calcite slickenfibres precipitated on their surfaces (Fig. 2.6c), which display kinematics consistent with that of the main fault zone, i.e. dip-slip extensional. The S-planes are also defined by seams of pressure-solution, which are generally <1 mm thick (Fig. 2.6d). They are inferred to have formed perpendicular to the direction of the local maximum principal stress induced by shearing along the C-planes (Fig. 2.6b). A less well-defined C'-type shear band cleavage locally overprints the primary S-C fabric (Fig. 2.6a-b). The spacing of the C-foliation ranges from <1 mm

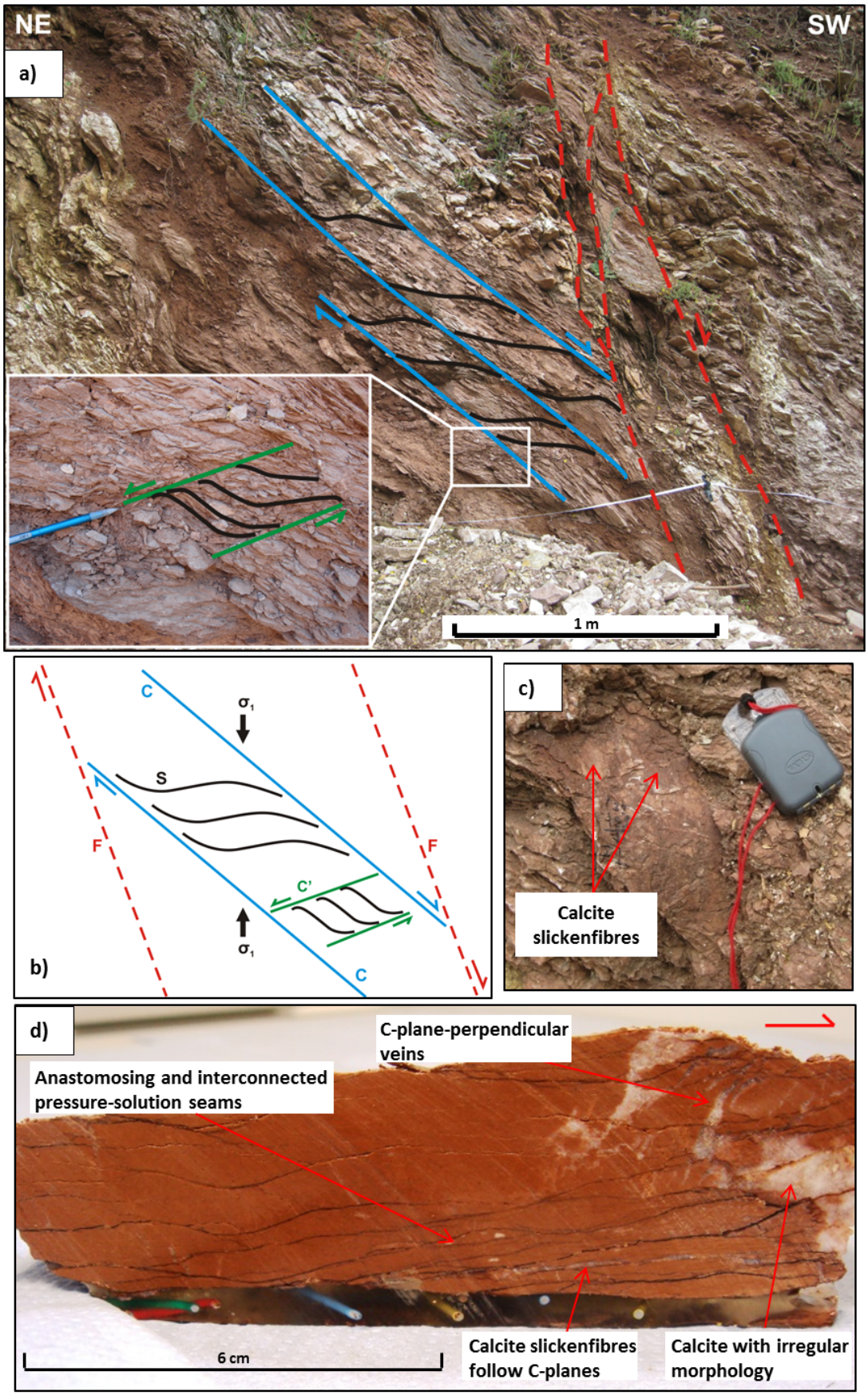
NE
SW
a)
1 m
b)
C
σ1
S
F
C'
σ1
C
F
c)
Calcite
slickenfibres
d)
C-plane-perpendicular
veins
Anastomosing and interconnected
pressure-solution seams
6 cm
Calcite slickenfibres
follow C-planes
Calcite with irregular
morphology

Figure 2.6 Mesoscale features associated with domain FD4. **a)** Deformation is distributed throughout the domain via a continuous, foliated S-C fabric. Inset shows the detail of a local and less well-defined C'-type shear band cleavage. A localised shear zone cuts through the domain on the right-hand side of the image (red-dashed lines). **b)** Kinematic summary of the main structures observed in FD4. **c)** Calcite slickenfibres precipitated on the surface of a C-plane provide evidence for fluid-assisted shearing along the plane. **d)** Hand sample from FD4, showing the internal structures within a lithon bounded by two S-planes. C-planes, defined by phyllosilicate-rich pressure-solution seams anastomose through the rock, creating interconnected networks. Calcite mineralisation is present, but less so than observed in domains FD1-FD3. Veins are typically perpendicular to the C-planes and have a tabular morphology, but occasional patches of calcite with an irregular morphology are present. Calcite slickenfibres are again present along C-planes.

up to 2 cm, so that in some places, the clay-rich seams comprise up to 20% of the rock volume. In contrast to the pressure-solution seams in domains FD1-FD3 and in the damage zone, the seams in FD4 have a very smooth, anastomosing morphology (Fig. 2.6d). This geometry is consistent with the relatively phyllosilicate-rich nature of the marls in FD4, since higher clay content promotes the pressure-solution process (e.g. Rutter, 1976) and favours the development of non-sutured morphologies (Logan and Semeniuk, 1976).

Calcite mineralisation is present but much more sparse than in FD1-FD3. Calcite veins only constitute up to 20% of the rock volume and they tend to be much narrower than those in FD1-FD3, typically <5 mm wide. They are formed predominantly perpendicular to the C-planes (Figs. 2.6d and 2.10a). The veins generally have a tabular morphology, although irregular forms are also present (e.g. Fig. 2.6d). The exception to the predominantly distributed deformation is a localised shear zone that cuts through the centre of FD4 (Fig. 2.6a). This shear zone, ~25 cm wide, is bounded by two slip surfaces. However, the foliated nature of the rocks within this shear zone does not differ significantly to those seen throughout FD4.

2.3.4.2 *Microstructural observations*

Domains FD1-FD3 (micritic limestone protolith)

Optical microscope analysis shows that the limestone clasts in the breccias have reduced sizes of <100 μm and are always very angular shapes. They are extensively fractured and transected by fine calcite veins ranging from 10 μm up to a few mm wide (e.g. Fig. 2.7a). Consistent with the observations made at outcrop scale, these veins form conjugate sets. The calcite veins typically have a blocky texture, and occasionally an elongate blocky texture (Fig. 2.7a). The size of the crystals depends on the width of the vein, but they may be up to 500 μm in diameter in the centre

of the widest veins, generally with smaller crystals at the vein boundaries (Fig. 2.7a). Veins typically have a discontinuous and/or branching geometry (Fig. 2.7a).

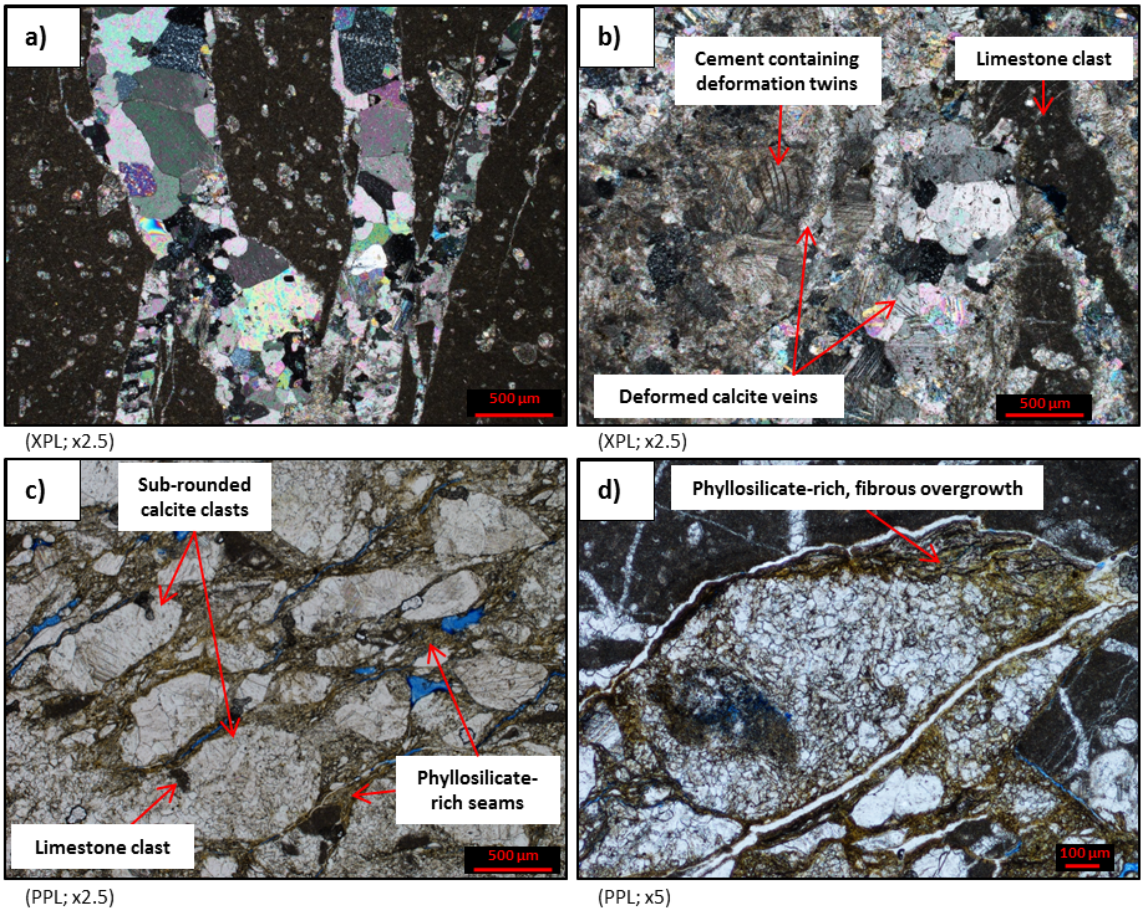

Figure 2.7 Typical microscale features in domains FD1-FD3. **a)** Branching calcite veins, transecting a clast of limestone. They predominantly have a blocky texture, although the bottom left-hand side vein has an elongate blocky texture. Smaller crystals are often concentrated at the limestone-vein boundaries. **b)** Calcite cement in breccia from FD2. Calcite crystals in the cement appear much more deformed than those in the veins, typically displaying type II/type III deformation twins (Burkhard, 1993). Earlier veins were incorporated into the cement through fracturing and brecciation. **c)** Anastomosing phyllosilicate-rich solution seams in FD3. The dissolution of clasts of limestone and calcite has produced sub-rounded shapes, compared to the typical angular clasts observed in many breccias in FD1-FD2. **d)** Bearded overgrowth on a clast of calcite within a pressure-solution seam from FD3.

The nature of the calcite crystals within the breccia cement contrasts significantly compared to the vein crystals. Calcite crystals in the cement are mostly anhedral with random orientations (Fig. 2.7b). They are also highly inequant, ranging from < 20 µm up to 5 mm in size. In addition, deformation twins are common within the calcite cement, particularly in the largest crystals, and

they may be >1 μm thick and can be curved and taper out within crystals (Fig. 2.7b). Although several twins correspond to type I deformation twins of Burkhard's (1993) classification, which is consistent with deformation at temperatures <200°C, ~50% correspond to type II-type III deformation twins. Typically type II-type III deformation twins are associated with temperatures of deformation in the range 150-250°C, which is high considering the 2.5-3 km of exhumation for the Gubbio fault. Further, Bussolotto et al. (2007), used palaeothermometric techniques to calculate temperatures of formation of the fault rocks at Cava Filippi of <50 °C. Thus, we infer that the high strain rates experienced within the fault core enhanced deformation twin morphology (e.g. Rybacki et al., 2013).

Pressure-solution seams average 50 μm to 1 mm wide and are filled with an extremely fine-grained crystal aggregate. EDX analysis with the SEM shows that the seams comprise up to 80% phyllosilicate with the remainder being very fine-grained calcite crystals. Calcite crystals are quite equant, ranging from ~25-50 μm in diameter, and are sub-rounded (Fig. 2.7c). Bearded overgrowths (Fig. 2.7d) occur in some solution seams in domain FD3, suggesting that pressure-solution creep is likely an active deformation mechanism within this domain. The solution seams typically cross-cut all other structures (i.e., clasts, cement, veins) in the breccias, indicating that they continued to develop after most other structures.

PSZs, F1-F4 (micritic limestone protolith)

PSSs appear as very sharp, straight boundaries that truncate all features within the host breccias (Fig. 2.8a). As described in Section 2.3.1, the PSS bounds a PSZ. The PSZs observed in this study range from ~0.5-1.5 mm thick and are one of two types: those defined by zones of ultracataclasite and those defined by PSS-parallel calcite veins.

F4 is an example of an ultracataclasite-dominated PSZ (Fig. 2.8a) with four well-defined sub-zones. Sub-zone 1, which ranges from 515-915 μm wide, consists of ultracataclasite. The ultracataclasite has a random fabric and contains sub-rounded clasts of limestone (10%) and calcite (50%) set in a matrix (40%) of ultrafine-grained calcite and clay (Fig. 2.8c). Clasts range from 20-600 μm in size. Anything less than 20 μm in size is attributed to the matrix. Sub-zones 2, 3 and 4, which have widths of up to 430 μm, 240 μm and 220 μm, respectively, consist of discontinuous, blocky calcite veins that contain crystals ranging from ~40-800 μm in size. Each sub-zone is bounded by a slip surface. These surfaces are highlighted by the presence of an orange-brown material (Fig. 2.8d), which at high magnification, and with the SEM, is seen to consist of sub-rounded calcite crystals, <20 μm in size, dispersed within phyllosilicate-rich material. The calcite

crystals within this material do not appear to have been particularly fractured or abraded, and many of them have concave boundaries.

SEM investigation of the uppermost slip surface corresponding to the striated F4 plane observed in the field reveals a more complex structure. It shows the presence of an ultrafine-grained,

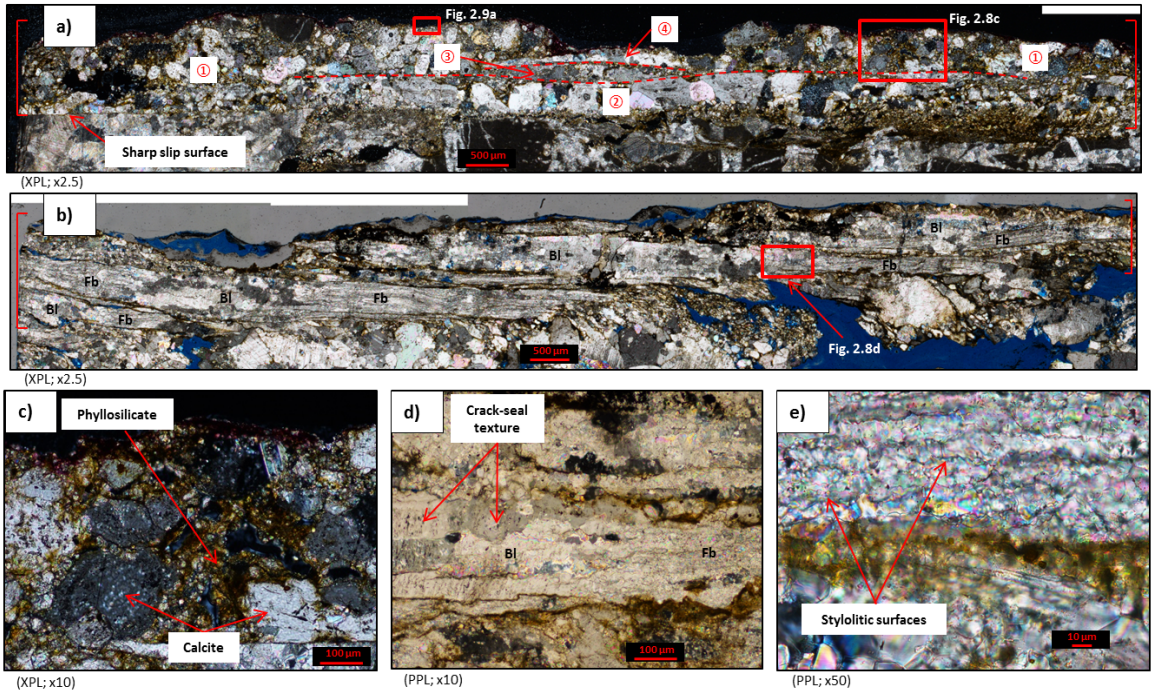

Figure 2.8 Typical microscale features associated with the PSSs F1-F4. **a)** Example of an ultracataclasite-dominated PSZ (bracketed) from F4 (hand sample is shown in Figs. 2.5e and 2.5f). Note the very sharp boundary between the host breccia and the PSZ on the left hand side of the image. This becomes less sharp towards the right-hand side as the slip surface is overprinted by pressure-solution. This PSZ comprises four subzones, labelled 1-4, which are bounded by discontinuous slip surfaces, highlighted in red. Subzone 1 is dominant and consists of ultracataclasite (see fig. **c**). Subzones 2-4 are discontinuous and consist of blocky calcite veins. **b)** Example of a calcite vein-dominated PSZ (bracketed) from F3. A number of calcite veins are present. Veins are characterised by transitions (see fig. **d**) from a blocky texture to a fibrous texture along their length (labelled Bl = blocky; Fb = fibrous). The blocky calcite veins contain crystals averaging 100 µm in diameter, displaying a crack-seal texture (see fig. **d**). The fibrous calcite veins contain much smaller, euhedral crystals, averaging 15 µm in diameter (see fig. **e**). **c)** Close-up image of the ultracataclasite in the PSZ of F4 (location shown in **a**). It contains sub-rounded clasts of calcite in a matrix of ultrafine-grained calcite and clay. **d)** Close up image of transition between blocky (Bl) and fibrous (Fb) calcite (location shown in **b**). The alignment of fluid inclusions that creates the crack-seal texture in the blocky calcite can be seen. The orange-brown material is interpreted to be a product of pressure-solution along planes sub-parallel to the PSS/vein boundaries. **e)** Close up of fibrous vein, showing the jagged stylolitic surfaces that create the fibrous texture. Again, the orange-brown material is inferred to be from pressure-solution between slip surfaces.

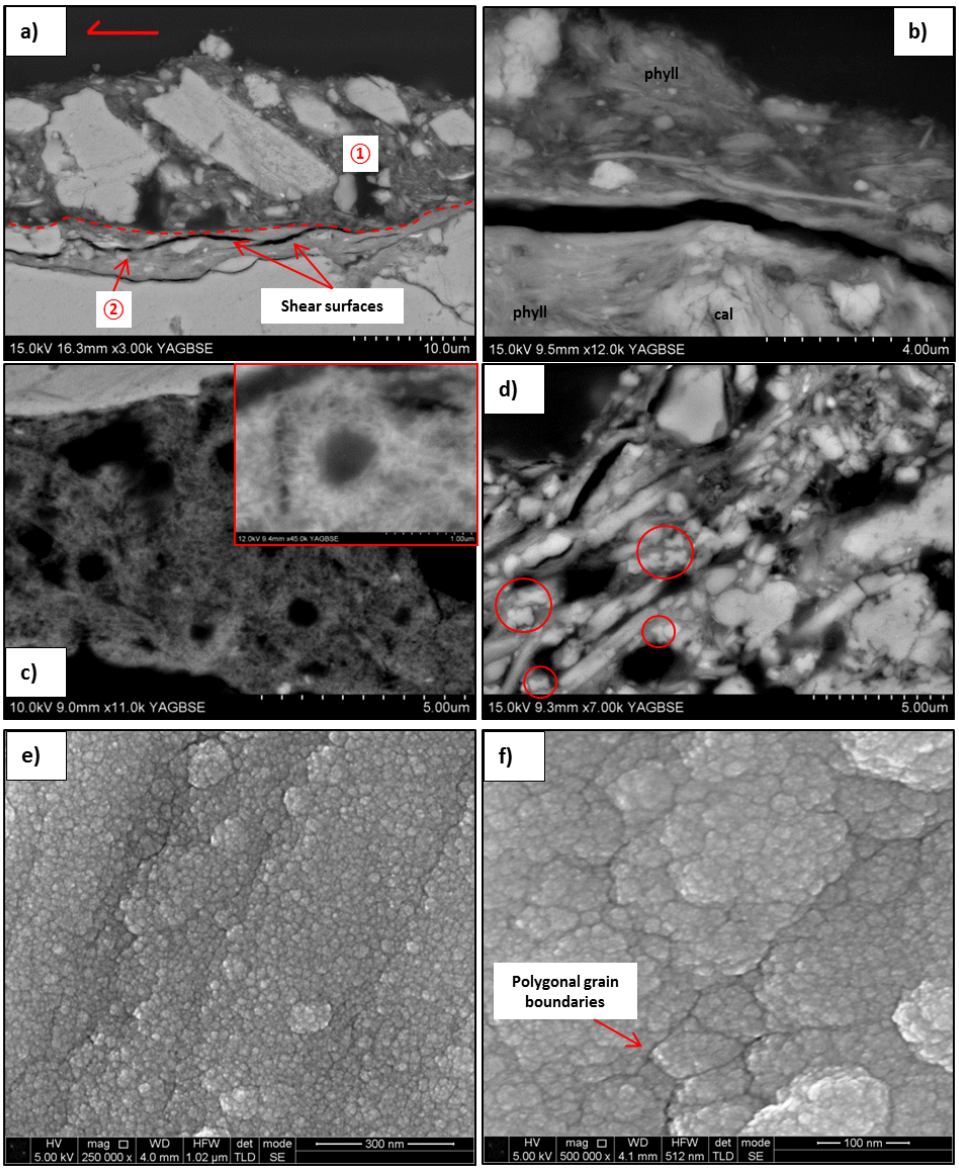

Figure 2.9 SEM images of features found along the PSSs F1-F4. **a)** The gouge that lines the PSS of F4 (see Fig. 2.8a for location) comprises two SLZs that are numbered in the photograph. **b)** A close-up image of a SLZ, showing the fractured nature of the calcite clasts and the foliated nature of the phyllosilicates. **c)** Another SLZ within the PSZ of F4 contains sub-spherical pores, surrounded by a combination of elongate calcite crystals and phyllosilicate. Inset shows a close-up image of one of these pores. **d)** "Dog-bone"/"H"-shaped calcite crystals (highlighted by red circles). **e)** Image taken parallel to the PSS of F4 showing striations on the slip surface from the top right-hand side to the bottom left-hand side of the image. The grooves and ridges between striations are composed of nanoparticles of calcite. **f)** Close up image of the nanoparticles that form the slip surface in **e**. The particles, which have dimensions ranging from 50-150 nm, are tightly packed with sub-polygonal boundaries and triple-junction contacts. The smaller 10-20 nm grains are an artefact of the coating applied to the sample prior to analysis.

phyllosilicate-rich gouge lining the slip surface (Fig. 2.9a), and this gouge displays further sub-zones, which we refer to here as "shear localisation zones" (SLZs) 1 and 2. SLZ 1, which is up to 15 μm thick, has a phyllosilicate content of ~50%, in which the phyllosilicates are randomly oriented, and contains sub-angular calcite clasts up to 20 μm in diameter. SLZ 2, which is <5 μm thick, is much finer-grained, containing nano-sized clasts of calcite, which have a smooth and asymmetric shape (Fig. 2.9a). These clasts are surrounded by finely foliated phyllosilicates, which comprise ~80% of SLZ 2. Also within SLZ 2, several shear surfaces are preserved (Fig. 2.9a). In some specimens from F4, we observed sub-spherical pores within the SLZs that resemble bubbles, which are surrounded by elongate calcite crystals and a small amount (<20%) of phyllosilicate (Fig. 2.9c). Other parts of the SLZs preserve "dog-bone" or "H"-shaped calcite crystals (Fig. 2.9d). SEM analyses have also been performed parallel to the slip surface of F4, i.e. looking down onto the striated fault surface. Here, we observed tightly-packed calcite grains with dimensions ranging from 50-150 nm, which sometimes exhibit polygonal boundaries and triple-junction contacts (Fig. 2.9e-f).

F3 exhibits an example of a calcite vein-dominated PSZ (Fig. 2.8b). The PSZ contains a number of calcite veins, which are characterised by transitions along their length over distances of <300 μm from a blocky to a fibrous texture (Figs. 2.8b and 2.8d). The areas of blocky calcite are characterised by crystals with an average size of 100 μm that display a crack-seal texture where fluid inclusions are aligned sub-perpendicular to the slip direction (Fig. 2.8d). The fibrous veins are characterised by much smaller, euhedral crystals, on average ~15 μm in size with the fibrous texture being created by micron-scale stylolitic surfaces lying sub-parallel to the PSS (Fig. 2.8e). Similar to F4, the slip surfaces that bound the veins within the PSZ are highlighted by the presence of orange-brown phyllosilicate and have a jagged, stylolitic morphology (Fig. 2.8d).

Domain FD4 (marly protolith)

The pressure-solution origin of both the C- and S-planes is evident under the microscope, due to the truncation of micro-fossils (Fig. 2.10b). The pressure-solution seams that define the C-planes have an anastomosing morphology, creating interconnected, phyllosilicate-rich networks (Fig. 2.10b). Solution seam spacings range from μm to cm scale (Fig. 2.10a-b), thus they are much more pervasive than initial field observations suggested, as are the S-planes. The C-planes link up with the S-planes, thus bounding lithons of relatively undeformed limestone. The solution seams that define the S- and C-planes may be up to 100 μm thick. EDX analysis shows that they are filled with ~50% phyllosilicate and 40% calcite with the remaining 10% comprising quartz and diagenetic apatite (Fig. 2.10d). This material is moderately foliated due to the alignment of

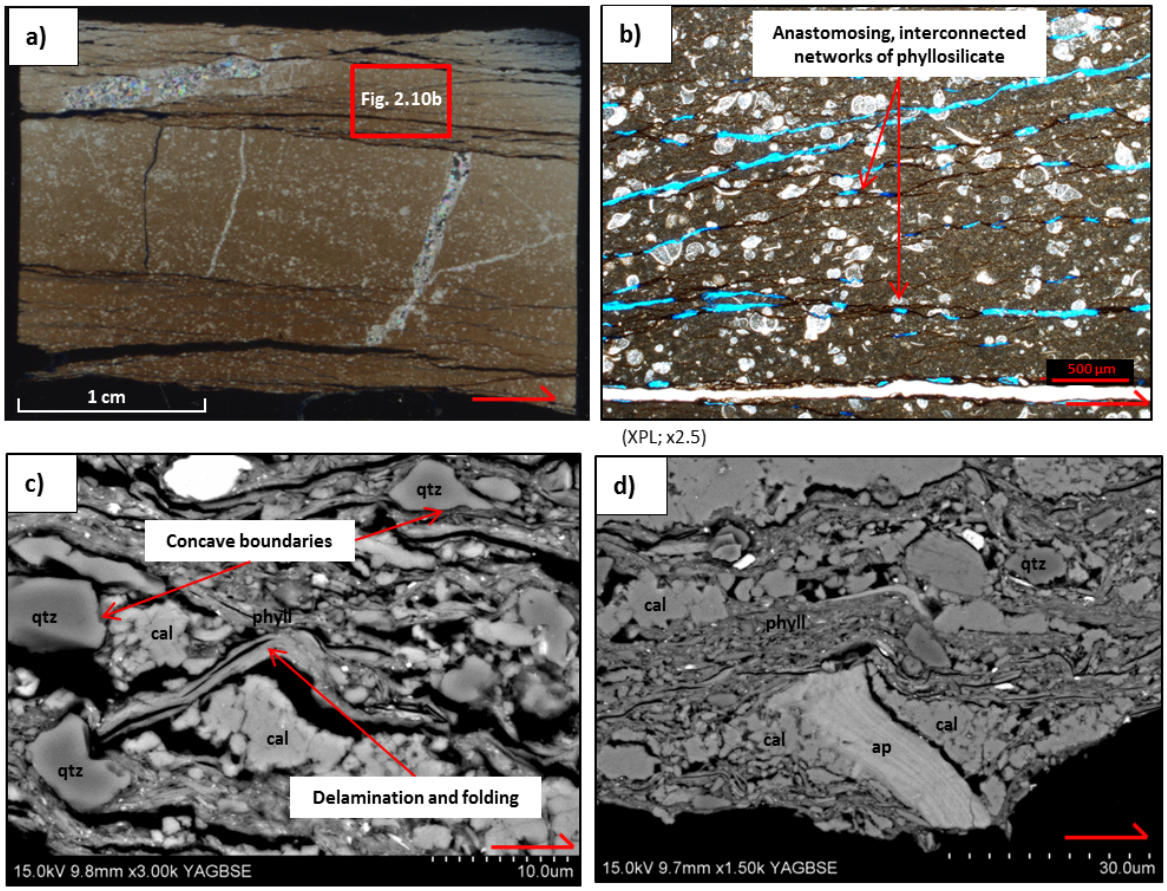

Figure 2.10 Typical microscale features in domain FD4. **a)** Thin section scan (crossed polars) of foliated marly limestone from within a lithon bounded by S-planes. Calcite veins trend predominantly sub-perpendicular to the C-planes and are offset by up to a few mm due to pressure solution along the C-planes. **b)** Optical microscope image of the foliated marly limestone (see fig. **a** for location). Truncation of fossils is observed adjacent to solution seams. The pressure-solution seams anastomose, bounding lithons of relatively undeformed limestone. **c)** SEM image of typical microstructures within the pressure-solution seams. Phyllosilicates exhibit delamination and folds/kinks, and quartz grains display smooth concave boundaries. **d)** SEM image showing a pressure shadow around a grain of apatite within a pressure-solution seam. The shadows on either side are composed of calcite. The alignment of phyllosilicates within the seams is the foliation. (ap = apatite; cal = calcite; phyll = phyllosilicate; qtz = quartz).

phyllosilicate grains (Fig. 2.10c-d). The clasts within the solution seams have relatively smooth, concave boundaries, typical of dissolution (Fig. 2.10c), and show little evidence of internal deformation that contrasts with the clasts in the phyllosilicate-rich SLZs of F1-F4, which are highly fractured and have sharp, angular boundaries (Fig. 2.9b).

Microstructures within the solution seams are inferred to indicate two coeval deformation mechanisms. Firstly, asymmetric delamination features and micro-folds (Fig. 2.10c) imply

foliation-parallel sliding along (001) clay lamellae. And secondly, pressure shadows around clasts (Fig. 2.10d) indicate the operation of pressure-solution creep. In all cases, the sense of shear interpreted from the asymmetry of these microstructures is consistent with that of the fault zone.

Calcite veins display similar characteristics to those in FD1-FD3. They have a drusy and blocky texture, ranging from <10 μm up to a few mm wide (Fig. 2.10a). Their consistent orientation orthogonal to the prevailing C-plane foliation is characteristic of deformation by pressure-solution. The veins are also offset by the pressure-solution seams by distances of up to a few cm (Fig. 2.10a). This geometry may be due to dissolution, or alternatively, some of the larger offsets may be caused by frictional sliding or creep along the solution seams.

2.4 *Mineralogical observations*

XRD analyses were performed on the clay fraction present within various parts of the fault zone to constrain what clays are present and to assess what influence clay mineral content may have on the behaviour of the different fault core domains. A total of six samples were analysed: two samples representing the protolith (one from the micritic limestone protolith and one from the marly protolith), two samples representing pressure-solution seams (one from domain FD3 and one from domain FD4), and two samples representing PSZs (one from F3 and one from F4). Sample details and results are summarised in Table 2.1 and representative XRD traces are shown in Fig. 2.11.

In the protolith, the clays present are illite, mixed layered illite-smectite and a very small amount (<1%) of kaolinite. These same clays are present in the pressure-solution seams from both domains FD3 and FD4, although the solution seams show a relative enrichment of kaolinite (up to 25%). However, a significant difference in clay content is observed within the PSZs of F3 and F4. Whilst illite and kaolinite are still present, smectite forms only 2% of the clay fraction within the PSZ of F4 and is completely absent within the PSZ of F3. These results are consistent with the chemical compositions obtained by in-situ EDX analyses of the clay minerals.

Sample #	Description	Illite	Smectite	Kaolinite
2	*Protolith (micritic limestone)*	6.15%	93.20%	0.64%
28	*Protolith (marly limestone)*	11.70%	87.60%	0.70%
21a	*Solution seam(FD3)*	79.60%	15.80%	4.60%
28(2010)	*Solution seam (FD4)*	45.54%	28.60%	25.85%
10	*PSZ (F3)*	92.60%	0.00%	7.40%
21b	*PSZ (F4)*	84.60%	2.00%	13.40%

Table 2.1 Summary of clay fraction XRD results. Percentages are estimates based on peak area.

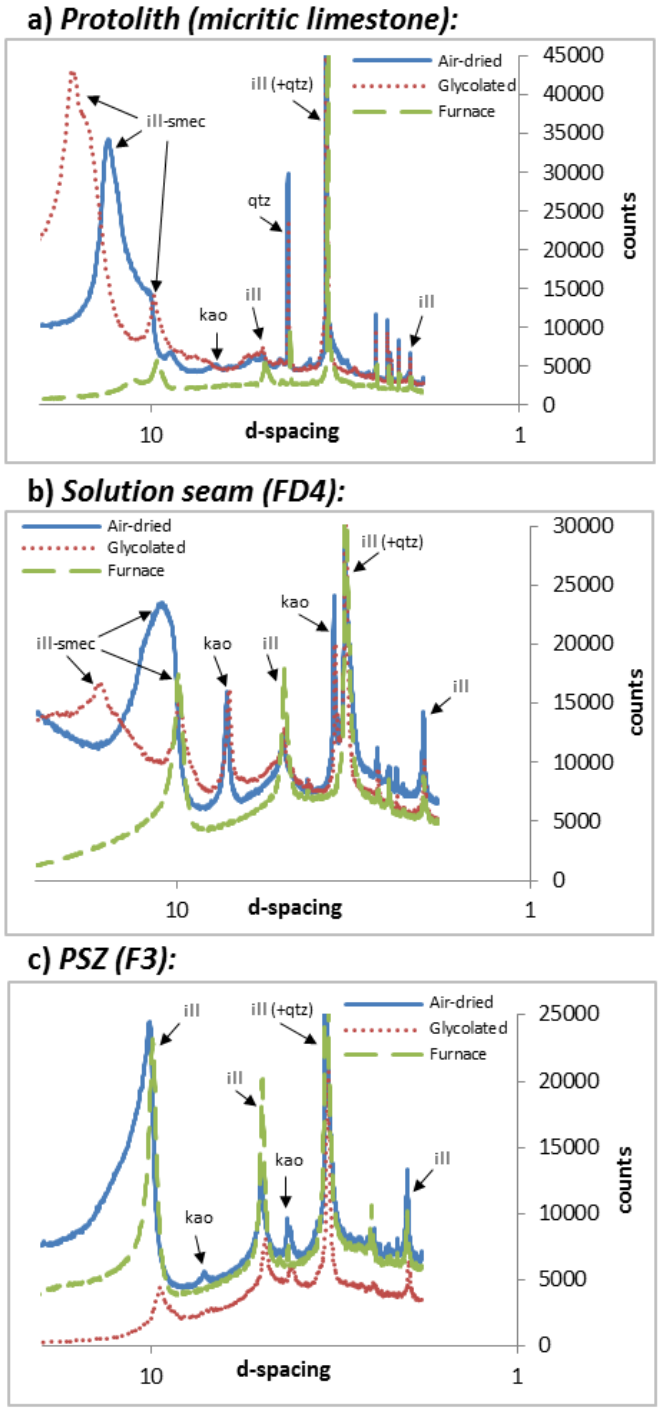

Figure 2.11 Representative XRD traces of the clay fraction present in different parts of the fault zone: **a)** The micritic limestone protolith. **b)** A pressure-solution seam from FD4. **c)** A PSZ from F3. See Table 2.1 for a summary of the results and see text for discussion. (ill-smec = mixed-layer illite-smectite; kao = kaolinite; ill = illite; qtz = quartz).

2.5 *Discussion*

2.5.1 *Deformation styles and mechanisms*

Three dominant styles of deformation are recognised within the core of the Gubbio fault. Domains FD1-FD3, derived from the micritic protolith, are characterised by pervasive fractures, veins and chaotic breccias. Other features include intermittent pressure-solution seams and subsidiary slip surfaces. The style of deformation is thus *discontinuous* and *distributed*. The main deformation mechanisms inferred from microstructural observations are fracturing and hydrofracturing, with minor amounts of diffusive mass transfer and local frictional sliding along minor faults.

The slip zones of F1-F4, also derived from the micritic limestone protolith, are up to 50 cm wide, containing chaotic breccias, which can also have a coarsely foliated S-C fabric. They each contain a PSS and an associated PSZ. PSZs are up to 1.5 mm wide, containing variable amounts of ultracataclasite and gouge, together with slip surface-parallel calcite veins. Even narrower SLZs (<5 μm wide) are observed within the PSZs. Thus, the deformation is *discontinuous* and *localised,* with the main inferred deformation mechanisms being cataclasis and frictional sliding. The foliated S-C fabrics within the slip zones and the development of phyllosilicate-rich stylolitic surfaces along some PSSs (e.g. that of F3 described in Section 2.3.4.2) indicate that diffusive mass transfer processes also play a role within the slip zones F1-F4.

In domain FD4, derived from the marly protolith, the style of deformation is very different to that observed in the rest of the fault core. The main deformation product is a pervasive S-C foliation, where the foliation is defined by abundant pressure-solution seams. The style of deformation is thus *continuous* and *distributed*, with the inferred dominant deformation mechanism being pressure-solution.

2.5.2 *Lithological controls on deformation mechanisms and frictional behaviour*

Our findings illustrate that marked contrasts in both the deformation styles and dominant deformation mechanisms occur across the fault core, and we correlate these contrasts to changes in lithology across the core. Also, the displacement distribution estimated by Bussolotto et al. (2007) appears to be influenced by lithology because for FD1-FD3 dominated by the micritic limestones, displacement is focused on domain boundaries (i.e. along the PSSs F1-F4), whereas for FD4, significant displacement is accommodated within the domain. Thus, with respect to the behaviour of the Gubbio fault during the seismic cycle, we now focus our discussion on those parts of the fault core where most of the displacements appear to be concentrated, i.e. F1-F4 and FD4. Although the total displacement accrued at the Cava Filippi outcrop only amounts to ~12% of the

total displacement of the Gubbio fault, the structures here are considered analogues for what may be encountered either along-strike or down-dip of the main Gubbio fault scarp as it traverses lithological heterogeneities in the host rock. To better understand the possible behaviour of the Gubbio fault during the seismic cycle, we compare our field, microstructural and mineralogical observations with previous studies of active faults and with experimental studies for deformation of rock types similar to those at Gubbio.

The displacements accommodated along F1-F4 are concentrated mostly along the PSSs themselves and also within the PSZs. The presence of fractured, sub-rounded clasts and ultrafine-grained gouge material suggests that cataclastic deformation occurred within the PSZs. The presence of SLZs <20 μm wide, which themselves contain further shear surfaces and an increasing proportion of phyllosilicates, suggests that shear becomes progressively localised into narrower zones during slip evolution. Similar styles of shear localisation are observed in a number of experimental studies and associated with a transition from stable sliding (velocity-strengthening) to unstable, stick-slip (velocity-weakening) behaviour (e.g. Engelder et al., 1975; Moore et al., 1988; Logan et al., 1992; Beeler et al., 1996; Collettini et al., 2011; Ikari et al., 2011). These experiments were performed on a wide range of crustal rock types (quartz, calcite, quartzo-felspathic and phyllosilicate gouges) and under a broad spectrum of experimental conditions. On this evidence, it seems possible that the PSSs F1-F4 have behaved in a velocity- and/or slip-weakening manner. This interpretation would be consistent with the fact that they are derived from the micritic limestone protolith, since carbonate rocks do experimentally exhibit both velocity- and slip-weakening behaviour under certain conditions. For example, Verberne et al. (2010) recorded a change from velocity-strengthening to velocity-weakening in limestone gouge at temperatures between 100-150°C; Collettini et al. (2011) observed an evolution from velocity-strengthening to velocity-weakening with increasing sliding velocity; and Logan et al. (1992) observed this transition at confining pressures >50 MPa.

In FD4, displacement is distributed throughout the domain with movement accommodated along pressure-solution seams in the S-C fabric. The common occurrence of slickenfibres on C-plane surfaces suggests that the shearing within this domain is fluid-assisted. The microstructures observed within the pressure-solution seams, such as folds and kinks of the phyllosilicates and pressure shadows around clasts, are indicative of bulk ductile flow by diffusive mass transfer. They are very similar to those reported by Holdsworth et al. (2011) and Hadizadeh et al. (2012) in the phyllosilicate-rich, actively creeping zone of the San Andreas fault, i.e. they are more typical of creeping deformation than seismic slip. Interpreting the structures in FD4 to be of aseismic origin would be consistent with their phyllosilicate-rich composition due to the marly protolith, because

phyllosilicates have been shown experimentally to be almost exclusively velocity-strengthening (e.g. Morrow et al., 2007; Tembe et al., 2010; Ikari et al., 2011 and references therein). The proportion of phyllosilicates within the solution seams is >50%, which experimental evidence suggests is enough for the frictional behaviour to be controlled by the weak phyllosilicates rather than by the stronger carbonate phases (e.g. Tesei et al., 2012), due to the formation of an interconnected clay network (e.g. Schleicher et al., 2010; Tembe et al., 2010). Although phyllosilicates comprise <20% of the rock volume in FD4, the fact that they are concentrated along the solution seams means that shear strain can preferentially be focused along these pre-existing zones of weakness (Collettini et al., 2009; Behnsen and Faulkner, 2012), so that ultimately, the strength and frictional behaviour of FD4 is likely dominated by the weak phyllosilicate-rich seams. Thus, we hypothesise that FD4 deforms predominantly in a velocity-strengthening, aseismic manner, with the potential to act as a barrier to rupture propagation (e.g. Boatwright and Cocco, 1996; Kaneko et al., 2010). Consequently, earthquake ruptures might tend to bypass FD4, and concentrate displacement along the PSSs F1-F4, which lie within the velocity-weakening, micritic limestone part of the fault core.

2.5.3 *Coseismic slip indicators*

As well as having the potential to exhibit velocity-weakening behaviour, carbonate rocks are also widely shown to demonstrate strong dynamic weakening behaviour at seismic slip rates (>1 m/s), when the frictional strength of carbonate faults reduces dramatically from Byerlee values (μ = 0.6-0.85) to values as low as 0.1 (Han et al., 2007, 2010, 2011; De Paola et al., 2011a; 2011b). The weakening mechanisms are thought to be thermally activated due to the frictional heat generated along highly localised slip surfaces during rapid seismic slip (Di Toro et al., 2011).

Temperatures attained within micron-scale width slip zones at seismic slip rates may be on the order of several hundreds of degrees Celsius and that would be sufficient to trigger physical and chemical modifications to the fault rocks and slip–zone materials. For example, in carbonates, these conditions can trigger decarbonation reactions, releasing CO_2 gas into the slip zone and producing a thin layer of sub-rounded and spherical nanoparticles of lime (CaO) within the slip zone. These nanoparticles may be able to undergo rolling along the slip surface, leading to fault lubrication (Han et al., 2010, 2011; De Paola et al., 2011a).

As described in Section 2.3.4.2, within one of the SLZs present within the PSZ of F4, we observed bubble-like features set within a matrix of elongate calcite crystals and phyllosilicate, together with some unusual “dog-bone” or “H”-shaped calcite crystals. These microstructures are strikingly similar to those observed by Collettini et al. (2013) within the PSZ of the Spoleto thrust in central

Italy. Collettini et al. (2013) performed transmission electron microscope analyses on the matrix material within the PSZ and found the presence of amorphous silicate. The fault rocks at Spoleto are derived from the Scaglia Rossa Formation, so they are formed from the same protolith as the fault rocks at Gubbio and also formed at similar depths of 2-3 km. Collettini et al. (2013) suggested that the observed microstructures are produced by thermally-triggered reactions in the PSZ as a result of rapid heating during earthquake slip. They propose that dehydroxylation of clays has resulted in amorphization, and that the skeletal habit of calcite is a result of disequilibrium crystallisation under rapid cooling conditions (e.g. Faure et al., 2003) following carbonate dissociation. The fact that we can make a direct comparison between the microstructures observed along F4 and those described above of Collettini et al. (2013) leads to the conclusion that F4 has slipped coseismically.

The absence of smectite in the PSZs of F1-F4, as revealed by XRD analyses, may also be due to frictional heating associated with seismic slip, since smectite becomes unstable at temperatures between 120-150°C and collapses to an illite-type structure (e.g. Pytte and Reynolds, 1989). The exact mechanism of this smectite-illite transformation has not been well constrained, but it is often associated with the loss of interlayer water (due to dehydration) (Colten-Bradley, 1987).

With knowledge of the thickness of the PSZ, the thermal properties of the PSZ constituents, plus the slip rates and displacements experienced during a seismic event of a given magnitude, it is possible to estimate the average temperature attained within the PSZ during the propagation of an earthquake. Given that the SLZs present within the PSZs are on the order of <20 μm wide, we can simplify our analysis to assume that slip occurred within a zone of zero thickness (Rice, 2006), making it possible to use the equation of Carlslaw and Jaeger (1959) to estimate the temperature rise:

$$T_{Av} = \frac{\tau_{av}\sqrt{Dv}}{\rho c_p \sqrt{\pi k}} \qquad (1),$$

where D = displacement (using values of earthquake slip for a given magnitude as presented by Sibson, 1989), τ_{av} = the shear strength of the fault for a hydrostatic fluid pressure of Λ=0.4, v = slip velocity, and ρ, c_p and κ are the density, specific heat capacity and thermal diffusivity, respectively, of the slip zone materials. We use values for calcite of ρ=2710 kgm^{-3}, c_p=820 Jkg^{-1}K^{-1} and κ=1.62x10^{-6} m^{2}s^{-1} (Wangen, 2010), values for smectite of ρ=2608 kgm^{-3}, c_p=795 Jkg^{-1}K^{-1} and κ=0.91x10^{-6} m^{2}s^{-1} (Wangen, 2010) and values for illite of ρ=2660 kgm^{-3}, c_p=808 Jkg^{-1}K^{-1} and κ=0.86x10^{-6} m^{2}s^{-1} (Wangen, 2010). Considering a depth of faulting of 2.5 km, this equation yields temperatures adequate for calcite decarbonation, which initiates at a temperature of ~720°C (Sharp,

2003), for earthquakes with M >3, in the case of a strong fault ($\mu = 0.85$), or M >6, in the case of a weak fault ($\mu = 0.2$). Dehydroxylation of smectite and illite initiate at temperatures of approximately 600°C (Shoval, 2003) and 900°C (Jordán et al., 1999) respectively. This behaviour would correspond to a M >3 earthquake in the case of a strong fault, and a M >5 earthquake in the case of a weak fault. Thus, the historical normal-faulting earthquakes that have occurred throughout the Apennines, which typically have M ≈ 5-6, could easily trigger thermal decomposition reactions and leave behind recrystallized calcite textures and clay transformations as signatures of seismic slip.

We have also observed nanoparticles coating the slip surfaces of F1-F4 (Section 2.3.4.2; Fig. 2.9e-f), providing further evidence that the thermal dissociation of carbonate may have occurred and that dynamic weakening was operative along these faults. In fact, their tightly packed geometries and polygonal boundaries resemble those produced experimentally by Smith et al. (2013), who suggested that they result from dynamic recrystallization due to intense frictional heating. Thus, there are several lines of evidence to suggest that seismic slip has occurred along the PSSs F1-F4, but we have been unable to identify any seismic signatures within domain FD4, further supporting our hypothesis that FD4 behaves predominantly aseismically.

2.5.4 *Seismic vs. aseismic behaviour during the seismic cycle*

While it would be useful if our hypothesis fully described the deformation behaviour of the fault core, evidence suggests that the simple seismic vs. aseismic differentiation between the PSSs F1-F4 and domain FD4 is unlikely. Firstly, carbonate rocks do not behave exclusively in a velocity-weakening manner (Logan et al., 1992; Verberne et al., 2010; Collettini et al., 2011) and shear localisation is not always associated with stick-slip behaviour (e.g. Logan et al., 1979; Marone et al., 1990; Rathbun and Marone, 2010). Similarly, phyllosilicates do not behave exclusively in a velocity-strengthening manner (e.g. Saffer and Marone, 2003; Ikari et al., 2007; Niemeijer et al., 2012). Frictional behaviour is dependent on a number of factors, including the ambient conditions (normal stress, temperature and pore fluid pressure), the imposed rupture velocity, pre-existing structures within the slip zone, and the composition and distribution of mineral phases within the slip zone.

Secondly, Kaneko et al. (2010) showed that under certain conditions, velocity-strengthening fault patches can host earthquake ruptures, for example, if the earthquake is of large-enough magnitude to overcome the negative stress drop encountered within the velocity-strengthening material, or because of high pre-stress in the velocity-strengthening patch as a consequence of it not being ruptured during previous seismic events. This would explain the occurrence of a localised zone of

shearing in the centre of FD4. Indeed, once transected, seismic ruptures may exploit this localised zone in FD4 by reactivation.

A complex interplay between seismic and aseismic behaviour is also evident from our microstructural observations. For example, we have observed that many slip surfaces associated with F1-F4 have stylolitic morphologies, highlighted by the presence of phyllosilicate (Section 2.3.4.2; Fig. 2.8d-e). We have also observed SLZs that are enriched in phyllosilicates (up to 80%; Fig. 2.9a). The concentration of phyllosilicates within PSZs is likely to be a result of pressure-solution processes operating along the PSSs during the interseismic period. And thus at certain times during the seismic cycle, diffusive mass transfer processes dominate over cataclasis and frictional sliding within the PSZs. In fact, grain-size reduction by cataclasis will promote diffusive mass transfer processes and may lead to a transition from frictional to frictional-viscous behaviour (Bos and Spiers, 2001), therefore promoting fault creep. Conversely, the dissolution of the asperities along a fault surface may reduce their strength, causing them to break successively and trigger fracturing of the fault plane (Gratier and Gamond, 1990).

Finally, the variations in calcite vein textures observed within the PSZ of F3 (Section 2.3.4.2; Figs. 2.8b and 2.8d) further point to variations in the seismic history of the fault. As proposed by Gratier and Gamond (1990), a crack-seal texture (Ramsay, 1980) may reflect sliding occurring at a very slow rate, during which successive microcracks are healed. The presence of small euhedral crystals, on the other hand, may reflect precipitation of calcite into larger fluid-filled cavities created during more rapid displacement events (Gratier and Gamond, 1990), whilst the PSS-parallel stylolites are indicative of fault healing by pressure-solution welding (e.g. Yasuhara et al., 2005).

Despite these complexities, we propose a simplified conceptual model, which summarises possible scenarios for the mechanical behaviour of the Gubbio fault (Fig. 2.12). During an earthquake, the micritic limestone-dominated portions of the fault core accommodate the co-seismic displacements along the localised PSSs F1-F4. This localisation is accompanied by fracturing and/or hydrofracturing within domains FD1-FD3. At these times, domain FD4, which does not accommodate either of these modes of deformation, remains loaded, and this residual stress is then relaxed during the post-seismic period by slow, creeping afterslip deformation concentrated in the marly sections of the fault core. Alternatively, it may be that domain FD4 and certain parts of domains FD1-FD3, i.e. the pressure-solution seams, and certain portions of the PSZs of F1-F4, creep continuously during the interseismic period, whilst the other parts of the fault core remain locked. This behaviour will increase the stresses in the locked parts of the fault core until they fail seismogenically. In addition, Sagi (2012) found that the marl-rich units of the Scaglia Rossa

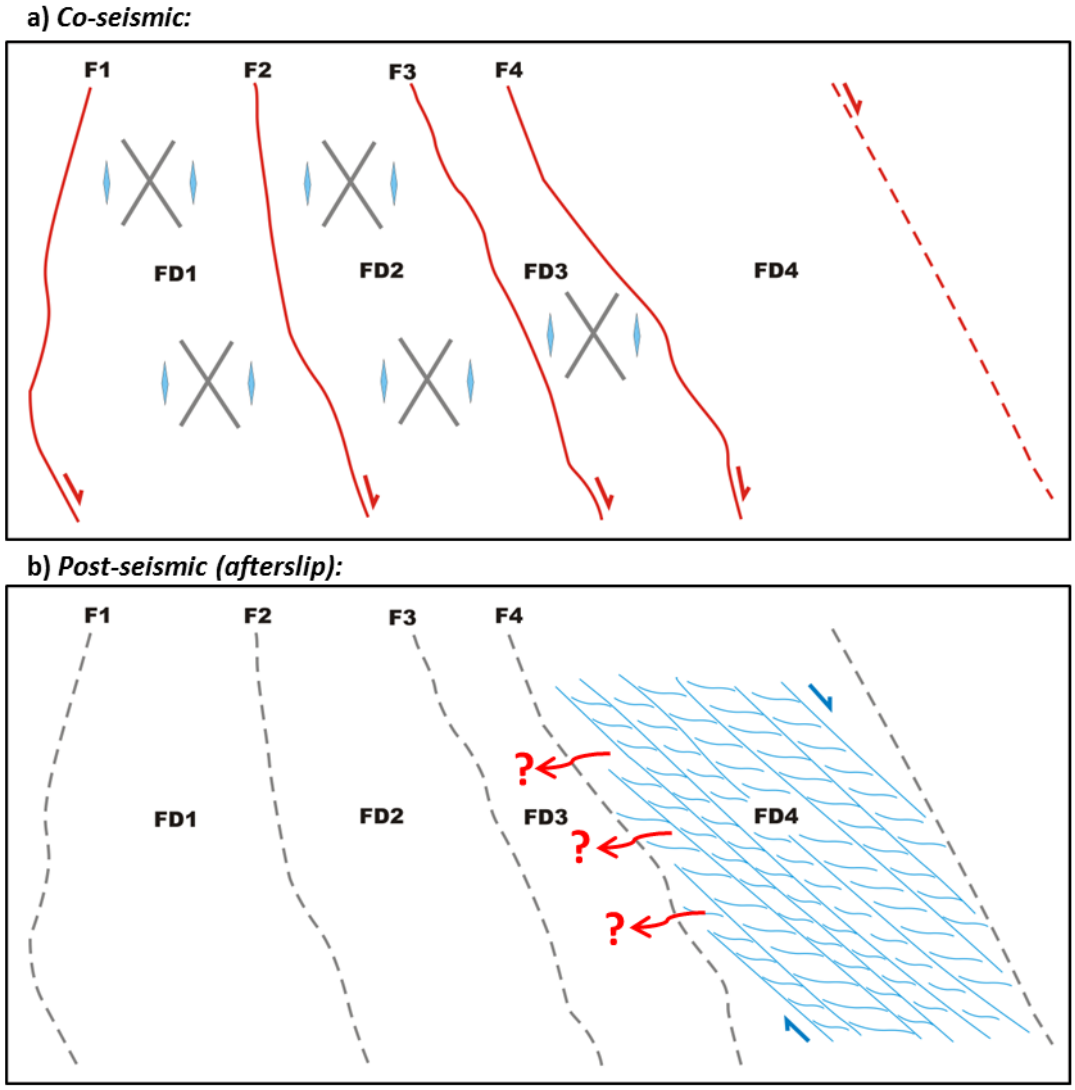

Figure 2.12 A conceptual model summarising our proposed behaviour of the Gubbio fault over the course of the seismic cycle. **a)** During the coseismic period, activity is concentrated within the micritic limestone-hosted parts of the fault core. Coseismic displacements are localised along the PSSs F1-F4 and seismic energy dissipated through domains FD1-FD3 produces fractures/hydrofractures, resulting in extensive brecciation over time within these domains. FD4 remains locked during the coseismic period due to its velocity-strengthening nature, resulting in stress accumulation within the domain. **b)** During the post-seismic period, the accumulated stress in FD4 is relaxed by slow, creeping afterslip deformation. If FD4 creeps continuously during the interseismic period, stress in the locked domains FD1-FD3 will increase, until they fail seismogenically. The possible transfer of fluids away from FD4, as shown by the red arrows, may further enhance stress accumulation in domains FD1-FD3.

Formation act as fault seals, inhibiting fluid flow. This behaviour is consistent with the observation that calcite veining in FD4 occurs to a much lesser extent than in domains FD1-FD3. It is possible that the fluids involved in the pressure-solution processes in FD4, transport material away from FD4 to be deposited in the veins within FD1-FD3. Either way, the preferential transport of fluids away from FD4 and towards FD1-FD3 will generate a fluid overpressure and result in the hydrofracturing and hydraulic brecciation that we observe in domains FD1-FD3. This fluid overpressure can also trigger seismic slip along the PSSs F1-F4, which would be consistent with the fact that some PSZs are characterised by calcite veining (e.g. Fig. 2.5d) and chaotic breccias (e.g. Fig. 2.5b). A similar mixed-mode fault slip behaviour has been proposed, and supported experimentally, by Collettini et al. (2011) for the Zuccale fault zone, which similarly consists of domains of competent carbonate material surrounded by foliated, phyllosilicate-rich horizons (Collettini and Holdsworth, 2004; Collettini et al., 2011).

Although there is no recorded evidence of afterslip deformation occurring at Gubbio specifically, one of the best-documented examples of afterslip deformation comes from L'Aquila, ~130 km south of Gubbio, after the 2009 Mw 6.1 earthquake, where post-seismic deformation may have amounted to as much as 50% of the co-seismic slip (Wilkinson et al., 2010; D'Agostino et al., 2012). Evidence of interseismic creep in the Apennines is also limited, but D'Agostino et al. (2009) identified, through the study of GPS velocity fields, a significant deficit in seismic release in the Umbria-Marche Apennines, which makes aseismic activity a real possibility. The one place where interseismic creep is documented in the northern Apennines is along the Alto-Tiberina low-angle normal fault, of which the Gubbio fault is an antithetic splay (Chiaraluce et al., 2007; Hreinsdóttir and Bennett, 2009). These observations show that the lithologies through which the Gubbio fault penetrates are able to accommodate aseismic creep. The driving forces and mechanisms by which afterslip and interseismic creep occur are not yet fully understood, but a number of recent studies show a coincidence between the operation of pressure-solution creep and the aseismic sliding of active faults (Gratier et al., 2011; Holdsworth et al., 2011; Hadizadeh et al., 2012; Gratier et al., 2013).

Other factors besides lithology can control the distribution of seismicity within a fault zone such as geometric complexities, which can induce different strain rates within a fault zone (e.g. Tesei et al., 2013), and the location of the mainshock rupture patch, since postseismic strains will preferentially occur in the areas surrounding the location of the mainshock (e.g. Johnson et al., 2006; Ozawa et al., 2011; D'Agostino et al., 2012). But still, playing down the importance of lithology is hard in these cases. Geometric complexities within fault zones are often a result of lithological heterogeneities within the sequences through which a fault traverses (e.g. Bonson et al., 2007;

Nemser and Cowan, 2009; Tesei et al., 2013). Also, lithology can control the location of earthquake rupture patches, since, as discussed in Section 2.5.2, earthquakes will only nucleate in materials that are velocity-weakening.

2.6 *Conclusions*

The majority of displacement at the Cava Filippi outcrop is accommodated along the PSSs F1-F4 and in domain FD4. Along F1-F4, the dominant deformation mechanisms are cataclasis and frictional sliding. The resulting microstructures and localised deformation features are similar to those observed in both natural and experimental examples of major earthquake-hosting faults. We therefore propose that earthquake nucleation and propagation are favoured along F1-F4, which are hosted in micritic limestones. Domain FD4 is characterised by continuous, distributed deformation with the dominant deformation mechanism being pressure-solution. The structures observed in FD4 are comparable to those observed in natural and experimental examples of creeping faults. Thus, we propose that domain FD4 behaves in an aseismic manner and we attribute this behaviour to its phyllosilicate-rich host rock. The behaviour of the Gubbio fault over the course of the seismic cycle is therefore likely to be complex, with a lithologically-controlled interplay between localised earthquake nucleation and propagation, and distributed interseismic and post-seismic deformation. Combined field, microstructural, geodetic and experimental studies of faults in varying lithologies, and under a range of conditions, will help us to better constrain the role of lithology in controlling fault behaviour, so that lithological variations along or across a fault may be considered when assessing the past seismicity and future seismic hazard of a fault.

References

Agosta, F., Aydin, A., 2006. Architecture and deformation mechanism of a basin-bounding normal fault in Mesozoic platform carbonates, central Italy. Journal of Structural Geology 28, 1445-1467.

Amato, A., Azzara, R., Chiarabba, C., Cimini, G., Cocco, M., Di Bona, M., Margheriti, L., Mazza, S., Mele, F., Selvaggi, G., 1998. The 1997 Umbria-Marche, Italy, Earthquake Sequence: A first look at the main shocks and aftershocks. Geophysical Research Letters 25, 2861-2864.

Barchi, M., DeFeyter, A., Magnani, M., Minelli, G., Pialli, G., Sotera, B., 1998a. Extensional tectonics in the Northern Apennines (Italy): evidence from the CROP03 deep seismic reflection line. Memorie della Societá Geologica Italiana 52, 528–538.

Barchi, M., DeFeyter, A., Magnani, M., Minelli, G., Pialli, G., Sotera, B., 1998b. The structural style of the Umbria-Marche fold and thrust belt. Memorie della Societá Geologica Italiana 52, 557–578.

Barchi, M., Pucci, S., Collettini, C., Mirabella, F., Massoli, D., Guzzetti, F., Reichenbach, P., Cardinali, M., Vergoni, N., Troiani, E., Chiraz, P., Giombini, L., 2001. A geologic map of the Colfiorito area. Geoitalia 3° forum first poster session, 333-334.

Bastesen, E., Braathen, A., 2010. Extensional faults in fine grained carbonates–analysis of fault core lithology and thickness–displacement relationships. Journal of Structural Geology 32, 1609-1628.

Beeler, N., Tullis, T., Blanpied, M., Weeks, J., 1996. Frictional behavior of large displacement experimental faults. Journal of Geophysical Research 101, 8697-8715.

Behnsen, J., Faulkner, D.R., 2012. The effect of mineralogy and effective normal stress on frictional strength of sheet silicates. Journal of Structural Geology 42, 49-61.

Benedicto, A., Schultz, R.A., 2010. Stylolites in limestone: magnitude of contractional strain accommodated and scaling relationships. Journal of Structural Geology 32, 1250-1256.

Boatwright, J., Cocco, M., 1996. Frictional constraints on crustal faulting. Journal of Geophysical Research: Solid Earth 101, 13895-13909.

Boncio, P., Brozzetti, F., Ponziani, F., Barchi, M., Lavecchia, G., Pialli, G., 1998. Seismicity and extensional tectonics in the northern Umbria-Marche Apennines. Memoirs of the Geological Society of Italy 52, 539-555.

Boncio, P., Lavecchia, G., 2000. A structural model for active extension in Central Italy. Journal of Geodynamics 29, 233-244.

Bonson, C.G., Childs, C., Walsh, J.J., Schöpfer, M.P., Carboni, V., 2007. Geometric and kinematic controls on the internal structure of a large normal fault in massive limestones: the Maghlaq Fault, Malta. Journal of Structural Geology 29, 336-354.

Bortolotti, V., Passerini, P., Sagri, M., Sestini, G., 1970. The miogeosynclinal sequences. Sedimentary Geology 4, 341-444.

Bos, B., Spiers, C., 2001. Experimental investigation into the microstructural and mechanical evolution of phyllosilicate-bearing fault rock under conditions favouring pressure solution. Journal of Structural Geology 23, 1187-1202.

Burkhard, M., 1993. Calcite twins, their geometry, appearance and significance as stress-strain markers and indicators of tectonic regime: a review. Journal of Structural Geology 15, 351-368.

Bussolotto, M., Benedicto, A., Invernizzi, C., Micarelli, L., Plagnes, V., Deiana, G., 2007. Deformation features within an active normal fault zone in carbonate rocks: The Gubbio fault (Central Apennines, Italy). Journal of Structural Geology 29, 2017-2037.

Byerlee, J., 1978. Friction of rocks. Pure and applied Geophysics 116, 615-626.

Carslaw, H., Jaeger, J., 1959. Conduction of Heat in Solids. Oxford University Press, New York, 2nd edition.

Carpenter, B., Marone, C., Saffer, D., 2011. Weakness of the San Andreas Fault revealed by samples from the active fault zone. Nature Geoscience 4, 251-254.

Chester, F., Logan, J., 1986. Implications for mechanical properties of brittle faults from observations of the Punchbowl fault zone, California. Pure and Applied Geophysics 124, 79-106.

Chester, F.M., Evans, J.P., Biegel, R.L., 1993. Internal Structure and Weakening Mechanisms of the San Andreas Fault. Journal of Geophysical Research 98, 771-786.

Chester, F.M., Chester, J.S., 1998. Ultracataclasite structure and friction processes of the Punchbowl fault, San Andreas system, California. Tectonophysics 295, 199-221.

Chiarabba, C., et al., 2009. The 2009 L'Aquila (central Italy) Mw6. 3 earthquake: Main shock and aftershocks. Geophysical Research Letters 36, L18308, doi:10.1029/2009GL039627.

Chiaraluce, L., 2012. Unravelling the complexity of Apenninic extensional fault systems: A review of the 2009 L'Aquila earthquake (Central Apennines, Italy). Journal of Structural Geology 42, 2-18.

Chiaraluce, L., Chiarabba, C., Collettini, C., Piccinini, D., Cocco, M., 2007. Architecture and mechanics of an active low-angle normal fault: Alto Tiberina Fault, northern Apennines, Italy. Journal of Geophysical Research, 112, B10310, doi:10.1029/2007JB005015.

Collettini, C., Barchi, M., Chiaraluce, L., Mirabella, F., Pucci, S., 2003. The Gubbio fault: can different methods give pictures of the same object? Journal of Geodynamics 36, 51-66.

Collettini, C., Holdsworth, R., 2004. Fault zone weakening and character of slip along low-angle normal faults: insights from the Zuccale fault, Elba, Italy. Journal of the Geological Society 161, 1039-1051.

Collettini, C., Niemeijer, A., Viti, C., Marone, C., 2009. Fault zone fabric and fault weakness. Nature 462, 907-910.

Collettini, C., Niemeijer, A., Viti, C., Smith, S.A.F., Marone, C., 2011. Fault structure, frictional properties and mixed-mode fault slip behavior. Earth and Planetary Science Letters 311, 316-327.

Collettini, C., Viti, C., Tesei, T., Mollo, S., 2013. Thermal decomposition along natural carbonate faults during earthquakes. Geology 41, 927-930.

Colten-Bradley, V.A., 1987. Role of pressure in smectite dehydration - effects on geopressure and smectite-to-illite transformation. AAPG Bulletin 71, 1414-1427.

D'Agostino, N., Cheloni, D., Fornaro, G., Giuliani, R., Reale, D., 2012. Space-time distribution of afterslip following the 2009 L'Aquila earthquake. Journal of Geophysical Research 117, B02402, doi: 10.1029/2011JB008523.

D'Agostino, N., Mantenuto, S., D'Anastasio, E., Avallone, A., Barchi, M., Collettini, C., Radicioni, F., Stoppini, A., Fastellini, G., 2009. Contemporary crustal extension in the Umbria–Marche Apennines from regional CGPS networks and comparison between geodetic and seismic deformation. Tectonophysics 476, 3-12.

De Paola, N., Chiodini, G., Hirose, T., Cardellini, C., Caliro, S., Shimamoto, T., 2011a. The geochemical signature caused by earthquake propagation in carbonate-hosted faults. Earth and Planetary Science Letters 310, 225-232.

De Paola, N., Collettini, C., Faulkner, D., Trippetta, F., 2008. Fault zone architecture and deformation processes within evaporitic rocks in the upper crust. Tectonics 27, TC4017, doi: 10.1029/2007TC002230.

De Paola, N., Hirose, T., Mitchell, T., Di Toro, G., Viti, C., Shimamoto, T., 2011b. Fault lubrication and earthquake propagation in thermally unstable rocks. Geology 39, 35-38.

De Paola, N., Mirabella, F., Barchi, M., Burchielli, F., 2006. Early orogenic normal faults and their reactivation during thrust belt evolution: the Gubbio Fault case study, Umbria-Marche Apennines (Italy). Journal of structural geology 28, 1948-1957.

Deschamps, A., Iannaccone, G., Scarpa, R., 1984. The Umbrian earthquake (Italy) of 19 September 1979. Annales Geophysicae 2, 29-36.

Di Toro, G., Han, R., Hirose, T., De Paola, N., Nielsen, S., Mizoguchi, K., Ferri, F., Cocco, M., Shimamoto, T., 2011. Fault lubrication during earthquakes. Nature 471, 494-498.

Dieterich, J.H., Kilgore, B.D., 1994. Direct observation of frictional contacts: New insights for state-dependent properties. Pure and Applied Geophysics 143, 283-302.

Dziewonski, A., Franzen, J., Woodhouse, J., 1985. Centroid-moment tensor solutions for April–June, 1984. Physics of the earth and planetary interiors 37, 87-96.

Ekström, G., Morelli, A., Boschi, E., Dziewonski, A.M., 1998. Moment tensor analysis of the central Italy earthquake sequence of September–October 1997. Geophysical Research Letters 25, 1971-1974.

Engelder, J.T., Logan, J.M., Handin, J., 1975. The sliding characteristics of sandstone on quartz fault-gouge. Pure and Applied Geophysics 113, 69-86.

Fagereng, Å., Sibson, R.H., 2010. Melange rheology and seismic style. Geology 38, 751-754.

Faulkner, D., Lewis, A., Rutter, E., 2003. On the internal structure and mechanics of large strike-slip fault zones: field observations of the Carboneras fault in southeastern Spain. Tectonophysics 367, 235-251.

Faulkner, D., Jackson, C., Lunn, R., Schlische, R., Shipton, Z., Wibberley, C., Withjack, M., 2010. A review of recent developments concerning the structure, mechanics and fluid flow properties of fault zones. Journal of Structural Geology 32, 1557-1575.

Faure, F., Trolliard, G., Nicollet, C., Montel, J.-M., 2003. A developmental model of olivine morphology as a function of the cooling rate and the degree of undercooling. Contributions to Mineralogy and Petrology 145, 251-263.

Fondriest, M., Smith, S.A.F., Di Toro, G., Zampieri, D., Mittempergher, S., 2012. Fault zone structure and seismic slip localization in dolostones, an example from the Southern Alps, Italy. Journal of Structural Geology 45, 52-67.

GE. MI.NA., 1963. Ligniti e torbe dell'Italia Centrale. GE.MI.NA., Geomineraria Nazionale, Torino.

Gratier, J., Gamond, J., 1990. Transition between seismic and aseismic deformation in the upper crust. Geological Society, London, Special Publications 54, 461-473.

Gratier, J.-P., Richard, J., Renard, F., Mittempergher, S., Doan, M.-L., Di Toro, G., Hadizadeh, J., Boullier, A.-M., 2011. Aseismic sliding of active faults by pressure solution creep: Evidence from the San Andreas Fault Observatory at Depth. Geology 39, 1131-1134.

Gratier, J.P., Thouvenot, F., Jenatton, L., Tourette, A., Doan, M.L., Renard, F., 2013. Geological control of the partitioning between seismic and aseismic sliding behaviours in active faults: Evidence from the Western Alps, France. Tectonophysics 600, 226-242.

Gu, Y., Wong, T., 1994. Development of shear localization in simulated quartz gouge: effect of cumulative slip and gouge particle size. Pure and Applied Geophysics 143, 387-423.

Hadizadeh, J., Mittempergher, S., Gratier, J.P., Renard, F., Di Toro, G., Richard, J., Babaie, H.A., 2012. A microstructural study of fault rocks from the SAFOD: Implications for the deformation mechanisms and strength of the creeping segment of the San Andreas Fault. Journal of Structural Geology 42, 246-260.

Haessler, H., Gaulon, R., Rivera, L., Console, R., Frogneux, M., Gasparini, G., Martel, L., Patau, G., Siciliano, M., Cisternas, A., 1988. The Perugia (Italy) earthquake of 29, April 1984: a microearthquake survey. Bulletin of the Seismological Society of America 78, 1948-1964.

Han, R., Hirose, T., Shimamoto, T., 2010. Strong velocity weakening and powder lubrication of simulated carbonate faults at seismic slip rates. Journal of Geophysical Research 115, B03412, doi: 10.1029/2008JB006136.

Han, R., Hirose, T., Shimamoto, T., Lee, Y., Ando, J., 2011. Granular nanoparticles lubricate faults during seismic slip. Geology 39, 599-602.

Han, R., Shimamoto, T., Hirose, T., Ree, J.H., Ando, J., 2007. Ultralow friction of carbonate faults caused by thermal decomposition. Science 316, 878-881.

Holdsworth, R., Van Diggelen, E., Spiers, C., De Bresser, J., Walker, R., Bowen, L., 2011. Fault rocks from the SAFOD core samples: Implications for weakening at shallow depths along the San Andreas Fault, California. Journal of Structural Geology 33, 132-144.

Hreinsdóttir, S., Bennett, R.A., 2009. Active aseismic creep on the Alto Tiberina low-angle normal fault, Italy. Geology 37, 683-686.

Ikari, M.J., Marone, C., Saffer, D.M., 2011. On the relation between fault strength and frictional stability. Geology 39, 83-86.

Ikari, M.J., Saffer, D.M., Marone, C., 2007. Effect of hydration state on the frictional properties of montmorillonite-based fault gouge. Journal of geophysical research 112, B06423, doi: 10.1029/2006JB004748.

Ikari, M.J., Saffer, D.M., Marone, C., 2009. Frictional and hydrologic properties of clay-rich fault gouge. Journal of Geophysical Research 114, B05409, doi: 10.1029/2008JB006089.

ISC, 2001. On-line Bulletin, http://www.isc.ac.uk. International Seismological Centre, Thatcham, United Kingdom, 2011.

Jefferies, S.P., Holdsworth, R.E., Wibberley, C.A.J., Shimamoto, T., Spiers, C.J., Niemeijer, A.R., Lloyd, G.E., 2006. The nature and importance of phyllonite development in crustal-scale fault cores: an example from the Median Tectonic Line, Japan. Journal of Structural Geology 28, 220-235.

Johnson, K.M., Bürgmann, R., Larson, K., 2006. Frictional Properties on the San Andreas Fault near Parkfield, California, Inferred from Models of Afterslip following the 2004 Earthquake. Bulletin of the Seismological Society of America 96, S321-S338.

Jordán, M.M., Boix, A., Sanfeliu, T., de la Fuente, C., 1999. Firing transformations of cretaceous clays used in the manufacturing of ceramic tiles. Applied Clay Science 14, 225-234.

Kaneko, Y., Avouac, J.-P., Lapusta, N., 2010. Towards inferring earthquake patterns from geodetic observations of interseismic coupling. Nature Geoscience 3, 363-369.

Kuo, L.-W., Hsiao, H.-C., Song, S.-R., Sheu, H.-S., Suppe, J., 2013. Coseismic thickness of principal slip zone from the Taiwan Chelungpu fault Drilling Project-A (TCDP-A) and correlated fracture energy. Tectonophysics, in press.

Li, H., Wang, H., Xu, Z., Si, J., Pei, J., Li, T., Huang, Y., Song, S.-R., Kuo, L.-W., Sun, Z., 2013. Characteristics of the fault-related rocks, fault zones and the principal slip zone in the Wenchuan Earthquake Fault Scientific Drilling Project Hole-1 (WFSD-1). Tectonophysics 584, 23-42.

Lockner, D.A., Morrow, C., Moore, D., Hickman, S., 2011. Low strength of deep San Andreas fault gouge from SAFOD core. Nature 472, 82-85.

Logan, B.W., Semeniuk, V., 1976. Dynamic metamorphism: processes and products in Devonian carbonate rocks, Canning Basin, Western Australia. Geological Society of Australia.

Logan, J., Friedman, M., Higgs, N., Dengo, C., Shimamoto, T., 1979. Experimental studies of simulated gouge and their application to studies of natural fault zones: Analyses of Actual Fault Zones in Bedrock. United States Geological Survey Open File Report 1239, 305-343.

Logan, J., Dengo, C., Higgs, N., Wang, Z., 1992. Fabrics of experimental fault zones: Their development and relationship to mechanical behavior. International Geophysics Series 51, 33-33.

Marone, C., 1998. Laboratory-derived friction laws and their application to seismic faulting. Annual Review of Earth and Planetary Sciences 26, 643-696.

Marone, C., Raleigh, C.B., Scholz, C., 1990. Frictional behavior and constitutive modeling of simulated fault gouge. Journal of Geophysical Research 95, 7007-7025.

Micarelli, L., Benedicto, A., Wibberley, C., 2006. Structural evolution and permeability of normal fault zones in highly porous carbonate rocks. Journal of Structural Geology 28, 1214-1227.

Mirabella, F., Ciaccio, M., Barchi, M., Merlini, S., 2004. The Gubbio normal fault (Central Italy): geometry, displacement distribution and tectonic evolution. Journal of Structural Geology 26, 2233-2249.

Molli, G., Cortecci, G., Vaselli, L., Ottria, G., Cortopassi, A., Dinelli, E., Mussi, M., Barbieri, M., 2010. Fault zone structure and fluid–rock interaction of a high angle normal fault in Carrara marble (NW Tuscany, Italy). Journal of Structural Geology 32, 1334-1348.

Moore, D., Summers, R., Byerlee, J., 1988. Relationship between textures and sliding motion of experimentally deformed fault gouge: Application to fault zone behavior. The 29th US Symposium on Rock Mechanics (USRMS).

Moore, D.E., Lockner, D.A., 2004. Crystallographic controls on the frictional behavior of dry and water-saturated sheet structure minerals. Journal of Geophysical Research 109, B03401, doi:10.1029/2003JB002582.

Moore, D.E., Lockner, D.A., 2011. Frictional strengths of talc-serpentine and talc-quartz mixtures. Journal of geophysical Research 116, B01403, doi:10.1029/2010JB007881.

Morrow, C., Solum, J., Tembe, S., Lockner, D., Wong, T.F., 2007. Using drill cutting separates to estimate the strength of narrow shear zones at SAFOD. Geophysical Research Letters 34, L11301, doi:10.1029/2007GL029665.

Nemser, E.S., Cowan, D.S., 2009. Downdip segmentation of strike-slip fault zones in the brittle crust. Geology 37, 419-422.

Niemeijer, A., Collettini, C., Smith, S.A.F., Spiers, C.J., 2012. Frictional properties of Zuccale fault rocks from room temperature to in-situ conditions: results from high strain rotary shear experiments. Geophysical Research Abstracts 14, EGU2012-8001.

Otsuki, K., Monzawa, N., Nagase, T., 2003. Fluidization and melting of fault gouge during seismic slip: Identification in the Nojima fault zone and implications for focal earthquake mechanisms. Journal of Geophysical Research 108, 2192, doi:10.1029/2001JB001711, B4.

Ozawa, S., Nishimura, T., Suito, H., Kobayashi, T., Tobita, M., Imakiire, T., 2011. Coseismic and postseismic slip of the 2011 magnitude-9 Tohoku-Oki earthquake. Nature 475, 373-376.

Piccinini, D., Cattaneo, M., Chiarabba, C., Chiaraluce, L., De Martin, M., Di Bona, M., Moretti, M., Selvaggi, G., Augliera, P., Spallarossa, D., 2003. A microseismic study in a low seismicity area of Italy: the Città di Castello 2000-2001 experiment. Annals of Geophysics 46, 1315-1324.

Pucci, S., De Martini, P.M., Pantosti, D., Valensise, G., 2003. Geomorphology of the Gubbio basin (central Italy): understanding the active tectonics and earthquake potential. Annals of Geophysics 46, 837-864.

Power, W.L., Tullis, T.E., 1989. The relationship between slickenside surfaces in fine-grained quartz and the seismic cycle. Journal of structural geology 11, 879-893.

Pytte, A., Reynolds, R., 1989. The thermal transformation of smectite to illite. Thermal history of sedimentary basins: Methods and case histories, 133-140.

Ramsay, J.G., 1980. The crack-seal mechanism of rock deformation. Nature 284, 135-139.

Rathbun, A.P., Marone, C., 2010. Effect of strain localization on frictional behavior of sheared granular materials. Journal of Geophysical Research 115, B01204, doi:10.1029/2009JB006466.

Rice, J.R., 2006. Heating and weakening of faults during earthquake slip. Journal of Geophysical Research 111, B05311, doi:10.1029/2005JB004006.

Rutter, E., 1976. The kinetics of rock deformation by pressure solution. Philosophical Transactions of the Royal Society of London. Series A, Mathematical and Physical Sciences 283, 203-219.

Rutter, E., Maddock, R., Hall, S., White, S., 1986. Comparative microstructures of natural and experimentally produced clay-bearing fault gouges. Pure and Applied Geophysics 124, 3-30.

Rutter, E., Faulkner, D., Burgess, R., 2012. Structure and geological history of the Carboneras Fault Zone, SE Spain: Part of a stretching transform fault system. Journal of Structural Geology 45, 68-86.

Rybacki, E., Evans, B., Janssen, C., Wirth, R., Dresen, G., 2013. Influence of stress, temperature, and strain on calcite twins constrained by deformation experiments. Tectonophysics 601, 20-36.

Saffer, D.M., Frye, K.M., Marone, C., Mair, K., 2001. Laboratory results indicating complex and potentially unstable frictional behavior of smectite clay. Geophysical Research Letters 28, 2297-2300, doi: 10.1029/2001GL012869.

Saffer, D.M., Marone, C., 2003. Comparison of smectite-and illite-rich gouge frictional properties: application to the updip limit of the seismogenic zone along subduction megathrusts. Earth and Planetary Science Letters 215, 219-235.

Sagi, D.A., 2012. Characterisation of the 2D and 3D density and connectivity attributes of fracture systems in carbonate reservoir analogues: implications for fluid flow. Ph.D. thesis, University of Durham, UK.

Schleicher, A., van der Pluijm, B., Warr, L., 2010. Nanocoatings of clay and creep of the San Andreas fault at Parkfield, California. Geology 38, 667-670.

Scholz, C.H., 1998. Earthquakes and friction laws. Nature 391, 37-42.

Selvaggi, G., 1998. Spatial distribution of horizontal seismic strain in the Apennines from historical earthquakes. Annals of Geophysics 41, 241-251.

Sharp, Z., Papike, J., Durakiewicz, T., 2003. The effect of thermal decarbonation on stable isotope compositions of carbonates. American Mineralogist 88, 87-92.

Shipton, Z.K., Soden, A.M., Kirkpatrick, J.D., Bright, A.M., Lunn, R.J., 2006. How thick is a fault? Fault displacement-thickness scaling revisited. Geophysical Monograph Series 170, 193-198.

Shoval, S., 2003. Using FT-IR spectroscopy for study of calcareous ancient ceramics. Optical materials 24, 117-122.

Sibson, R., 1977. Fault rocks and fault mechanisms. Journal of the Geological Society 133, 191-213.

Sibson, R.H., 1989. Earthquake faulting as a structural process. Journal of Structural Geology 11, 1-14.

Sibson, R.H., 2003. Thickness of the seismic slip zone. Bulletin of the Seismological Society of America 93, 1169-1178.

Smith, S.A.F., Billi, A., Toro, G.D., Spiess, R., 2011a. Principal slip zones in limestone: microstructural characterization and implications for the seismic Cycle (Tre Monti Fault, Central Apennines, Italy). Pure and Applied Geophysics 168, 2365-2393.

Smith, S.A.F., Holdsworth, R.E., Collettini, C., Pearce, M.A., 2011b. The microstructural character and mechanical significance of fault rocks associated with a continental low-angle normal fault: the Zuccale Fault, Elba Island, Italy. Geological Society, London, Special Publications 359, 97-113.

Smith, S., Di Toro, G., Kim, S., Ree, J.H., Nielsen, S., Billi, A., Spiess, R., 2013. Coseismic recrystallization during shallow earthquake slip. Geology 41, 63-66.

Sone, H., Shimamoto, T., Moore, D.E., 2012. Frictional properties of saponite-rich gouge from a serpentinite-bearing fault zone along the Gokasho-Arashima Tectonic Line, central Japan. Journal of Structural Geology 38, 172-182.

Tembe, S., Lockner, D.A., Wong, T.F., 2010. Effect of clay content and mineralogy on frictional sliding behavior of simulated gouges: Binary and ternary mixtures of quartz, illite, and montmorillonite. Journal of geophysical Research 115, B03416, doi:10.1029/2009JB006383.

Tesei, T., Collettini, C., Carpenter, B.M., Viti, C., Marone, C., 2012. Frictional strength and healing behavior of phyllosilicate-rich faults. Journal of Geophysical Research 117, B09402, doi:10.1029/2012JB009204.

Tesei, T., Collettini, C., Viti, C., Barchi, M.R., 2013. Fault architecture and deformation mechanisms in exhumed analogues of seismogenic carbonate-bearing thrusts. Journal of Structural Geology 55, 167-181.

Trabucho-Alexandre, J., Negri, A., de Boer, P.L., 2011. Early Turonian pelagic sedimentation at Moria (Umbria-Marche, Italy): Primary and diagenetic controls on lithological oscillations. Palaeogeography, Palaeoclimatology, Palaeoecology 311, 200-214.

Tschegg, C., Ntaflos, T., Hein, I., 2009. Thermally triggered two-stage reaction of carbonates and clay during ceramic firing—A case study on Bronze Age Cypriot ceramics. Applied Clay Science 43, 69-78.

Verberne, B.A., He, C., Spiers, C.J., 2010. Frictional properties of sedimentary rocks and natural fault gouge from the Longmen Shan fault zone, Sichuan, China. Bulletin of the Seismological Society of America 100, 2767-2790.

Walker, R.J., Holdsworth, R.E., Armitage, P.J., Faulkner, D.R., 2013. Fault zone permeability structure evolution in basalts. Geology 41, 59-62.

Wangen, M., 2010. Physical principles of sedimentary basin analysis. Cambridge University Press, Cambridge.

Westaway, R., Gawthorpe, R., Tozzi, M., 1989. Seismological and field observations of the 1984 Lazio-Abruzzo earthquakes: implications for the active tectonics of Italy. Geophysical Journal International 98, 489-514.

Wibberley, C.A.J., Shimamoto, T., 2003. Internal structure and permeability of major strike-slip fault zones: the Median Tectonic Line in Mie Prefecture, Southwest Japan. Journal of Structural Geology 25, 59-78.

Wilkinson, M., McCaffrey, K., Roberts, G., Cowie, P., Phillips, R., Michetti, A.M., Vittori, E., Guerrieri, L., Blumetti, A., Bubeck, A., 2010. Partitioned postseismic deformation associated with the 2009 Mw 6.3 L'Aquila earthquake surface rupture measured using a terrestrial laser scanner. Geophysical Research Letters 37, L10309, doi:10.1029/2010GL043099.

Woodcock, N., Mort, K., 2008. Classification of fault breccias and related fault rocks. Geological Magazine 145, 435-440.

Yasuhara, H., Marone, C., Elsworth, D., 2005. Fault zone restrengthening and frictional healing: the role of pressure solution. Journal of geophysical research 110, B06310, doi:10.1029/2004JB003327.

Zoback, M., Hickman, S., Ellsworth, W., 2010. Scientific Drilling Into the San Andreas Fault Zone. Eos, Transactions American Geophysical Union 91, 197-199.

Chapter 3

An experimental investigation into the role of phyllosilicate content on earthquake propagation during seismic slip in carbonate faults

Abstract

Carbonate faults commonly contain small amounts of phyllosilicate in their slip zones, due to pressure-solution and/or clay smear. To assess the effect of phyllosilicate content on earthquake propagation in carbonate faults, friction experiments were performed at 1.3 m/s on end-members and mixtures of calcite, illite-smectite and smectite gouge. Experiments were performed at 9 MPa normal load, under room-humidity and water-saturated conditions. All dry gouges show initial friction values (μ_i) of 0.51-0.58, followed by slip-hardening to peak values of 0.61-0.76. Slip-weakening then ensues, with friction decreasing to steady-state values (μ_{ss}) of 0.19-0.33 within 0.17-0.58 m of slip. Contrastingly, wet gouges containing 10-50 wt.% phyllosilicate exhibit μ_i values between 0.07-0.52 followed by negligible or no slip-hardening; rather, steady-state sliding (μ_{ss} <<0.2) is attained almost immediately. Microstructurally, dry gouges show intense cataclasis and wear within localized principal slip zones, plus evidence for thermal decomposition of calcite. Wet gouges exhibit distributed deformation, less intense cataclasis, and no evidence of thermal decomposition. It's proposed that in wet gouges, slip is distributed across a network of weak phyllosilicate formed during axial loading compaction prior to shear. This explains the: 1) subdued cataclasis and associated lack of slip-hardening; 2) distributed nature of deformation; 3) lack of evidence for thermal decomposition, due to low friction and lack of slip-localization. These findings imply that just 10% phyllosilicate in the slip zone of fluid-saturated carbonate faults can: 1) dramatically change their frictional behaviour, facilitating rupture propagation to the surface; 2) significantly lower frictional heating, preventing development of micro-scale seismic markers.

3.1 *Introduction*

Phyllosilicates are traditionally viewed as having a stabilizing influence on the behaviour of upper crustal fault zones. Experimental studies have shown that most phyllosilicates behave in a predominantly velocity-strengthening manner when deformed at sub-seismic slip rates (< 1 cm/s) (Behnsen and Faulkner, 2012; Ikari et al., 2009; Moore and Lockner, 2011; Saffer and Marone, 2003; Sone et al., 2012; Tembe et al., 2010; Tesei et al., 2012). Therefore, earthquakes are unable to nucleate in upper-crustal fault zones that are rich in phyllosilicates. Instead, phyllosilicate-rich fault zones are widely believed to deform predominantly aseismically by fault creep (Marone, 1998; Scholz, 1998). For example, the creeping behaviour of the Parkfield segment of the San Andreas Fault is attributed to the presence of smectitic phyllosilicates in fault gouges (e.g. Carpenter et al., 2011; Holdsworth et al., 2011; Lockner et al., 2011). In addition, crustal regions containing a significant proportion of such velocity-strengthening materials, such as poorly

lithified, clay-rich fault gouges, are viewed as energy sinks, due to a negative stress drop, with the potential to attenuate, or even arrest, an earthquake rupture as it propagates towards the surface (Scholz, 1998).

The frictional behaviour of phyllosilicates at seismic slip rates is quite different to that observed at sub-seismic slip rates. When subject to slip velocities in excess of 1 cm/s, phyllosilicates can undergo dynamic weakening; after attaining a peak in friction at the onset of slip, they undergo an exponential decay in frictional strength, of up to 90% (e.g. Boutareaud et al., 2008; Brantut et al., 2008; Faulkner et al., 2011; Ferri et al., 2010; Ujiie and Tsutsumi, 2010). This is a phenomenon observed for a wide range of rock types, and has been attributed to mechanically- and thermally-activated reactions which weaken the fault during fast, localized slip (see Di Toro et al., 2011).

Wet phyllosilicates subject to seismic slip again show a different frictional behaviour; they do not attain a peak in friction and instead attain steady-state sliding immediately at the onset of slip (Faulkner et al., 2011; Ferri et al., 2011; Ferri et al., 2010; Ujiie et al., 2013; Ujiie and Tsutsumi, 2010; Ujiie et al., 2011). These results from high-velocity friction experiments suggest that, particularly when wet, velocity-strengthening phyllosilicates may offer less resistance to seismic slip than other rock types, provided that dynamic stresses continue to produce a large enough velocity jump to trigger dynamic weakening. The reasons why saturated clay-rich gouges are so weak when subject to seismic slip velocities are not well understood. Suggestions have included rapid thermal pressurization at the onset of slip (Faulkner et al., 2011) and pore-fluid pressurization due to a combination of shear-enhanced compaction and frictional heating (Ujiie and Tsutsumi, 2010). Alternatively, Ferri et al. (2010) proposed that the low friction coefficients associated with water-saturated clays may be due either to water molecules bonding to the surfaces of clay grains, forming thin, lubricating films (as per Moore and Lockner, 2004), or to water being extruded from the gouge layer during compaction and localizing at the gouge-wall rock interface, so that friction is controlled by a lubricating film of water. However, these theories lack robust experimental evidence.

The complex range of frictional behaviours observed in the lab presents us with the challenge of trying to understand what role phyllosilicates may play in the behaviour of natural fault zones. Phyllosilicates are widely recognised to be prevalent within clay-rich fault gouges of upper-crustal faults (e.g. Faulkner et al., 2003; Holdsworth, 2004; Vrolijk and van der Pluijm, 1999; Wu et al., 1975), and within accretionary wedges at subduction zones, which frequently host tsunamigenic earthquakes (e.g. Chester et al., 2013; Ide et al., 2011; Lay et al., 2005). But they are also common

constituents of carbonate fault zones, for example, if the protolith is a marly limestone, or a limestone formation with marl interbeds (e.g. Bullock et al., 2014; Gratier et al., 2013; Tesei et al., 2013). Several recent studies have documented the influence of phyllosilicates on the architecture and frictional behaviour of carbonate fault zones. These studies include examples of strike-slip faults, e.g. the active Vuache fault in the French Alps (Gratier et al., 2013), thrust faults, e.g. within the exhumed northern Apennines fold-thrust belt in Italy (Fig. 3.1) (Tesei et al., 2013), and normal faults, e.g. the active Gubbio fault in the northern Apennines (Fig. 3.1) (Bullock et al., 2014) and the active Clansayes fault system in the French Alps (Gratier et al., 2013). These studies have concluded, through a combination of geological, laboratory and seismological observations, that marl- or phyllosilicate-rich fault domains host predominantly distributed deformation and aseismic slip, whilst limestone-dominated fault domains tend to host localized, brittle deformation and seismic rupture. This is attributed to the fact that pressure-solution processes, and associated creep, are more efficient in polymineralic marls than in monomineralic limestone (Gratier et al., 2013), and that the phyllosilicates present within marls are almost exclusively velocity-strengthening (e.g. Ikari et al., 2011; Morrow et al., 2007; Tembe et al., 2010), whereas limestone, under certain conditions, can behave in an unstable, velocity-weakening manner (Collettini et al., 2011; Logan et al., 1992; Verberne et al., 2010; Verberne et al., 2014).

As well as being associated with zones of distributed deformation within carbonate faults, phyllosilicates are also observed to be concentrated within the principal slip zones (PSZs) of many carbonate faults (Fig. 3.1b-e; see also Appendix 1.1) (Bullock et al., 2014; Collettini et al., 2013; Tesei et al., 2013). These phyllosilicates may have become concentrated in the PSZs either by smearing of clay interbeds along the fault during slip, or by pressure solution acting on the fault planes or within the slip zones, preferentially removing the soluble carbonate phases and leaving behind the insoluble phyllosilicates. The phyllosilicate content within the PSZs may be as high as 50%, and often these minerals form interconnected networks of strongly aligned grains oriented sub-parallel to the PSZs (e.g. see Chapter 2, Fig. 2.9). In many cases, there is evidence that the phyllosilicate-enriched carbonate PSZs have hosted past seismic events (Bullock et al., 2014; Collettini et al., 2013; Tesei et al., 2013). The effect that phyllosilicate content may have on the frictional behaviour of carbonate faults during seismic slip represents a subject of critical importance, particularly since earthquakes within the Italian Apennines, one of the most seismically active zones in Europe (Fig. 3.1a) (e.g. Chiaraluce, 2012; D'Agostino et al., 2009; Lavecchia et al., 2003; Ventura and Di Giovambattista, 2013), all nucleate within and propagate through a carbonate multilayer sequence comprising interbedded limestones and marls (e.g. Barchi et al., 1998). Thus, in order to assess the effect of variable phyllosilicate content on the frictional

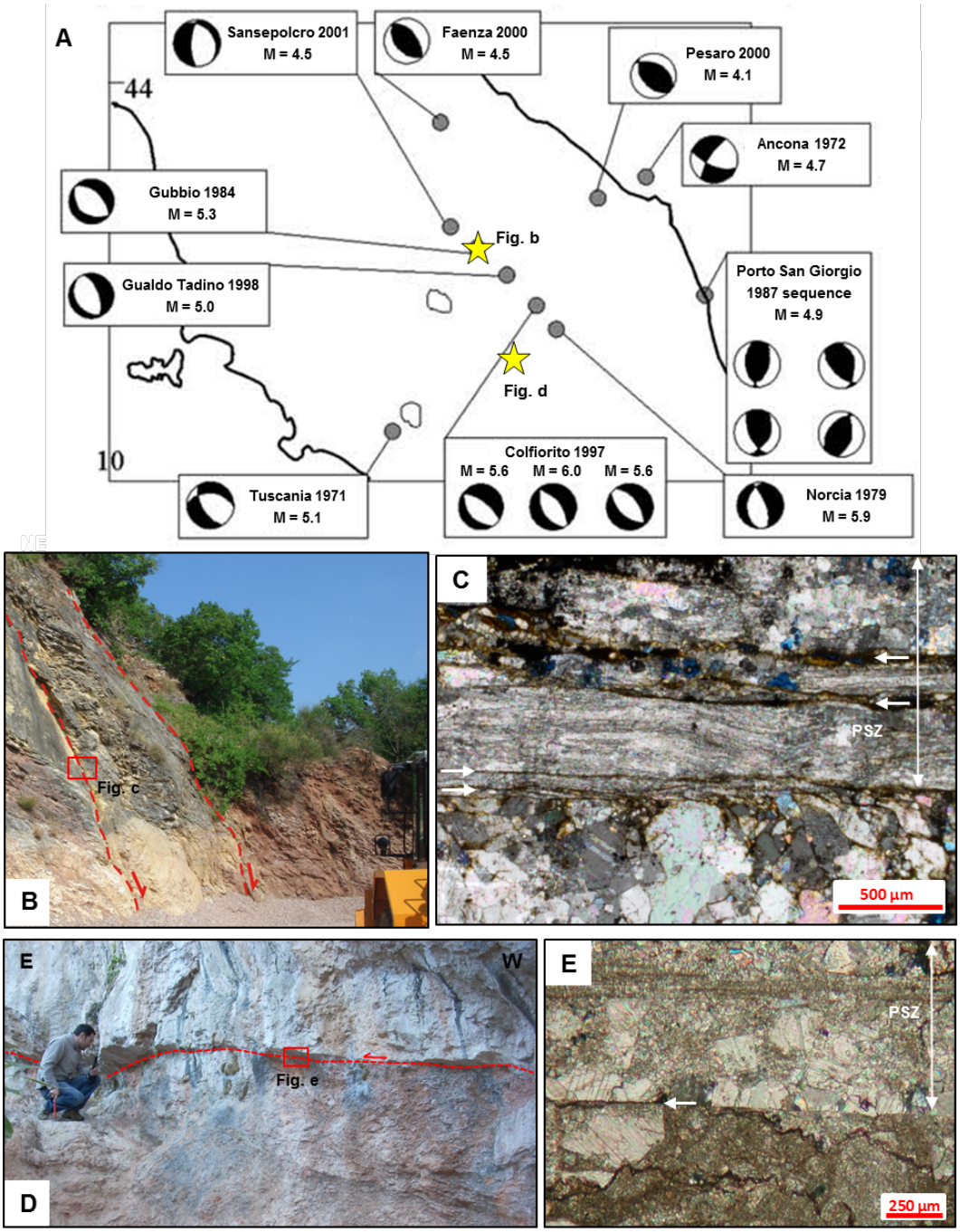

Figure 3.1 a) Focal mechanism distribution within the Northern Apennines seismic belt in central Italy. Figure taken from Collettini et al. (2006). **b)** The active Gubbio normal fault (see fig. **a** for location), which deforms a mixture of Jurassic-Oligocene micritic limestone (yellow in colour) and marly limestone (red in colour). **c)** Optical microscope image of a PSZ within the core of the Gubbio fault (see fig. **b** for sample location). The PSZ contains numerous slip surfaces (indicated by arrows), which are highlighted by the presence of dark brown phyllosilicate. The rest of the PSZ is dominated by calcite veining. Additional examples of phyllosilicate-enriched PSZs from the northern Apennines are presented in Appendix 1.1. **d)** The exhumed Spoleto thrust fault (see fig. **a** for location), which brings Lower Jurassic massive limestones in the hangingwall on top of Cretaceous layered limestones in the footwall. **e)** Optical microscope image of the PSZ of the Spoleto fault (see fig. **d** for sample location). Again the PSZ is dominated by calcite veining, and the PSS is contaminated by brown phyllosilicate (indicated by arrow) from pressure-solution. Figs. **d** and **e** are courtesy of Telemaco Tesei.

behaviour of phyllosilicate-bearing carbonate faults during seismic slip, we present the results from a set of high-velocity friction experiments carried out on gouges containing different proportions of calcite and phyllosilicate, under dry and water-saturated conditions. The mechanical data from our experiments is accompanied by microstructural observations of the deformed gouges, which we use to devise a micro-mechanical model that can be used to explain their frictional behaviour.

3.2 *Experimental setup and procedure*

Friction experiments were performed using the Low to High Velocity Rotary Shear Apparatus at Durham University (Chapter 1, Section 1.3.4.1). We deformed end-member gouges of calcite, mixed-layer illite-smectite, and smectite, as well as 50:50, 80:20 and 90:10 mixtures of calcite+illite-smectite and calcite+smectite. These are representative of the PSZ compositions observed in the northern Apennines (Bullock et al., 2014; Collettini et al., 2013). The calcite gouges were prepared from undeformed samples of the Scaglia Rossa limestone (~95% calcite), which were collected from field locations close to the exposure of the Gubbio fault (see Bullock et al., 2014). The mixed-layer illite-smectite clay (90-98% purity) was obtained from the Clay Minerals Society Special Clays Repository and the smectite was obtained as Na-montmorillonite (90-100% purity) from the Clay Minerals Society Source Clays Repository. All samples were crushed by hand using a fly press, and were subsequently ground to a fine powder using a pestle and mortar. These powders were then sieved to create synthetic gouges with a grain size range of 180-250 μm.

The samples were assembled for testing by sandwiching 1.5 g of gouge (or 1.2 g of gouge for wet experiments, to allow for volume increase when swelling clays were saturated) between two steel cylinders of 25 mm diameter. The surfaces of the steel cylinders are radially grooved to depths of 500 μm in order to ensure that slip localization occurs within the gouge layer rather than along the boundaries between the cylinders and the gouge. The gouge is confined by fixing a Teflon ring around the sample assembly (Mizoguchi et al., 2007) (Chapter 1, Fig. 1.3). The sample is then set within a vertical loading frame in which the lower cylinder remains stationary whilst the upper cylinder is rotated by a servomotor. An axial load is applied from the base of the loading frame via a pneumatic Bellofram cylinder. Friction during the experiments is measured using compression load cells attached to a high precision arm-type torque meter, and output values were recorded by a data logger at a sampling frequency of 1 KHz.

Experiments were conducted at room temperature and each sample was run both at room-humidity ('dry') and under water-saturated ('wet') conditions. Prior to the room-humidity experiments, the clays were oven-dried overnight at 105°C to remove adsorbed water. For water-saturated experiments, ~0.27 ml of deionised water was applied to the gouge layer to achieve saturation. After application of normal load, samples were held for 3 minutes prior to shearing to allow for an initial phase of compaction. The experiments were then run at an equivalent velocity (Shimamoto and Tsutsumi, 1994) (Chapter 1, Section 1.3.4.3) of 1.3 m/s, representative of seismic slip, and a normal load of 9 MPa (with the exception of Experiment 416, which had to be run at 1.2 MPa due to the excessive mobilization of saturated montmorillonite gouge at higher normal loads).

Experiments were terminated at 3 different stages for sampling of deformed gouges. These stages were (Fig. 3.2): 1) after application of normal load for 3 minutes, prior to shearing; 2) on attainment of peak friction, before slip-weakening has occurred (or during the very early stages of slip in the case of gouges that do not exhibit a peak in friction); 3) on attainment of steady-state friction, subsequent to weakening. This systematic sampling enables observation of microstructural evolution during slip and an assessment of how grain- and aggregate-scale deformation mechanisms may influence frictional behaviour.

The experimental configuration does not enable us to measure variations in pore fluid pressure, temperature or gas emissions during our experiments. Indeed, the inability to monitor pore fluid pressure is a common technical limitation during high-velocity friction experiments, which only

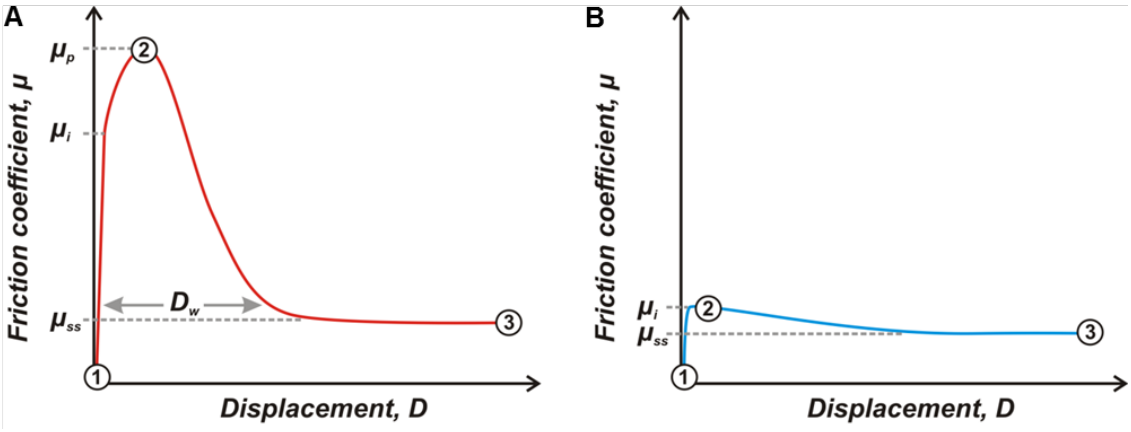

Figure 3.2 Schematic representation of frictional evolution during the experiments. Fig. **a** shows the case for gouges which exhibit a peak in friction during the experiments and fig. **b** shows the case for gouges which do not exhibit a peak in friction. Numbering refers to the three stages at which samples were recovered for inspection. See text for explanation.

recent works have attempted to overcome (Violay et al., 2013). Therefore, in this manuscript we do not attempt to speculate on the dynamic weakening mechanisms that may be in operation during our experiments. Instead, we rely on microstructural observations of the deformed gouges to explain differences in mechanical behaviour.

3.3 *Results*

3.3.1 *Mechanical data*

3.3.1.1 *Dry gouges*

Plots of friction coefficient against displacement for all experiments run until steady-state are shown in Figs. 3.3 and 3.4. These results are also summarised in Table 3.1 and Fig. 3.5. Results of experiments terminated at peak friction are shown in Appendix 1.2. All of the experiments exhibit an initial phase of linear-elastic deformation prior to yielding. The yield point, at which the friction curve deviates from being linear, gives us the initial frictional strength of the gouge, μ_i (Fig. 3.2, see also Appendix 1.3). For the dry end-member gouges, μ_i values are all similar, falling within the range 0.53-0.58 (Figs. 3.3 and 3.5a). μ_i is followed by a slip-hardening phase within the first ~0.1 m of slip, during which friction evolves to a peak value, μ_p (Fig. 3.3). The end-member calcite gouge has a μ_p value of 0.75 (Figs. 3.3 and 3.5b), which is slightly higher than that of the clay end-members, which have μ_p values of 0.63 for illite-smectite (Fig. 3a) and 0.61 for montmorillonite (Fig. 3.3b). μ_p is followed by a dramatic decrease in frictional strength, over a slip-weakening distance, D_w, to steady-state values (μ_{ss}), which for all dry end-member gouges lies in the range 0.25-0.26 (Figs. 3.3 and 3.5c). The slip-weakening distance is defined as the displacement at which (μ_p-μ_{ss}) reduces to 5% of (μ_p-μ_{ss}) (Fig. 3.2) (Mizoguchi et al., 2007). The end-member calcite gouge displays a slip-weakening distance of 0.58 m, whereas the clay end-members become weaker over shorter distances of 0.17 m and 0.2 m for the illite-smectite and montmorillonite gouges, respectively (Figs. 3.3 and 3.5d).

As would be expected, the curves for the gouges of mixed composition plot in positions intermediate between those of the end-members, although their overall trend is the same (Fig. 3.3). Initial friction values again show little variation, ranging from 0.51-0.56 (Fig. 3.5a), but μ_p decreases systematically as clay content increases, in both the calcite+illite-smecite and calcite+montmorillonite gouges (Figs. 3.3 and 3.5b), as does D_w (Fig. 3.5d).

Dry gouges

Calcite+illite-smectite

Exp. #	wt.% calcite	wt.% clay	μ_i	μ_p	μ_{ss}	D_w	Total displacement (m)
394	100	0	0.53	0.75	0.25	0.58	7.05
455	80	20	0.54	0.72	0.33	0.29	0.92
452	50	50	0.56	0.76	0.23	0.44	1.92
405	0	100	0.54	0.63	0.25	0.17	0.73

Calcite+montmorillonite

Exp. #	wt.% calcite	wt.% clay	μ_i	μ_p	μ_{ss}	D_w	Total displacement (m)
394	100	0	0.53	0.75	0.25	0.58	7.05
424	80	20	0.51	0.75	0.33	0.36	0.62
420	50	50	0.55	0.69	0.31	0.19	0.54
395	0	100	0.58	0.61	0.26	0.2	1.04

Wet gouges

Calcite+illite-smectite

Exp. #	wt.% calcite	wt.% clay	μ_i	μ_p	μ_{ss}	D_w	Total displacement (m)
414	100	0	0.56	0.6	0.19	0.36	1.6
479	90	10	0.52	0.49	0.26	0.34	1.06
457	80	20	0.37	0.25	0.18	-	1.42
454	50	50	0.31	-	0.16	-	1.44
418	0	100	0.09	-	0.08	-	1.48

Calcite+montmorillonite

Exp. #	wt.% calcite	wt.% clay	μ_i	μ_p	μ_{ss}	D_w	Total displacement (m)
414	100	0	0.56	0.6	0.19	0.36	1.6
477	90	10	0.38	0.38	0.09	-	1.36
451	80	20	0.16	-	0.09	-	1.57
422	50	50	0.07	-	0.05	-	1.97
416	0	100	0.17	-	0.13	-	3.13

Table 3.1 Summary of experiments run until steady-state and frictional parameters obtained.

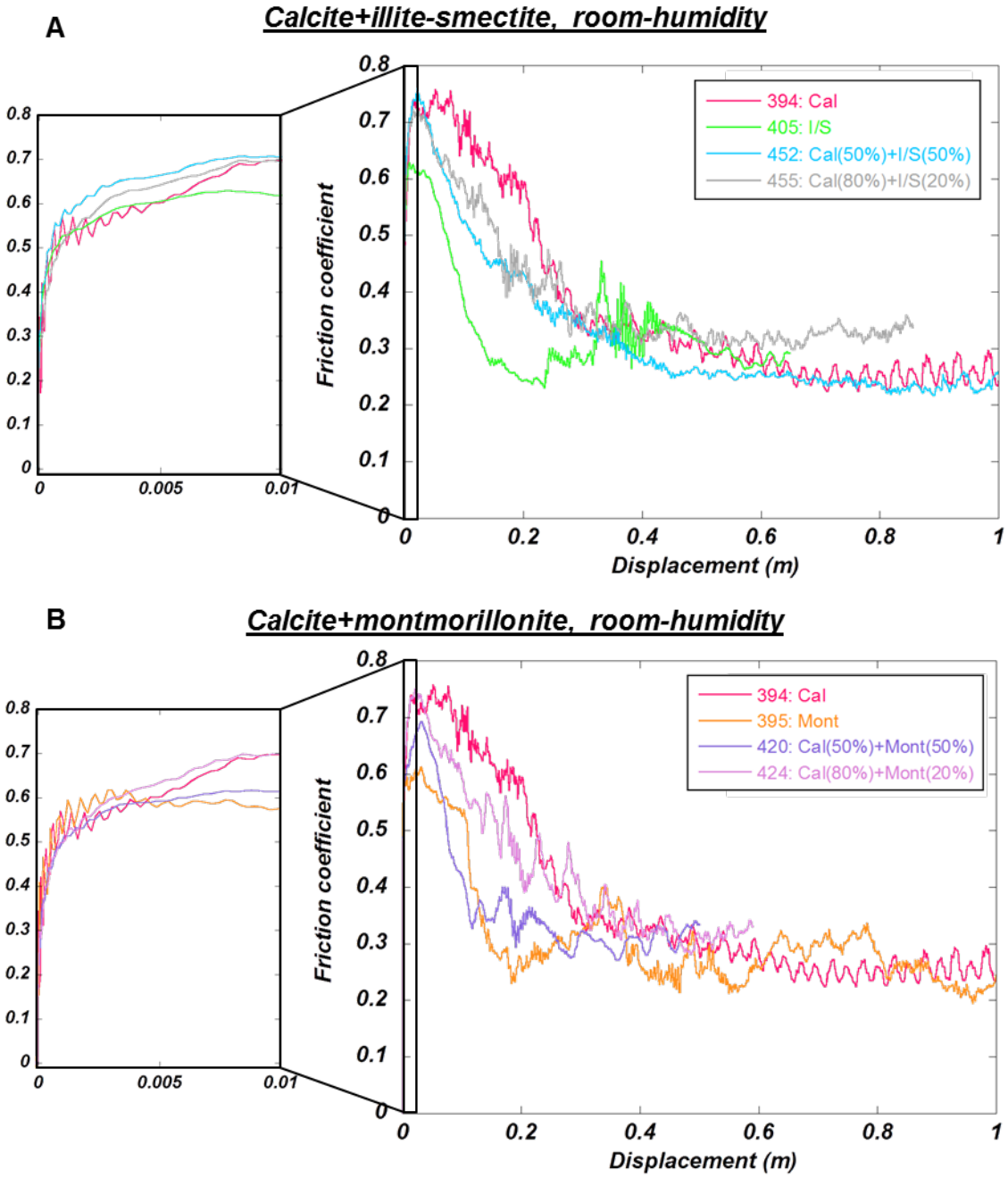

Figure 3.3 Experimental results for dry gouges sheared until the attainment of steady-state sliding. The magnified section of the curve shows the initial slip-hardening phase during which the initial value of friction attained at the very start of the experiment increases towards a peak value. **a)** Calcite and illite-smectite end-members and mixtures. **b)** Calcite and montmorillonite end-members and mixtures.

3.3.1.2 *Wet gouges*

The 100 wt.% wet calcite gouge displays a slip-weakening curve similar to that of its dry equivalent (Fig. 3.4), although values of μ_p, μ_{ss} and D_w are slightly reduced (0.6, 0.19 and 0.36 m, respectively) (Fig. 3.5). The other difference observed between the dry and wet calcite gouge is that whereas the dry gouge undergoes an immediate slip-hardening phase towards μ_p following the attainment of μ_i, the wet calcite gouge undergoes a brief slip-weakening phase, over a distance of just a few mm, before re-strengthening and evolving towards μ_p (Fig. 3.4).

Wet gouges containing 100% illite-smectite (Fig. 3.4a) and 100% montmorillonite (Fig. 3.4b), on the other hand, exhibit friction evolution curves that are markedly different to their dry equivalents. First, they display a significantly reduced μ_i of 0.09 for illite-smectite and 0.17 for montmorillonite (Fig. 3.5a). Then, as for the wet calcite gouge, μ_i is followed by an immediate slip-weakening phase. The difference is that as slip proceeds, slip-hardening does not occur at any stage in the wet clay gouges, and consequently, the large peak in friction that is observed during the dry-run experiments is never attained. Instead, friction evolves towards steady-state values almost immediately at the onset of slip (Fig. 3.4). Furthermore, the μ_{ss} values are very low: 0.08 for the illite-smectite end-member and 0.13 for the montmorillonite end-member (Fig. 3.5c). Considering that theses gouges are weak from the onset of slip, we do not assign them a slip-weakening distance.

The behaviour of the mixtures of calcite+phyllosilicate is very much dependent on the phyllosilicate composition and content. In calcite+illite-smectite gouges (Fig. 3.4a), there is a systematic decrease in frictional strength as the clay content is increased (Fig. 3.5a-c). At 10% clay, there is still a peak in friction, but its attainment is delayed; as in the wet calcite gouge, after the attainment of μ_i, the gouge undergoes slip-weakening, followed by a brief re-strengthening phase to a peak value of 0.49, before again undergoing slip-weakening to steady-state sliding. A similar friction evolution is observed at 20% illite-smectite, but the peak in friction is drastically reduced to just 0.25, which may be considered to be negligible. At 50 wt.% illite-smectite, the peak in friction is eradicated altogether. μ_{ss} values also decrease with increasing clay content, falling from 0.26 at 10% illite-smectite, to 0.16 at 50%.

In the calcite+montmorillonite gouges under wet conditions (Fig. 3.4b), μ_i values decrease as clay content increases (Fig. 3.5a), but during subsequent slip, they display very similar strengths, regardless of clay content (Fig. 5c). The exception is the 50 wt.% montmorillonite gouge, which

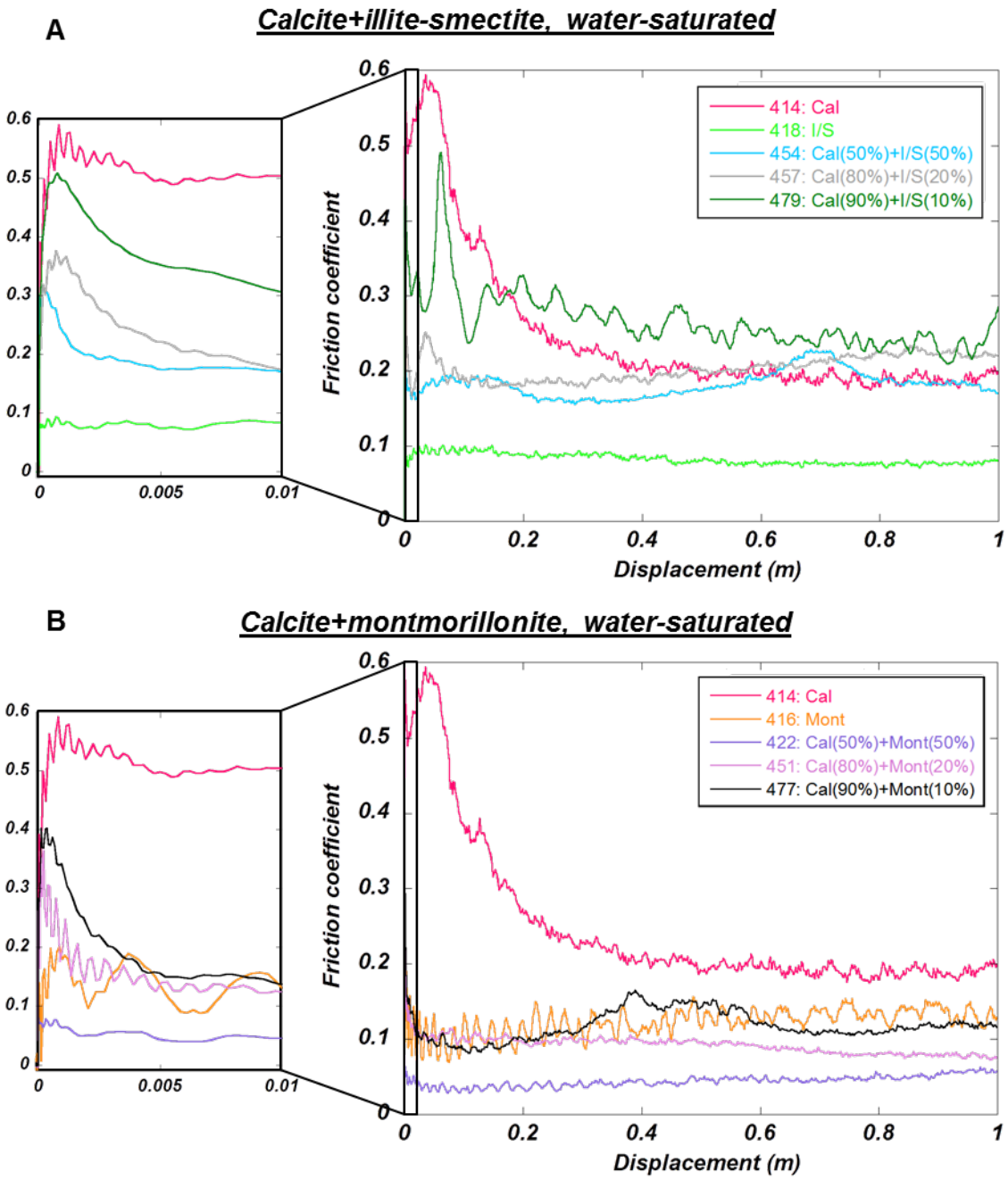

Figure 3.4 Experimental results for wet gouges sheared until the attainment of steady-state sliding. The magnified section of the curve shows the initial slip-weakening phase during which the initial value of friction attained at the very start of the experiment decreases before either 1) re-strengthening towards a peak value (in the case of experiments 414, 457 and 479); or 2) attaining steady-state sliding without undergoing any slip-hardening. **a)** Calcite and illite-smectite end-members and mixtures. **b)** Calcite and montmorillonite end-members and mixtures.

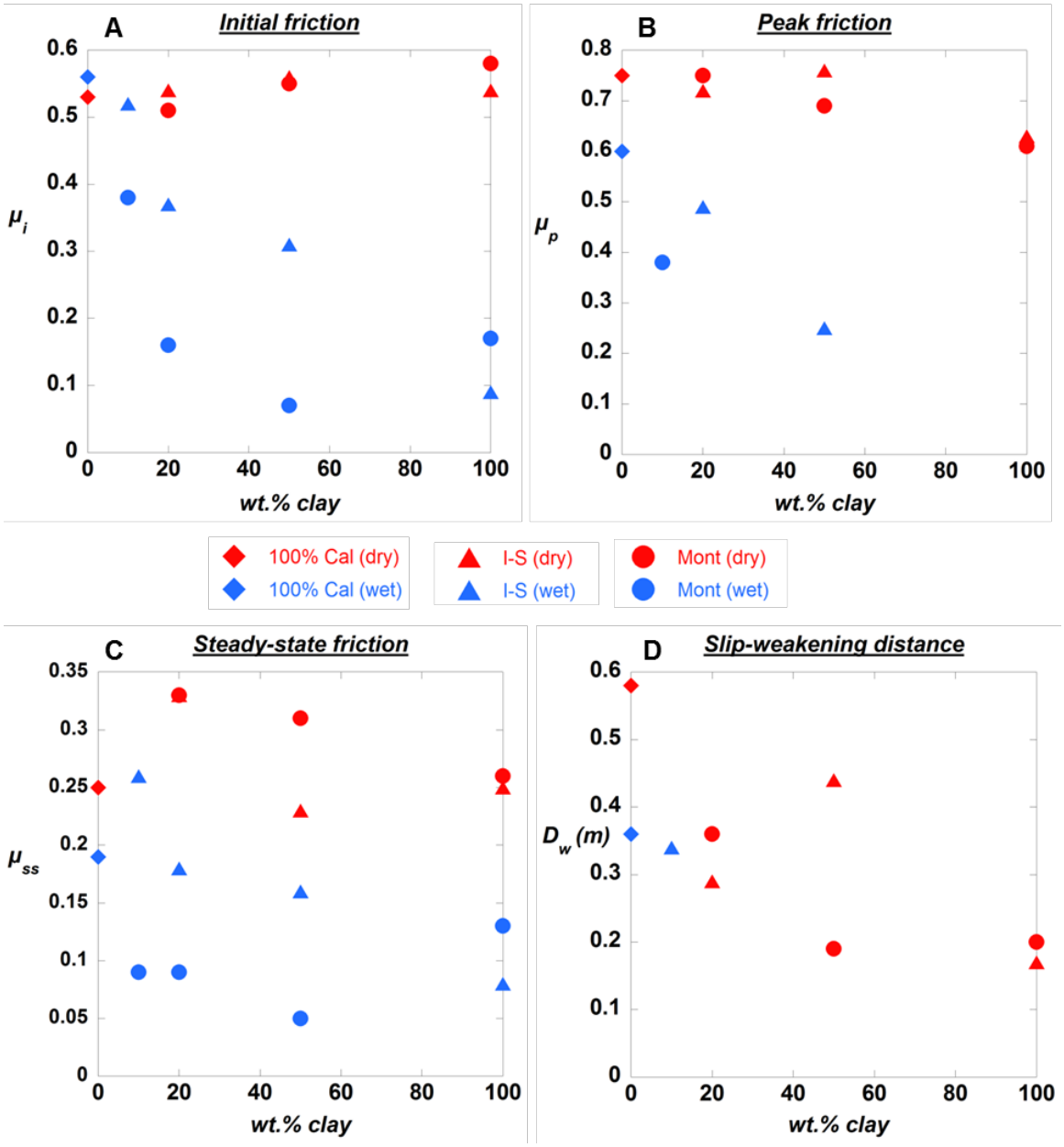

Figure 3.5 Summary plots showing evolution of frictional parameters as a function of increasing clay content. Key for all plots is shown in centre of figure. **a)** Initial friction values are relatively constant for dry gouges, but decrease with increasing clay content for wet gouges. **b)** Peak friction values decrease slightly with increasing clay content for dry gouges, but this trend is much more enhanced for the wet gouges, to the extent that a peak in friction is absent for the most clay-rich gouges. **c)** Steady-state friction values show an overall decrease with increasing clay content for both dry and wet gouges. **d)** D_w values again show an overall decreasing trend with increasing clay content, although in the case of wet clay-bearing gouges that do not exhibit a peak in friction, a slip-weakening distance is not applicable.

has a μ_i value of just 0.07, less than half that of the montmorillonite end-member, and it remains anomalously weak throughout the experiment. It should, however, be remembered that the 100% montmorillonite gouge was deformed under a lower normal load of 1.2 MPa, which could explain why it displays greater strength than the 50% montmorillonite gouge. Despite these subtle anomalies, all of the montmorillonite-bearing gouges exhibit the same frictional evolution during the experiments, in that none of them display a peak in friction, even when clay content is just 10 wt.%. All of the mixtures evolve to steady-state sliding, at values of μ_{ss} between 0.05-0.09, as soon as slip initiates. It should also be noted that for ≥20 wt.% montmorillonite, the μ_i value is less than the yield strength of the gouge (see Figs. A1.9b and A1.11 in Appendix 1.3); this further illustrates just how weak these gouges are right from the onset of slip.

3.3.2 *Microstructural observations*

Thin sections were analysed using a Field Emission Scanning Electron Microscope. Un-sheared gouges were prepared by sectioning gouges that had been held under 9 MPa of normal load for 3 minutes, allowing examination of the initial microstructure of the gouge prior to shearing. Deformed gouges were prepared by sectioning the sheared gouges in an orientation normal to the shear plane and tangential to the direction of rotary shear. We refer to the entire width of the deformed gouge as the 'slip zone' produced during the experiment. Each slip zone contains a principal slip surface (PSS), where the majority of the rotary shear displacement is accommodated. The sample typically splits along the PSS on removal from the apparatus. In some experiments, slip appears to localize into a narrow zone adjacent to the PSS and this region is referred to as the principal slip zone (PSZ). Alongside the images presented in Figs. 3.6-3.9, we present supporting images in Appendices 1.4-1.6.

3.3.2.1 *Un-sheared gouges (post-compaction)*

The initial microstructure of the 100 wt.% calcite gouge under dry conditions comprises discrete, angular grains of calcite (Fig. 3.6a). The gouges were sieved to obtain an average starting grain size < 250 μm. Many of the calcite grains are rimmed by a much finer powder of calcite grains averaging ~1 μm diameter (Fig. 3.6a). These finer grains were likely produced during crushing and sieving of the gouges and adhered to the larger grains due to electrostatic charges and/or moisture on grain surfaces. The appearance of the 100 wt.% calcite gouge under wet conditions is very similar to its dry equivalent, except that there is a greater amount of the fine calcite powder surrounding and in between the larger calcite grains (Fig. 3.6b). This is likely due to the wet gouge

being more cohesive and therefore the powder being more easily retained during thin section preparation.

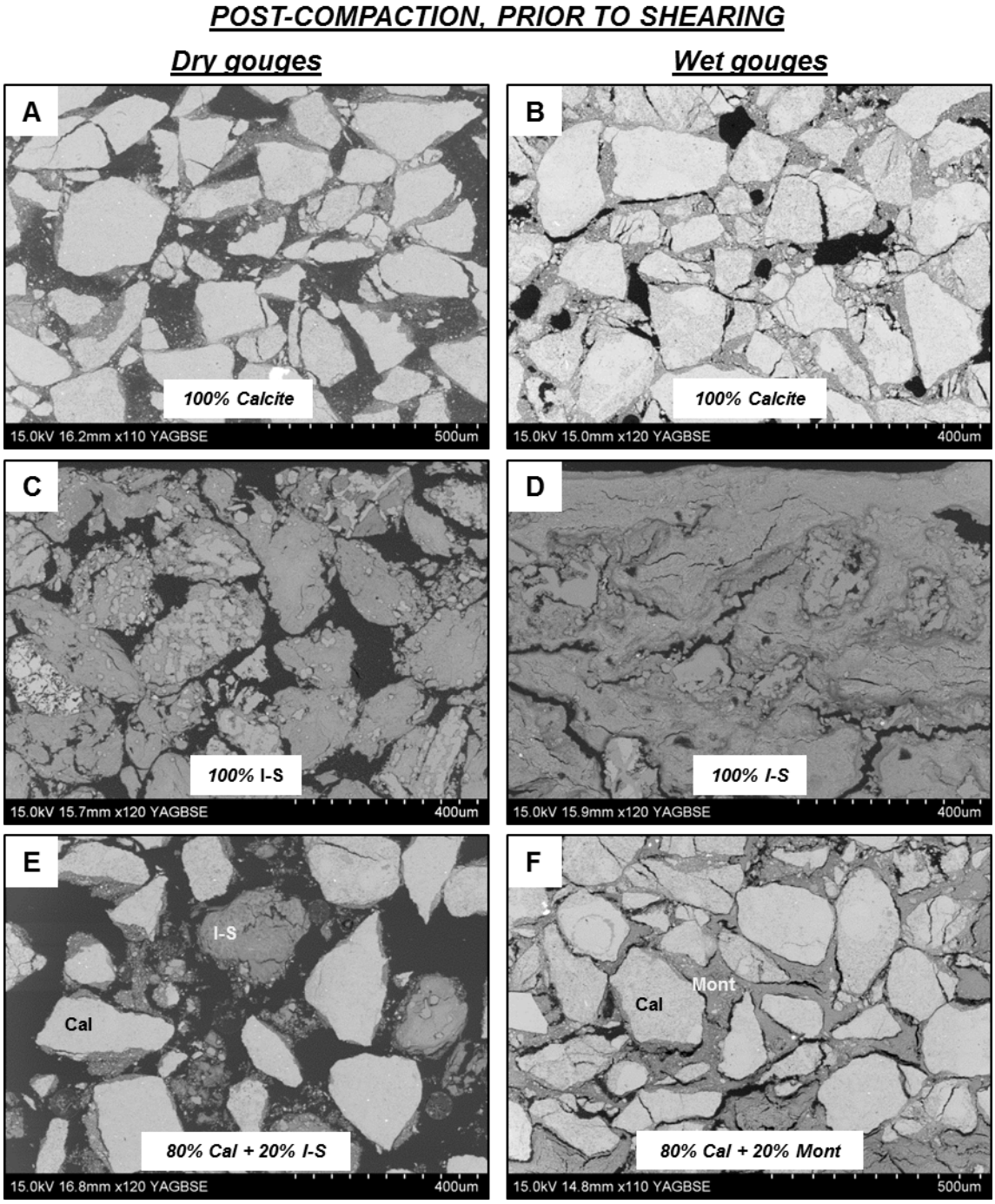

Figure 3.6 Initial microstructure of the gouges recovered after being held under 9 MPa normal load for 3 minutes, prior to shearing. See main text for full description. **a)** 100% calcite, dry. **b)** 100% calcite, wet. **c)** 100% illite-smectite, dry. **d)** 100% illite-smectite, wet. **e)** 80% calcite + 20% illite-smectite, dry. **f)** 80% calcite + 20% montmorillonite, wet.

The initial microstructure of the 100 wt.% clay gouges under dry conditions comprises discrete agglomerates of clay particles, which have random shapes and orientations (Fig. 3.6c); no fabric is developed. The initial microstructure of the 100 wt.% clay gouges under wet conditions is rather different. Discrete agglomerates no longer exist; instead, when wet, the agglomerates appear to merge together upon compaction to form a mass of interconnected clay material, although still no fabric is formed (Fig. 3.6d).

For the mixed calcite+phyllosilicate gouges, the initial microstructure when dry again comprises discrete grains of calcite and agglomerates of clay (Fig. 3.6e). However, when wet, the clays once again merge together upon compaction and disperse throughout the gouge, forming a network of interconnected clay surrounding the calcite grains (Fig. 3.6f).

3.3.2.2 *Sheared gouges: peak friction*

The microstructure of dry gouges sheared until peak friction is characterized by the formation of a sharp, but sometimes wavy, PSS (Fig. 3.7a-b, see also Figs. A1.13-A1.16 in Appendix 1.5). R_1-shears are already well-developed within the slip zone at this stage, and R_2-, P- and Y-shears are present in some, but not all cases (Fig. 3.7a). Significant grain size reduction is evident throughout the gouge layers recovered at peak friction (Fig. 3.7a-c), when compared with the initial starting material (Fig. 3.6a, c and e). Grain size reduction is more intense in close proximity to the PSS (Fig. 3.7b) than it is in the lower parts of the slip zone (Fig. 3.7c), in some cases producing nanoparticle-sized material adjacent to the PSS (Fig. 3.7b).

The wet gouges display quite a different microstructure when sheared until peak friction. There is no well-defined PSS in the wet gouges, but instead just a poorly-defined wavy surface, which likely corresponds to the PSS (Fig. 3.7d-e). Unlike the dry gouges, there is no Riedel shear development within the slip zone. Significant grain size reduction has occurred, but it is not as intense as in the dry gouges. This is particularly evident when examining the region adjacent to the PSS (Fig. 3.7e), where grain size appears very similar to that observed away from the PSS (Fig. 3.7f). In addition, large grains up to 200 μm diameter, which appear to have undergone minimal deformation, remain in the slip zone (compare Fig. 3.7d with 3.6a).

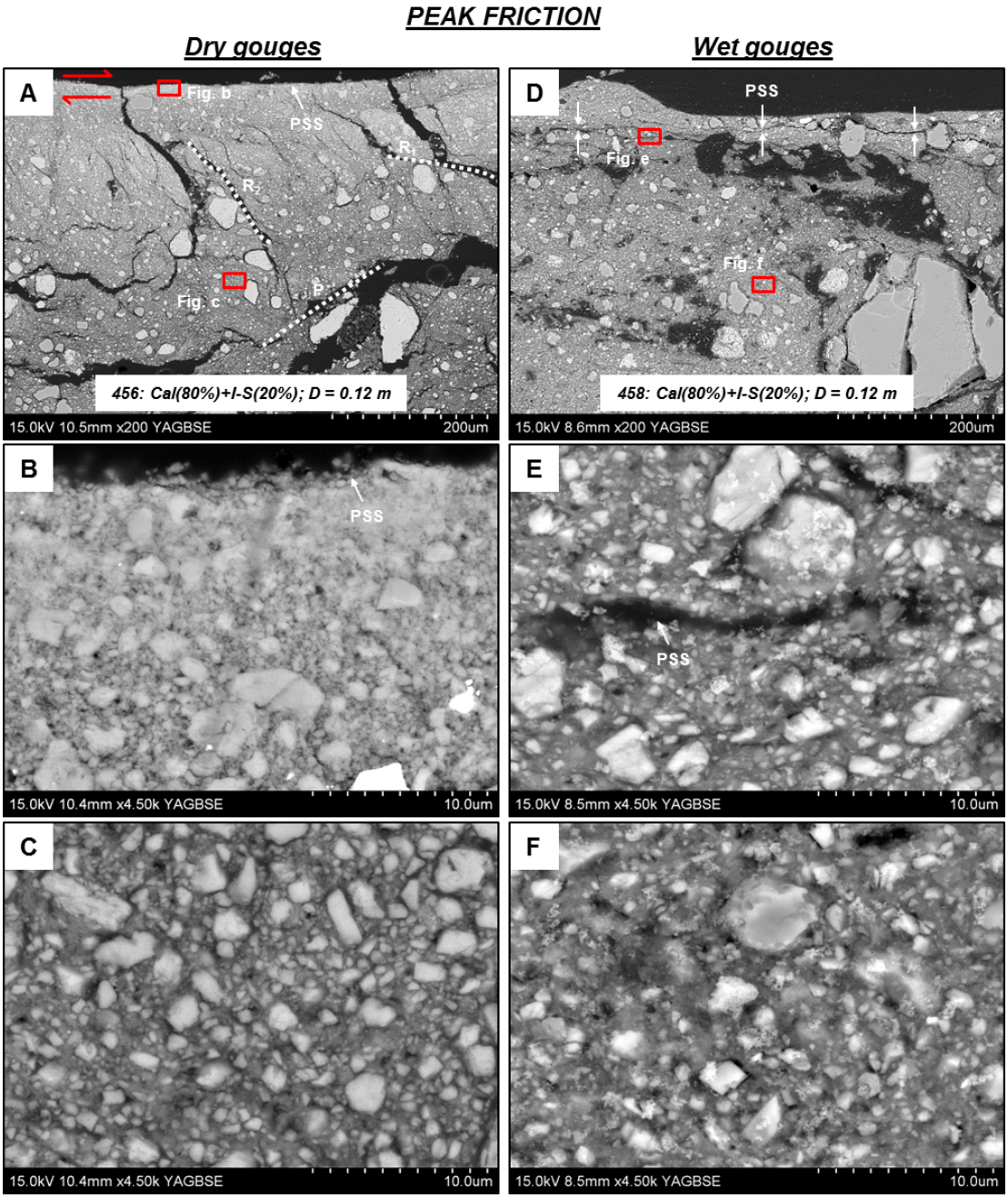

Figure 3.7 Deformed microstructures after recovery of gouges at peak friction. See main text for full description. **a)** 80% calcite + 20% illite-smectite, dry. Overview of slip zone showing location of PSS. Examples of Riedel shear structures are labelled and the sense of shear inferred. R_2-shears dominate the fabric in the upper part of the slip zone and P-shears dominate the fabric in the central part of the slip zone in the lower portion of the image. **b)** Zoomed in image of PSS and adjacent region in fig. **a**. **c)** Zoomed in image of matrix within central slip zone of fig. **a**. **d)** 80% calcite + 20% illite-smectite, wet. Overview of slip zone, showing location of a very vague and undulating PSS. **e)** Zoomed in image of PSS and adjacent region shown in fig. **d**. **f)** Zoomed in image of matrix within central slip zone of fig. **d**.

3.3.2.3 *Sheared gouges: steady-state*

The microstructure of the dry gouges deformed until steady-state friction varies slightly depending on gouge composition. In the 100% dry calcite gouge, the PSS (Fig. 3.8a and b) is much sharper and straighter than it was at peak friction (see Fig. A1.13a-b in Appendix 1.5). As at peak friction, there is a marked reduction in grain size towards the PSS. In addition, a PSZ, up to 60 μm wide, is formed adjacent to the PSS. The PSZ comprises highly compacted, ultra-fine grained calcite, which is scattered with bubbles (Fig. 3.8b). The grain size in the bulk of the gouge, i.e., away from the PSZ, does not differ greatly to that observed at peak friction (compare Figs. 3.8c and Fig. A1.13c in Appendix 1.5). R_1-shears are extensive in the lower part of the slip zone and are sometimes rotated into a Y-orientation (Fig. 3.8a). R_2-shears are also common, more so towards the upper part of the slip zone. Smaller-scale R_1-, Y- and P-shears are also common within the PSZ (Fig. 3.8b).

In the 100% dry clay gouges (Fig. 3.8d-f and Fig. A1.17 in Appendix 1.6), the PSSs are not as sharp and straight as in the 100% calcite sample (Fig. 3.8a-b). It should be noted that the 100% illite-smectite and 100% montmorillonite gouges have experienced smaller displacements (0.73 m and 1.04 m total displacement respectively) than the 100% calcite gouge (7.05 m total displacement). However, we see that in other calcite-rich gouges deformed to similar displacements as the clay end-members, the PSSs are still very sharp and straight compared to the in the clay gouges (e.g. Figs. 3.9a-b and 3.10a-b, plus Figs. A1.18 and A1.19 in Appendix 1.6). Thus it appears that a wispy, undulating PSS is a feature unique to the 100% clay gouges, regardless of displacement. In addition, grain size reduction adjacent to the PSS (Fig. 3.8e) is not as intense in the clay end-member gouges as in the 100% calcite gouge; grain size is more uniform over the whole slip zone (compare Figs. 3.8e and f), and subsequently no PSZ is present. However, there are Riedel shears developed throughout the slip zone (Fig. 3.8d).

In the dry gouges of mixed composition (Figs. 3.9a-c and 3.10a-c), the microstructure at steady-state is somewhat intermediate between those of the end-members described above. In the presence of 20 wt.% clay, microstructures are comparable to those in the calcite end-member. PSSs are very sharp and straight, and intense grain-size reduction has occurred towards these surfaces (Fig. 3.9a-b, see also Fig. A1.18 in Appendix 1.6). In the 20 wt.% illite-smectite gouge, there is a very well-developed, continuous PSZ up to 65 μm wide (Fig. 3.9a-b), whereas in the 20 wt.% montmorillonite gouge, the PSZ is highly variable in width, being only a few microns in some places, but up to 35 μm in others (Fig. A1.18, Appendix 1.6). Despite differences in development, the PSZs in the illite-smectite- and montmorillonite-bearing gouges are of similar nature: they

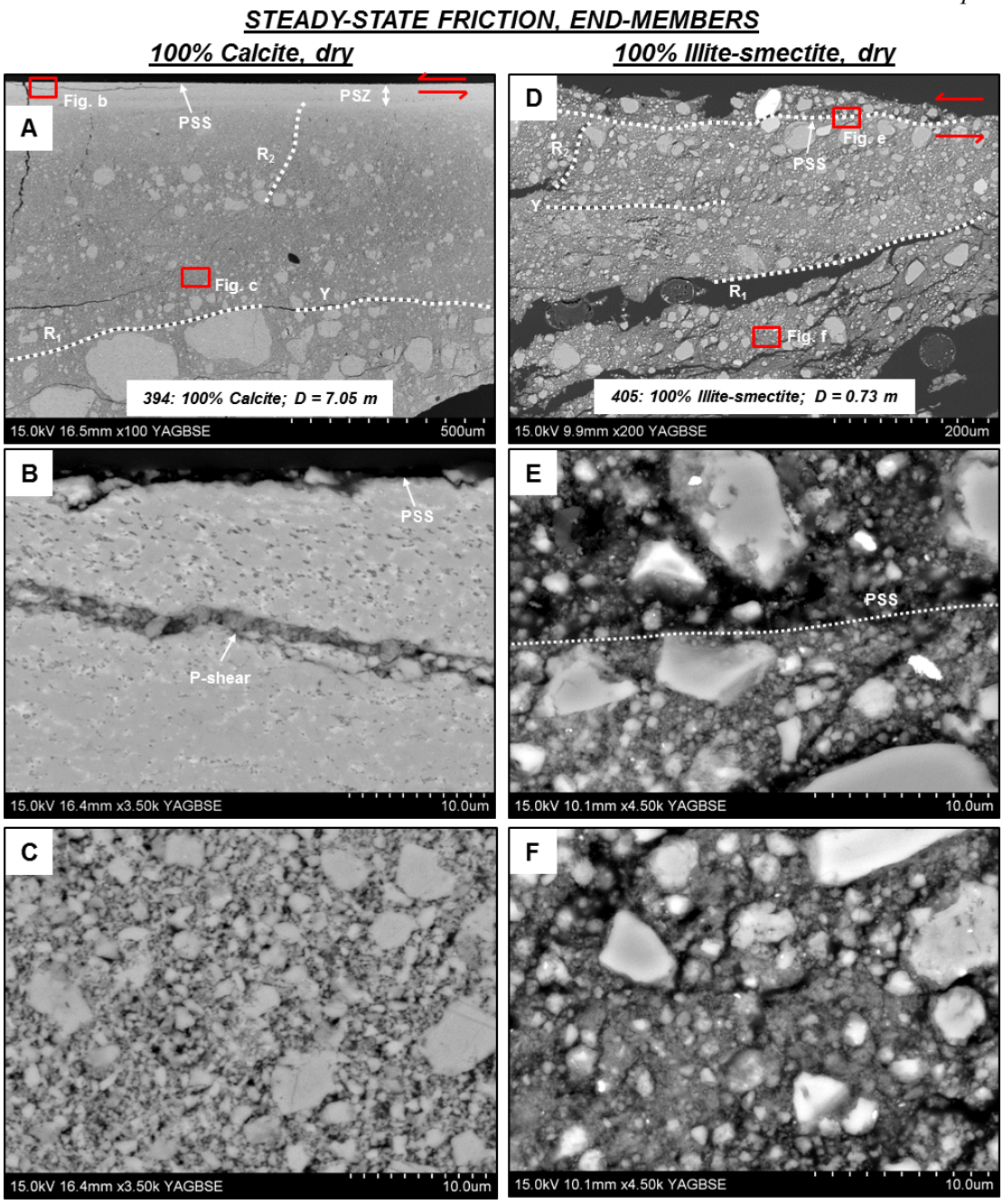

Figure 3.8 Deformed microstructures of dry end-member gouges after recovery during steady-state sliding. See main text for full description. **a)** 100% calcite, dry. Overview of slip zone showing location of PSS and PSZ. Examples of Riedel shear structures are labelled and the sense of shear inferred. R_1-shears dominate the fabric in the lower part of the slip zone, whilst higher-angle R_2-shears dominate the fabric in the upper part of the slip zone. **b)** Zoomed in image of region adjacent to PSS and PSZ shown in fig. **a**. A P-shear transects the centre of the image. The dark spots scattered throughout the PSZ are holes, inferred to be the result of degassing as a consequence of thermal decomposition of calcite. **c)** Zoomed in image of matrix within central slip zone of fig. **a**. **d)** 100% illite-smectite, dry. Overview of slip zone, showing location of PSS. Examples of Riedel shear structures are labelled and the sense of shear inferred. **e)** Zoomed in image of PSS and adjacent region shown in fig. **d**. **f)** Zoomed in image of matrix within central slip zone of fig. **d**.

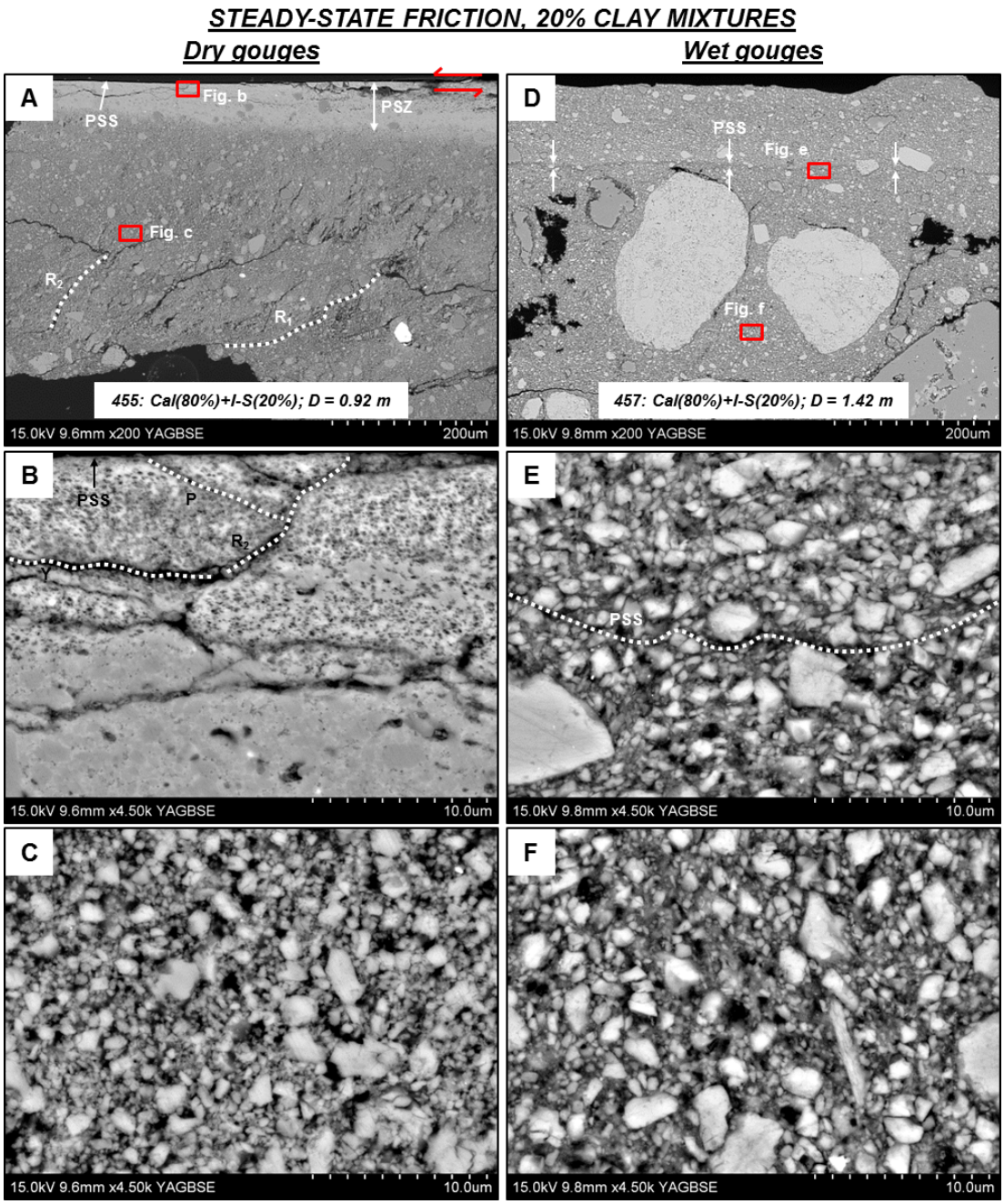

Figure 3.9 Deformed microstructures after recovery of gouges containing 20 wt.% clay during steady-state sliding. See main text for full description. **a)** 80% calcite + 20% illite-smectite, dry. Overview of slip zone showing location of PSS and PSZ. Examples of Riedel shear structures are labelled and the sense of shear inferred. Fabric within the slip zone is dominated by R_1-shears. **b)** Zoomed in image of PSZ shown in fig. **a**. R_1-, P- and Y-shears are present within the PSZ. The black spots scattered throughout the PSZ are holes, inferred to be degassing bubbles as a consequence of calcite decarbonation. **c)** Zoomed in image of matrix within central slip zone of fig. **a**. **d)** 80% calcite + 20% illite-smectite, wet. Overview of slip zone showing location of PSS. **e)** Zoomed in image of PSS and adjacent region shown in fig. **d**. **f)** Zoomed in image of matrix within central slip zone of fig. **d**.

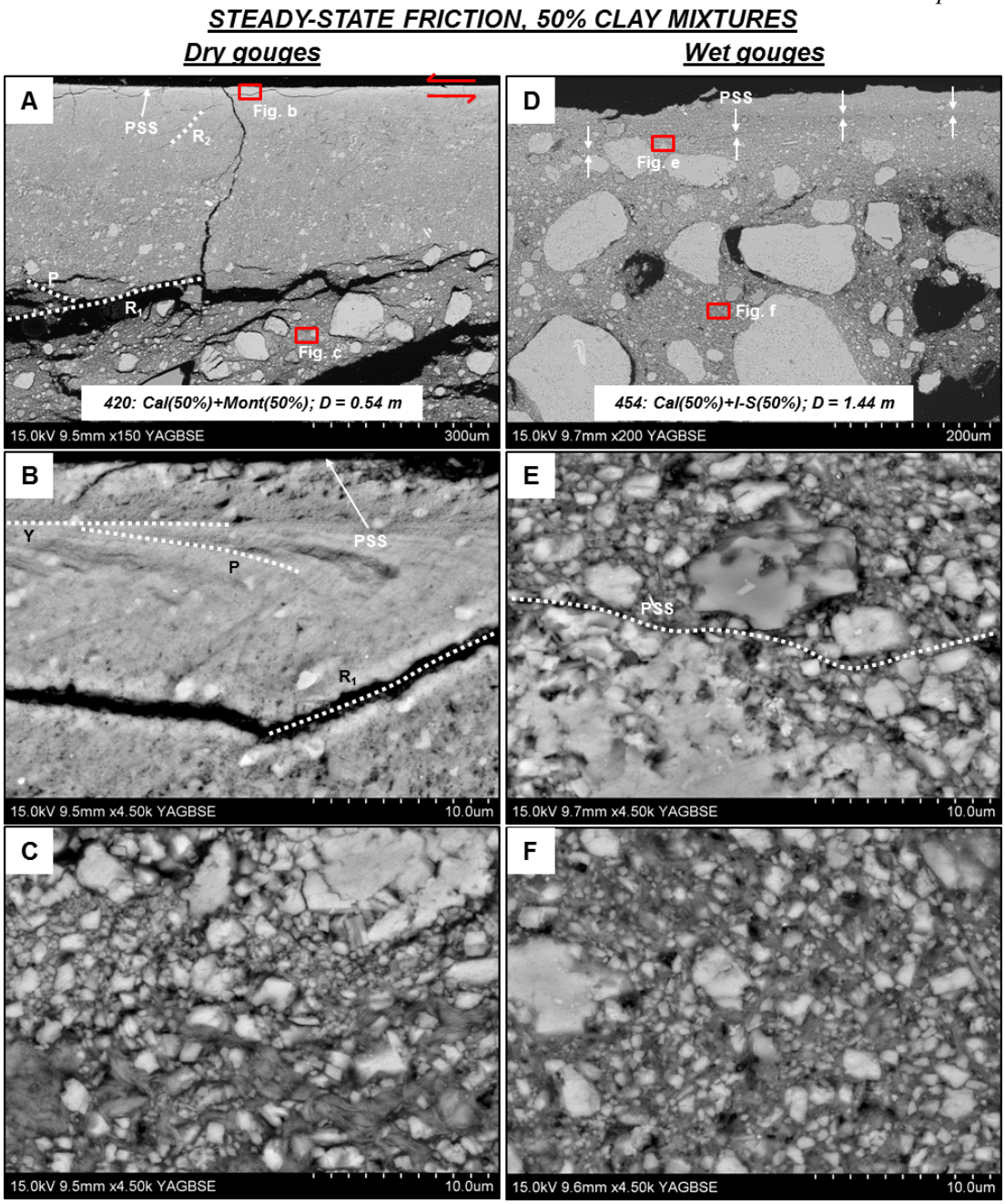

Figure 3.10 Deformed microstructures after recovery of gouges containing 50 wt.% clay during steady-state sliding. See main text for full description. **a)** 50% calcite + 50% montmorillonite, dry. Overview of slip zone showing location of PSS. Examples of Riedel shear structures are labelled and the sense of shear inferred. R_1-shears dominate the fabric within the slip zone. A PSZ up to 30 µm wide is formed adjacent to the PSS (see fig. **b**) but is unresolvable at the scale of the image. **b)** Zoomed in image of PSS and PSZ shown in fig. **a**. The 5 µm wide zone right at the top of the image, delimited from the rest of the PSZ by a sub-horizontal Y-shear, contains rounded to elongate black spots, which we interpret to be degassing bubbles as a result of calcite decarbonation. Several very fine P-shears are visible just beneath this zone as well as the intersecting P- and R_1-shears in the lower part of the image. **c)** Zoomed in image of matrix within central slip zone of fig. **a**. **d)** 50% calcite + 50% illite-smectite, wet. Overview of slip zone showing location of PSS, which is very vague and almost unresolvable at the scale of the image. **e)** Zoomed in image of PSS and adjacent region in fig. **d**. **f)** Zoomed in image of matrix within central slip zone of fig. **d**.

comprise a matrix of highly compacted, ultra-fine grained calcite+clay and both contain bubbles, replicating the PSZ microstructure observed in the 100% calcite gouge (Fig. 3.9b and Fig. A1.18b, Appendix 1.6). As in the 100% calcite gouge, the slip zone has a fabric characterized by R_1-, R_2- and Y-shears (Fig. 3.9a and Fig. A1.18a), and the grain size out width of the PSZ does not vary greatly from peak friction to steady-state (compare Figs. 3.7c and 3.9c).

In the presence of 50 wt.% clay, the microstructures are different for the illite-smectite-bearing and the montmorillonite-bearing gouge. The 50 wt.% illite-smectite gouge has a microstructure unlike any of the other gouges in that there is quite a distinct partitioning of strain across the slip zone, with different domains separated by Y-shears (Fig. A1.19a, Appendix 1.6). Despite this, it still has a sharp PSS as in all the other dry gouges, but it is relatively rough in comparison (Fig. A1.19b). Increased grain-size reduction is also observed in areas adjacent to the PSS (Fig. A1.19b). There is not a well-developed PSZ, but the compacted, ultrafine-grained material associated with PSZs in the 20 wt.% clay samples is present in localized patches along the PSS (Fig. A1.19b). Where this compacted ultrafine-grained material is not present, the material adjacent to the PSS is characterized by predominantly sub-micron sized, sub-angular to sub-rounded clasts of calcite and flakes of phyllosilicate (Fig. A1.19b).

The 50 wt.% montmorillonite gouge is similar to the 20 wt.% montmorillonite gouge, in that it has a sharp, smooth PSS and a variably developed PSZ (up to 30 μm wide) (Fig. 3.10a-b). Plus it has a pervasive fabric dominated by R_1-shears (plus some R_2- and P-shears present within the PSZ) (Fig. 3.10a-b). Once again, the PSZ (Fig. 3.10b) is characterized by a matrix of compacted, ultra-fine grained calcite+clay and, in places, contains bubbles, although the bubbles are not as ubiquitous as in the gouges containing just 20 wt.% clay (Fig. 3.9b).

We were not able to recover any wet clay end-member gouges for thin-sectioning; the swelling nature of the clays causes them to be easily extruded from the sample assembly during the experiments. Thus, we only describe here the observations made for gouges of mixed calcite+phyllosilicate composition. The wet clay-bearing gouges recovered after steady-state sliding have a more fully-developed, through-going PSS (Figs. 3.9d and 3.10d, see also Figs. A1.20 and A1.21 in Appendix 1.6) than those recovered at peak friction (Fig. 3.7d). However, the PSS is still quite a vague and undulating feature (Figs. 3.9e and 3.10e) and not as sharp and straight as in the dry gouges (Figs. 3.9b and 3.10b). The PSS does not appear to be defined by anything in particular, e.g. we do not observe any alignment of phyllosilicates along the PSS. Several large, sub-rounded grains, up to 230 μm in diameter, remain within the central portion of the slip zone

(Figs. 3.9d and 3.10d). This is more than twice the size of the largest grains in the central slip zone of their dry equivalents, which are also more sub-angular in nature (Figs. 3.9a and 3.10a). In addition, no PSZ is developed; the matrix grain size adjacent to the PSS (Figs. 3.9d and 3.10d) is comparable to that in the lower parts of the slip zone (Figs. 3.9f and 3.10f), and is certainly much coarser than in the dry gouge equivalents (Figs. 3.9b and 3.10b). Finally, none of the PSZ characteristics observed in the dry gouges sheared until steady-state, i.e. the presence of highly compacted ultrafine-grained material or bubbles, are observed in the wet gouges. Fabric development in the slip zone, in the form of Riedel shears, is also absent. These microstructures are consistent for all wet clay-bearing gouges, the only difference being that in the gouges containing just 10 wt.% clay (Figs. A1.20 and A1.21, Appendix 1.6), the large grains in the central portion of the slip zone are more angular than in the gouges that have higher clay contents.

3.4 *Discussion*

3.4.1 *Frictional evolution of dry vs. wet clay-bearing gouges*

Our experimental results show a dramatic contrast in frictional behaviour between dry and wet clay-bearing carbonate gouges. The dry clay-bearing gouges display typical high-velocity friction evolution curves that have been produced in numerous experiments on a wide range of materials (Di Toro et al., 2011). The wet clay-bearing gouges, on the other hand, do not conform to a typical high-velocity frictional evolution, in that they undergo little or no slip-hardening after the attainment of the initial friction value, and thus do not attain a peak in friction during the experiments. This behaviour replicates that observed during previous high-velocity friction experiments on saturated clay-bearing gouges (Faulkner et al., 2011; Ferri et al., 2011; Ferri et al., 2010; Ujiie et al., 2013; Ujiie and Tsutsumi, 2010; Ujiie et al., 2011). However, these previous studies used natural gouges, in most cases with >50% clay. What we are able to show here by systematically varying the clay content in synthetic gouges, is that just 10 wt.% clay (in the case of montmorillonite) or 20 wt.% clay (in the case of mixed-layer illite-smectite) is required to produce the same weakening behaviour that is observed in clay-dominated gouges.

3.4.2 *Microstructural evolution of dry vs. wet clay-bearing gouges*

The contrasting frictional behaviours of the dry vs. wet clay-bearing gouges are accompanied by starkly contrasting microstructures. The dry clay-bearing gouges are characterized by localized slip, which is accommodated along a very sharp, smooth PSS and within a variably developed PSZ.

The PSS and PSZ have undergone intense cataclasis and wear, and show evidence for frictional heating in excess of ~700°C, in the form of degassing bubbles within PSZs, which we infer to be a result of calcite decarbonation. The wet clay-bearing gouges, on the other hand, are characterized by a much more distributed style of deformation, whereby they lack a sharp PSS and a PSZ, and cataclasis appears to have been less intense. Additionally, none of the wet clay-bearing gouges show any evidence for calcite decarbonation, suggesting significantly lower amounts of frictional heating than in their dry equivalents. The observation of contrasting microstructures between dry and wet clay-bearing gouges sheared at seismic velocity is consistent with observations made in previous studies (e.g. Ferri et al., 2011; French et al., 2014; Ujiie et al., 2011). A direct comparison would not be appropriate, due to the fact that these previous studies were conducted at much lower normal load (~1 MPa) than in our experiments, but it seems that wet clay-bearing gouges typically experience a less intense grain size reduction and shear fabric or foliation development than their dry counterparts.

The contrasting microstructures observed in the dry vs. wet clay-bearing gouges suggest that it may be possible to explain their contrasting frictional behaviours through micro-mechanical processes. We propose a micro-mechanical model as follows. In the dry clay-bearing gouges, the initial microstructure comprises discrete clasts of calcite and agglomerates of clay (Fig. 3.11a, panel 1). When slip initiates in these gouges, it is necessary for pervasive cataclasis to occur before slip can localize along a through-going PSS (Fig. 3.11a, panel 2). Once the PSS has formed, then a large amount of wear must also occur in order to produce the smooth surfaces observed in the microstructures (Figs. 3.9b and 3.10b). These processes explain the slip-hardening phase at the start of the dry experiments (e.g. Biegel et al., 1992 and references therein). Once a PSS is well established, then slip localizes here and a PSZ forms adjacent to it (Fig. 3.11a, panel 3). Because strain is concentrated along the PSS and within the PSZ, grain-size in the remainder of the slip zone does not change significantly from peak friction to steady-state sliding. The localization of slip results in intense frictional heating along the PSS and within the PSZ, enough to trigger calcite decarbonation (and perhaps implying that clay dehydration has also taken place, although microstructural evidence of this is not obvious). Mechanical wear and thermal decomposition processes also result in the production of nanoparticles within the PSZ and coating the PSS. A combination of thermal pressurization, dynamic recrystallization and nanoparticle lubrication are likely responsible for the dynamic weakening behaviour of the dry gouges, as invoked by previous studies (De Paola et al., 2011a; De Paola et al., 2011b; De Paola et al., 2014; Han et al., 2011; Han et al., 2007; Smith et al., 2013).

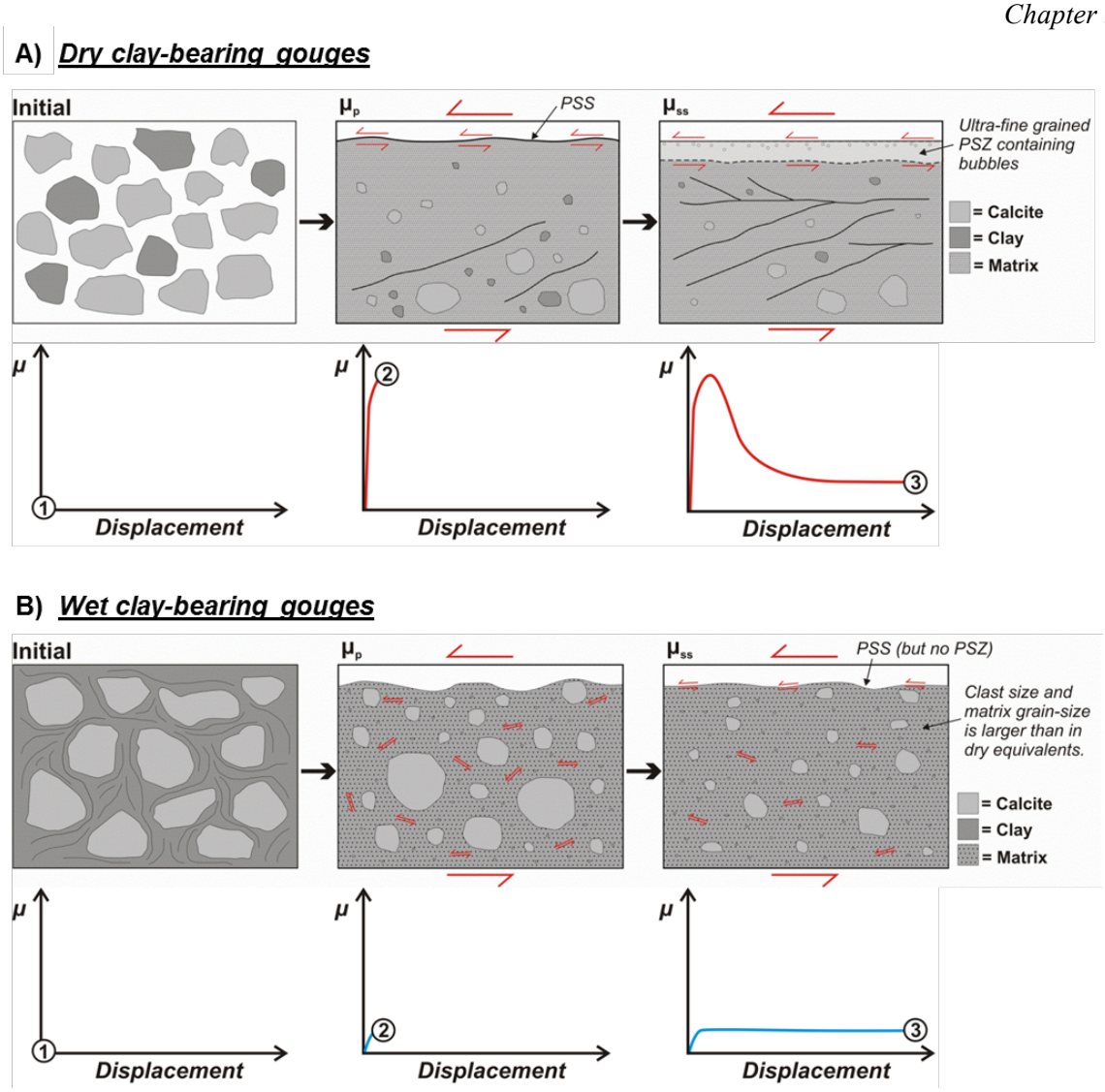

Figure 3.11 Proposed micro-mechanical model, based on microstructural observations, to explain the contrasting mechanical behaviour, also depicted, of: **a)** dry clay-bearing gouges and **b)** wet clay-bearing gouges. Panels show microstructural evolution from the initial starting material through to peak friction and steady-state sliding. See main text for explanation.

In the wet clay-bearing gouges, on the other hand, the initial microstructure comprises an interconnected matrix of wet clay surrounding calcite grains (Fig. 3.11b, panel 1). Saturated clays have been shown to be inherently weak, even at low slip velocities. The average coefficient of friction reported in the literature for wet montmorillonite is 0.18 (Behnsen and Faulkner, 2012; Ikari et al., 2007; Moore and Lockner, 2007; Saffer et al., 2001; Saffer and Marone, 2003; Tembe et al., 2010) and for wet illite is 0.37 (Behnsen and Faulkner, 2012; Ikari et al., 2009; Morrow et al., 1992; Saffer and Marone, 2003; Tembe et al., 2010). Thus, when slip initiates, it preferentially occurs on the pre-existing, weak clay lamellae, which are distributed throughout the gouge (Fig. 3.11b, panel 2). This reduces the need for pervasive cataclasis to occur before slip is able to

localize, and explains the lack of slip-hardening in the wet clay-bearing gouges. This theory is supported by the distributed style of deformation observed in the wet gouges, including the absence of a PSZ (Fig. 3.11b, panel 3), plus the larger grain sizes in the deformed wet clay-bearing gouges in comparison to their dry equivalents. The fact that slip is not localized within a narrow zone, plus the low values of friction, would result in a far lesser amount of frictional heating in the wet gouges than in the dry ones. This would explain why there is no microstructural evidence for thermal decomposition of calcite having occurred in the wet clay-bearing gouges.

A PSS still forms in the wet gouges, and so it is evident that slip does attempt to localize. However, the mechanical processes involved during slip localization are different. In the dry clay-bearing gouges, slip localization is driven by cataclasis and wear, whereas in the wet clay-bearing gouges, it is likely driven by sliding on weak, water-saturated clay lamellae (Moore and Lockner, 2004; Moore and Lockner, 2007). This is reflected in the nature of the PSSs in the wet gouges, which are rather undulating (Figs. 3.9e and 3.10e), suggesting that they are located where weak clay horizons are most readily available, as opposed to on a sharp slip plane where asperities have been broken and worn down by shearing. Given that we do not observe a through-going layer of aligned phyllosilicates along the PSS for slip to occur on, we would not rule out the possibility that slip may actually occur on a thin film of water, which has been expelled from the gouge and become trapped along the PSS, as suggested by Ferri et al. (2010).

The reason for the slight difference in behaviour between the wet illite-smectite bearing gouges and the wet montmorillonite-bearing gouges can be explained through the expansive capabilities of smectite clays. Upon saturation, smectite group clays allow water into their interlayer structure. It has been suggested that the extreme weakness of smectites may be due to sliding occurring on thin lubricating films of water located between clay interlayers (e.g. Moore and Lockner, 2004). If this is the case, then it is not surprising that the mixed-layer illite-smectite clay should be stronger, because the illite component of the clay does not have the same expansive capability. Thus, the delayed peak in friction in experiments 479 and 457, containing 10 wt.% and 20 wt.% of illite-smectite, respectively, may be due to water-saturated smectite horizons within the gouge being consumed through comminution, before slip has fully localized. Thus in order for slip to localize and proceed, some cataclasis is still necessary, hence the delayed slip-hardening phase.

As well as the saturated clays being inherently weak, the impermeable nature of the starting material created by the interconnected clay network (Fig. 3.6d and f) would enhance pore fluid pressurization generated by shear-induced compaction, which would further reduce the strength of

the gouge (e.g. Blanpied et al., 1992). Gouge dilatancy triggered by pore-fluid pressurization may also inhibit the localization of shear (Rice et al., 2014), consistent with our observation of a distributed style of deformation in the wet clay-bearing gouges. The initial weakening phase observed during experiments 457 and 479, and also during experiment 414 on the water-saturated 100% calcite gouge (Fig. 3.4a), before they undergo slip-hardening to attain their peak friction, is most likely due to a sudden pore fluid overpressure generated at the onset of slip.

3.4.3. *Implications*

3.4.3.1 *Rupture propagation in clay-bearing carbonate faults*

Our results show that the presence of clay in fault gouge alone does not significantly affect the frictional behaviour of a fault during earthquake propagation. However, if water is present within gouges containing as little as 10-20% clay, then they can become very weak and resistance to earthquake propagation is significantly reduced. As highlighted by Faulkner et al. (2011), the negligible fracture energy associated with saturated clay-bearing gouges means that very little energy is required to maintain rupture propagation, and so it would be energetically more feasible for a rupture to propagate all the way to the surface. Thus, whilst wide, phyllosilicate-rich zones in the shallow portions of faults may promote stable fault slip due to their velocity-strengthening properties (e.g. Holdsworth et al., 2011; Hsu et al., 2006), if these phyllosilicates become concentrated within narrow PSZs, they will likely facilitate earthquake propagation. The results have significant implications for seismic hazard assessment, particularly in the northern Apennines of Italy, which has experienced a number of large earthquakes in recent years (e.g. D'Agostino et al., 2009). This is an area where clays are sometimes present within the PSZs of earthquake-hosting carbonate faults (e.g. Fig. 3.1) (Bullock et al., 2014; Collettini et al., 2014; Collettini et al., 2013; Tesei et al., 2013). These natural gouges often display a foliated fabric as a result of previous slip events and/or aseismic creep during the interseismic period (e.g. Fig. 2.9 in Chapter 2 and Figs. A1.1-A1.3 in Appendix 1.1). Rock/gouge samples with a pre-existing fabric have been shown experimentally to have significantly lower strength than powdered gouge samples with no fabric (e.g. Collettini et al., 2009; Niemeijer et al., 2010). It is therefore plausible that natural clay-bearing fault gouges could be even weaker than the results we have presented here for experiments on powdered gouges with no pre-existing fabric. In addition, seismological models have invoked fluids as playing an important role in active seismicity in the northern Apennines (e.g. Di Luccio et al., 2010; Malagnini et al., 2012; Miller et al., 2004). The presence of fluids is supported by geological observations documenting pervasive calcite mineralization within and adjacent to PSZs,

in the form of both veins (e.g. Fig. 3.1c and e) and hydraulic breccias (Bullock et al., 2014; Collettini et al., 2014; Tesei et al., 2013). The clays within the PSZs likely act as seals, and promote the generation of high fluid pressures along faults (Blanpied et al., 1992). The evident interaction of fluids with clay-bearing carbonate fault gouges may be a contributing factor towards the common occurrence of surface-breaking scarps in the northern Apennines (e.g. Guerrieri et al., 2009; Vittori et al., 2000).

So far, such results concerning the extreme weakness of saturated clay gouges at seismic slip velocities have been considered with relation to subduction zone earthquakes (Faulkner et al., 2011; Ujiie et al., 2013; Ujiie and Tsutsumi, 2010), which appear to propagate through the clay-rich sediments of accretionary wedges with relative ease (e.g. Ide et al., 2011). However, clays are a common feature of many upper-crustal earthquake-hosting faults (e.g. Holdsworth, 2004; Vrolijk and van der Pluijm, 1999; Wu et al., 1975), where fluids are often invoked to play a major role during faulting (e.g. Sibson, 1981). Thus, these results are relevant for assessing the behaviour and potential capability of any clay-bearing seismogenic fault, regardless of its tectonic setting.

3.4.3.2 *Seismic markers in clay-bearing carbonate faults*

In recent years, it has become increasingly common for structural geologists to try and distinguish indicators of seismic vs. aseismic slip, both from laboratory and field observations. A growing range of so-called 'co-seismic slip indicators' have been documented, for example, pseudotachylytes (Sibson, 1975), dynamically recrystallized calcite (De Paola et al., 2014; Smith et al., 2013), fault mirrors (Fondriest et al., 2013; Siman-Tov et al., 2013), clay mineral transformations (Bullock et al., 2014; Yamaguchi et al., 2011), biomarkers (Savage et al., 2014), degassing bubbles and 'quenched' calcite crystals (Bullock et al., 2014; Collettini et al., 2013). All of these co-seismic signatures are associated with localized slip and frictional heating. In contrast, fault gouges exhibiting distributed deformation, particularly those rich in velocity-strengthening phyllosilicates, are generally interpreted as representing aseismic portions of faults (e.g. Faulkner et al., 2003; Holdsworth et al., 2011). The fault gouges such as those produced during our high-velocity experiments on water-saturated clay-bearing gouges do not contain any seismic markers and exhibit distributed deformation. Thus, they may be overlooked as seismogenic faults if observed in nature, when in fact they have the potential to allow capable faulting and the production of devastating surface ruptures. Add to this the fact that phyllosilicates are prone to creep, then it becomes highly likely that even seismic markers such as those produced during our dry-run experiments, e.g. localized PSZs containing signatures of thermal decomposition, would be

overprinted during the interseismic period. Therefore, clay-bearing carbonate gouges should be approached with a high degree of caution when considering the seismic history and potential of a natural fault zone.

3.5 *Conclusions*

High-velocity friction experiments performed on mixtures of calcite+illite-smectite and calcite+montmorillonite produce very different results depending on whether the gouges are deformed under room-humidity ('dry') or water-saturated ('wet') conditions. Dry clay-bearing gouges display a friction evolution curve that is typical of those associated with high-velocity friction experiments on a wide range of rock types. The wet clay-bearing gouges, on the other hand, do not exhibit a typical frictional evolution, in that they undergo little or no slip-hardening, and therefore do not attain a peak in friction. Instead they attain steady-state frictional sliding almost immediately at the onset of slip, at values of μ_{ss} <<0.2. This behaviour is observed even when the clay content is just 10 wt.%, in the case of montmorillonite, and 20 wt.%, in the case of illite-smectite. These results have significant implications for seismic hazard assessment, as they show that calcite gouges containing small amounts of wet clay will potentially present very little resistance to seismic rupture propagation, enhancing the potential for surface-rupturing capable faulting in a variety of tectonic settings

In our experiments we attribute the observed weak behaviour of the wet-clay bearing gouges to their initial microstructure prior to shearing, which consists of an interconnected network of wet clay surrounding the calcite grains. Thus, as slip initiates, it preferentially occurs on the clay horizons distributed throughout the gouge, which are inherently weak. In the dry gouges, cataclasis must occur before slip can localize and trigger dynamic weakening, and thus they present a much greater resistance to frictional sliding. The lack of slip localization and the low friction values in the wet clay-bearing gouges significantly reduce the amount of frictional heating generated. This means that natural seismogenic fault gouges containing small amounts of wet clay will not necessarily exhibit the signatures that are so commonly thought to be associated with seismic slip.

References

Barchi, M., Minelli, G., Pialli, G., 1998. The CROP 03 profile: a synthesis of results on deep structures of the Northern Apennines. Mem. Soc. Geol. It 52, 383-400.
Behnsen, J., Faulkner, D.R., 2012. The effect of mineralogy and effective normal stress on frictional strength of sheet silicates. Journal of Structural Geology.

Biegel, R.L., Wang, W., Scholz, C.H., Boitnott, G.N., Yoshioka, N., 1992. Micromechanics of rock friction 1. Effects of surface roughness on initial friction and slip hardening in westerly granite. Journal of Geophysical Research: Solid Earth 97, 8951-8964.
Blanpied, M.L., Lockner, D.A., Byerlee, J.D., 1992. An earthquake mechanism based on rapid sealing of faults. Nature 358, 574-576.
Boutareaud, S., Calugaru, D.-G., Han, R., Fabbri, O., Mizoguchi, K., Tsutsumi, A., Shimamoto, T., 2008. Clay-clast aggregates: A new textural evidence for seismic fault sliding? Geophysical Research Letters 35, L05302.
Brantut, N., Schubnel, A., Rouzaud, J.N., Brunet, F., Shimamoto, T., 2008. High-velocity frictional properties of a clay-bearing fault gouge and implications for earthquake mechanics. Journal of Geophysical Research 113, B10401.
Bullock, R.J., De Paola, N., Holdsworth, R.E., Trabucho-Alexandre, J., 2014. Lithological controls on the deformation mechanisms operating within carbonate-hosted faults during the seismic cycle. Journal of Structural Geology 58, 22-42.
Carpenter, B., Marone, C., Saffer, D., 2011. Weakness of the San Andreas Fault revealed by samples from the active fault zone. Nature Geoscience 4, 251-254.
Chester, F.M., Rowe, C., Ujiie, K., Kirkpatrick, J., Regalla, C., Remitti, F., Moore, J.C., Toy, V., Wolfson-Schwehr, M., Bose, S., Kameda, J., Mori, J.J., Brodsky, E.E., Eguchi, N., Toczko, S., 343, E., Scientists, T., 2013. Structure and Composition of the Plate-Boundary Slip Zone for the 2011 Tohoku-Oki Earthquake. Science 342, 1208-1211.
Chiaraluce, L., 2012. Unravelling the complexity of Apenninic extensional fault systems: A review of the 2009 L'Aquila earthquake (Central Apennines, Italy). Journal of Structural Geology 42, 2-18.
Collettini, C., Carpenter, B.M., Viti, C., Cruciani, F., Mollo, S., Tesei, T., Trippetta, F., Valoroso, L., Chiaraluce, L., 2014. Fault structure and slip localization in carbonate-bearing normal faults: An example from the Northern Apennines of Italy. Journal of Structural Geology 67, Part A, 154-166.
Collettini, C., De Paola, N., Holdsworth, R., Barchi, M., 2006. The development and behaviour of low-angle normal faults during Cenozoic asymmetric extension in the Northern Apennines, Italy. Journal of Structural Geology 28, 333-352.
Collettini, C., Niemeijer, A., Viti, C., Marone, C., 2009. Fault zone fabric and fault weakness. Nature 462, 907-910.
Collettini, C., Niemeijer, A., Viti, C., Smith, S.A.F., Marone, C., 2011. Fault structure, frictional properties and mixed-mode fault slip behavior. Earth and Planetary Science Letters 311, 316-327.
Collettini, C., Viti, C., Tesei, T., Mollo, S., 2013. Thermal decomposition along natural carbonate faults during earthquakes. Geology 41, 927-930.
D'Agostino, N., Mantenuto, S., D'Anastasio, E., Avallone, A., Barchi, M., Collettini, C., Radicioni, F., Stoppini, A., Fastellini, G., 2009. Contemporary crustal extension in the Umbria–Marche Apennines from regional CGPS networks and comparison between geodetic and seismic deformation. Tectonophysics 476, 3-12.
De Paola, N., Chiodini, G., Hirose, T., Cardellini, C., Caliro, S., Shimamoto, T., 2011a. The geochemical signature caused by earthquake propagation in carbonate-hosted faults. Earth and Planetary Science Letters 310, 225-232.
De Paola, N., Hirose, T., Mitchell, T., Di Toro, G., Viti, C., Shimamoto, T., 2011b. Fault lubrication and earthquake propagation in thermally unstable rocks. Geology 39, 35-38.
De Paola, N., Holdsworth, R.E., Viti, C., Collettini, C., Faoro, I., Bullock, R.J., 2014. Can grain size sensitive creep lubricate faults during earthquake propagation?, AGU Fall meeting, San Francisco.
Di Luccio, F., Ventura, G., Di Giovambattista, R., Piscini, A., Cinti, F., 2010. Normal faults and thrusts reactivated by deep fluids: The 6 April 2009 Mw 6.3 L'Aquila earthquake, central Italy. Journal of Geophysical Research: Solid Earth (1978–2012) 115.
Di Toro, G., Han, R., Hirose, T., De Paola, N., Nielsen, S., Mizoguchi, K., Ferri, F., Cocco, M., Shimamoto, T., 2011. Fault lubrication during earthquakes. Nature 471, 494-498.

Faulkner, D., Lewis, A., Rutter, E., 2003. On the internal structure and mechanics of large strike-slip fault zones: field observations of the Carboneras fault in southeastern Spain. Tectonophysics 367, 235-251.
Faulkner, D.R., Mitchell, T.M., Behnsen, J., Hirose, T., Shimamoto, T., 2011. Stuck in the mud? Earthquake nucleation and propagation through accretionary forearcs. Geophysical Research Letters 38, L18303.
Ferri, F., Di Toro, G., Hirose, T., Han, R., Noda, H., Shimamoto, T., Quaresimin, M., de Rossi, N., 2011. Low-to high-velocity frictional properties of the clay-rich gouges from the slipping zone of the 1963 Vaiont slide, northern Italy. Journal of Geophysical Research: Solid Earth (1978–2012) 116.
Ferri, F., Di Toro, G., Hirose, T., Shimamoto, T., 2010. Evidence of thermal pressurization in high-velocity friction experiments on smectite-rich gouges. Terra Nova 22, 347-353.
Fondriest, M., Smith, S.A., Candela, T., Nielsen, S.B., Mair, K., Di Toro, G., 2013. Mirror-like faults and power dissipation during earthquakes. Geology 41, 1175-1178.
French, M.E., Kitajima, H., Chester, J.S., Chester, F.M., Hirose, T., 2014. Displacement and dynamic weakening processes in smectite-rich gouge from the Central Deforming Zone of the San Andreas Fault. Journal of Geophysical Research: Solid Earth 119, 1777-1802.
Gratier, J.P., Thouvenot, F., Jenatton, L., Tourette, A., Doan, M.L., Renard, F., 2013. Geological control of the partitioning between seismic and aseismic sliding behaviours in active faults: Evidence from the Western Alps, France. Tectonophysics 600, 226-242.
Guerrieri, L., Blumetti, A., Esposito, E., Michetti, A., Porfido, S., Serva, L., Tondi, E., Vittori, E., 2009. Capable faulting, environmental effects and seismic landscape in the area affected by the 1997 Umbria–Marche (Central Italy) seismic sequence. Tectonophysics 476, 269-281.
Han, R., Hirose, T., Shimamoto, T., Lee, Y., Ando, J., 2011. Granular nanoparticles lubricate faults during seismic slip. Geology 39, 599-602.
Han, R., Shimamoto, T., Hirose, T., Ree, J.H., Ando, J., 2007. Ultralow friction of carbonate faults caused by thermal decomposition. Science 316, 878-881.
Holdsworth, R., Van Diggelen, E., Spiers, C., De Bresser, J., Walker, R., Bowen, L., 2011. Fault rocks from the SAFOD core samples: Implications for weakening at shallow depths along the San Andreas Fault, California. Journal of Structural Geology 33, 132-144.
Holdsworth, R.E., 2004. Weak Faults--Rotten Cores. Science 303, 181-182.
Hsu, Y.-J., Simons, M., Avouac, J.-P., Galetzka, J., Sieh, K., Chlieh, M., Natawidjaja, D., Prawirodirdjo, L., Bock, Y., 2006. Frictional Afterslip Following the 2005 Nias-Simeulue Earthquake, Sumatra. Science 312, 1921-1926.
Ide, S., Baltay, A., Beroza, G.C., 2011. Shallow Dynamic Overshoot and Energetic Deep Rupture in the 2011 Mw 9.0 Tohoku-Oki Earthquake. Science 332, 1426-1429.
Ikari, M.J., Marone, C., Saffer, D.M., 2011. On the relation between fault strength and frictional stability. Geology 39, 83-86.
Ikari, M.J., Saffer, D.M., Marone, C., 2007. Effect of hydration state on the frictional properties of montmorillonite-based fault gouge. Journal of geophysical research 112, B06423.
Ikari, M.J., Saffer, D.M., Marone, C., 2009. Frictional and hydrologic properties of clay-rich fault gouge. Journal of Geophysical Research 114, B05409.
Lavecchia, G., Boncio, P., Creati, N., 2003. A lithospheric-scale seismogenic thrust in central Italy. Journal of Geodynamics 36, 79-94.
Lay, T., Kanamori, H., Ammon, C.J., Nettles, M., Ward, S.N., Aster, R.C., Beck, S.L., Bilek, S.L., Brudzinski, M.R., Butler, R., DeShon, H.R., Ekström, G., Satake, K., Sipkin, S., 2005. The Great Sumatra-Andaman Earthquake of 26 December 2004. Science 308, 1127-1133.
Lockner, D.A., Morrow, C., Moore, D., Hickman, S., 2011. Low strength of deep San Andreas fault gouge from SAFOD core. Nature 472, 82-85.
Logan, J., Dengo, C., Higgs, N., Wang, Z., 1992. Fabrics of experimental fault zones: Their development and relationship to mechanical behavior. International Geophysics Series 51, 33-33.

Malagnini, L., Lucente, F.P., De Gori, P., Akinci, A., 2012. Control of pore fluid pressure diffusion on fault failure mode: Insights from the 2009 L'Aquila seismic sequence. Journal of geophysical research 117, B05302.
Marone, C., 1998. Laboratory-derived friction laws and their application to seismic faulting. Annual Review of Earth and Planetary Sciences 26, 643-696.
Miller, S.A., Collettini, C., Chiaraluce, L., Cocco, M., Barchi, M., Kaus, B.J., 2004. Aftershocks driven by a high-pressure CO2 source at depth. Nature 427, 724-727.
Mizoguchi, K., Hirose, T., Shimamoto, T., Fukuyama, E., 2007. Reconstruction of seismic faulting by high-velocity friction experiments: An example of the 1995 Kobe earthquake. Geophysical Research Letters 34, L01308.
Moore, D.E., Lockner, D.A., 2004. Crystallographic controls on the frictional behavior of dry and water-saturated sheet structure minerals. Journal of Geophysical Research 109, B03401.
Moore, D.E., Lockner, D.A., 2007. Friction of the smectite clay montmorillonite. The Seismogenic Zone of Subduction Thrust Faults, 317-345.
Moore, D.E., Lockner, D.A., 2011. Frictional strengths of talc-serpentine and talc-quartz mixtures. Journal of geophysical Research 116, B01403.
Morrow, C., Radney, B., Byerlee, J., 1992. Frictional strength and the effective pressure law of montmorillonite and illite clays. INTERNATIONAL GEOPHYSICS SERIES 51, 69-69.
Morrow, C., Solum, J., Tembe, S., Lockner, D., Wong, T.F., 2007. Using drill cutting separates to estimate the strength of narrow shear zones at SAFOD. Geophysical Research Letters 34, L11301.
Niemeijer, A., Marone, C., Elsworth, D., 2010. Fabric induced weakness of tectonic faults. Geophysical Research Letters 37, L03304.
Rice, J.R., Rudnicki, J.W., Platt, J.D., 2014. Stability and localization of rapid shear in fluid-saturated fault gouge: 1. Linearized stability analysis. Journal of Geophysical Research: Solid Earth 119, 4311-4333.
Saffer, D.M., Frye, K.M., Marone, C., Mair, K., 2001. Laboratory results indicating complex and potentially unstable frictional behavior of smectite clay. Geophysical Research Letters 28, 2297-2300.
Saffer, D.M., Marone, C., 2003. Comparison of smectite-and illite-rich gouge frictional properties: application to the updip limit of the seismogenic zone along subduction megathrusts. Earth and Planetary Science Letters 215, 219-235.
Savage, H.M., Polissar, P.J., Sheppard, R., Rowe, C.D., Brodsky, E.E., 2014. Biomarkers heat up during earthquakes: New evidence of seismic slip in the rock record. Geology 42, 99-102.
Scholz, C.H., 1998. Earthquakes and friction laws. Nature 391, 37-42.
Shimamoto, T., Tsutsumi, A., 1994. A new rotary-shear high-speed frictional testing machine: Its basic design and scope of research (in Japanese with English abstract). Journal of the Tectonic Research group of Japan 39, 65-78.
Sibson, R.H., 1975. Generation of Pseudotachylyte by Ancient Seismic Faulting. Geophysical Journal International 43, 775-794.
Sibson, R.H., 1981. Fluid flow accompanying faulting: field evidence and models. Earthquake prediction, 593-603.
Siman-Tov, S., Aharonov, E., Sagy, A., Emmanuel, S., 2013. Nanograins form carbonate fault mirrors. Geology 41, 703-706.
Smith, S., Di Toro, G., Kim, S., Ree, J.H., Nielsen, S., Billi, A., Spiess, R., 2013. Coseismic recrystallization during shallow earthquake slip. Geology 41, 63-66.
Sone, H., Shimamoto, T., Moore, D.E., 2012. Frictional properties of saponite-rich gouge from a serpentinite-bearing fault zone along the Gokasho-Arashima Tectonic Line, central Japan. Journal of Structural Geology 38, 172-182.
Tembe, S., Lockner, D.A., Wong, T.F., 2010. Effect of clay content and mineralogy on frictional sliding behavior of simulated gouges: Binary and ternary mixtures of quartz, illite, and montmorillonite. Journal of geophysical Research 115, B03416.

Tesei, T., Collettini, C., Carpenter, B.M., Viti, C., Marone, C., 2012. Frictional strength and healing behavior of phyllosilicate-rich faults. Journal of Geophysical Research 117, B09402.
Tesei, T., Collettini, C., Viti, C., Barchi, M.R., 2013. Fault architecture and deformation mechanisms in exhumed analogues of seismogenic carbonate-bearing thrusts. Journal of Structural Geology 55, 167-181.
Ujiie, K., Tanaka, H., Saito, T., Tsutsumi, A., Mori, J.J., Kameda, J., Brodsky, E.E., Chester, F.M., Eguchi, N., Toczko, S., 343, E., Scientists, T., 2013. Low Coseismic Shear Stress on the Tohoku-Oki Megathrust Determined from Laboratory Experiments. Science 342, 1211-1214.
Ujiie, K., Tsutsumi, A., 2010. High-velocity frictional properties of clay-rich fault gouge in a megasplay fault zone, Nankai subduction zone. Geophysical Research Letters 37, L24310.
Ujiie, K., Tsutsumi, A., Kameda, J., 2011. Reproduction of thermal pressurization and fluidization of clay-rich fault gouges by high-velocity friction experiments and implications for seismic slip in natural faults. Geological Society, London, Special Publications 359, 267-285.
Ventura, G., Di Giovambattista, R., 2013. Fluid pressure, stress field and propagation style of coalescing thrusts from the analysis of the 20 May 2012 ML 5.9 Emilia earthquake (Northern Apennines, Italy). Terra Nova 25, 72-78.
Verberne, B.A., He, C., Spiers, C.J., 2010. Frictional properties of sedimentary rocks and natural fault gouge from the Longmen Shan fault zone, Sichuan, China. Bulletin of the Seismological Society of America 100, 2767-2790.
Verberne, B.A., Spiers, C.J., Niemeijer, A.R., De Bresser, J.H.P., De Winter, D.A.M., Plümper, O., 2014. Frictional Properties and Microstructure of Calcite-Rich Fault Gouges Sheared at Sub-Seismic Sliding Velocities. Pure and Applied Geophysics 171, 2617-2640.
Violay, M., Nielsen, S., Spagnuolo, E., Cinti, D., Di Toro, G., Di Stefano, G., 2013. Pore fluid in experimental calcite-bearing faults: Abrupt weakening and geochemical signature of co-seismic processes. Earth and Planetary Science Letters 361, 74-84.
Vittori, E., Deiana, G., Esposito, E., Ferreli, L., Marchegiani, L., Mastrolorenzo, G., Michetti, A., Porfido, S., Serva, L., Simonelli, A., 2000. Ground effects and surface faulting in the September–October 1997 Umbria–Marche (Central Italy) seismic sequence. Journal of Geodynamics 29, 535-564.
Vrolijk, P., van der Pluijm, B.A., 1999. Clay gouge. Journal of Structural Geology 21, 1039-1048.
Wu, F.T., Blatter, L., Roberson, H., 1975. Clay gouges in the San Andreas Fault System and their possible implications. pure and applied geophysics 113, 87-95.
Yamaguchi, A., Sakaguchi, A., Sakamoto, T., Iijima, K., Kameda, J., Kimura, G., Ujiie, K., Chester, F.M., Fabbri, O., Goldsby, D., 2011. Progressive illitization in fault gouge caused by seismic slip propagation along a megasplay fault in the Nankai Trough. Geology 39, 995-998.

Chapter 4

Structure and deformation mechanisms of near-surface, seismogenic fault zones in poorly lithified sediments

Abstract

Constraining the structure and deformation mechanisms of faults in the shallowest part of the Earth's crust is necessary to understand how seismic energy is either dissipated or transmitted during rupture propagation towards the surface. We describe the architecture, geometries and microstructures of cm- to m-scale displacement seismogenic faults of the Masada fault zone, Israel, which formed at just a few metres depth in high-porosity (up to 50%), brine-saturated, poorly lithified lake sediments of the Pleistocene Lisan Formation. The Lisan Formation comprises alternating 1-3 mm thick, seasonal laminae of ultrafine-grained aragonite, present as acicular crystals which are sometimes radially arranged in rosette-like structures, and clay-rich clastic detritus, which facilitate easy identification of mm-scale slip.

Fault cores, which range from 5 mm to 30 cm wide depending on fault displacement, are characterized by clusters of interconnected deformation bands. The majority of displacement within fault cores is localized within narrow principal slip zones (PSZs), which average 2-3 mm wide. Displacement profiles constructed for the faults show that displacement tapers to zero towards the upper tip-points of the faults, and that there is mechanical interaction between adjacent overlapping fault segments. At the microscale, the slip surfaces which bound PSZs do not sharply cut clasts, and there is no grain-size reduction towards them. In addition, there is no fracturing or cataclasis of grains within the PSZs; acicular aragonite crystals and rosette structures are well preserved.

We conclude that the geometric attributes of the faults are the same as those of faults in low-porosity, cohesive rocks formed at greater depths. However, the dominant deformation mechanism is particulate flow, as opposed to fracturing and cataclasis. The particulate flow mechanism is facilitated by the low effective stress, plus the high-porosity, ultrafine grain-size and fluid-saturated nature of the sediment, plus the presence of weak clays. The combination of frictionally weak wet clays, plus the lack of fracturing during fault slip, will result in earthquakes rupturing the faults having very low fracture energy, thus greatly facilitating rupture propagation to the surface. This interpretation contradicts the traditional conception that poorly lithified sediments in the shallow part of the crust may act as effective barriers to rupture propagation, and may go some way to explaining the recently acknowledged large, near-surface co-seismic displacements produced during great earthquakes.

4.1 *Introduction*

A differentiation is often made between the deformation of low-porosity and high-porosity rocks in the upper few km of the Earth's crust. At these depths, deformation in low-porosity rocks typically

occurs by fracturing. Fracturing is a strain-weakening process that leads to localization of deformation: the interaction of tensile microcracks (Reches and Lockner, 1994) leads to the development of mesoscopic fractures, which, if favourably oriented, may accommodate shear displacement and become fault surfaces on which displacement will localize during subsequent slip events (Fossen, 2010). Thus, fault zone architecture in upper-crustal fault zones hosted by low-porosity rocks, such as carbonate or crystalline lithologies, typically comprises a high-strain fault core, up to a few tens of metres wide, containing one or more principal slip surfaces and characterized by cataclastically deformed fault rocks, such as gouges, cataclasites and breccias (Faulkner et al., 2010). The fault core is surrounded by a damage zone, up to a few hundred metres wide, comprising secondary slip surfaces and variably fractured protolith rocks, the frequency of which decays exponentially with increasing distance from the fault core (e.g. Anders and Wiltschko, 1994; Mitchell and Faulkner, 2009; Wesnousky, 1988; Wilson et al., 2003). Fault core and damage zone widths are highly dependent upon factors such as host-rock lithology and geometrical complexities, but they tend to scale with fault displacement (Childs et al., 2009; Shipton et al., 2006; Walker et al., 2013).

In high-porosity rocks, it is easier for grains to shift around rather than crack (Schultz and Siddharthan, 2005). Therefore, strain localization in high-porosity rocks does not occur by fracturing, but by the formation of deformation bands. Deformation bands are "low displacement deformation zones of millimetres to centimetres thickness that tend to have enhanced cohesion and reduced permeability compared with ordinary fractures" (Fossen et al., 2007). Deformation bands also commonly lack a discrete fracture surface (Johansen and Fossen, 2008). Fault formation in porous rocks occurs due to the failure of a zone of deformation bands (Fossen et al., 2007), with slickensided fault surfaces typically occurring on one or both margins of a well-developed zone of deformation bands (Aydin and Johnson, 1978). The fault core, then, corresponds to such a zone of densely clustered deformation bands containing a principal slip surface. The damage zones of deformation band faults are characterized by the presence of further deformation bands and compaction bands (e.g. Fossen et al., 2007; Johansen et al., 2005), which decay exponentially in frequency away from fault cores, in similar style to the structure of damage zones in low-porosity rocks (Berg and Skar, 2005; De Joussineau and Aydin, 2007; Johansen and Fossen, 2008).

There are different classes of deformation band, depending on the deformation mechanism by which they were formed, which in turn depends on rock properties, such as composition, grain size, grain shape, sorting, cementation and porosity, and on environmental conditions such as stress state and depth of burial (Fossen et al., 2007).

The most commonly described deformation band in the literature is the *cataclastic band* (Aydin and Johnson, 1978; Aydin and Johnson, 1983), where the dominant deformation mechanism is cataclasis, i.e. grain fracturing and comminution. Cataclastic bands are characterized by angular grains with a wide range of sizes, plus an increased matrix content and reduced porosity relative to the host rock (e.g. Antonellini et al., 1994). The cataclasis involved in the formation of these bands promotes strain-hardening (Aydin and Johnson, 1978), resulting in broad zones of deformation band clusters up to 10 m wide, where individual bands have displacements of just a few cm (Fossen et al., 2007; Johansen and Fossen, 2008). Cataclastic bands are typically associated with porous sandstones at burial depths of 1-2 km (Fossen et al., 2007; Johansen and Fossen, 2008).

The second type is the *disaggregation band*, where the dominant deformation mechanism is particulate flow (Fossen et al., 2007), which involves grain rotation and translation via grain-boundary sliding (Borradaile, 1981; Fossen et al., 2007). This allows the disaggregation and re-arrangement of grains without any fracturing taking place; porosity reduction is negligible (Fisher and Knipe, 1998). Thus the appearance of deformed material within disaggregation bands may be almost identical to that of the surrounding host rock (Fossen et al., 2007). Disaggregation bands occur in poorly lithified sediments deformed at depths of <1 km (Johansen and Fossen, 2008). They are associated with narrower zones of deformation band clusters than those observed for cataclastic bands, and individual bands may accommodate displacements up to several tens of cm (Johansen and Fossen, 2008). This is attributed to the fact that strain-hardening is not an influential process in the formation of disaggregation bands, since they are formed in fine-grained sediments at shallow depths, resulting in lower grain-contact stresses (Schultz and Siddharthan, 2005).

A third type is the *phyllosilicate band*, which forms in porous rocks with phyllosilicate content >10-15% (Fossen et al., 2007). These can be considered a type of disaggregation band, within which grain boundary sliding is facilitated by the presence of phyllosilicates. If clay content is >~40% (Fisher and Knipe, 2001), a clay smear may develop. This is a continuous layer of clay entrapped within the deformation band, due to incorporation of a clay-rich layer from the host rock (Yielding et al., 1997). Phyllosilicate bands and clay smears tend to accommodate greater displacements than cataclastic bands because interconnected phyllosilicate networks within the band prevent interlocking of grains and promote strain-softening (Fossen et al., 2007).

The final type is a *solution-cementation* band, which results from the fact that deformation bands are often favourable sites for stress-induced dissolution and precipitation processes (Fossen et al., 2007).

The majority of studies concerning fault zone architecture in poorly lithified sediments have focused on fault zones in sandstone-dominated lithologies, due to the fact that hydrocarbon reservoirs often occur within sandstone or interbedded sandstone-shale sequences. In poorly lithified sands, fault zones are typically dominated by cataclastic deformation bands and conform to the standard fault core plus damage zone architectures discussed above (e.g. Antonellini et al., 1994; Aydin and Johnson, 1978; Balsamo and Storti, 2010; Cashman and Cashman, 2000; Shipton and Cowie, 2003). The architecture of fault zones in poorly lithified sediments of a more heterogeneous composition, e.g. siltstones, clays, marls and gravels, in addition to fine- to coarse-grained sands, tend to have slightly different characteristics. For example, the fault core may be defined by a zone of cataclastic deformation bands, or it may be defined by clay smear (e.g. Balsamo et al., 2014; Balsamo and Storti, 2011; Caine and Minor, 2009; Heynekamp et al., 1999; Rawling et al., 2001). They are also often observed to have a third architectural element referred to as a 'mixed zone' (e.g. Heynekamp et al., 1999; Loveless et al., 2011; Minor and Hudson, 2006; Rawling and Goodwin, 2006). This zone occurs between the fault core and the damage zone and contains entrained beds from the host rock, which become increasingly deformed and intermixed with increasing displacement (Heynekamp et al., 1999).

Most studies on deformation in poorly lithified sediments have focussed on the impact of fault zone architecture on fluid flow. The impact that fault structure and operative deformation mechanisms may have on seismicity in the shallow part of the crust has been largely overlooked, with the exception of a study by Cashman et al. (2007). The devastating nature of surface-rupturing earthquakes along so-called 'capable faults' (IAEA, 2010), however, demonstrates the critical importance of better constraining the properties of fault zones in the shallow part of the crust, as they play a crucial role in determining how seismic energy and displacement are transmitted to the surface (Evans and Bradbury, 2007).

In this chapter, we document the fault zone architecture, individual fault geometries and microstructures of cm- to m-scale displacement normal faults of the Masada fault zone (MFZ), located on the shores of the Dead Sea in Israel. These faults formed under near-surface conditions in brine-saturated, ultrafine-grained and finely laminated lake deposits, and are known to have hosted past seismic events. The only previous studies of fault geometries and microstructures found in similar sedimentary deposits are by Kristensen (2005) and Kristensen et al. (2008, 2013), who studied fault growth processes, fault zone structure, microstructures and permeability of cm-scale displacement normal faults in coastal exposures of finely bedded sands, silts and clays in eastern Denmark. We use our observations to construct a model for fault evolution, and to constrain the dominant deformation mechanisms operating in the MFZ. The implications of these findings for

the deformation behaviour of seismogenic faults in near-surface, brine-saturated, poorly lithified sediments are then discussed.

4.2 *Geological context and previous work*

The MFZ is located ~1 km to the east of the ancient fortress of Masada on the western shore of the central Dead Sea in Israel (Fig. 4.1a). It deforms sediments belonging to the Pleistocene Lisan Formation, which was deposited between 63±7 Ka – 18 Ka (Schramm et al., 2000) in Lake Lisan, the precursor to the modern day Dead Sea (Fig. 4.1a). Canyon incision during periods of sea-level retreat has resulted in excellent cliff-like exposures up to 10 m in height (Fig. 4.2a).

The faults are part of a system of normal faults that bound the western side of the Dead Sea Basin (Fig. 4.1b-c). The Dead Sea Basin lies in a pull-apart graben located between two segments of the Dead Sea transform fault, which forms the boundary between the Arabia and Sinai plates, running for ~1000 km from the Red Sea spreading centre in the south to the Taurus-Zagros collision zone in the north (Fig. 4.1a) (e.g. Freund et al., 1968; Garfunkel, 1981; Quennell, 1958). The Dead Sea fault is known to be seismically active, with an average long-term motion of ~5 mm/yr (Hamiel et al., 2009); normal faulting is estimated to account for ~10% of the total fault motion (Hamiel et al., 2009). The level of seismic activity is broadly similar on all segments of the Dead Sea fault, although there appears to be a concentration of microseismicity within the Dead Sea Basin (Hamiel et al., 2009). The largest earthquake to occur for at least two centuries was the 1995 M_W=7.2 Nuweiba earthquake in the Gulf of Elat (Dziewonski et al., 1997), whilst the most recent large event to occur in the Dead Sea area itself was the 1927 M_L=6.2 Jericho earthquake (Fig. 4.1a) (Zohar and Marco, 2012).

Mapping of the MFZ by Marco and Agnon (1995) showed that the faults at the surface have an overall N-S striking trend, paralleling the main graben-bounding faults (Fig. 4.1b-c). Fault planes dip to both the east and west at angles of 50-70° (Marco and Agnon, 1995). A combination of ground-penetrating radar and seismic reflection survey studies have traced the faults down to depths of 250-300 m (Marco et al., 1996a), extending them below the base of the Lisan Formation and confirming that they are tectonic, rather than syn-depositional in origin. If the dips of the fault planes do not change significantly at depth, then it is suggested that they should link to form a single fault zone (Fig. 4.1c) (Marco, 2007).

The Lisan Formation comprises alternating very fine laminae (~1-3 mm thick) (Fig. 4.2b) of white aragonite, precipitated during summer months (Fig. 4.2c), and dark clastic detritus deposited during winter flooding events (Fig. 4.2d). The aragonite crystals are acicular, with widths up to 2 μm and

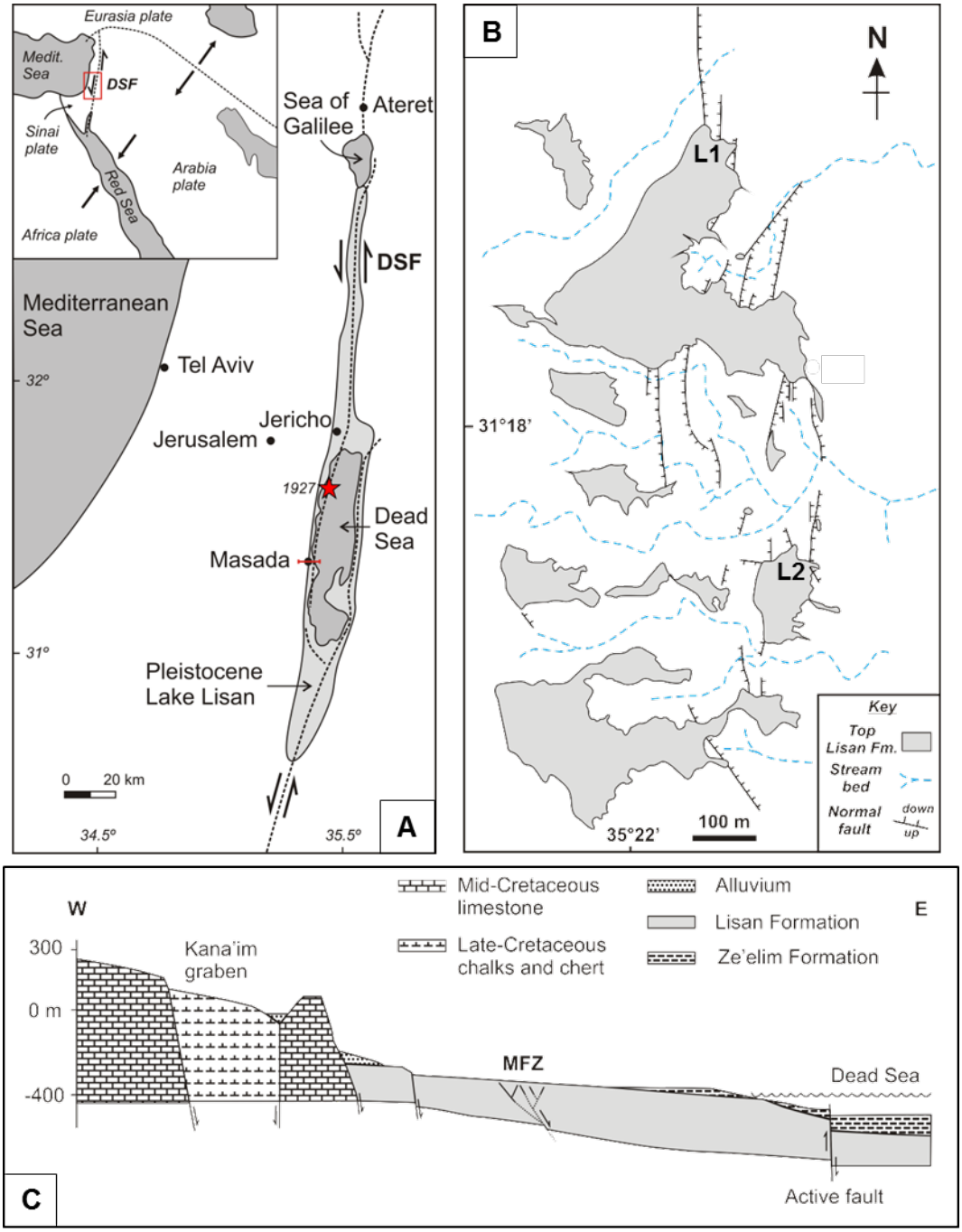

Figure 4.1 a) Location map, showing the main segments of the Dead Sea Fault (DSF) and the maximum extent of Lake Lisan at 26 Ka (shaded pale grey, data from Hall (1994)). The inferred epicentre of the 1927 Jericho earthquake (Zohar and Marco, 2012) is indicated by the red star. Inset shows the position of the DSF in relation to Middle East tectonics. Figure modified from Hamiel et al. (2009). **b)** Map of the Masada Fault Zone (MFZ) produced by Marco and Agnon (1995). Localities 1 (L1) and 2 (L2), which are referred to in the text, are labelled. **c)** Schematic cross-section across the area highlighted in fig. **a**, showing the context of the MFZ in relation to the main graben-bounding normal faults and the currently active strand of the Dead Sea fault. It has been interpreted that the faults of the MFZ should link at depth. Horizontal scale is equal to vertical scale. Figure modified from Marco (2007).

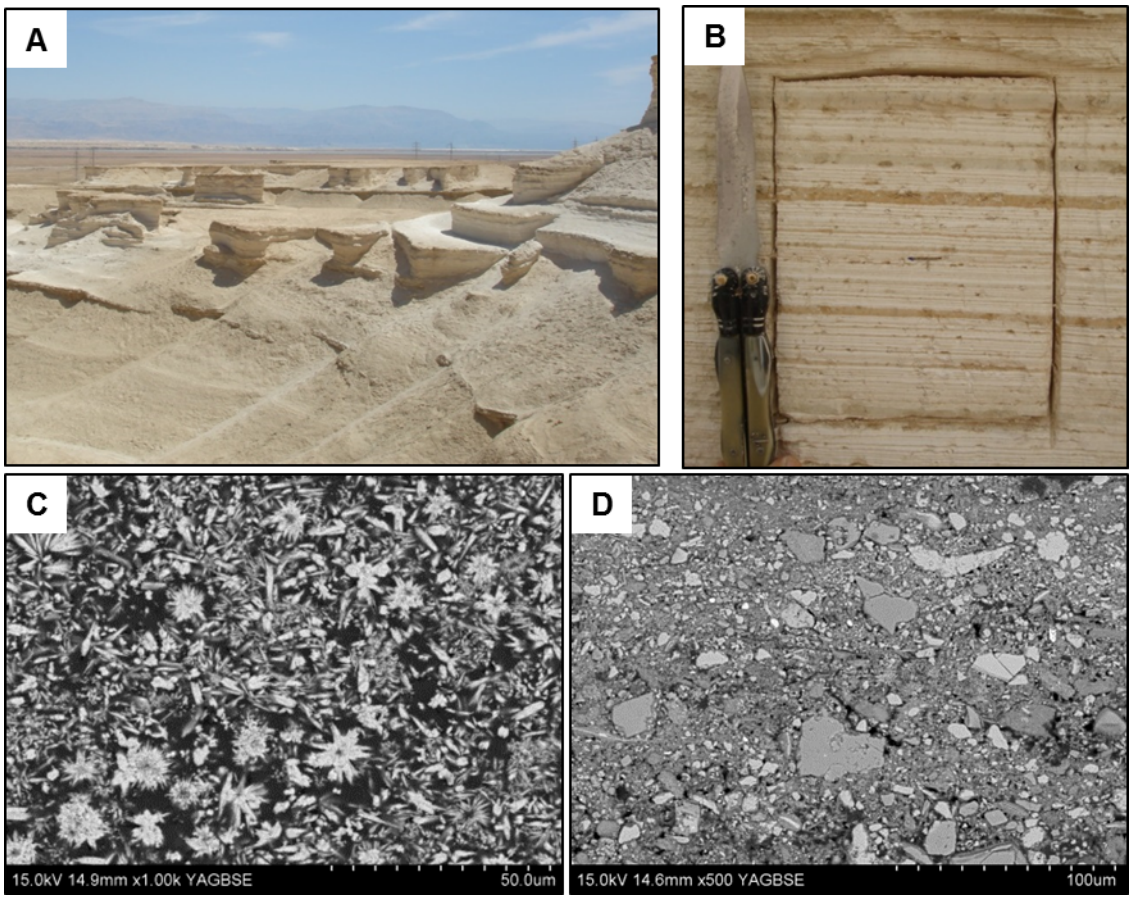

Figure 4.2 The protolith. **a)** Poorly lithified cliffs of the Lisan Formation exposed on the shores of the Dead Sea. Photo is taken looking east towards the Dead Sea, with Jordan in the far distance. **b)** Undeformed Lisan sediment as observed in the field. Samples were cut out with a knife, again testament to the very soft, poorly lithified nature of the material. The white laminae are the aragonite layers and the darker grey and brown layers are the clastic laminae. **c)** SEM image of an undeformed aragonite layer. The aragonite crystals are acicular with sharp, pointed terminations, and sometimes arranged in radiating aggregates resembling rosettes. **d)** SEM image of an undeformed clastic layer. Clastic layers comprise a random and chaotic mixture of clasts – predominantly quartz, calcite, aragonite and dolomite.

lengths up to 15 μm (Fig. 4.2c). Sometimes they are arranged radially in rosette-like structures, which have diameters of up to 20 μm (Fig. 4.2c). The clastic layers comprise sub-angular to sub-rounded grains of calcite, dolomite, minor quartz and feldspars, with maximum grain dimensions of up to ~100 μm, plus up to ~70% clay - a mixture of kaolinite, montmorillonite and illite. Gypsum layers and nodules up to a few cm in size are also present intermittently throughout the Formation. The Lisan Formation has high porosity; in-situ porosity measurements range from 43-51% (Arkin and Michaeli, 1986).

Bedding throughout the formation dips at <1°, indicating stable conditions both syn- and post-deposition (Alsop and Marco, 2011a). The thickness of the Lisan Formation at Masada is ~30 m (Bartov et al., 2002). The sediments have never been buried and are therefore very poorly lithified and were deformed under virtually no lithostatic load. However, the sediments were subaqueous at the time of deformation, under a water column which on the Masada plain fluctuated between depths of 0-170 m (Bartov et al., 2002). Therefore they would have been brine-saturated and subject to a normal load of up to 2.5 MPa. The brine contained within the pores of the Lisan Formation has a total dissolved salt content of 40 g/l (Arkin and Starinsky, 1981), which is slightly higher than the present day salt content of the oceans (35 g/l) but low in comparison to that of Dead Sea water, which is ~345 g/l (Reznik et al., 2009).

The upper layers of the Lisan Formation are unfaulted, indicating that the faults are syn-sedimentary, and that the MFZ has been inactive since ~20-25 Ka (Marco and Agnon, 2005). This is believed to be a consequence of the migration and progressive localization of activity towards the centre of the Dead Sea Basin (Marco, 2007). Their syn-sedimentary nature is also evident from the thickening of sedimentary layers in the hangingwalls of many exposed faults compared to in the footwalls (e.g. Fig. 4.3).

The faults are believed to have hosted seismic ruptures due to the close association of seismites with the fault scarps (Fig. 4.3). In the Lisan Formation, these seismites come in two forms. The first is slumped sedimentary horizons (Fig. 4.3), which have been interpreted as being created by seismically-induced gravitational instabilities (Alsop and Marco, 2011b; El-Isa and Mustafa, 1986). The second is “breccia” layers (Fig. 4.3) (Agnon et al., 2006), which were originally termed “mixed layers” by Marco and Agnon (1995). Breccia layers are typically up to a few tens of cm thick, although locally up to 1 m thick, and are laterally extensive over distances of hundreds of m (Marco and Agnon, 1995). These layers contain a chaotic mixture of brecciated host-rock laminae, ranging from millimetre- up to several centimetre-sizes, set in a matrix of ultrafine-grained sand and mud (Fig. 4.3). Typically they are graded, with the largest and greatest proportion of host rock fragments at the base of the layer, fining upwards to ultrafine-grained matrix material at the top of the layer. The formation of the mixed layers has been attributed to the shaking of sediments on the top of the lake bed during an earthquake, which are then thrown into suspension and subsequently re-deposited (Marco and Agnon, 1995). In some cases, the slumped and mixed layers are concomitant, with slumped layers showing an upward transition into mixed layers as they start to become fragmented. This suggests that they formed contemporaneously during the same events, the differing end products being related to differences in sediment physical properties: the least consolidated sediments at the surface of the lake bed are fluidized during shaking and become

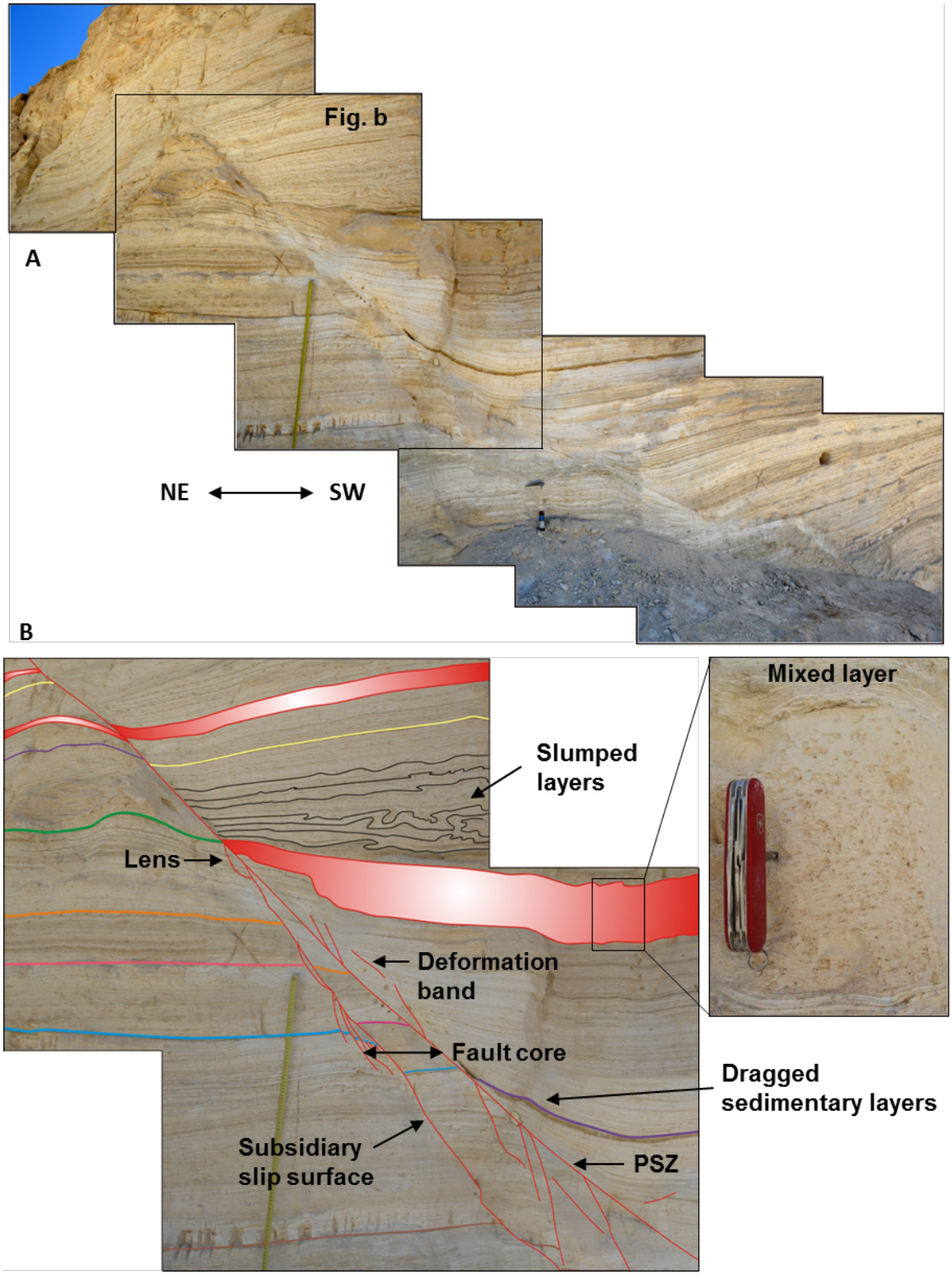

Figure 4.3 a) Example of one of the faults studies (LIF 2.2; 31°18'27.18"N, 35°22'31.38"E). Measuring tape = 90 cm. **b)** A close-up, annotated photograph of the boxed area of the fault shown in fig. **a**, showing the main components of faults in the MFZ. Certain sedimentary layers, which can be correlated across the fault, are highlighted, including mixed layers, which are shaded red. Slumped layers in the hangingwall are highlighted in black. – continued overleaf.

It is evident that the thickness of sedimentary packages is greater in the hangingwall than in the footwall of the fault, indicating the syn-sedimentary nature of the faulting. Inset image shows an example of one of the mixed layers, which in this case comprises very fine-grained re-deposited silt. Fault core width corresponds to the width represented by a zone of connected deformation bands, thus in the upper part of the image, the fault core is narrow, corresponding to just the width of the PSZ, but it increases in width towards the middle and lower parts of the image, where several deformation bands and fault strands are connected to the PSS.

suspended, the more cohesive beds fragment and become brecciated, and the beds which are deeper still deform hydroplastically by folding (Marco and Agnon, 1995).

The dependence of seismite character and thickness on local sediment properties and lake bed topography means that attempts to associate seismite layer thickness or extent with a palaeo-earthquake of given magnitude have been avoided. Indeed, some earthquake events may not even have resulted in the production of a seismite, or in the case of closely-spaced events or aftershocks, one seismite may overprint a previous one. However, sediment liquefaction requires earthquake magnitudes ≥6 (Allen, 1982), which provides at least a lower bound on event magnitudes. In addition to this, the thickness of mixed layers and subsequent sedimentary packages is frequently greater in the hangingwall than in the footwall of the faults (Fig. 4.3), and local slumping in the hangingwall, immediately adjacent to the fault, is frequently present, suggesting down-slope movement of footwall sediment over the fault scarp (Marco and Agnon, 2005). These observations indicate that movements on the faults were syn-sedimentary and produced surface rupturing scarps. This supports the lower bound on earthquake magnitudes inferred from the seismites, because surface ruptures are typically only produced during events of at least M >5.5 (Bonilla et al., 1984; Wells and Coppersmith, 1994).

The exceptional preservation of seismite layers within the high-resolution annually varved sediments of the Lisan Formation, along with the excellent exposures, provides an almost continuous 50,000 yr palaeoseismic record for the Dead Sea Graben (Marco and Agnon, 2005; Marco et al., 1996b). However, despite comprehensive studies concerning the occurrence and formation of the seismites and their use in palaeoseismic studies (Agnon et al., 2006; Alsop and Marco, 2011b; Hamiel et al., 2009; Heifetz et al., 2005; Marco and Agnon, 1995, 2005; Marco et al., 1996b; Wetzler et al., 2010), very little attention has been paid to the style of faulting in these sediments.

4.3 *Fault architecture and geometry*

4.3.1 *Terminology*

We studied faults at two locations on the Masada plain: Locality 1, where individual faults are numbered 1.1, 1.2, etc., and Locality 2, where individual faults are numbered 2.1, 2.2, etc. These localities are labelled on Fig. 4.1b and the coordinates for each fault studied are included in the following fault descriptions. The principal components of the faults are labelled in Fig. 4.3. The fundamental component is the *deformation band*. Thus, following conventions described previously, the *fault core* refers to a zone of interconnected, densely clustered, deformation bands. The anastomosing nature of the deformation bands leads to local variations in fault core thickness and sometimes results in fault-bound *lenses* of sediment. Strain localization within certain deformation band clusters has resulted in the development of *slip zones*. In each fault core there is a *principal slip zone (PSZ)*, which accommodates the majority of the displacement within the fault core. Typically, the boundaries between slip zones and the host rock are very sharp and distinct, and we refer to these boundaries as *slip surfaces.* Often the slip surface on one side of the PSZ is much straighter than on the other side, in which case we term it the principal slip surface (PSS), as it appears to have experienced greater wear, and hence slip, than the opposing PSZ boundary. Deformation bands that are not connected to the PSZ are not considered to be a component of the fault core, and instead are allocated to the *damage zone*.

4.3.2 *Fault orientation data*

The faults we studied display a scatter of orientations (Fig. 4.4a). Some of the faults strike N-S, in accordance with the main trend of the faults in the MFZ (Marco and Agnon, 1995), but two other dominant trends of faults striking either NW-SE or NE-SW are also present. This polymodal fault pattern implies a regional non-plane strain, consistent with transtension along the Dead Sea fault system (e.g. Garfunkel, 1981; Sagy et al., 2003). Regardless of the strike orientation, the faults form apparent conjugate patterns in cross-sectional view, with opposing dip directions averaging between 40-60°. Deformation bands within the damage zone display similar trends, although they may dip either synthetically or antithetically to the associated faults (Fig. 4.4b). Although 2-D cross-sections through the fault planes are very well exposed, there is a lack of exposure of the planar fault surfaces themselves, and thus a detailed analysis of fault kinematics is not possible.

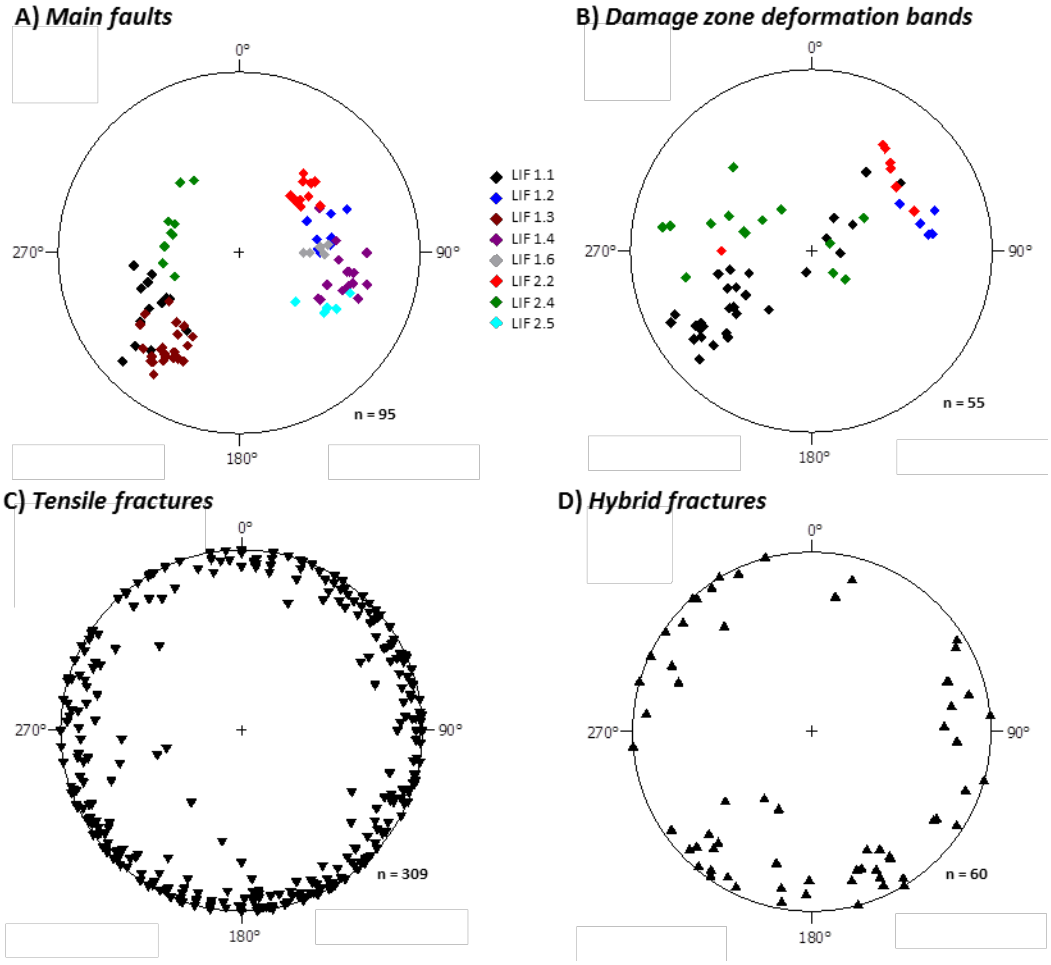

Figure 4.4 Equal-area, lower hemisphere stereographic projections of **a)** The main faults studied; **b)** Deformation bands which are found within the damage zones of the main faults; **c)** Tensile fractures, which are pervasive throughout the outcrops, but are inferred to not be related to the studied faults. **d)** Hybrid extensional-shear fractures found within the damage zones of the main faults.

4.3.3 *Damage zone characteristics*

In order to study the nature and extent of the damage zones associated with the faults, we conducted a transect across one of the best exposed outcrops (Fig. 4.5), recording the number and style of deformation features that could be observed from the base to the top of the cliff section, standing at a distance of 2.5 m away. Sub-vertical tensile fractures are pervasive features (Fig. 4.5a), ranging from a few cm, up to over 6 m in length (height), transecting the whole cliff. Their orientations are rather scattered (Fig. 4.4c), as is their frequency across the outcrop, which does not appear to fluctuate in a systematic way in proximity to major faults (Fig. 4.5b). In addition, these

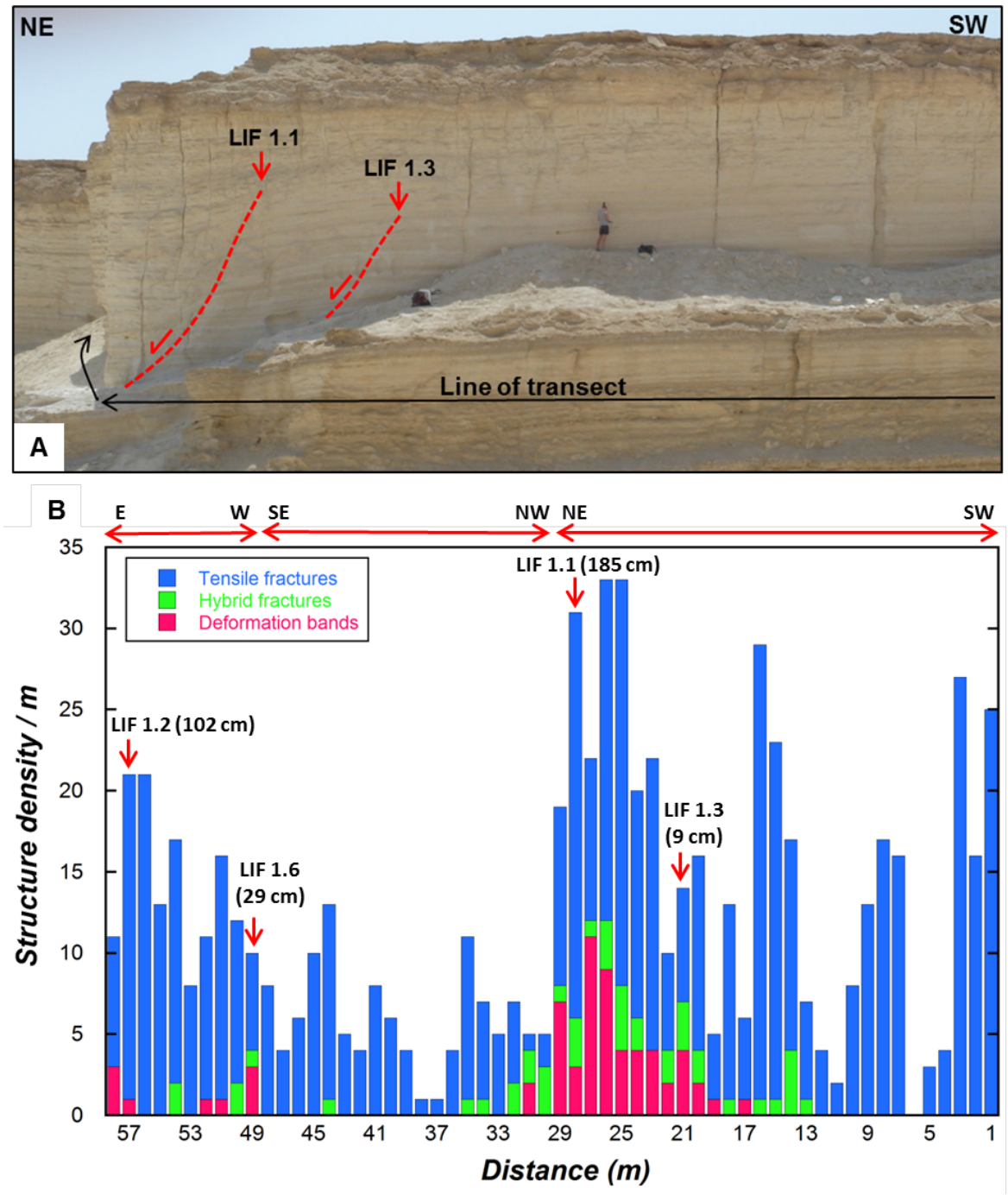

Figure 4.5 a) Photo of a section of outcrop across which a structure transect was conducted, the results of which are presented in fig. **b**. Faults 1.1 and 1.3 are labelled; Faults 1.2 and 1.6, also included in the transect data, are around the corner of the outcrop photographed here, indicated by the curved arrow. Note the presence of sub-vertical tensile fractures, which transect the whole outcrop, whereas faults terminate before the top of the outcrop. **b)** Structural transect data that includes four faults, the locations and displacements of which are labelled on the plot. See text for full description.

fractures often intersect the top of the Lisan Formation, whereas the faults do not (Fig. 4.5a). This suggests that at least some of the tensile fractures post-date faulting, and could either be related to sediment unloading during periods of water-level retreat, or to local salt diapir intrusion (e.g. Marco et al., 2002), which would also explain their scattered and varying orientations relative to the faults, so we have chosen not to study these features in detail.

It is evident from Fig. 4.5b that a damage zone does exist around each fault, characterized by an elevated frequency of deformation bands and hybrid extensional-shear fractures, which decreases to zero away from the faults. The deformation bands range from a few mm to tens of cm in length and are characterized by zones of shear, typically <<1 mm wide, across which cohesion is maintained, accommodating displacements of up to a few cm (Fig. 4.6a). The hybrid extensional-shear fractures are typically several tens of cm in length with displacements of up to a few mm and are characterized by either en-echelon or stepped geometries with a number of dilational jogs and restraining bends along their lengths (Fig. 4.6b). Compared to the deformation bands, the extensional-shear fractures display a much wider scatter of orientations relative to the faults, and are much higher-angle features, with dip angles averaging 78° (Fig. 4.4d). However, given the increase in the number of extensional-shear fractures in proximity to the faults, it does seem

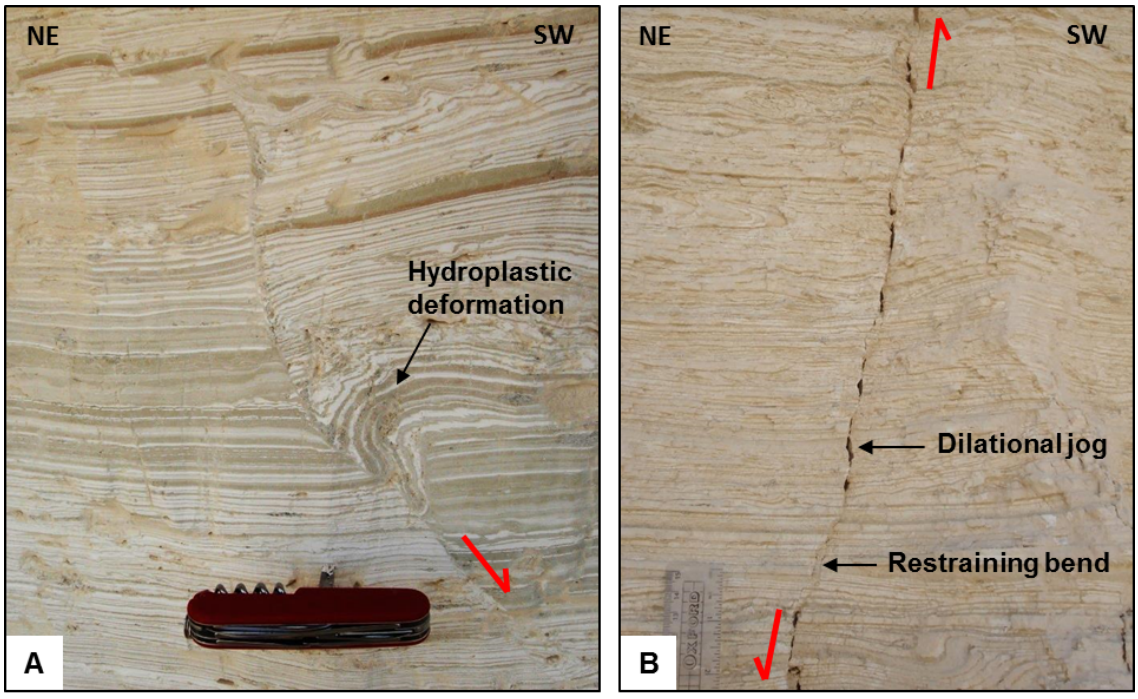

Figure 4.6 Damage zone structures. **a)** An example of a deformation band within the damage zone, in this case with a curved geometry and a maximum of a few cm of offset. Shear movement has also resulted in hydroplastic deformation of the sediment in the hangingwall of the deformation band. **b)** An example of a hybrid extensional-shear fracture with stepped geometry.

appropriate to include these features when calculating the extent of the fault damage zones. We suggest that they may have formed to accommodate strain heterogeneities in the sediment, caused by deformation related to the main faults. The damage zone width increases according to fault displacement, or where faults are close enough to interact. For example, Faults 1.6 and 1.2, which are isolated from one another and have maximum exposed displacements of 29 cm and 102 cm, respectively, both have hangingwall damage zones <1 m wide, and footwall damage zones up to 4 m and 2 m wide, respectively. Fault 1.1, on the other hand, which has a maximum exposed displacement of 185 cm, has a hangingwall damage zone up to 8 m wide, and its footwall damage zone merges with the hangingwall damage zone of Fault 1.3 (maximum exposed displacement = 9 cm), which is 8 m away. In this case, it is not possible to categorically attribute damage zone structures to specific faults, but collectively they create a damaged zone with a total width of 23 m.

In addition to the increase in brittle deformation in the vicinity of faults, sedimentary layers are often dragged (Fig. 4.3), indicating that a small portion of the displacement is accommodated by distributed ductile strain. In some cases layers are dragged to the extent that they are dipping at very steep angles of up to 65°, sub-parallel to the faults themselves. The amount of ductile deformation varies greatly between layers. Some layers abutting a fault accommodate up to 35% of the total fault offset by ductile deformation, whereas others do not appear to accommodate any such strain. Variations in the amount of brittle vs. ductile deformation do not appear to be lithologically controlled; i.e. there is no systematic relationship between drag features and the ratio of aragonite to clastic laminae abutting the fault. In most cases, following the classifications laid out by Ferrill et al. (2005), we consider the dragging of sedimentary layers adjacent to the fault to be due to frictional dragging during fault slip. We do not rule out the possibility that some layer dragging has been produced by fault-propagation folding, but there is a lack of convincing evidence to suggest that this was a common process.

4.3.4 *Fault core characteristics*

Here we describe the geometry and microstructure of four groups of faults in order of increasing exposed maximum displacement, D_{max}. In each case, we have selected representative example faults, which were chosen due to a combination of their good exposure and the suitability of the hand samples taken for thin section preparation for microstructural analysis. For each fault we have constructed a displacement profile, to show how displacement is distributed up- and down-dip. The lower tip points of faults are usually not exposed, and it is therefore unknown where the point of true maximum displacement is and so the profiles presented are just for the available outcrop. Dragged layers were restored manually to their original sub-horizontal orientation before

construction of the profiles. Micro-scale observations were made with a Hitachi SU70 Analytical high resolution Scanning Electron Microscope (SEM; G.J. Russell Microscopy Facility, Durham University, UK).

4.3.4.1 *Small-displacement faults (e.g. Fault 1.4, D_{max} = 3.8 cm)*

Fault 1.4 (31°18'46.34"N, 35°22'29.07"E) comprises a narrow fault core, up to 5 mm wide, and a poorly developed damage zone, where just a few deformation bands with maximum normal offsets of 2 mm are present in the footwall (Fig. 4.7a). Due to its simple geometry, the displacement profile for the fault conforms to an elliptical shape, whereby displacement tapers towards the tip point (Fig. 4.7b).

In hand specimen (Fig. 4.7c), it can be seen that for the majority of the exposed section, the fault core comprises just a single slip zone (hence this is the PSZ). The width of the PSZ is so narrow that it is not possible to measure with the naked eye, resulting in a fault core that is, for the most part, <0.5 mm wide. The fault core only reaches its maximum width of 5 mm where thin (<0.5 mm wide) deformation bands, no greater than a cm in length, are connected to the PSZ. These deformation bands have an anastomosing geometry creating fault-bound lenses of host rock within which the original host rock laminae can still be identified (Fig. 4.7c). The PSZ sharply truncates host rock laminae and is easily identifiable in areas where the fault offset is greater than bed thickness, juxtaposing contrasting laminae across the fault. However, it is harder to discern where bed thickness is greater than the fault offset and the faulted material is of the same nature on either side of the PSZ. Some mm-scale dragging of host rock laminae into the fault is observed.

We found that high-resolution scans of thin sections showed in greater clarity the nature of the PSZs. In the case of Fault 1.4, this revealed that the apparent 'simple' geometry of the PSZ actually comprises a cluster of anastomosing and interconnected deformation bands (Fig. 4.7d), each no more than a few cm in length. The deformation bands enclose regions of host rock up to 2.5 mm wide, within which laminae are variably rotated (Fig. 4.7d). No off-fault damage is visible at this scale, with the exception of some minor mm-scale dragging of layers into the fault. Further investigation of the deformation band zone using the SEM shows that where deformation bands transect clay-rich clastic laminae, they are often characterized by clay smear (Fig. 4.7e-f). It is also evident that between two adjacent deformation bands, a mixture of clastic and aragonite laminae can become incorporated into the PSZ (Fig. 4.7f).

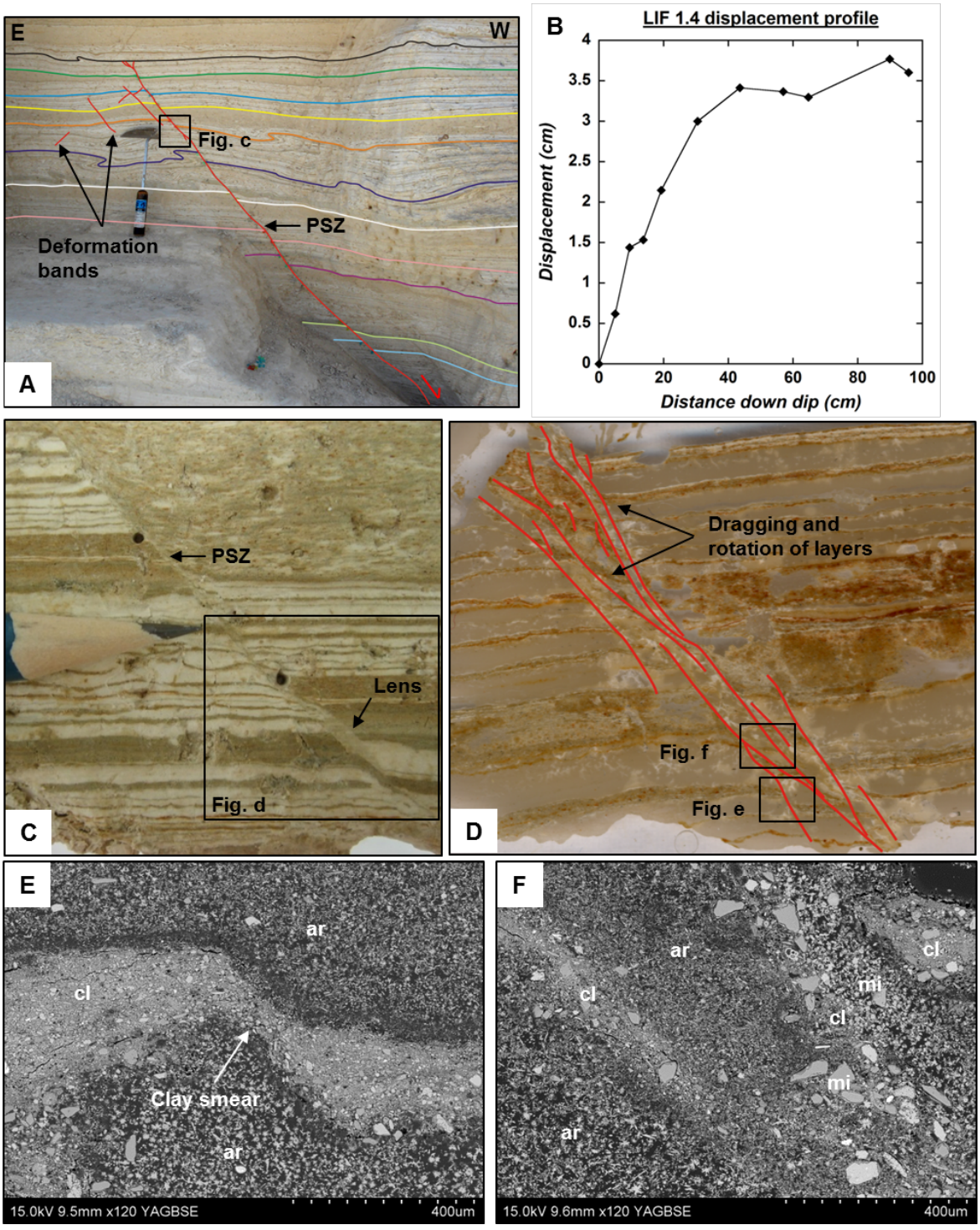

Figure 4.7 a) Fault 1.4, D_{max} = 3.8 cm, viewed at the meso-scale in outcrop. Scraper for scale measures 27 cm in length. **b)** Displacement profile constructed for Fault 1.4. The plotted points correspond to the highlighted sedimentary layers in fig. **a**. **c)** Hand sample from Fault 1.4. The location from which it is taken is shown in fig. **a**. The displacement at this point is ~1.4 cm. **d)** High-resolution scan of thin section taken from boxed area in fig. **c**, showing how the PSZ comprises several anastomosing deformation bands. **e)** SEM image of a deformation band defined by smearing of a clay-rich clastic layer, the location of which is shown in figure **d**. ar = aragonite, cl = clay-rich clastic material. – continued overleaf.

f) SEM image of a zone of deformation bands, the location of which is also shown in fig. **d**. In this case, a mixture of aragonite and clastic laminae are incorporated into the deformation band zone. The diagonally-inclined orientation of patches of clay-rich clastic material (cl), such as that towards the left hand side of the image, suggests that this material has been smeared, as in fig. **e**. mi = areas where the aragonite and clastic material have mixed.

4.3.4.2 *Modest-displacement faults (e.g. Fault 1.3, D_{max} = 9 cm)*

Fault 1.3 (31°18'47.14"N, 35°22'28.19"E) has a complex geometry at the meso-scale, comprising several deformation bands and slip surfaces that branch from the PSZ, and sometimes create lenses (Fig. 4.8a). The fault core thus shows a range of widths, from <0.5 mm where it comprises only the PSZ, to up to 8 cm where branches are present. There is also a subsidiary fault located ~40 cm into the footwall of Fault 1.3 (Fig. 4.8a). The fault's complex geometry, plus interaction with the subsidiary fault in the footwall, results in a displacement profile that is much more jagged (Fig. 4.8b) compared to the relatively smooth, elliptical profile of Fault 1.4 (Fig. 4.7b). Displacement deficits on the PSZ, which accommodates a maximum displacement of 8.2 cm, are accommodated by displacement on either branches, which accommodate displacements of up to 2.7 cm, or on the subsidiary fault, which accommodates a maximum displacement of 3.1 cm (Fig. 4.8b).

Also apparent at the meso-scale are three slumped layers (highlighted in red on Fig. 4.8a and shown in the inset image) that are present in the hangingwall of the fault but not the footwall. Folds within these slumped layers verge away from the fault, and die out over a distance of up to 1.4 m into the hangingwall. This observation suggests that the fault could have experienced at least three individual seismic events which generated instabilities in the hangingwall sediment.

In hand specimen, the PSZ is observed to sharply truncate the host rock laminae (Fig. 4.8c). It does not have a measureable width along much of the length of the fault. In places where it does, it is <0.5 mm wide and marked by a thin zone of dark-coloured, smeared, clay-rich material. Where fault strands exhibit only mm-scale displacements, the intervening host rock preserves its original bedding (Fig. 4.8c), although the bedding is sometimes rotated by up to ~15°. Between fault strands with cm-scale displacements, however, original bedding textures are often not recognizable. Gypsum mineralization is associated with Fault 1.3, both as nodules up to ~5 mm in diameter within the fault core (Fig. 4.8c), or precipitated along the fault plane itself. We attribute the incohesive appearance of the fault strands in some places along their lengths (Fig. 4.8c) to the dissolution of gypsum along the fault plane.

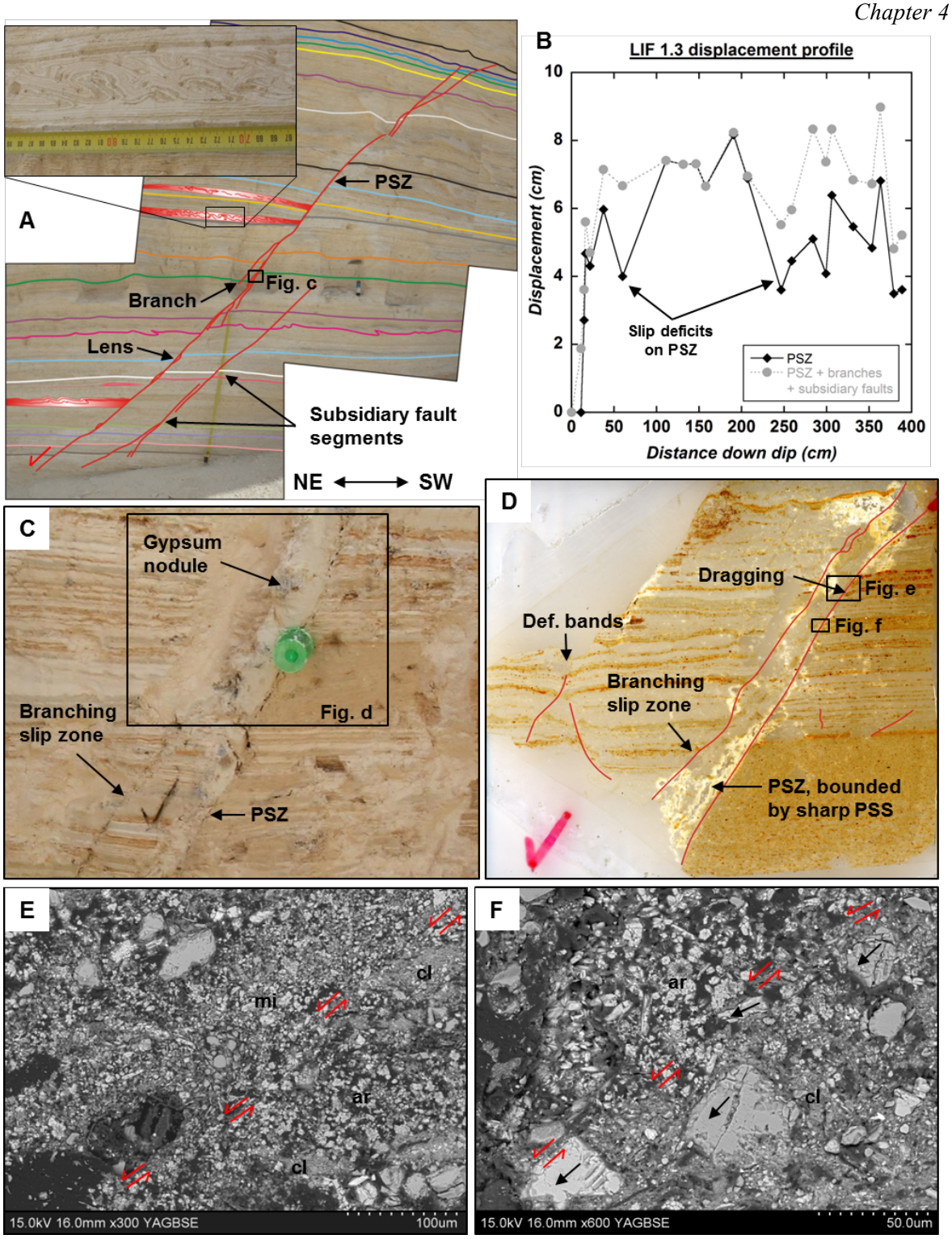

Figure 4.8 a) Fault 1.3, D_{max} = 9 cm, viewed at the meso-scale in outcrop. Hangingwall slumps, inferred to be a product of seismicity on the fault, are highlighted in red, and the inset image shows an example of one of these features. **b)** Displacement profile constructed for Fault 1.3. The profile plotted for the PSZ displays slip deficits, which are accommodated to some extent by the connected branches and the subsidiary fault. The plotted points correspond to the highlighted sedimentary layers in fig. **a**. **c)** Hand sample from Fault 1.3. The location from which it is taken is shown in fig. **a**. The displacement at this point is ~7 cm. – continued overleaf.

d) High-resolution scan of thin section taken from boxed area in fig. **c**. The PSS associated with the PSZ is observed to be much straighter than the slip surface associated with the branching strand. **e)** SEM image of the PSS. The location from where the image is taken is shown in fig. **d**. The location of the PSS is indicated by shear-sense arrows; its location is only discernible due to the termination of the two clastic laminae in the footwall. ar = aragonite, cl = clay-rich clastic material, mi = areas where the aragonite and clastic material have mixed. **f)** SEM image of a different part of the PSS, where clasts have aligned adjacent to the PSS, as indicated by the arrows on clasts. There is no evident comminution of clasts. The location from where the image is taken is shown in fig. **d**.

Thin section analysis reveals that the PSZ is a single, through-going strand, which is bounded on one side by a very straight PSS (Fig. 4.8d). This is in contrast to the anastomosing, wavy deformation bands of Fault 1.4 (e.g. Fig. 4.7d). The adjacent branching slip zone shown in Fig. 4.8d, which has accommodated up to only a couple of mm of displacement compared to the ~7 cm of displacement accommodated by the PSZ at this location, is much wavier. Off-fault damage at this scale is present in the form of mm-scale normal offset deformation bands and mm-scale dragging of laminae into the fault (Fig. 4.8d). In other places along the fault, deformation bands with up to 2 mm of normal offset and layers dragged by up to 7 mm are observed.

Although the PSS, i.e. the PSZ-host rock boundary, appears as a discrete, sharp surface when viewed in hand specimen, due to the manner in which it offsets and juxtaposes contrasting laminae, it is more difficult to resolve at high magnification with the SEM (Fig. 4.8e-f). The material on either side of the PSS, i.e. the material comprising the host rock and that comprising the PSZ, is very similar: clasts are not cut by the PSS and there is little obvious fracturing or comminution or reduction in grain size of the material adjacent to the PSS (Fig. 4.8e-f). The only observable shear-related fabric is a weak alignment of clasts sub-parallel to the PSS (Fig. 4.8f).

4.3.4.3 *Moderate-displacement faults (e.g. Fault 1.2, D_{max} = 102 cm)*

For much of its exposed length, Fault 1.2 (31°18'46.45"N, 35°22'28.94"E) has a relatively simple geometry, comprising just the PSZ. However, some local complexity occurs due to minor branching in its mid-section and some more intense branching in its exposed lower section (Fig. 4.9a). These geometrical variations result in a fault core which ranges from <1 mm up to 7.5 cm wide. Fault branches accommodate no more than a few cm of displacement, which is negligible compared to the total fault displacement, and therefore they are not considered in construction of the displacement profile (Fig. 4.9b). The limited contribution of branches to the overall displacement on the fault results in the fault having a displacement profile with an elliptical shape

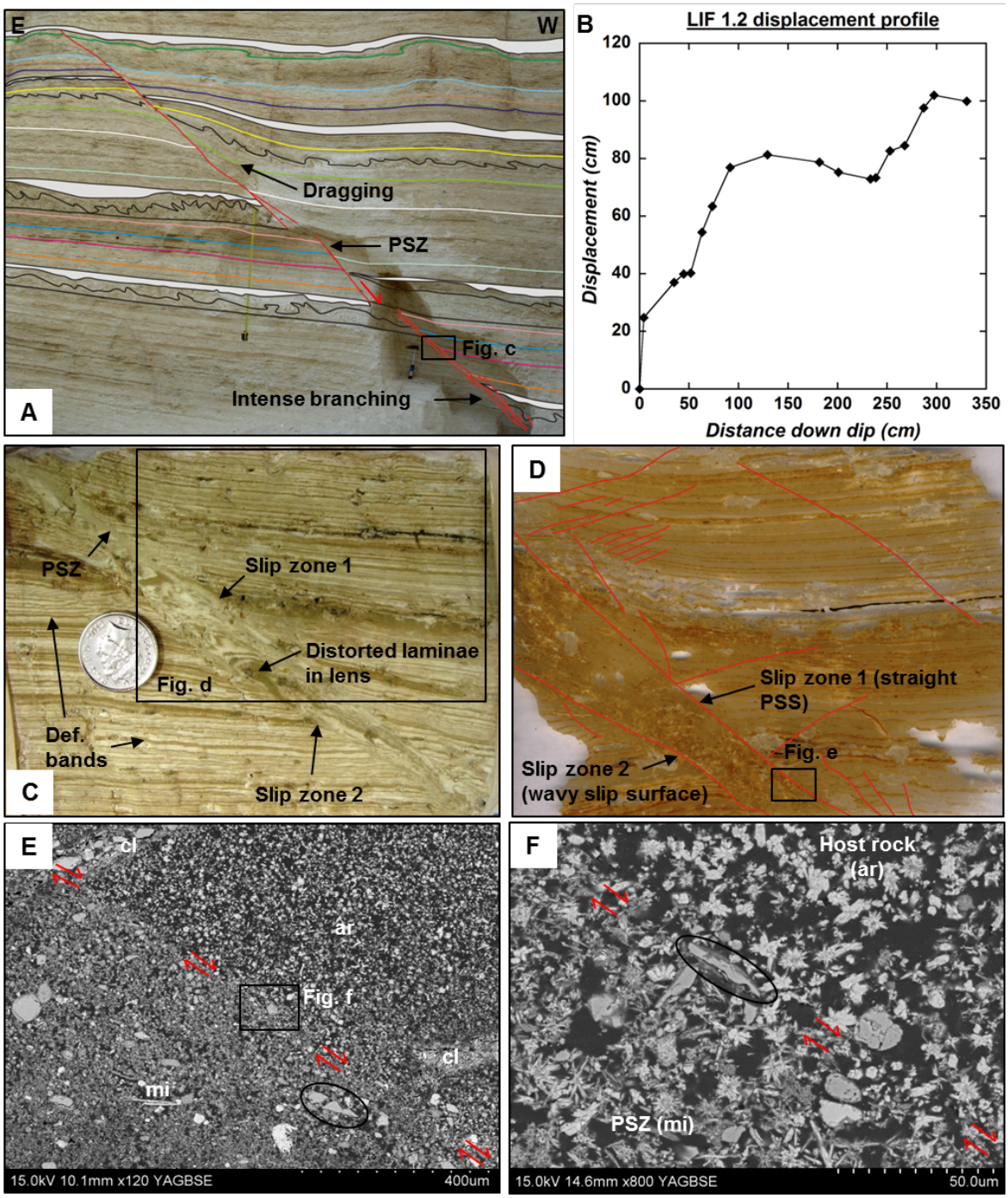

Figure 4.9 a) Fault 1.2, D_{max} = 102 cm, viewed at the meso-scale in outcrop. Mixed layers are shaded grey and slumps are marked in black, but none of these features can be confidently attributed to seismicity on this fault. **b)** Displacement profile constructed for Fault 1.2. The plotted points correspond to the highlighted sedimentary layers in fig. **a**. **c)** Hand sample from Fault 1.2. The location from which it is taken is shown in fig. **a**. The displacement at this point is ~98 cm. **d)** High-resolution scan of thin section taken from boxed area in fig. **c**. The slip surface bounding slip zone 1 is observed to be straighter than that bounding slip zone 2, thus we infer it to be the PSS. – continued overleaf.

e) SEM image of the PSS. The location from where the image is taken is shown in fig. **d**. The location of the PSS is indicated by shear-sense arrows; its location is discernible due to the subtle difference in composition between the host rock, which is predominantly aragonite, and the PSZ material, which is more clay rich. A group of aligned clasts close to the PSS is circled. ar = aragonite, cl = clay-rich clastic material, mi = areas where the aragonite and clastic material have mixed. **f)** Close up image of PSS and PSZ shown in fig. **e**, showing the similarity in grain size of the material within the PSZ compared to the host rock. Several aragonite crystals within the slip zone maintain their concentric structures. Again some alignment of clasts along the PSS is evident (circled).

(Fig. 4.9b), similar to that of Fault 1.4 (Fig. 4.7b), for which the PSZ also accommodates the majority of displacement.

Several slumps and mixed layers are found adjacent to Fault 1.2, but seeing as they are found in both the footwall and hangingwall and do not display an obvious thickening in the hangingwall (Fig. 4.9a), they cannot be confidently associated with movements on this particular fault – they could be related to seismic events on other nearby faults. The current levels of exposure are insufficient to resolve this issue. Significant dragging of laminae into the fault by up to 29 cm is also evident (Fig. 4.9a), equivalent to 28% of the maximum exposed displacement on the fault.

The PSZ now has an identifiable width along the whole length of the fault, varying from <1 mm up to 6 mm in thickness (Fig. 4.9c), with an average thickness of ~2 mm. The hand sample shown in Fig. 4.9c shows an area where the PSZ divides into two sub-parallel slip zones, resulting in a fault core that is here up to 1.1 cm wide. Both slip zones average <1 mm wide and are bounded by sharp slip surfaces. The slip zones comprise ultrafine-grained grey material. The two slip zones enclose a lens up to 9 mm wide in which the host rock laminae are highly distorted (Fig. 4.9c). The two slip zones adjoin towards the upper part of the sample, where the fault again comprises just the PSZ, which here reaches a maximum width of 2 mm (Fig. 4.9c). At the hand-sample and thin section scale, off-fault damage is present in the form of several normal offset deformation bands, predominantly in the hangingwall, with both synthetic and antithetic orientations (Fig. 4.9c-d). They typically only have offsets of up to a few mm, but in some places, they have offsets up to a few cm. The antithetic deformation bands in the hangingwall are formed at angles oriented approximately perpendicular to the fault plane (Fig. 4.9d).

Thin section analysis reveals that, similar to Fault 1.3, the slip zones are through-going, and one of them is bounded by a much straighter PSS than the other (Fig. 4.9d). Upon investigation with the SEM, the PSZ-host rock boundary can again be difficult to locate because clasts are not cut by the PSS, and the nature of the material within the PSZ is very similar to that in the host rock

juxtaposing it (Fig. 4.9e). It is particularly striking that even the aragonite crystals within the PSZ have retained their radial, rosette-like arrangements of needles during deformation (Fig. 4.9f). As observed for Fault 1.3, there is sometimes a preferred orientation of clasts in proximity to the PSS (Fig. 4.9e-f) and very little evidence of fracturing and cataclasis.

4.3.4.4 *Larger-displacement faults (e.g. Fault 2.4, D_{max} = 337 cm)*

Fault 2.4 (31°18'27.06"N, 35°22'33.54"E) has the largest maximum displacement of any of the faults studied. Despite this, there are no seismites associated with the fault. As with the previous faults described, in many places, the fault comprises only the PSZ (Fig. 4.10a). In these places, the fault core ranges from just 1-16 mm wide. However, the presence of branches in some parts (Fig. 4.10a) results in a fault core with a maximum width of up to 30 cm. As with Fault 1.2, the displacements on the fault branches are not great enough to impact on the overall shape of the displacement profile so their effects are neglected (Fig. 4.10b). The displacement profile does not quite have the same elliptical shape as that of Faults 1.4 and 1.2, in that the profile has more of a linear than a curved shape (Fig. 4.10b). We attribute this to the fact that, although the fault in its later stages of activity appears to have operated as a single, through-going PSZ, the geometry of its central portion (Fig. 4.10a) suggests that it originated as two individual, overlapping fault segments that later became one. This would explain why the displacement profile tapers more gradually towards the upper tip point than one would expect (Fig. 4.10b). The irregular form of the beds at the top of the section (Fig. 4.10a) could also contribute to the upper part of the slip profile having a slightly different shape to what one would expect. Also, as with Fault 1.2, there is significant dragging of layers into the fault (Fig. 4.10a), by up to 52 cm, equivalent to 15% of the overall displacement.

The hand sample shown in Fig. 4.10c-d shows an area where the fault core comprises just the PSZ. The PSZ has a notably straight PSS bounding it on one side, whereas the opposing PSZ-host rock boundary is more undulating; this is consistent with observations made for both Faults 1.3 (Fig. 4.8d) and 1.2 (Fig. 4.9d). The PSZ here ranges from 0.5-6 mm in width (the average PSZ width along the fault is 2-3 mm) and is composed of a pale brown coloured silty material (Fig. 4.10c). It should be noted that, regardless of displacement and fault development, hand samples do not split cleanly along PSSs, and so it is not possible to comment on the nature of the slip surfaces in plan view.

At the hand-sample scale, off-fault damage is present in the form of synthetic and antithetic deformation bands, predominantly in the hangingwall, with normal offsets of up to a few cm in some places (Fig. 4.10c). Again, antithetic deformation bands in the hangingwall lie at a high angle

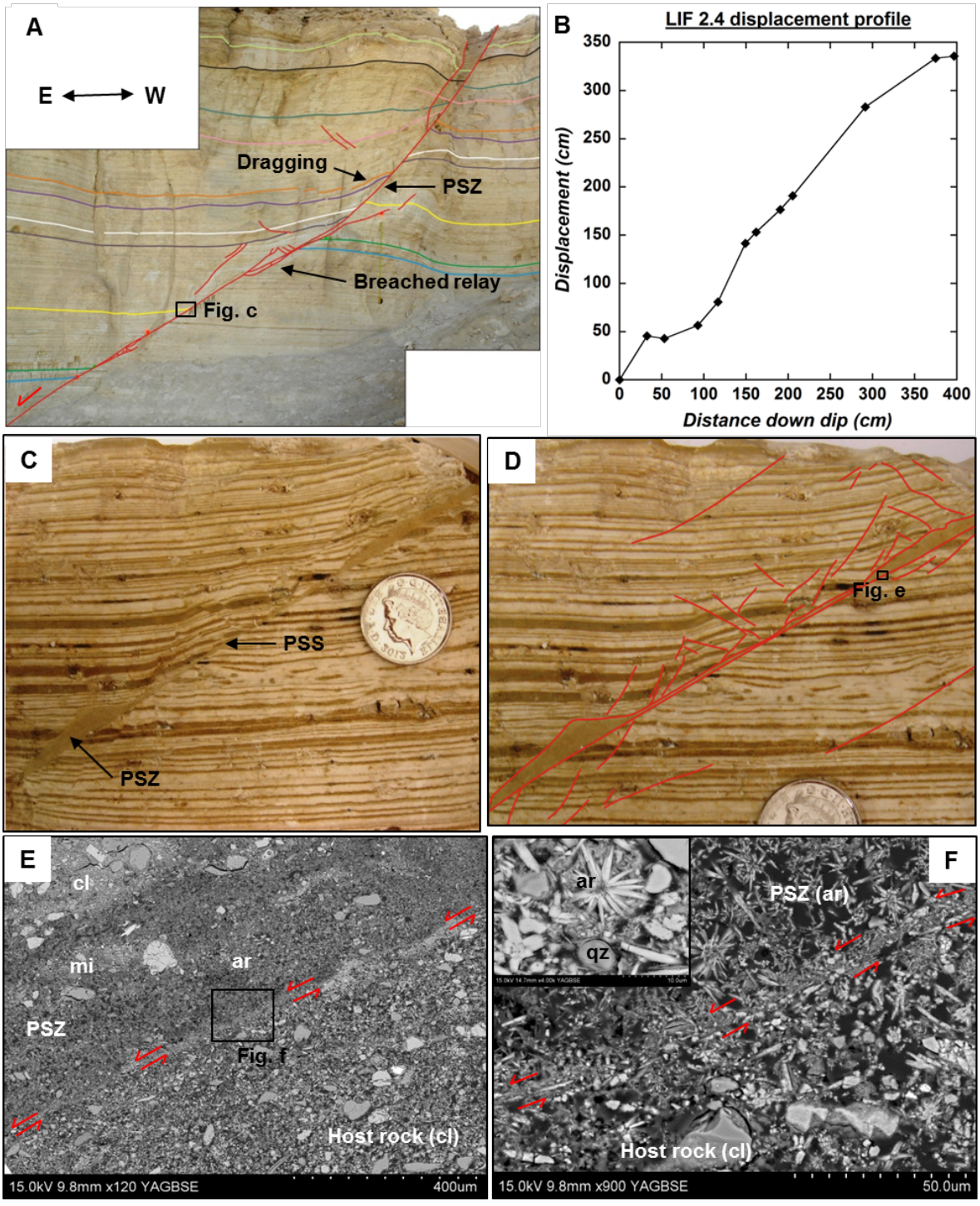

Figure 4.10 a) Fault 2.4, D_{max} = 337 cm, viewed at the meso-scale in outcrop. **b)** Displacement profile constructed for Fault 2.4. The plotted points correspond to the highlighted sedimentary layers in fig. **a**. **c)** Hand sample from Fault 2.4. The location from which it is taken is shown in fig. **a**. The displacement at this point is ~280 cm. **d)** As the thin section taken from the hand sample in fig. **c** was very small, we instead show an annotated version of fig. **c**, to highlight PSZ boundaries and off-fault damage. Again, one PSZ boundary (labelled PSS) is observed to be much straighter than the opposite PSZ boundary. – continued overleaf.

e) SEM image of the PSS. The location from where the image is taken is shown in fig. **d**. The location of the PSS is indicated by shear-sense arrows; its location is discernible due to the subtle difference in composition between the host rock and the PSZ material, and also an enrichment of clay along the PSS due to clay smear. The PSZ is very heterogeneous in composition, e.g. note the clump of clay-rich clastic material labelled in the top left hand size of the image, compared to the rest of the PSZ, which is aragonite-rich. ar = aragonite, cl = clay-rich clastic material, mi = areas where the aragonite and clastic material have mixed. **f)** Close up image of PSS shown in fig. **e**; location of PSS is indicated by shear-sense arrows and highlighted by clay smear and an alignment of acicular aragonite needles. Note how aragonite crystals in the PSZ retain their concentric arrangements of needles, showing little evidence for fracturing or comminution. Inset shows an example of an aragonite crystal and quartz (qz) clasts within the PSZ which are surrounded by a cortex of clay.

to the fault (Fig. 4.10c). Layer dragging at the hand-sample scale is up to 5 cm. Where fault branches occur, the material encompassed between the PSZ and the fault branch, or enclosed within fault-bound lenses, is typically highly deformed; host-rock laminae are either highly rotated (by up to 40˚ towards the PSZ) or are transected by many mm-scale displacement deformation bands, or often by a combination of these two features.

SEM observations are consistent with those made in previous samples. There is evidence for smearing and incorporation of both clastic and aragonite laminae into the PSZ of the fault (Fig. 4.10e-f), sometimes resulting in a PSZ with rather heterogeneous composition (Fig. 4.10e). Once again, we observe that there is commonly an alignment of clasts adjacent to the PSS in an orientation sub-parallel to the PSS (Fig. 4.10f), but there is little evidence for grain fracturing or cataclastic comminution within the PSZ (Fig. 4.10f). Sometimes, clasts within the PSZ are observed to have a cortex of clay surrounding them (Fig. 4.10f, inset).

4.4 *Discussion*

4.4.1 *Structure, deformation mechanisms and evolution of seismogenic faults in near-surface, brine-saturated, poorly-lithified sediments*

The faults of the MFZ formed and developed in near-surface (<2.5 MPa), high-porosity (up to 50%), poorly-lithified, brine-saturated sediments composed of a mixture of aragonite and clay-rich clastic material. The faults have been inferred to have been seismogenic during their history. Our general outcrop-scale observations, plus meso- to micro-scale observations, allow us to propose a model for the evolution of the internal structure of seismogenic faults, in near-surface, brine-saturated, poorly-lithified sediments, based on increasing fault displacement. Furthermore,

microstructural observations allow us to infer the dominant deformation mechanisms during fault activity.

All studied faults exhibit at the meso-scale a fault core, comprising deformation bands, within which shear localization takes place within a narrow PSZ, which accommodates the majority of the displacement (Figs. 4.7-4.10). Micro-scale observations show that for low displacement faults (a few cm offset), the PSZ, which is <0.5 mm wide, comprises a cluster of several anastomosing, sometimes interconnected, deformation bands (Fig. 4.7d). Individual deformation bands are no more than a few cm in length, and accommodate no more than a few mm of offset, but they cluster together, forming zones that are up to several mm wide. When observed at smaller, micrometre scales, the individual deformation bands are characterized by the smearing of clay-rich clastic layers (Fig. 4.7e). We therefore infer that the first increments of bulk strain are accommodated by the re-arrangement of particles, or groups of particles, into deformation bands (Fig. 4.11, stage 1). This occurs via particle rotation and/or intergranular slip (e.g. Maltman, 1987). When this occurs in the clay-rich clastic layers, it results in very obvious clay smears, but the aragonite layers appear to deform in a similar, ductile manner, as we do not observe any distinct brittle deformation fabrics, i.e. fracturing or cataclastic processes, associated with the aragonite layers. The 'ductile' style of deformation may be promoted by one, or a combination, of several factors, such as the very fine grain size, low effective stress, high porosity, or the fluid-saturated nature of the medium, which allow particles to re-arrange themselves without undergoing internal deformation by fracturing, in response to an applied stress. According to the classifications of Fossen et al. (2007), the initial deformation bands would be classed as disaggregation bands, or phyllosilicate bands in the cases where they cross phyllosilicate-rich laminae.

As displacement along the fault increases to several cm, the PSZ is observed to comprise a single, through-going, but wavy, slip zone (Fig. 4.8c-d). However, the PSZ in many places is still typically <0.5 mm wide. When investigated at the micron-scale, the slip surfaces bounding the PSZ do not sharply cut clasts and there is no grain size reduction towards them (Figs. 4.8e-f, 4.9e-f and 4.10e-f), as would typically be associated with slip surfaces in many upper crustal fault zones (e.g. Bullock et al., 2014; Chester and Chester, 1998; Smith et al., 2011); aragonite crystals retain their acicular shapes and rosette structures (Figs. 4.8f, 4.9f and 4.10f). This is despite the fact that shear has evidently taken place, as evidenced by the alignment of tabular and elongate clasts and aragonite crystals sub-parallel to the slip surfaces (Figs. 4.8f, 4.9f and 4.10f). From these observations, we infer that with increasing strain, individual deformation bands link up to form through-going, wavy slip zones (Fig. 4.11, stage 2). The slip zones bound lenses and regions of host rock in which laminae are variably rotated and become increasingly dragged and smeared due

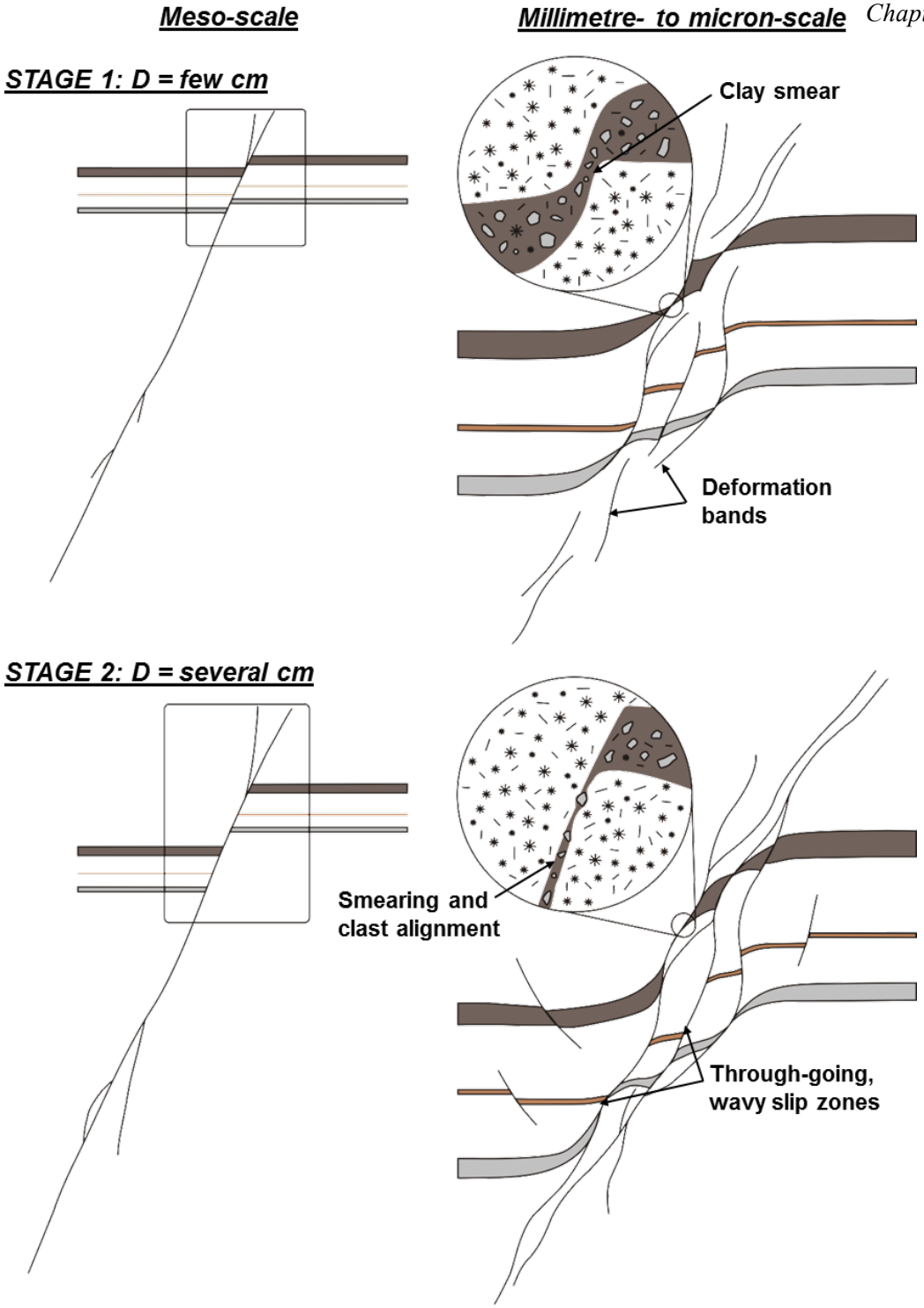

Figure 4.11 (Stages 1-2) Model for fault evolution in the Lisan Formation. **Stage 1:** Faults initiate as clusters of disaggregation and phyllosilicate bands, defined at the millimetre- and micron-scales by smearing of layers. Each deformation band accommodates no more than a few cm of displacement. Host rock laminae are enclosed between adjacent deformation bands. Off-fault damage is minimal. **Stage 2:** With increasing strain, deformation bands link up to form through-going, wavy slip zones, which can accommodate several cm of displacement. At the meso-scale, fault branching becomes more evident. At the millimetre- to micron-scale, entrapped laminae between neighbouring slip zones/deformation bands become more rotated and smeared. Under the microscope, a weak alignment of clasts adjacent to slip surfaces may be observed.

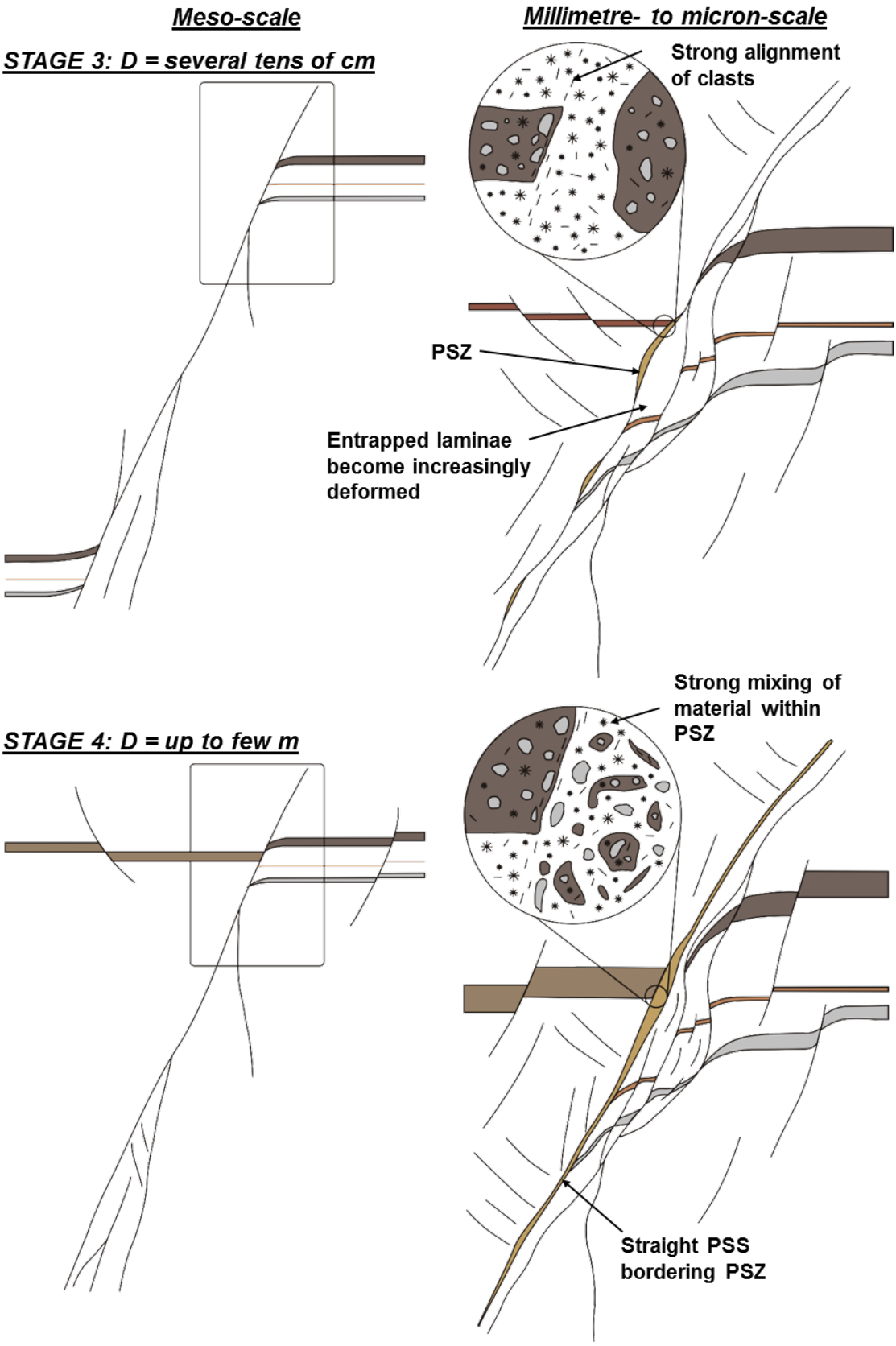

Figure 4.11 (Stages 3-4) – see caption overleaf.

Stage 3: As displacement along the fault increases to several tens of cm, fault branching and off-fault deformation increases significantly. Slip localizes within certain slip zones. The slip zone which accommodates the majority of slip establishes itself as the PSZ. Asperity bifurcation during slip localization may result in widening of slip zones, and their bounding slip surfaces become much straighter. Entrapped laminae between neighbouring slip zones may become smeared out and disaggregated to the extent that original host rock features are no longer recognizable. Under the microscope, a stronger alignment of clasts is observed adjacent to slip surfaces, and slip zones comprise a mixture of aragonite-rich and clay-rich clastic material. **Stage 4:** As m-scale displacements accumulate on the fault, slip continues to localize within the PSZ. Material within the PSZ becomes increasingly mixed. Typically, one PSZ boundary is straighter than the opposing boundary, suggesting slip is most localized here; we refer to this as the PSS. In addition, there is a further increase in off-fault damage, likely related to the passage of earthquakes along the fault.

to movements on the bounding slip zones. The absence of cataclasis, plus the alignment of clasts adjacent to slip surfaces, suggests that even though through-going slip zones are now formed, deformation still occurs primarily by intergranular slip and grain rotation.

The slip surfaces bounding the PSZs of the m-scale displacement faults are much straighter than those of the cm-scale displacement faults (Figs. 4.9d and 4.10d). Typically the slip surface on one side of the PSZ is much straighter than that on the other side, suggesting that slip is concentrated towards one side of the PSZ; we refer to the straighter surface as the principal slip surface (PSS). The nature of slip surfaces at the microscale does not differ much from that of the cm-scale displacement faults, although there may be a stronger alignment of clasts (e.g. Fig. 4.10f). PSZs have an average width of 2-3 mm, but can reach widths of up to 16 mm. Thus, the average thickness of the PSZ seems to increase with increasing displacement. We suggest that the PSSs of the faults become straighter with increasing displacement due to asperity bifurcation (e.g. Childs et al., 2009) (Fig. 4.11, stages 3 and 4); it is more efficient for slip to occur along a straight surface than on a wavy surface. In the process, the asperities become incorporated into the PSZ, resulting in widening of the PSZ, consistent with our observations (Fig. 4.11, stage 4).

PSZs contain a mixture of material derived from both clastic and aragonite laminae, which have become entrapped between neighbouring slip surfaces (Figs. 4.9e, 4.10e and Fig. 4.11, stages 3 and 4). Sometimes the clastic material appears to be well mixed with the aragonite (Fig. 4.9e-f), but other times it remains as clumps of clay-rich material (Fig. 4.10e). We suggest that the material becomes increasingly mixed with increasing displacement on the fault (Fig. 4.11, stage 4). Despite this, aragonite crystals and clasts of quartz and carbonate derived from the clastic layers still appear

to have accrued very little damage during deformation; there is no evident grain size reduction and aragonite crystals have retained their acicular shapes and rosette structures. At greater displacement, the alignment of elongate clasts and acicular aragonite crystals along slip surfaces becomes even more evident (Fig. 4.10f and Fig. 4.11, stages 3 and 4).

Our microstructural observations are comparable to those of the similarly deformed sediments described by Kristensen et al. (2013). The lack of evidence for cataclasis suggests that the dominant deformation mechanism operating within the PSZs, from the initial to the more mature stages of fault activity, is particulate flow (Borradaile, 1981), which is typical of deformation of high-porosity sediments at shallow burial depths (e.g. Fisher and Knipe, 2001; Johansen and Fossen, 2008; Kristensen et al., 2013). The rolling and sliding of particles would be facilitated not only by the low confining pressure, which facilitates dilation (Borradaile, 1981), but also by the presence of frictionally weak clay minerals (e.g. Behnsen and Faulkner, 2012; Bullock et al., 2015; Faulkner et al., 2011; Ikari et al., 2009) and the fluid-saturated nature of the material (Borradaile, 1981; Marques et al., 2010). Evidence for particle rolling facilitated by clays is provided by the observation of clay cortices (e.g. Boutareaud et al., 2008; Rempe et al., 2014) around grains (Fig. 4.10f, inset).

Not only does the PSZ increase in width with increasing displacement, but so does the width of the fault core and the damage zone. Thus, these faults conform to the standard fault displacement-thickness scaling relationship observed for upper crustal faults in a range of lithologies (Childs et al., 2009; Shipton et al., 2006). For the cm-scale faults described here, maximum fault core width ranges from 5 mm up to 8 cm, whereas for the m-scale displacement faults it ranges from 7.5 cm up to 30 cm. This is due to the presence of a greater number of branching slip zones and deformation bands, plus the fact that these branches extend for a greater distance from the PSZ. These observations are consistent with an increasing and expanding stress field being generated around the faults as they propagate (Fig. 4.11, stages 1 through to 4). The sediment enclosed between two adjacent slip zones or within fault-bound lenses becomes more intensely deformed as displacement on one of the bounding slip zones increases. If bounding slip zones have only mm- to cm-scale displacements, the enclosed sediment remains more-or-less in its undeformed state (Fig. 4.11, stages 1 and 2), but with increasing displacement, the laminae become increasingly rotated and smeared, and deformation bands start to develop within the enclosed rock volume (Fig. 4.11, stages 3 and 4), so that original host rock features may become unrecognizable. These fault-bounded zones of deformed sediment could be compared in some ways to the mixed zones described in previous studies of fault zones in poorly lithified sediments (e.g. Heynekamp et al., 1999; Loveless et al., 2011; Minor and Hudson, 2006; Rawling and Goodwin, 2006). Fault

displacement profiles display evidence for interaction between PSZs and accompanying fault branches and segments (e.g. Fig. 4.8b), showing that the faults behave as geometrically coherent arrays (Walsh and Watterson, 1991).

The total width of the damage zone is typically no more than a few metres for cm-scale displacement faults, but is up to 16 m for m-scale displacement faults, and can be even greater where two neighbouring faults interact. In addition, off-fault damage observed at the hand-sample scale increases with increasing fault displacement (e.g. compare Figs. 4.7d and 4.8d with 4.9d and 4.10d). This is manifested by both the density and the offsets of deformation bands present in both the hangingwall and footwall, although there seems to be a preferential concentration of these features in the hangingwall of the fault. In addition, there are a greater proportion of antithetic deformation bands at a high-angle to the fault plane in the hangingwall than there is in the footwall (Figs. 4.9d and 4.10d). This observation is consistent with the expected asymmetrical distribution of stresses about the fault plane during upwards propagation of earthquake ruptures (Scholz et al., 1993; Vermilye and Scholz, 1998). Therefore, we interpret the increased number of high-angle, antithetic deformation bands in the hangingwall of the m-scale displacement faults as a further evidence for the passage of earthquake ruptures along these structures. Although the scaling and orientations of off-fault damage associated with the Lisan faults are comparable to observations of off-fault damage associated with faults in more cohesive rocks, it should be remembered that off-fault damage in cohesive rocks is characterized by fracturing and the generation of cataclastic fault rocks, whereas in the Lisan Formation it is characterized by deformation bands and layer dragging/rotation, so it is in general much more ductile in these poorly consolidated host rocks. This may have significant implications in terms of the evaluation of the earthquake energy budget, as described below.

4.4.2 *Implications for seismicity in near-surface, poorly-lithified sediments*

It is often assumed that the shallow portions of fault zones, occupied by poorly lithified sediments, or incohesive, clay-rich fault gouges, should behave predominantly aseismically (Marone and Scholz, 1988; Scholz, 1998). This is because incohesive gouges and clay-rich rock/gouge samples have been shown experimentally to behave in a predominantly velocity-strengthening manner when deformed at sub-seismic velocities (e.g. Byerlee and Summers, 1976; Ikari et al., 2009; Marone et al., 1990; Tesei et al., 2012). This is an inherently stable behaviour, which favours aseismic fault creep (Marone, 1998; Scholz, 1998 and references therein). Velocity-strengthening behaviour is typically associated with a distributed style of deformation (e.g. Beeler et al., 1996; Collettini et al., 2011; Ikari et al., 2011), and thus faults deforming by creep may be expected to be

manifest as broad zones of distributed deformation. Earthquakes are unable to nucleate in velocity-strengthening regions of the crust, and if an earthquake were to propagate through such a region, it would encounter a negative stress drop, which would slow down, or even arrest the earthquake, depending on the energy of the rupture (Scholz, 1998). This would result in a slip deficit in the shallow part of the crust, which again is expected to be accommodated by distributed aseismic afterslip (e.g. Fialko et al., 2005; Marone et al., 1991).

In the last ten years, 18 large earthquakes ($M_w \geq 8.0$) have occurred globally (Lay, 2015). This surge of 'great' earthquakes has coincided with recent technological advancements in seismology (e.g. the advent of broadband seismology and GPS), and the greatly expanded global deployment of geophysical instrumentation, which has enabled the collection of an unprecedented quantity and quality of seismological data (Ammon et al., 2010; Kanamori, 2014; Lay, 2015). We now know that large tsunamigenic earthquakes, such as the 2010 M_w 8.8 Maule, Chile (Delouis et al., 2010; Lay et al., 2010) and 2011 M_w 9.0 Tohoku, Japan (Ide et al., 2011) earthquakes, can unexpectedly rupture the entire width of the megathrust from below the coast to the trench, with shallow patches of coseismic slip of up to 60 m. Furthermore, so-called 'tsunami earthquakes', which are shallow events (<15 km) characterized by large slip for a given seismic moment, slow rupture velocity and low frequency seismic radiation (Bilek and Lay, 2002; Kanamori, 1972) have now been directly observed. An example is the 2010 M_w 7.8 Mentawai (Bilek et al., 2011; Lay et al., 2011) earthquake, that nucleated within and ruptured the very shallow portion of the megathrust up-dip from the 2007 M_w 8.5 Sumatra earthquake. The occurrence of such events suggests that the traditional conceptual models of fault zone stability are oversimplifications of natural fault zone behaviour. The unusual and unexpected characteristics of these event types highlight our poor knowledge and understanding of the mechanical and frictional properties of faults in shallow, poorly lithified sediments, and of the structure and deformation mechanisms within these fault zones. This, in turn, severely limits our ability to accurately forecast earthquakes (e.g. Kanamori, 2014).

Our observations of faulting in the Lisan Formation at least shed some light in terms of disclosing the internal architecture of, and deformation mechanisms operative in, seismogenic faults in near-surface, poorly lithified sediments. The studied faults are very localized features, characterized by narrow fault cores, where slip is localized within PSZs that are typically up to only a few mm wide. Thus, the faults in the Lisan Formation have geometrical and seismic attributes that would more typically be associated with faults in velocity-weakening, cohesive rocks that have been exhumed from depths of a few km or more (Sibson, 2003 and references therein). The important difference lies in the dominant deformation mechanisms. In low-porosity, cohesive rocks at greater depths, the

dominant deformation mechanisms are fracturing and cataclasis (Fossen, 2010), whereas in the near-surface, high-porosity, poorly-lithified sediments studied herein, fracturing and cataclasis appear to be absent, and the dominant deformation mechanism is instead inferred to be particulate flow.

The questions then arise as to: 1) How the sediments of the Lisan Formation are able to host localized, seismic ruptures? 2) Would particulate flow influence rupture dynamic processes? Our model of fault evolution goes some way towards answering these questions. First, clay smear plays a major role in the initial stages of development of the faults. Phyllosilicates promote strain-softening (e.g. White and Knipe, 1978) and so once through-going, clay-rich shear planes are formed, strain will preferentially localize along these structures, resulting in a localized style of faulting. Once a localized fault is formed, it will be a favourable pathway for the passage of earthquake ruptures to the surface. Furthermore, fluid-saturated phyllosilicate-bearing fault gouges, although exhibiting velocity-strengthening behaviour at sub-seismic slip rates (e.g. Ikari et al., 2011; Tembe et al., 2010; Tesei et al., 2012), have been shown to have very low frictional strength (μ <0.1) and exhibit very low fracture energy when subject to seismic slip rates (e.g. Bullock et al., 2015; Faulkner et al., 2011; Ferri et al., 2010; Ujiie et al., 2013). The presence of phyllosilicates in the Lisan faults would therefore not only facilitate the localization of deformation, but also the propagation of earthquakes towards the surface. The suggestion that earthquakes passing through the Lisan sediment should have very low fracture energy is wholly consistent with the lack of grain fracturing within the PSZs of the faults, and also the lack of brittle deformation in the damage zones. If the work done by frictional and fracture processes during rupture propagation is very low, as our observations suggest, then the majority of the energy budget of an earthquake rupturing the Lisan faults would be dissipated as radiated energy (Kanamori and Rivera, 2006). Such a scenario is consistent with the association of shaking-derived seismites with these faults.

Rupture velocity through low-rigidity materials, such as the poorly lithified Lisan sediments, may be limited by low shear wave velocities (Fossum and Freund, 1975; Geller, 1976). The presence of low-rigidity sediments in accretionary wedges at subduction zones has thus lead several authors to suggest that they may be accountable for the long-duration, slow-rupture velocity and low frequency ground motions that characterize tsunami earthquakes (e.g. Bilek and Lay, 1999; Pelayo and Wiens, 1992; Satake and Tanioka, 1999). The MFZ may therefore serve as an analogue for the type of setting in which tsunami earthquakes may occur. Of course it should also be considered that the dynamics of an earthquake rupture passing through the Lisan Formation, which has a maximum thickness of ~110 m at its depocentre (Neugebauer et al., 2014), would be strongly influenced by

the properties of the underlying formations, but nevertheless, we suggest that the Lisan faults have played an important role in the transmission of seismic energy to the surface.

We do not rule out the possibility that these faults may have accommodated a significant amount of aseismic slip, but it is not possible to constrain from our field observations what the ratio of seismic to aseismic slip is accommodated by the faults. Micro-scale indicators of seismic versus aseismic slip, which are often sought in field studies of active fault zones (e.g. Bullock et al., 2014; Collettini et al., 2013; Kirkpatrick and Shipton, 2009; Rowe et al., 2012; Smith et al., 2013; Ujiie et al., 2007), may not be discernible in the MFZ for two reasons. First, due to the environmental conditions during deformation, i.e., the low confining pressure and high porosity, the mechanism of deformation is likely to be particulate flow in either case. Therefore the resulting microstructures would be the same. Second, due to the shallow depth of faulting and the low dynamic friction coefficient values of the fluid-saturated clays that are present in the PSZ (e.g. Bullock et al., 2015; Faulkner et al., 2011; Ferri et al., 2010; Ujiie et al., 2013), the amount of frictional heating within the PSZ would not be great enough to significantly alter the chemical and physical properties of slip zone constituents. It may be that macro-scale dragging of sedimentary packages, such as that associated with faults 1.2 (Fig. 4.9a) and 2.4 (Fig. 4.10a), represents periods of aseismic slip.

4.5 *Conclusions*

We have described a set of seismogenic faults with up to m-scale displacements, which deform high-porosity, poorly lithified, ultrafine-grained lake sediments of the Lisan Formation, composed of alternating aragonite and clay-rich clastic laminae. The faults formed under brine-saturated conditions and at burial depths of just a few metres. They comprise a localized PSZ, which is typically up to only a few mm wide; the PSZ accommodates the majority of displacement on the faults. The PSZ is hosted within a fault core, which is surrounded by a damage zone. The widths of the PSZs, fault cores and damage zones increase with increasing fault displacement. Displacement profiles constructed for the faults show that displacement tapers to zero towards the exposed upper tip points of the faults; they also show evidence for mechanical interaction between adjacent and overlapping fault segments. These architectural and geometrical attributes are very similar to those of faults formed in low-porosity, cohesive rocks at greater depth.

However, there is a significant difference between the faults described here and faults formed in low-porosity, cohesive rocks: this is the deformation mechanism. Low-porosity, cohesive rocks in the upper crust typically deform by fracturing and cataclasis, whereas the rocks described herein have deformed via particulate flow and the formation of disaggregation and phyllosilicate bands. This mode of deformation is facilitated by the fine-grained, high-porosity, fluid-saturated and

phyllosilicate-rich nature of the Lisan sediment. This mechanism of deformation is likely to facilitate rupture propagation through the Lisan sediment because: 1) it involves little or no fracturing and 2) it produces slip zones enriched in phyllosilicates. Both of these factors would result in earthquakes rupturing these faults having negligible fracture energy, making it energetically very favourable for earthquakes to propagate all the way to the surface. This interpretation contradicts the traditional conception that poorly lithified sediments in the shallow part of the crust may act as effective barriers to rupture propagation and may go some way to explaining the recently acknowledged large, near-surface co-seismic displacements produced during great earthquakes.

This work adds to the array of previous works conducted on fault zones in shallow, poorly lithified sediments. All of these studies expose subtle but important differences in the style of deformation in poorly lithified materials in the upper few km of the crust. This is due to the fact that deformation mechanisms in the shallowest part of the crust are very sensitive to factors such as grain sorting within sediment, grain shape, grain size, composition and fluid presence, as well as depth. These variations highlight the need to conduct further studies of a similar nature, in order to document the range of faulting styles and behaviours possible in shallow sediments. Insights into the structure of, and deformation mechanisms operating in, shallow crustal fault zones will improve our ability to interpret on-fault palaeoseismic observations and aid a more informed construction of earthquake records. This will subsequently improve our ability to construct scenario earthquake models which allow for more accurate forecasting of earthquakes and an assessment of their associated hazards (Kanamori, 2014). This should be considered a topic of utmost importance, given that earthquakes that rupture through the shallowest part of the crust are typically the most damaging, causing vast amounts of damage to infrastructure and generating devastating tsunamis.

References

Agnon, A., Migowski, C., Marco, S., 2006. Intraclast breccias in laminated sequences reviewed: Recorders of paleo-earthquakes. Geological Society of America Special Papers 401, 195-214.

Allen, J.R.L., 1982. Sedimentary Structures: Their Character and Physical Basis. Elsevier, New York.

Alsop, G., Marco, S., 2011a. Soft-sediment deformation within seismogenic slumps of the Dead Sea Basin. Journal of Structural Geology 33, 433-457.

Alsop, G.I., Marco, S., 2011b. Soft-sediment deformation within seismogenic slumps of the Dead Sea Basin. Journal of Structural Geology 33, 433-457.

Ammon, C.J., Lay, T., Simpson, D.W., 2010. Great earthquakes and global seismic networks. Seismological Research Letters 81, 965-971.

Anders, M.H., Wiltschko, D.V., 1994. Microfracturing, paleostress and the growth of faults. Journal of Structural Geology 16, 795-815.

Antonellini, M.A., Aydin, A., Pollard, D.D., 1994. Microstructure of deformation bands in porous sandstones at Arches National Park, Utah. Journal of structural geology 16, 941-959.
Arkin, Y., Michaeli, L., 1986. The significance of shear strength in the deformation of laminated sediments in the Dead Sea area. Israel Journal of Earth Sciences 35, 61-72.
Arkin, Y., Starinsky, A., 1981. Lisan sediment porosity and porewater as indicators of original Lake Lisan composition. Current Research, Geological Survey of Israel, 83-85.
Aydin, A., Johnson, A., 1978. Development of faults as zones of deformation bands and as slip surfaces in sandstone. pure and applied geophysics 116, 931-942.
Aydin, A., Johnson, A.M., 1983. Analysis of faulting in porous sandstones. Journal of Structural Geology 5, 19-31.
Balsamo, F., Aldega, L., De Paola, N., Faoro, I., Storti, F., 2014. The signature and mechanics of earthquake ruptures along shallow creeping faults in poorly lithified sediments. Geology 42, 435-438.
Balsamo, F., Storti, F., 2010. Grain size and permeability evolution of soft-sediment extensional sub-seismic and seismic fault zones in high-porosity sediments from the Crotone basin, southern Apennines, Italy. Marine and Petroleum Geology 27, 822-837.
Balsamo, F., Storti, F., 2011. Size-dependent comminution, tectonic mixing, and sealing behavior of a "structurally oversimplified" fault zone in poorly lithified sands: Evidence for a coseismic rupture? Geological Society of America Bulletin 123, 601-619.
Bartov, Y., Stein, M., Enzel, Y., Agnon, A., Reches, Z.e., 2002. Lake Levels and Sequence Stratigraphy of Lake Lisan, the Late Pleistocene Precursor of the Dead Sea. Quaternary Research 57, 9-21.
Beeler, N., Tullis, T., Blanpied, M., Weeks, J., 1996. Frictional behavior of large displacement experimental faults. Journal of Geophysical Research 101, 8697-8715.
Behnsen, J., Faulkner, D.R., 2012. The effect of mineralogy and effective normal stress on frictional strength of sheet silicates. Journal of Structural Geology.
Berg, S.S., Skar, T., 2005. Controls on damage zone asymmetry of a normal fault zone: outcrop analyses of a segment of the Moab fault, SE Utah. Journal of Structural Geology 27, 1803-1822.
Bilek, S., Lay, T., 2002. Tsunami earthquakes possibly widespread manifestations of frictional conditional stability. Geophysical Research Letters 29, 18-11-18-14.
Bilek, S.L., Engdahl, E.R., DeShon, H.R., El Hariri, M., 2011. The 25 October 2010 Sumatra tsunami earthquake: Slip in a slow patch. Geophysical Research Letters 38, n/a-n/a.
Bilek, S.L., Lay, T., 1999. Rigidity variations with depth along interplate megathrust faults in subduction zones. Nature 400, 443-446.
Bonilla, M.G., Mark, R.K., Lienkaemper, J.J., 1984. Statistical relations among earthquake magnitude, surface rupture length, and surface fault displacement. Bulletin of the Seismological Society of America 74, 2379-2411.
Borradaile, G.J., 1981. Particulate flow of rock and the formation of cleavage. Tectonophysics 72, 305-321.
Boutareaud, S., Calugaru, D.-G., Han, R., Fabbri, O., Mizoguchi, K., Tsutsumi, A., Shimamoto, T., 2008. Clay-clast aggregates: A new textural evidence for seismic fault sliding? Geophysical Research Letters 35, L05302.
Bullock, R.J., De Paola, N., Holdsworth, R.E., 2015. An experimental investigation into the role of phyllosilicate content on earthquake propagation during seismic slip in carbonate faults. Journal of Geophysical Research submitted.
Bullock, R.J., De Paola, N., Holdsworth, R.E., Trabucho-Alexandre, J., 2014. Lithological controls on the deformation mechanisms operating within carbonate-hosted faults during the seismic cycle. Journal of Structural Geology 58, 22-42.
Byerlee, J., Summers, R., 1976. A note on the effect of fault gouge thickness on fault stability. International Journal of Rock Mechanics and Mining Sciences & Geomechanics Abstracts 13, 35-36.

Caine, J.S., Minor, S.A., 2009. Structural and geochemical characteristics of faulted sediments and inferences on the role of water in deformation, Rio Grande Rift, New Mexico. Geological Society of America Bulletin 121, 1325-1340.
Cashman, S., Cashman, K., 2000. Cataclasis and deformation-band formation in unconsolidated marine terrace sand, Humboldt County, California. Geology 28, 111-114.
Cashman, S.M., Baldwin, J.N., Cashman, K.V., Swanson, K., Crawford, R., 2007. Microstructures developed by coseismic and aseismic faulting in near-surface sediments, San Andreas fault, California. Geology 35, 611-614.
Chester, F.M., Chester, J.S., 1998. Ultracataclasite structure and friction processes of the Punchbowl fault, San Andreas system, California. Tectonophysics 295, 199-221.
Childs, C., Manzocchi, T., Walsh, J.J., Bonson, C.G., Nicol, A., Schöpfer, M.P.J., 2009. A geometric model of fault zone and fault rock thickness variations. Journal of Structural Geology 31, 117-127.
Collettini, C., Niemeijer, A., Viti, C., Smith, S.A.F., Marone, C., 2011. Fault structure, frictional properties and mixed-mode fault slip behavior. Earth and Planetary Science Letters 311, 316-327.
Collettini, C., Viti, C., Tesei, T., Mollo, S., 2013. Thermal decomposition along natural carbonate faults during earthquakes. Geology 41, 927-930.
De Joussineau, G., Aydin, A., 2007. The evolution of the damage zone with fault growth in sandstone and its multiscale characteristics. Journal of Geophysical Research: Solid Earth (1978–2012) 112.
Delouis, B., Nocquet, J.M., Vallée, M., 2010. Slip distribution of the February 27, 2010 Mw= 8.8 Maule earthquake, central Chile, from static and high-rate GPS, InSAR, and broadband teleseismic data. Geophysical Research Letters 37.
Dziewonski, A.M., Ekström, G., Salganik, M.P., 1997. Centroid-moment tensor solutions for October–December 1995. Physics of the Earth and Planetary Interiors 101, 1-12.
El-Isa, Z., Mustafa, H., 1986. Earthquake deformations in the Lisan deposits and seismotectonic implications. Geophysical Journal International 86, 413-424.
Evans, J.P., Bradbury, K.K., 2007. Fractured dirt: Deformation textures and processes in sediment and other unconsolidated deposits. Geology 35, 671-672.
Faulkner, D., Jackson, C., Lunn, R., Schlische, R., Shipton, Z., Wibberley, C., Withjack, M., 2010. A review of recent developments concerning the structure, mechanics and fluid flow properties of fault zones. Journal of Structural Geology 32, 1557-1575.
Faulkner, D.R., Mitchell, T.M., Behnsen, J., Hirose, T., Shimamoto, T., 2011. Stuck in the mud? Earthquake nucleation and propagation through accretionary forearcs. Geophysical Research Letters 38, L18303.
Ferri, F., Di Toro, G., Hirose, T., Shimamoto, T., 2010. Evidence of thermal pressurization in high-velocity friction experiments on smectite-rich gouges. Terra Nova 22, 347-353.
Ferrill, D.A., Morris, A.P., Sims, D.W., Waiting, D.J., Hasegawa, S., 2005. Development of synthetic layer dip adjacent to normal faults.
Fialko, Y., Sandwell, D., Simons, M., Rosen, P., 2005. Three-dimensional deformation caused by the Bam, Iran, earthquake and the origin of shallow slip deficit. Nature 435, 295-299.
Fisher, Q., Knipe, R., 2001. The permeability of faults within siliciclastic petroleum reservoirs of the North Sea and Norwegian Continental Shelf. Marine and Petroleum Geology 18, 1063-1081.
Fisher, Q., Knipe, R.J., 1998. Fault sealing processes in siliciclastic sediments. Geological Society, London, Special Publications 147, 117-134.
Fossen, H., 2010. Structural geology. Cambridge University Press.
Fossen, H., Schultz, R.A., Shipton, Z.K., Mair, K., 2007. Deformation bands in sandstone: a review. Journal of the Geological Society 164, 755-769.
Fossum, A., Freund, L., 1975. Nonuniformly moving shear crack model of a shallow focus earthquake mechanism. Journal of Geophysical Research 80, 3343-3347.
Freund, R., Zak, I., Garfunkel, Z.W.I., 1968. Age and Rate of the Sinistral Movement along the Dead Sea Rift. Nature 220, 253-255.

Garfunkel, Z., 1981. Internal structure of the Dead Sea leaky transform (rift) in relation to plate kinematics. Tectonophysics 80, 81-108.
Geller, R.J., 1976. Scaling relations for earthquake source parameters and magnitudes. Bulletin of the Seismological Society of America 66, 1501-1523.
Hall, J.K., 1994. Digital shaded-relief map of Israel and environs 1:500,000.
Hamiel, Y., Amit, R., Begin, Z.B., Marco, S., Katz, O., Salamon, A., Zilberman, E., Porat, N., 2009. The Seismicity along the Dead Sea Fault during the Last 60,000 Years. Bulletin of the Seismological Society of America 99, 2020-2026.
Heifetz, E., Agnon, A., Marco, S., 2005. Soft sediment deformation by Kelvin Helmholtz Instability: A case from Dead Sea earthquakes. Earth and Planetary Science Letters 236, 497-504.
Heynekamp, M.R., Goodwin, L.B., Mozley, P.S., Haneberg, W.C., 1999. Controls on Fault-Zone Architecture in Poorly Lithified Sediments, Rio Grande Rift, New Mexico: Implications for Fault-Zone Permeability and Fluid Flow. Faults and subsurface fluid flow in the shallow crust, 27-49.
IAEA, 2010 Chapter 8: Potential for Fault Displacement at the Site, In: Seismic Hazards in Site Evaluation for Nuclear Installations. International Atomic Energy Agency, Viena, Austria.
Ide, S., Baltay, A., Beroza, G.C., 2011. Shallow Dynamic Overshoot and Energetic Deep Rupture in the 2011 Mw 9.0 Tohoku-Oki Earthquake. Science 332, 1426-1429.
Ikari, M.J., Marone, C., Saffer, D.M., 2011. On the relation between fault strength and frictional stability. Geology 39, 83-86.
Ikari, M.J., Saffer, D.M., Marone, C., 2009. Frictional and hydrologic properties of clay-rich fault gouge. Journal of Geophysical Research 114, B05409.
Johansen, T.E.S., Fossen, H., 2008. Internal geometry of fault damage zones in interbedded siliciclastic sediments. Geological Society, London, Special Publications 299, 35-56.
Johansen, T.E.S., Fossen, H., Kluge, R., 2005. The impact of syn-faulting porosity reduction on damage zone architecture in porous sandstone: an outcrop example from the Moab Fault, Utah. Journal of Structural Geology 27, 1469-1485.
Kanamori, H., 1972. Mechanism of tsunami earthquakes. Physics of the earth and planetary interiors 6, 346-359.
Kanamori, H., 2014. The Diversity of Large Earthquakes and Its Implications for Hazard Mitigation. Annual Review of Earth and Planetary Sciences 42, 7-26.
Kanamori, H., Rivera, L., 2006. Energy partitioning during an earthquake. Earthquakes: Radiated Energy and the Physics of Faulting, 3-13.
Kirkpatrick, J., Shipton, Z., 2009. Geologic evidence for multiple slip weakening mechanisms during seismic slip in crystalline rock. Journal of Geophysical Research: Solid Earth (1978–2012) 114.
Kristensen, M.B., Childs, C., Olesen, N.Ø., Korstgård, J.A., 2013. The microstructure and internal architecture of shear bands in sand–clay sequences. Journal of Structural Geology 46, 129-141.
Lay, T., 2015. The surge of great earthquakes from 2004 to 2014. Earth and Planetary Science Letters 409, 133-146.
Lay, T., Ammon, C., Kanamori, H., Koper, K., Sufri, O., Hutko, A., 2010. Teleseismic inversion for rupture process of the 27 February 2010 Chile (Mw 8.8) earthquake. Geophysical Research Letters 37.
Lay, T., Ammon, C., Kanamori, H., Yamazaki, Y., Cheung, K., Hutko, A., 2011. The 25 October 2010 Mentawai tsunami earthquake (Mw 7.8) and the tsunami hazard presented by shallow megathrust ruptures. Geophysical Research Letters 38.
Loveless, S., Bense, V., Turner, J., 2011. Fault architecture and deformation processes within poorly lithified rift sediments, Central Greece. Journal of Structural Geology 33, 1554-1568.
Maltman, A.J., 1987. Shear zones in argillaceous sediments—an experimental study. Geological Society, London, Special Publications 29, 77-87.
Marco, S., 2007. Temporal variation in the geometry of a strike–slip fault zone: Examples from the Dead Sea Transform. Tectonophysics 445, 186-199.

Marco, S., Agnon, A., 1995. Prehistoric earthquake deformations near Masada, Dead Sea graben. Geology 23, 695-698.
Marco, S., Agnon, A., 2005. High-resolution stratigraphy reveals repeated earthquake faulting in the Masada Fault Zone, Dead Sea Transform. Tectonophysics 408, 101-112.
Marco, S., Agnon, A., Bruner, I., Landa, E., Ron, H., 1996a. The Masada fault zone (Dead Sea Graben) in outcrop and geophysical images. Institute for Petroleum Research and Geophysics P54/180/95.
Marco, S., Stein, M., Agnon, A., Ron, H., 1996b. Long-term earthquake clustering: A 50,000-year paleoseismic record in the Dead Sea Graben. Journal of Geophysical Research: Solid Earth (1978–2012) 101, 6179-6191.
Marco, S., Weinberger, R., Agnon, A., 2002. Radial clastic dykes formed by a salt diapir in the Dead Sea Rift, Israel. Terra Nova 14, 288-294.
Marone, C., 1998. Laboratory-derived friction laws and their application to seismic faulting. Annual Review of Earth and Planetary Sciences 26, 643-696.
Marone, C., Raleigh, C.B., Scholz, C., 1990. Frictional behavior and constitutive modeling of simulated fault gouge. J. geophys. Res 95, 7007-7025.
Marone, C., Scholz, C., 1988. The depth of seismic faulting and the upper transition from stable to unstable slip regimes. Geophysical Research Letters 15, 621-624.
Marone, C.J., Scholtz, C., Bilham, R., 1991. On the mechanics of earthquake afterslip. Journal of Geophysical Research: Solid Earth (1978–2012) 96, 8441-8452.
Marques, F.O., Burg, J.P., Lechmann, S.M., Schmalholz, S.M., 2010. Fluid-assisted particulate flow of turbidites at very low temperature: A key to tight folding in a submarine Variscan foreland basin of SW Europe. Tectonics 29, n/a-n/a.
Minor, S.A., Hudson, M.R., 2006. Regional survey of structural properties and cementation patterns of fault zones in the northern part of the Albuquerque basin, New Mexico--implications for ground-water flow.
Mitchell, T., Faulkner, D., 2009. The nature and origin of off-fault damage surrounding strike-slip fault zones with a wide range of displacements: a field study from the Atacama fault system, northern Chile. Journal of Structural Geology 31, 802-816.
Neugebauer, I., Brauer, A., Schwab, M.J., Waldmann, N.D., Enzel, Y., Kitagawa, H., Torfstein, A., Frank, U., Dulski, P., Agnon, A., Ariztegui, D., Ben-Avraham, Z., Goldstein, S.L., Stein, M., 2014. Lithology of the long sediment record recovered by the ICDP Dead Sea Deep Drilling Project (DSDDP). Quaternary Science Reviews 102, 149-165.
Pelayo, A.M., Wiens, D.A., 1992. Tsunami earthquakes: Slow thrust-faulting events in the accretionary wedge. Journal of Geophysical Research: Solid Earth (1978–2012) 97, 15321-15337.
Quennell, A.M., 1958. The structural and geomorphic evolution of the dead sea rift. Quarterly Journal of the Geological Society 114, 1-24.
Rawling, G.C., Goodwin, L.B., 2006. Structural record of the mechanical evolution of mixed zones in faulted poorly lithified sediments, Rio Grande rift, New Mexico, USA. Journal of Structural Geology 28, 1623-1639.
Rawling, G.C., Goodwin, L.B., Wilson, J.L., 2001. Internal architecture, permeability structure, and hydrologic significance of contrasting fault-zone types. Geology 29, 43-46.
Reches, Z.e., Lockner, D.A., 1994. Nucleation and growth of faults in brittle rocks. Journal of Geophysical Research: Solid Earth 99, 18159-18173.
Rempe, M., Smith, S.A.F., Ferri, F., Mitchell, T.M., Di Toro, G., 2014. Clast-cortex aggregates in experimental and natural calcite-bearing fault zones. Journal of Structural Geology 68, Part A, 142-157.
Reznik, I.J., Gavrieli, I., Ganor, J., 2009. Kinetics of gypsum nucleation and crystal growth from Dead Sea brine. Geochimica et Cosmochimica Acta 73, 6218-6230.
Rowe, C.D., Fagereng, Å., Miller, J.A., Mapani, B., 2012. Signature of coseismic decarbonation in dolomitic fault rocks of the Naukluft Thrust, Namibia. Earth and Planetary Science Letters 333–334, 200-210.

Sagy, A., Reches, Z.e., Agnon, A., 2003. Hierarchic three-dimensional structure and slip partitioning in the western Dead Sea pull-apart. Tectonics 22.
Satake, K., Tanioka, Y., 1999. Sources of tsunami and tsunamigenic earthquakes in subduction zones, Seismogenic and Tsunamigenic Processes in Shallow Subduction Zones. Springer, pp. 467-483.
Scholz, C.H., 1998. Earthquakes and friction laws. Nature 391, 37-42.
Scholz, C.H., Dawers, N.H., Yu, J.Z., Anders, M.H., Cowie, P.A., 1993. Fault growth and fault scaling laws: Preliminary results. Journal of Geophysical Research: Solid Earth 98, 21951-21961.
Schramm, A., Stein, M., Goldstein, S., 2000. Calibration of the 14 C time scale to 50 kyr by 234 U-230 Th dating of sediments from Lake Lisan (the paleo-Dead Sea): earth Planet. Sci Lett 175, 27-40.
Schultz, R., Siddharthan, R., 2005. A general framework for the occurrence and faulting of deformation bands in porous granular rocks. Tectonophysics 411, 1-18.
Shipton, Z.K., Cowie, P.A., 2003. A conceptual model for the origin of fault damage zone structures in high-porosity sandstone. Journal of Structural Geology 25, 333-344.
Shipton, Z.K., Soden, A.M., Kirkpatrick, J.D., Bright, A.M., Lunn, R.J., 2006. How thick is a fault? Fault displacement-thickness scaling revisited. Geophysical Monograph Series 170, 193-198.
Sibson, R.H., 2003. Thickness of the seismic slip zone. Bulletin of the Seismological Society of America 93, 1169-1178.
Smith, S., Di Toro, G., Kim, S., Ree, J.H., Nielsen, S., Billi, A., Spiess, R., 2013. Coseismic recrystallization during shallow earthquake slip. Geology 41, 63-66.
Smith, S.A.F., Billi, A., Toro, G.D., Spiess, R., 2011. Principal slip zones in limestone: microstructural characterization and implications for the seismic Cycle (Tre Monti Fault, Central Apennines, Italy). Pure and Applied Geophysics 168, 2365-2393.
Tembe, S., Lockner, D.A., Wong, T.F., 2010. Effect of clay content and mineralogy on frictional sliding behavior of simulated gouges: Binary and ternary mixtures of quartz, illite, and montmorillonite. Journal of geophysical Research 115, B03416.
Tesei, T., Collettini, C., Carpenter, B.M., Viti, C., Marone, C., 2012. Frictional strength and healing behavior of phyllosilicate-rich faults. Journal of Geophysical Research 117, B09402.
Ujiie, K., Tanaka, H., Saito, T., Tsutsumi, A., Mori, J.J., Kameda, J., Brodsky, E.E., Chester, F.M., Eguchi, N., Toczko, S., 343, E., Scientists, T., 2013. Low Coseismic Shear Stress on the Tohoku-Oki Megathrust Determined from Laboratory Experiments. Science 342, 1211-1214.
Ujiie, K., Yamaguchi, A., Kimura, G., Toh, S., 2007. Fluidization of granular material in a subduction thrust at seismogenic depths. Earth and Planetary Science Letters 259, 307-318.
Vermilye, J.M., Scholz, C.H., 1998. The process zone: A microstructural view of fault growth. Journal of Geophysical Research: Solid Earth 103, 12223-12237.
Walker, R., Holdsworth, R., Imber, J., Faulkner, D., Armitage, P., 2013. Fault zone architecture and fluid flow in interlayered basaltic volcaniclastic-crystalline sequences. Journal of Structural Geology 51, 92-104.
Walsh, J.J., Watterson, J., 1991. Geometric and kinematic coherence and scale effects in normal fault systems. Geological Society, London, Special Publications 56, 193-203.
Wells, D.L., Coppersmith, K.J., 1994. New empirical relationships among magnitude, rupture length, rupture width, rupture area, and surface displacement. Bulletin of the Seismological Society of America 84, 974-1002.
Wesnousky, S.G., 1988. Seismological and structural evolution of strike-slip faults. Nature 335, 340-343.
Wetzler, N., Marco, S., Heifetz, E., 2010. Quantitative analysis of seismogenic shear-induced turbulence in lake sediments. Geology 38, 303-306.
White, S., Knipe, R., 1978. Transformation-and reaction-enhanced ductility in rocks. Journal of the Geological Society 135, 513-516.

Wilson, J.E., Chester, J.S., Chester, F.M., 2003. Microfracture analysis of fault growth and wear processes, Punchbowl Fault, San Andreas system, California. Journal of Structural Geology 25, 1855-1873.
Yielding, G., Freeman, B., Needham, D.T., 1997. Quantitative fault seal prediction. AAPG bulletin 81, 897-917.
Zohar, M., Marco, S., 2012. Re-estimating the epicenter of the 1927 Jericho earthquake using spatial distribution of intensity data. Journal of Applied Geophysics 82, 19-29.

Chapter 5

The frictional properties and deformation mechanisms of faults in near-surface, poorly lithified sediments: implications for rupture propagation in the shallow crust

Abstract

In order to improve our understanding of the factors that control rupture propagation to the surface it is critical to constrain the frictional properties and deformation mechanisms of shallow-crustal fault zones cutting through poorly lithified sediments. We designed a set of rotary shear friction experiments, on synthetic gouges containing ultrafine-grained aragonite and clay-rich clastic detritus, derived from poorly lithified sediments collected from the seismogenic Masada fault zone in Israel. We investigated their frictional stability and healing behaviour by performing low-velocity (0-130 μm/s, displacements up to 0.42m) rate-and-state friction experiments, and the evolution of their coseismic frictional strength by performing high-velocity (1.3 m/s, displacements up to 40 m) friction experiments, at normal loads of 1-18 MPa (equivalent to a depth range of 0.05-1 km), and under room-humidity, water-saturated and brine-saturated conditions. Microstructural analyses were performed on deformed gouges to determine whether there is a link between frictional behaviour and deformation mechanisms/microstructure.

During low-velocity experiments at 1 MPa, all gouges behave in a velocity-strengthening manner, particularly when fluid-saturated. The dominant deformation mechanism in these gouges is distributed particulate flow. During high-velocity experiments at 1 MPa, all gouges have large slip-weakening distances of >16 m. The dominant deformation mechanism is again distributed particulate flow. During low-velocity experiments at 18 MPa, a transition to velocity-weakening behaviour is observed in the room-humidity and water-saturated gouges at displacements >~15 cm, corresponding to the formation of through-going Y-shears within the gouge. However, the brine-saturated gouge remains velocity-strengthening throughout. The dominant deformation mechanism in these gouges is distributed cataclasis. During high-velocity experiments at 9 and 18 MPa, all gouges exhibit small slip-weakening distances of <1.7 m for dry gouges, and <<0.1 m for fluid-saturated gouges, which also exhibit low fracture energy. The dominant deformation mechanism is localized cataclasis in the dry gouge, with evidence for frictional heating to temperatures >720˚C, and distributed particulate flow in the fluid-saturated gouges, with no evidence of significant frictional heating. Slide-hold-slide tests show that frictional healing rates increase with accumulated displacement and are greater at 1 MPa than at 18 MPa, and in the fluid-saturated gouges compared to the dry gouges.

Our results show that frictional behaviour and deformation mechanisms are not simply a function of depth or strain-rate or fluid presence, but depend on complex interactions between these different environmental factors. Therefore, linking certain microstructures to a certain type of frictional behaviour should be avoided. In particular, the fact that the fluid-saturated gouges deform

via the same mechanism (particulate flow) at both sub-seismic and seismic slip velocities, suggests that it is not possible to use microstructural observations alone to differentiate seismic from aseismic fault gouges in shallow-crustal, fluid-saturated fault zones. In terms of rupture propagation, our results suggest that although faults in poorly lithified sediments very close to the Earth's surface (<0.05 km depth) may act as barriers to rupture propagation, seismic ruptures propagating from greater depth (0.5-1 km) may have enough energy to overcome such a barrier. The high healing rates of the gouges at 1 MPa imply that faults at shallow depth will remain locked during the interseismic period, which will also enhance their potential to fail during future earthquakes. Our results thus go some way towards explaining the common occurrence of surface-rupturing earthquakes.

5.1 *Introduction*

According to rate-and-state friction theory, earthquakes should only nucleate in regions of the crust formed by materials which exhibit velocity-weakening behaviour, a condition which is unstable and a pre-requisite for the stick-slip behaviour associated with earthquake nucleation (e.g. Brace and Byerlee, 1966; Dieterich and Kilgore, 1996; Scholz, 1998). It is therefore generally believed that earthquakes cannot nucleate in regions of the crust occupied by materials which are velocity-strengthening, a condition which is intrinsically stable and favours fault creep (Scholz, 1998). In addition, if an earthquake propagates into a velocity-strengthening region of the crust, it should lead to a negative stress drop, which will slow down and maybe even terminate the rupture if the velocity jump is not great enough to destabilize the system (Scholz, 1998).

The majority of earthquakes nucleate in the approximate depth range 5-15 km, in the case of continental earthquakes, or 10-40 km, in the case of subduction zone earthquakes (Scholz, 1998). It is consequently believed that rocks in these depth ranges exhibit predominantly velocity-weakening behaviour. Earthquake distribution data show that there is often a cut-off in seismicity above and below these depth ranges (Scholz, 1998). The lower cut-off is attributed to increasing temperature with depth, which brings about a transition from unstable to stable slip, corresponding to the onset of crystal-plastic deformation (Sibson, 1977; Sibson, 1989; Tse and Rice, 1986). The upper cut-off has been attributed to the fact that the upper few km of fault zones are typically occupied by either unconsolidated sedimentary packages or incohesive fault gouges (Marone and Scholz, 1988); experimental results have shown that thick gouge layers tend to exhibit velocity-strengthening behaviour, because of their ability to dilate during shear (Byerlee and Summers, 1976; Engelder et al., 1975; Marone et al., 1990). It is also supported by seismologic data, which show a clear correlation of the upper cut-off in seismicity with the base of thick sedimentary packages for a

number of large and well-documented continental earthquakes (Marone and Scholz, 1988 and references therein). Fault gouge zones in the upper crust also tend to be rich in phyllosilicates, which again have been shown experimentally to be predominantly velocity-strengthening (e.g. Ikari et al., 2009; Tembe et al., 2010; Tesei et al., 2012), adding to the widely held view that the shallow portions of fault zones should deform predominantly aseismically.

Subsequently, earthquake prediction models often consider that where the shallow portions of fault zones are occupied by unconsolidated/poorly lithified and/or phyllosilicate-rich sediments/gouges, these materials may act as barriers to rupture propagation, reducing the potential for surface rupturing and inherent seismic hazard. However, advances in technology and the acquisition of seismological data over the past decade (Kanamori, 2014; Lay, 2015) have shown that 'great' tsunamigenic earthquakes, such as the 2010 M_w 8.8 Maule, Chile (Delouis et al., 2010; Lay et al., 2010) and 2011 M_w 9.0 Tohoku, Japan (Ide et al., 2011) events, are associated with large patches of co-seismic slip (of up to 60 m in the case of Tohoku) located very close to the sea-floor in parts of the accretionary wedge which were previously assumed to be creeping and stable. In addition, it has been observed that so-called 'tsunami earthquakes', which are characterized by large slip for a given seismic moment, slow rupture velocity and low frequency seismic radiation, can nucleate at, and rupture very shallow depths (<15 km) (Bilek and Lay, 2002; Kanamori, 1972). An example is the 2010 M_w 7.8 Mentawai earthquake, which nucleated within and ruptured the very shallow portion of the megathrust up-dip from the 2007 M_w 8.5 Sumatra earthquake (Bilek et al., 2011; Lay et al., 2011). Given the devastation caused by surface-rupturing events, there is a clear need for us to better constrain the mechanical and frictional behaviour of sediments in the shallow portion of the crust so as to improve our understanding of what factors control, or affect, the propagation of earthquake ruptures towards the surface.

Seeing as the majority of large, surface-rupturing earthquakes occur at subduction zones, field exposures of seismogenic, surface-rupturing faults are uncommon. However, in Chapter 4, we described the structures and deformation mechanisms of faults of the Masada fault zone (MFZ), a part of the Dead Sea fault system in Israel. These faults deform poorly lithified lake sediments belonging to the Lisan Formation, which comprise alternating 1-3 mm thick laminae of ultrafine-grained aragonite and clay-rich clastic detritus. The faults formed at just a few metres depth and are known to have hosted seismic events which ruptured the surface (Marco and Agnon, 1995). They therefore provide an ideal opportunity to study the processes which may facilitate the propagation of earthquakes through shallow, poorly lithified sediments. To this end, we designed a set of rotary shear friction experiments to be performed on synthetic gouges derived from the Lisan sediment, collected from the MFZ. The aim of this experimental study is to investigate how the frictional

behaviour and deformation mechanisms of faults in near-surface, poorly lithified sediments vary as a function of: 1) depth, by varying the applied normal load from 1 to 18 MPa; 2) fluid presence and composition, by deforming gouges under room-humidity, water-saturated and brine-saturated conditions; and 3) displacement, by subjecting gouges to incremental displacements of up to almost 40 m.

5.2 *Experimental setup*

Experiments were performed using the low- to high-velocity rotary shear apparatus at Durham University, UK (Chapter 1, Section 1.3.4.1). Synthetic gouges were prepared for testing by disaggregating undeformed samples of the Lisan sediment collected in the field. We passed the disaggregated material through a 1 mm sieve, to remove anomalously large grains or aggregates, such as late-stage mineralisation crystals (predominantly gypsum) and fragments of fossil wood, and to ensure that all experiments had a reasonably consistent starting grain size. X-Ray diffraction (XRD) analyses of the material which passed through the sieve, and of the residual material that did not, show that their compositions are almost identical and thus the sieving process did not result in a biased sampling of finer-grained components of the sediment (Appendix 2.1). The gouge is composed predominantly of aragonite and clays, which comprise between 40-60% and 30-50% of the deformed gouges, respectively, plus small amounts (up to 10%) of gypsum, quartz and calcite. Separate XRD analysis of the clay fraction (<2 μm grain size) shows that it comprises mixed layer illite-smectite and kaolinite (Appendix 2.1). The aragonite crystals, which comprise the majority of clasts within the gouge, have an ultrafine grain size of <15 μm and distinctive acicular habits, which are sometimes radially arranged in rosette-type structures (Fig. 5.1). The less frequent

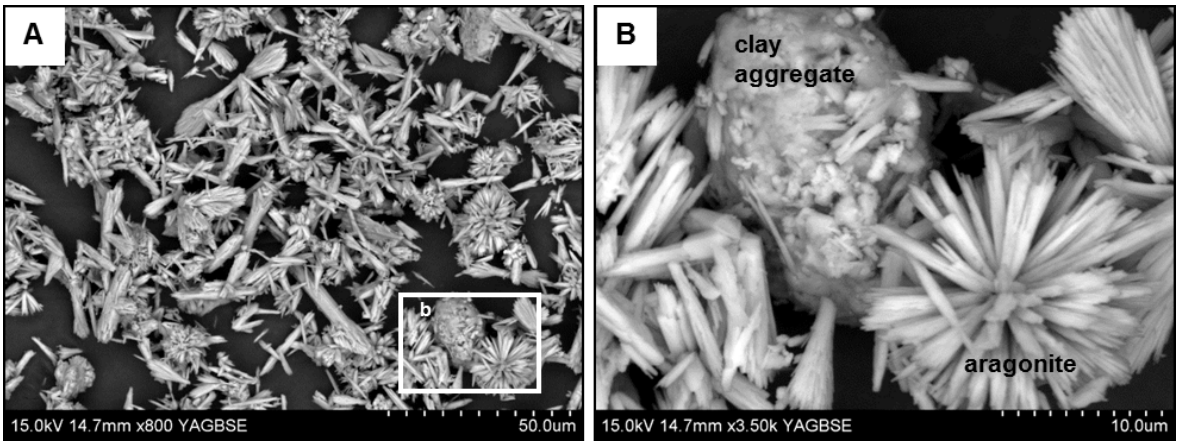

Figure 5.1 a) SEM image of the sieved gouge used for the experiments. **b)** Higher magnification image of the boxed area in fig. **a**. It is evident from both images that clay aggregates and radial arrangements of acicular aragonite crystals retain their structures, so have not been disturbed or damaged during the disaggregation and sieving process.

clasts of gypsum, quartz and calcite have grain sizes up to 100 μm. The reason for using a relatively coarse 1 mm sieve was to minimise disruption and damage to individual grains and aggregates. Scanning electron microscope images of the sieved gouge (Fig. 5.1) confirm that the acicular aragonite crystals are un-damaged by sieving and retain their radial arrangements; they therefore closely resemble the natural state of the Lisan material (see Chapter 4).

Samples were assembled for testing by sandwiching 1.4 g of gouge (or 1.0 g of gouge for fluid-saturated gouges, to allow for volume increase) between two steel cylinders of 25 mm diameter. The surfaces of the steel cylinders are grooved to a depth of 500 μm in a gridded fashion, to ensure that slip localizes within the gouge layer, rather than along the gouge-cylinder boundaries. The gouge is confined by fixing a Teflon ring around the sample assembly (Mizoguchi et al., 2007) (see Chapter 1, Section 1.3.4.2). The sample is then set within the vertical loading frame of the apparatus, in which the lower cylinder remains stationary whilst the upper cylinder is rotated by a servomotor (see Chapter 1, Section 1.3.4.1).

An axial load is applied from the base of the loading frame via a pneumatic Bellofram cylinder. The axial load system is equipped with a high-precision (resolution = ±0.005 kN) air regulator to reduce and automatically correct any load fluctuations, including those due to pore-fluid pressurization, during the experiments. After application of the normal load, all samples were held for 3 minutes prior to shearing to allow for an initial phase of compaction and permeation of fluids through the gouge layer. Axial displacement during the experiments is measured using a linear variable differential transformer (LVDT) with a resolution of $\pm 2*10^{-3}$ mm.

Experiments were manually controlled; under manual operation the apparatus can accelerate to its maximum peripheral target slip rate of 2m/s at a rate of 3.6-4.8 m/s^2 at normal stresses of 3 and 18 MPa, respectively. Shear stress during the experiments is measured using compression load cells attached to an arm-type torque meter with a resolution of $\pm 5*10^{-4}$ kN. Values of the friction coefficient are then calculated as the measured shear stress, τ, divided by the applied normal load, σ_n, according to the equation:

$$\tau = \mu\sigma_n + c \qquad (1)$$

(Byerlee, 1978; Handin, 1969), where c is cohesion, which is assumed to be negligible in our experiments due to the unconsolidated nature of the gouge (Handin, 1969). Output values were recorded by a data logger at a sampling frequency of 100 Hz for low-velocity (v ≤130 μm/s) experiments and 1 KHz for high-velocity (v = 1.3 m/s) experiments.

Because of the cylindrical shape of the samples, slip rate, v increases with sample radius, r ($v = 2\pi Rr/60$ *m/s*, where R is the revolution rate of the motor in RPM). Therefore, the slip rates experienced by the gouges are calculated as an "equivalent slip rate", V_e, at $2/3r$ (Hirose and Shimamoto, 2005; Shimamoto and Tsutsumi, 1994):

$$V_e = \frac{4\pi Rr}{3\times 60} \qquad (2).$$

From here on, we refer to the equivalent slip rate simply as the slip rate, v, and the displacement, d, is calculated as

$$d = V_e t \qquad (3),$$

where t is the time.

Experiments were conducted at room temperature, and each experiment was performed under either room-humidity, water-saturated or brine-saturated conditions. 0.45 ml of de-ionized water was used to saturate the gouges for the water-saturated experiments, and 0.45 ml of brine collected from the Dead Sea was used for the brine-saturated experiments, chosen to best assimilate the composition of the brine interacting with the naturally deformed Lisan sediments. This is a hypersaline brine, with a salinity of ~345 g/l, which is approximately one order of magnitude greater than the salinity of sea water (Reznik et al., 2009). The composition is also significantly different to that of sea water, as it is relatively enriched in Cl^-, Br^-, Mg^{2+}, Ca^{2+} and K^+ ions and depleted in Na^+ and SO_4^{2-} ions (Reznik et al., 2009). Each experiment was also run at both 1 MPa and 18 MPa normal load and, in the case of the high-velocity experiments, we included an additional set of experiments at an intermediate normal load of 9 MPa. The 1 MPa normal load experiments are the most representative of the ambient conditions during deformation of the naturally observed Lisan faults, corresponding to ~50 m burial depth of sediment with no overlying water column, or surficial sediments with an overlying water column of ~100 m depth. The 18 MPa experiments correspond to a sediment burial depth of ~1 km and allow us to assess how sensitive frictional behaviour is to burial depth in the uppermost part of the crust. Details of the experiments for which results are described herein are presented in Table 1. Details and results of additional experiments, performed to check for data reproducibility, can be found in Appendices 2.2 and 2.3.

It should be noted that the experimental configuration does not enable us to measure variations in pore fluid pressure, temperature or gas emissions during our experiments. Such variations would likely be negligible during low-velocity experiments (e.g. Ikari et al., 2009). However, they would be much more significant during the high-velocity experiments. For example, a greater amount of

frictional heat would be generated when sliding at faster velocities and the amount of pore-fluid pressurization would be greater due to a more rapidly applied shear-induced compaction, and due to thermal pressurization and possible triggering of decarbonation/dehydration reactions. Therefore, in this manuscript we do not attempt to speculate on the dynamic weakening mechanisms that may be in operation during the high-velocity experiments. Instead, we rely on microstructural observations of the deformed gouges to explain differences in mechanical behaviour and their implications for fault seismicity.

Deformed gouges were recovered at the end of each experiment in order to examine microstructures produced during shearing. Samples were prepared by slicing at ~2/3 of the radius of our cylindrical samples, to make observations consistent with the calculated values of velocity and displacement, in an orientation normal to the shear plane and tangential to the direction of rotary shear. In addition to examining the microstructure of sheared samples, we also examined the microstructure of the samples post-compaction (i.e. after application of the normal load) but prior to shearing, in order to check for any differences in the initial microstructure of the gouges, which may affect their mechanical behaviour during shearing (as per Chapter 3).Thin sections were analysed using a Hitachi SU-70 field emission SEM at the G.J. Russell microscopy facility, Durham University.

Exp. #	Conditions	σ_n	Total displacement (m)
Low-velocity			
508	room-humidity	1	0.34
607	water-saturated	1	0.35
518	brine-saturated	1	0.36
608	room-humidity	18	0.38
611	water-saturated	18	0.42
522	brine-saturated	18	0.41
High-velocity			
532	room-humidity	1	36.77
534	water-saturated	1	39.03
535	brine-saturated	1	33.35
624	room-humidity	9	4.6
625	water-saturated	9	2.12
627	brine-saturated	9	1.07
519	room-humidity	18	0.72
520	water-saturated	18	1.08
521	brine-saturated	18	2.25

Table 5.1 Summarised details of the experiments for which results are presented.

5.2.1 *Experimental procedure: low-velocity*

Low-velocity experiments commenced with a run-in phase at a velocity of 13 μm/s. During this phase, the gouges undergo strain-hardening before steady-state sliding is attained. Once friction had reached steady-state, we imposed two sets of velocity-step followed by slide-hold-slide tests on the gouges, and then a further four sets of velocity-step tests (Fig. 5.2). Each set of tests was separated by a period of displacement accumulation of ~ 6 cm, sliding at 130 μm/s, so that we could investigate how frictional behaviour evolves as a function of increasing displacement. The total displacement during the low-velocity experiments was therefore in the range of 0.34-0.44 m, depending on the amount of sliding necessary before a steady-state was established (which was greatest in the gouges deformed at higher normal load). These displacements are equivalent to those of moderate-displacement faults in the Lisan Formation, and may be considered more representative of earthquake-hosting faults than the majority of rate-and-state friction experiments, which are often performed in a direct shear configuration where displacements are limited to a few

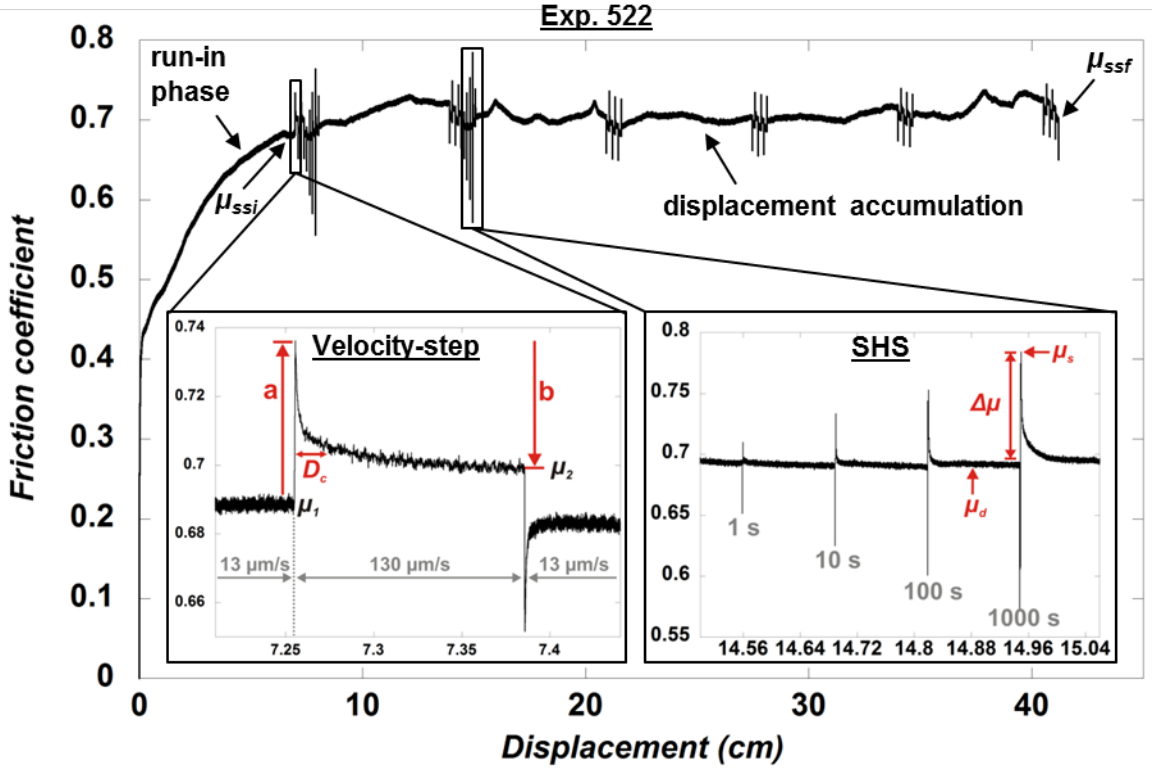

Figure 5.2 Example of a typical friction vs. displacement curve produced during a low-velocity experiment, with the key stages of the experiment labelled. μ_{ssi} and μ_{ssf} mark the locations where the values of the initial and final steady-state sliding friction coefficients are measured. Note that the gouge undergoes several alternating phases of strain-hardening and strain-weakening over the course of the experiment. Insets show examples of a velocity-step test and a slide-hold-slide (SHS) test, with the key parameters labelled. See text for full explanation.

tens of mm.

Each set of velocity-step tests involved a manually imposed instantaneous increase in velocity from 13 μm/s to 130 μm/s (Fig. 5.2). Each step was imposed for 10 s, equivalent to 1.3 mm of shear displacement, after which the velocity was instantaneously decelerated back to 13 μm/s. 100 s later, again equivalent to 1.33 mm of displacement, a second velocity-step of the same nature was imposed. Upon the initial increase in velocity, there is an increase *a* in friction, known as the direct effect, which is followed by an evolutionary decrease *b* in friction over a critical slip distance D_c (Fig. 5.2) (e.g. Marone, 1998b; Scholz, 1998). The velocity-dependence of friction is quantified using the friction rate parameter *(a-b)*, which is defined as:

$$a - b = \frac{\Delta\mu_{ss}}{\ln(V/V_0)} \qquad (4)$$

where $\Delta\mu_{ss}$ is the change in the steady-state friction coefficient (equivalent to μ_2-μ_1 on the inset in Fig. 5.2) when the sample is subject to an instantaneous change in sliding velocity from V_0 to V (e.g. Marone, 1998b; Scholz, 1998). (a-b) values provide a measure of the frictional stability of a sample. If (a–b) <0, then a sample is velocity-weakening, and if (a–b) >0, a sample is velocity-strengthening.

Values of the constitutive parameters a, b and D_c, plus the combined stiffness, *k*, of the testing apparatus and sample assembly, were obtained by inverse modelling of the data using an iterative least squares method (e.g. Reinen and Weeks (1993), Noda and Shimamoto (2009); modelling script provided by Hiroyuki Noda). The data were modelled according to the Dieterich rate- and state-dependent friction law (also referred to as the aging or slowness law):

$$\mu = \mu_0 + a\ln\left(\frac{V}{V_0}\right) + b_1\ln\left(\frac{V_0\theta_1}{D_{c1}}\right) + b_2\ln\left(\frac{V_0\theta_2}{D_{c2}}\right) \qquad (5)$$

$$\frac{d\theta_i}{dt} = 1 - \frac{V_0\theta_i}{D_{ci}}, i = 1,2 \qquad (6)$$

(Dieterich, 1979; Dieterich, 1981) where μ is the new steady-state friction value when sliding at V, μ_0 is the reference steady-state friction value when sliding at V_0, and θ_1 and θ_2 are the state variables, representing the average lifetime of the contacting asperities that control friction (Dieterich and Kilgore, 1994), which are renewed over D_{c1} and D_{c2} respectively. This two state variable model was selected to model the data from the experiments performed at 18 MPa as it provides a better fit to the data than employing just a single state variable. The value of b in the combined parameter (a-b) therefore equates to (b_1+ b_2). For the experiments performed at 1 MPa, a single state variable model provided an adequate fit to the data, and in such cases, b_2 is equal to

zero. The use of both one and two state variables to model data sets has been employed in other studies (e.g. Carpenter et al., 2014; Ikari et al., 2014), but the physical processes governing the variability in the number of state variables are not well constrained (e.g. Blanpied et al., 1998). Phases of strain-hardening and strain-weakening were often observed throughout the course of the experiments; the script used to model the data removes these background trends, in line with standard practice (e.g. Blanpied et al., 1998; Tembe et al., 2010), to ensure that the frictional constitutive parameters are calculated using true steady-state friction values.

Slide-hold-slide tests involved steady-state sliding at a velocity of 13 μm/s interrupted by hold periods of 1, 10, 100 and 1000 s (Fig. 5.2). The change in friction, $\Delta\mu$, from the dynamic friction value, μ_d, before the hold, to the static friction value, μ_s, taken as the peak friction value (Dieterich, 1972) attained on resumption of sliding after the hold (Fig. 5.2), gives the amount of frictional healing. From this we can derive the healing rate, β, according to the equation:

$$\beta = \Delta\mu / \log_{10}(t) \qquad (7)$$

where t is the hold time in seconds (Dieterich, 1972; Marone, 1998b). The higher the healing rate of a material, the greater its ability is to accumulate elastic strain energy following a slip event, thus representing the potential for a fault to remain locked during the interseismic period and produce a large stress drop in future events (e.g. Marone, 1998a and references therein). As well as measuring the rate and state friction parameters, we measured the steady-state friction coefficient during the initial stage of the experiment, μ_{ssi} (before the first set of velocity steps), and the final value at the end of the experiment, μ_{ssf} (after the last set of velocity steps) (Fig. 5.2).

5.2.2 *Experimental procedure: high-velocity*

For the high-velocity experiments, we imposed a slip velocity of 1.3 m/s, representative of seismic slip velocity, onto the assembled samples. During these experiments, a dynamic weakening curve is produced, which may take on one of two forms. In the first form, after yielding at an initial friction value, μ_i, the gouge undergoes a phase of slip-hardening to attain a peak in friction, μ_p, which is subsequently followed by an abrupt weakening to low values of steady-state friction, μ_{ss} (Fig. 5.3a). Weakening occurs over a slip-weakening distance, D_w, defined as the displacement at which (μ_p-μ_{ss}) reduces to 5% of (μ_p-μ_{ss}) (Mizoguchi et al., 2007). In the second form, after yielding at μ_i, the gouge undergoes an immediate slip-weakening, so that a peak in friction is not attained and rather, steady-state sliding at low values of μ occurs almost from the outset (Fig. 5.3b).

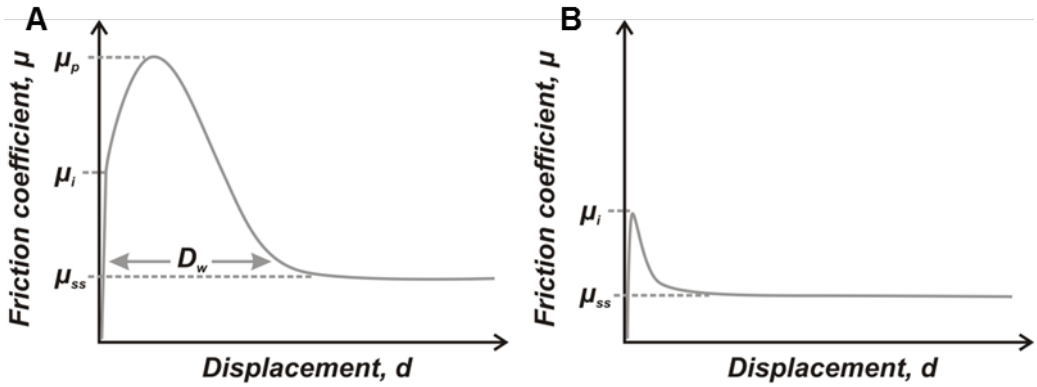

Figure 5.3 Schematic representation of frictional evolution during the high-velocity experiments. **a)** The case for an experiment in which strain-hardening occurs after yielding (μ_i) and friction attains a peak value (μ_p) before weakening over a slip-weakening distance (D_w) to steady-state friction (μ_{ss}). **b)** The case for an experiment in which no strain-hardening occurs after yielding and instead the sample immediately weakens and friction evolves towards steady-state.

5.3 *Results*

5.3.1 *Mechanical data*

5.3.1.1 *Low-velocity experiments*

5.3.1.1.1 *1 MPa*

Frictional strength

Fig. 5.4a shows the evolution of frictional strength during the low-velocity experiments performed at 1 MPa. It can be seen that the gouges undergo several alternating strain-weakening and strain-hardening cycles, during the experiments, but that these cycles are superimposed upon an overall trend in frictional strength evolution (Figs. 5.4a and c). The room-humidity gouge undergoes an overall slight strain-weakening from a μ_{ssi} value of 0.77 at the start of the experiment ($d \approx 0.01$ m) to a μ_{ssf} value of 0.73 ($\Delta\mu_{ss} = -0.04$) at the end ($d \approx 0.35$ m; Fig. 5.4c). The fluid-saturated gouges, on the other hand, undergo a significant overall strain-hardening during the experiments. The water-saturated gouge strengthens from a μ_{ssi} value of 0.65 at the start of the experiment to a value of $\mu_{ssf} = 0.85$ at the end ($\Delta\mu_{ss} = +0.2$; Fig. 5.4c), and the brine-saturated gouge strengthens from $\mu_{ssi} = 0.57$ to $\mu_{ssf} = 0.84$ ($\Delta\mu_{ss} = +0.27$; Fig. 5.4c). Thus, although the fluid-saturated gouges are frictionally weaker than the room-humidity gouge during the initial stage of the experiment, they are frictionally stronger by the end.

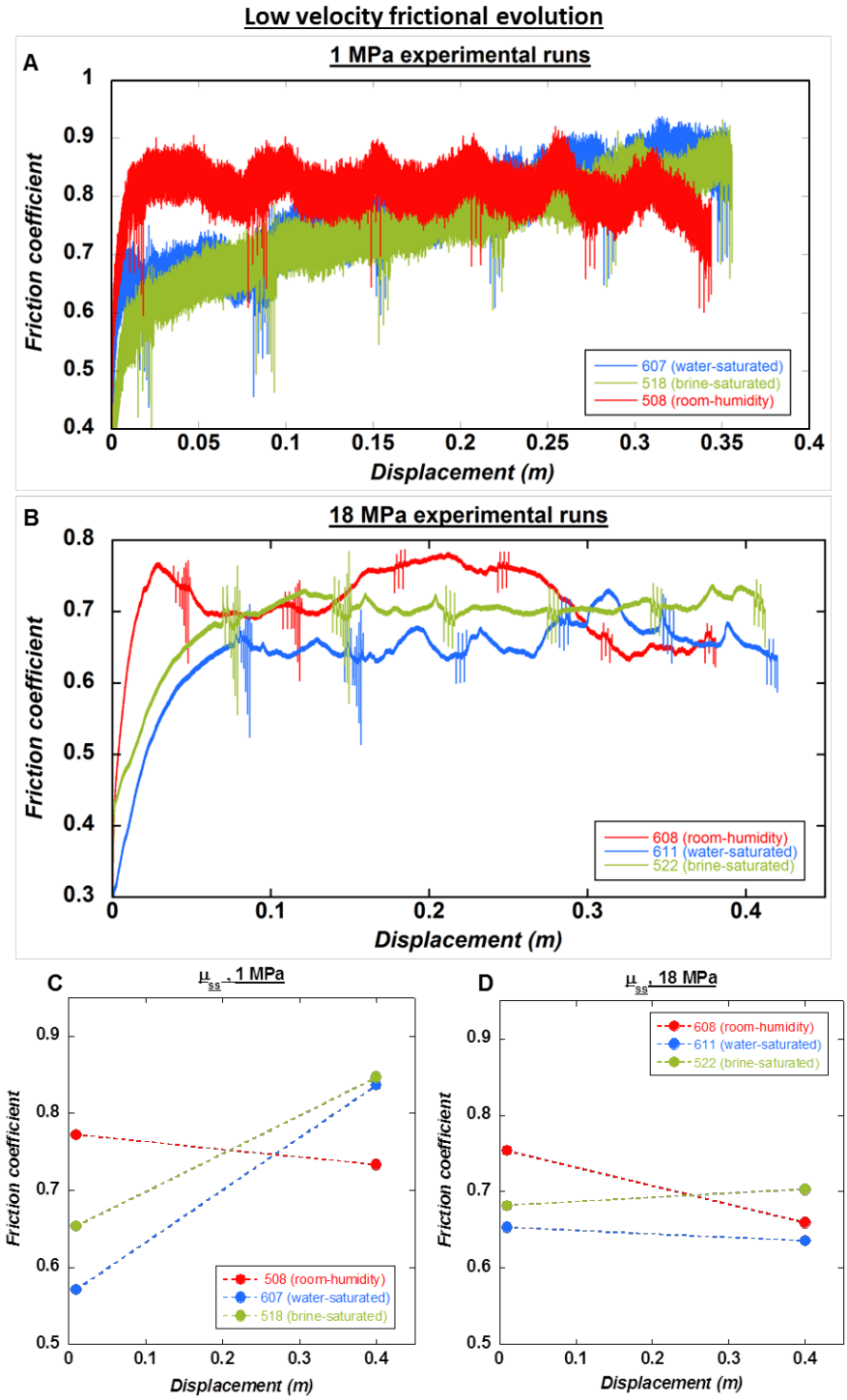

Figure 5.4 Plots showing the evolution of frictional strength with displacement during low-velocity experiments. **a)** Experiments run at 1 MPa normal stress. **b)** Experiments run at 18 MPa. **c)** Summary plot of the overall trend in frictional strength evolution during experiments run at 1 MPa. **d)** Summary plot of the overall trend in frictional strength evolution during experiments run at 18 MPa. In figures **c** and **d**, the points at ~0.01 m displacement represent the initial steady-state friction values and the points at ~0.4 m displacement represent the final steady-state friction values.

Frictional stability

The room-humidity gouge is strongly velocity-strengthening during the first set of velocity-steps (d ≈ 0.01 m), with (a-b) = 0.011-0.012 (Fig. 5.5a). However, it quickly evolves towards a more neutral behaviour as displacement increases, so that by the final set of velocity-steps (d ≈ 0.35 m), (a-b) = 0.0004-0.0014 (Fig. 5.5a). The water-saturated and brine-saturated gouges also start off as strongly velocity-strengthening, with (a-b) values of 0.006-0.011 and 0.012, respectively. In contrast to the room-humidity gouge, the fluid-saturated gouges retain this strengthening behaviour throughout the experiment, displaying no clear evolution of frictional behaviour with increasing displacement (Fig. 5.5a). The average value of (a-b) during the water-saturated experiment is 0.011, and during the brine-saturated experiment is 0.012.

Frictional healing

At 1 MPa, the rate of frictional healing, β, in the room-humidity gouge is 0.0061 per decade during the first set of slide-hold-slides, and increases to 0.017 per decade during the second set (Fig. 5.6a). In the water-saturated gouge, the rate of healing is much higher at β = 0.027 for the first set and β = 0.033 for the second set (Fig. 5.6b). For the brine-saturated gouge, the healing rates are again higher than for the room-humidity gouge, with β = 0.0073 for the first set and β = 0.022 for the second set (Fig. 5.6c). Thus, there is a clear increase in the rate of frictional healing from the room-

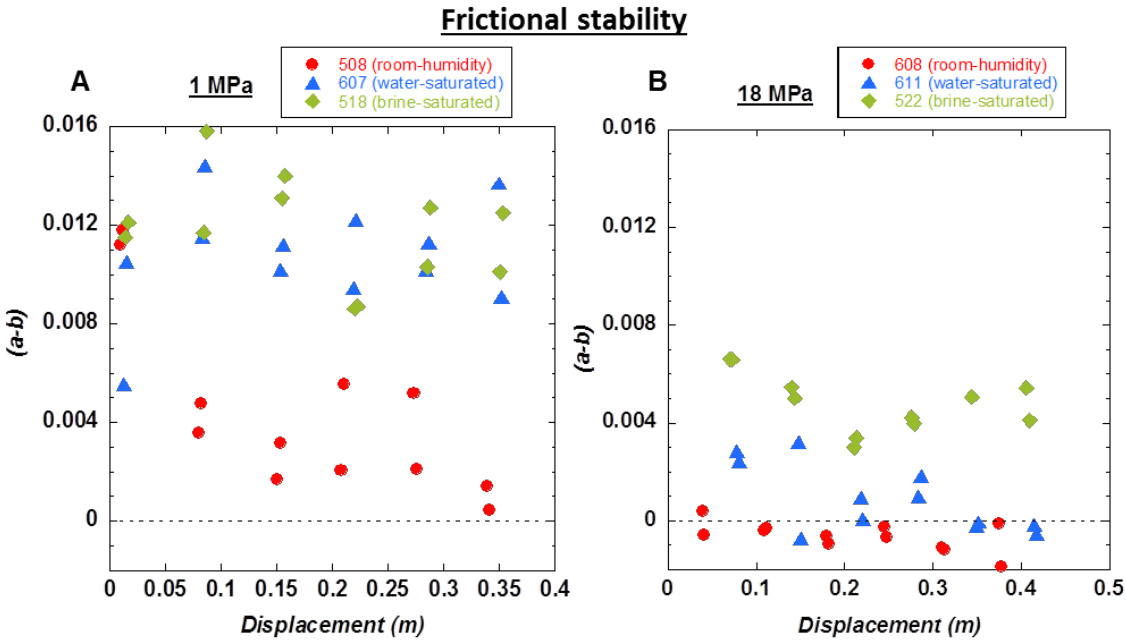

Figure 5.5 Plots showing the evolution of the frictional stability parameter (a-b) with displacement during low-velocity experiments performed at **a)** 1 MPa and **b)** 18 MPa. Data shown is for up-steps in velocity from 13-130 μm/s. Both plots are plotted with the same axes to enable easier comparison of the data.

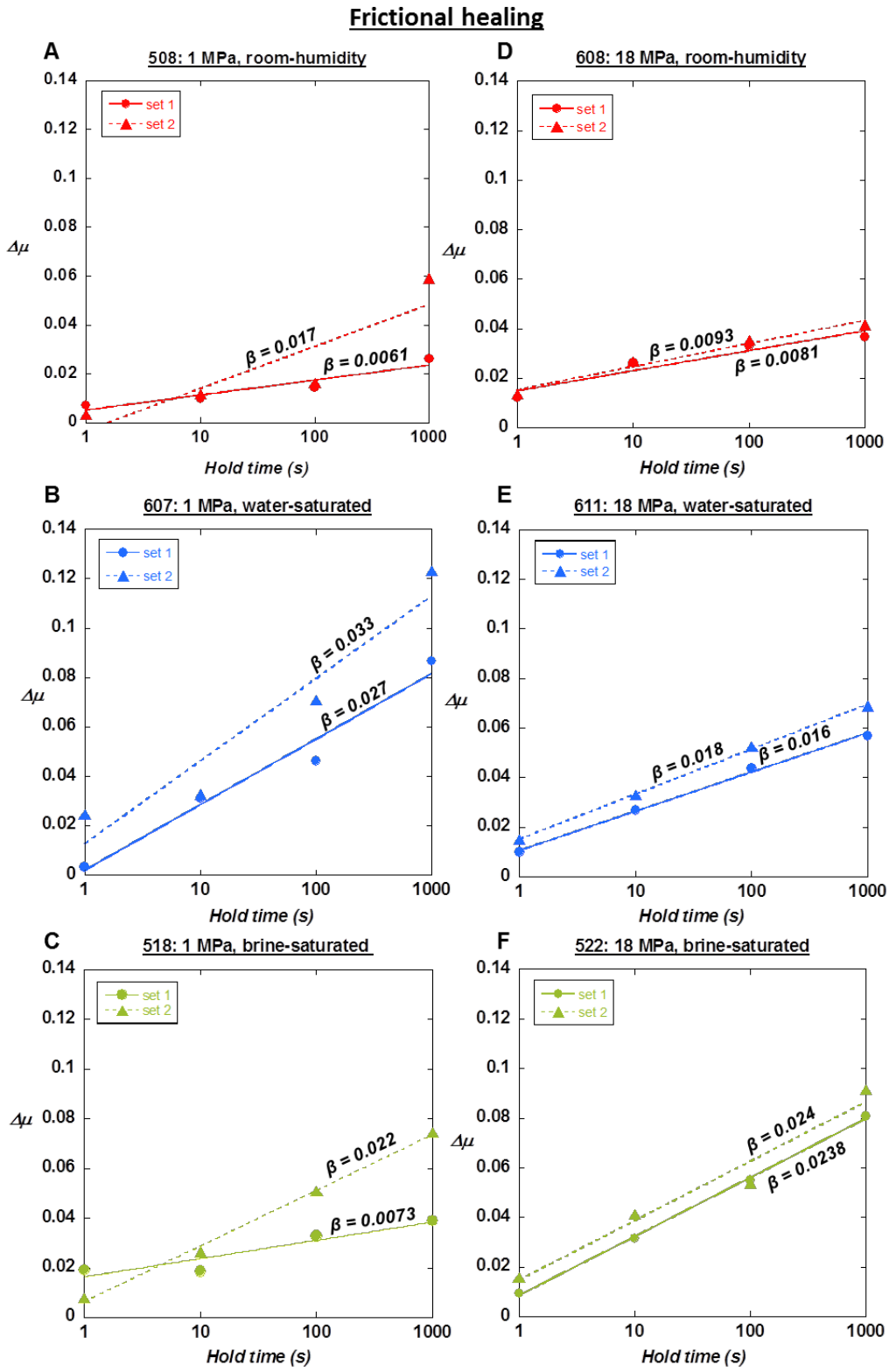

Figure 5.6 Plots showing the amount of frictional healing, $\Delta\mu$, as a function of the hold time during slide-hold-slide tests. Figures **a-c** are the results from experiments performed at 1 MPa under room-humidity, water-saturated and brine-saturated conditions, respectively. Figs **d-f** are the results from experiments performed at 18 MPa under room-humidity, water-saturated and brine-saturated conditions, respectively. All plots are plotted with the same axes to enable easier comparison of the data.

humidity to the fluid-saturated gouges. There is also a clear increase in the rate of frictional healing from the first set of slide-hold-slide tests to the second set.

5.3.1.1.2 *18 MPa*

Frictional strength

At 18 MPa, we again observe numerous strain-weakening and strain-hardening cycles during the course of the experiments (Fig. 5.4b). However, it is still possible to detect an overall trend in the frictional evolution of each of the gouges. The μ_{ssi} values of the room-humidity, water-saturated and brine-saturated gouges are 0.75, 0.65 and 0.68, respectively (Fig. 5.4d). These values are not dissimilar to those at 1 MPa, and it is again the case that the fluid-saturated gouges are weaker than the room-humidity gouge. The room humidity gouge undergoes an overall strain-weakening over the course of the experiment (Fig. 5.4d), as it did at 1 MPa, but the degree of strain-weakening is slightly greater: $\Delta\mu_{ss}$ = -0.09 as opposed to -0.04. The water-saturated gouge, on the other hand, undergoes an overall slight strain-weakening ($\Delta\mu_{ss}$ = -0.01, Fig. 5.4d), as opposed to the strong strain-hardening observed at 1 MPa. The brine-saturated gouge also displays only a very minor evolution in frictional strength relative to that observed at 1 MPa: $\Delta\mu_{ss}$ = +0.02 (Fig. 5.4d) as opposed to +0.27.

Frictional stability

The gouge deformed under room-humidity conditions at 18 MPa exhibits velocity-neutral to velocity-weakening behaviour during the first set of velocity steps (d ≈ 0.04 m), with (a-b) = -0.0006-0.0004 (Fig. 5.5b). The gouge then gradually evolves towards a more velocity-weakening behaviour as displacement increases, so that by the end of the experiment (d ≈ 0.38 m), (a-b) ranges from -0.0001 to -0.0019 (Fig. 5.5b). The water-saturated gouge displays a similar, gradual evolution in frictional behaviour, but does not show as strong a tendency for velocity-weakening behaviour as the room-humidity gouge does (Fig. 5.5b). At the start of the experiment (d ≈ 0.08 m), (a-b) = 0.0024-0.0029 and thus the gouge is velocity-strengthening. At intermediate displacements, the sample alternates between velocity-weakening to velocity-strengthening behaviour, before displaying a more consistent velocity-neutral to velocity-weakening behaviour with (a-b) ≈ -0.0002 during the final two sets of velocity-steps when d is in the range 0.35-0.42 m. The brine-saturated gouge displays velocity-strengthening behaviour over the course of the whole experiment from d = 0.07-0.41 m, with an average (a-b) value of 0.0048 (Fig. 5.5b).

Frictional healing

For the room-humidity gouge at 18 MPa, the rate of frictional healing, β, is 0.0081 per decade for the first set of slide-hold-slides and increases to 0.0093 during the second set (Fig. 5.6d). For the water-saturated gouge, β = 0.0158 during the first set and increases to 0.0181 during the second (Fig. 5.6e). For the brine-saturated gouges, β = 0.0238 during the first set and increases slightly to 0.0240 during the second set (Fig. 5.6f). Thus, as at 18 MPa, there is a clear increase in β from the room-humidity to the fluid-saturated gouges. There is also still the same increase in β from set 1 to set 2 in all experiments, as observed at 1 MPa, although the increase is less marked than it was at 1 MPa.

5.3.1.2 *High-velocity experiments*

5.3.1.2.1 *1 MPa*

At 1 MPa, after yielding, the room-humidity gouge undergoes a phase of strain-hardening during the first ~0.05 m of slip to attain a peak friction value (μ_p) of 1.23 (Fig. 5.7a). The coefficient of friction then drops sharply to approximately half of μ_p over the next 4 m of slip, before undergoing a more gradual evolution towards a steady-state friction value of 0.38 over a total slip-weakening distance of 21.3 m (Fig. 5.7a). The water-saturated gouge also undergoes a phase of strain-hardening during the first ~0.1 m of slip to attain a peak friction value of 0.87 (Fig. 5.7a). It then undergoes a sharp decrease in friction to a value of $\mu \approx 0.65$ over the next 0.4 m of slip before undergoing a gradual weakening to a steady-state friction value of 0.21 over a slip-weakening distance of 33.2 m (Fig. 5.7a). However, the overall weakening trend is interrupted twice. The first interruption is a brief strain-hardening phase between 1-2 m of slip, where friction increases slightly to a value of 0.7 (Fig. 5.7a). Weakening then resumes between 2-3.7 m of slip, where friction decreases to a value of 0.5. The second interruption then occurs between 3.7 and 4.2 m of slip, where friction again increases to ~0.6 before resuming a gradual evolution towards steady-state (Fig. 5.7a). The behaviour of the brine-saturated gouge resembles that of the water-saturated sample. It undergoes strain-hardening during the first ~0.1 m of slip to attain a peak friction value of 0.85 (Fig. 5.7a). Friction then decreases rapidly during the next 0.7 m of slip to a value of 0.56 before evolving to a steady-state value of 0.22 over a slip-weakening distance of 16.5 m (Fig. 5.7a). Two interruptions to the overall slip-weakening trend occur at very similar points to those observed for the water-saturated gouge. The first occurs between 0.9-1.7 m of slip, where friction increases to a value of 0.63, before weakening resumes (Fig. 5.7a). The second occurs between 3.7-3.8 m of slip, where there is a very brief increase in friction from 0.49 to 0.54 (Fig. 5.7a).

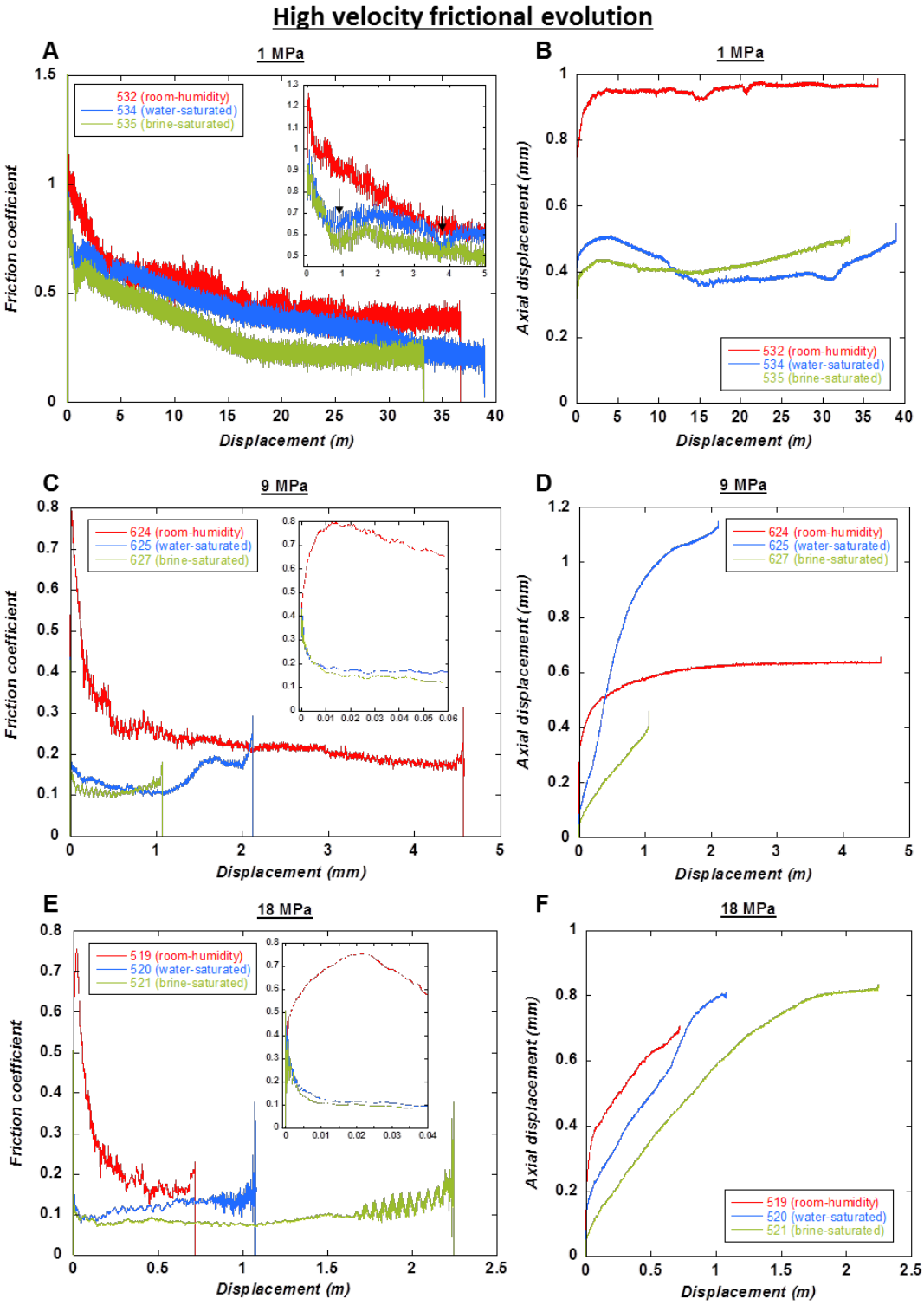

Figure 5.7 Plots showing the evolution of friction and axial displacement with shear displacement during experiments performed at seismic slip velocity (1.3 m/s). Each plot shows the results for the room-humidity gouge, plus the water-saturated and brine-saturated gouges. **a)** Frictional evolution at 1 MPa normal load. **b)** Evolution of axial displacement at 1 MPa normal load. An increase in axial displacement corresponds to compaction and a decrease in axial displacement corresponds to dilation. Very little gouge loss occurred during experiments performed at 1 MPa, and so the curves show true changes in compaction and dilation. – continued overleaf.

c) Frictional evolution at 9 MPa normal load. **d)** Evolution of axial displacement at 9 MPa normal load. Note that gouge was progressively lost during the fluid-saturated experiments, hence why these curves do not level out in the same manner as for the room-humidity gouge. Gouge loss could also cause any dilation events to be masked. **e)** Frictional evolution at 18 MPa normal load. **f)** Evolution of axial displacement at 18 MPa normal load. Again, gouge was progressively lost during all of these experiments.

Fig. 5.7b shows the evolution of axial displacement during the high-velocity experiments at 1 MPa. An increase in axial displacement corresponds to the occurrence of compaction in the gouge layer and a decrease in axial displacement corresponds to dilation. Although there is no apparent correlation between compaction/dilation events and trends in frictional behaviour, it is evident that the fluid-saturated gouges undergo a significantly greater amount of dilation than the room-humidity gouge. This is true first during the early stages of the experiments (d <4 m), when the gouges undergo shear-induced compaction, but where the rate and total amount of compaction are less in the fluid-saturated gouges, suggesting greater competition between compaction and dilation. It is also true during the evolutionary stage of friction towards steady-state, where a steady decrease in the axial displacement is observed in the fluid-saturated gouges, up to the point at which steady-state sliding is established; the onset of steady-state sliding appears to coincide with the cessation of dilation.

5.3.1.2.2 *9 MPa and 18 MPa*

We present the results for the high-velocity tests performed at 9 and 18 MPa together, as the results are very similar. After yielding, the room-humidity gouges undergo strain-hardening during the first ~0.02 m of slip to attain a peak in friction of 0.79 and 0.75 at 9 MPa (Fig. 5.7c) and 18 MPa (Fig. 5.7e), respectively. This is followed by a rapid decrease in friction to steady-state values of 0.17 and 0.16 over slip-weakening distances of 1.67 and 0.29 m, respectively. Thus although the values of μ_p and μ_{ss} are almost the same for the gouges deformed at 9 MPa and 18 MPa, the slip-weakening distance is greatly reduced at 18 MPa.

The fluid-saturated gouges display quite a different behaviour in that after yielding, they do not undergo strain-hardening to attain a peak in friction, but rather, they immediately undergo slip-weakening towards steady-state sliding (Figs. 5.7c and e). Steady-state friction values are 0.11 and 0.1 for the water-saturated and brine-saturated gouges deformed at 9 MPa, respectively, and 0.09 and 0.08 for the water-saturated and brine-saturated gouges deformed at 18 MPa, respectively. Because no peak in friction is attained, we calculated the slip-weakening distance for the fluid-saturated gouges as the displacement at which (μ_i-μ_{ss}) reduces to 5% of (μ_i-μ_{ss}), where μ_i is the

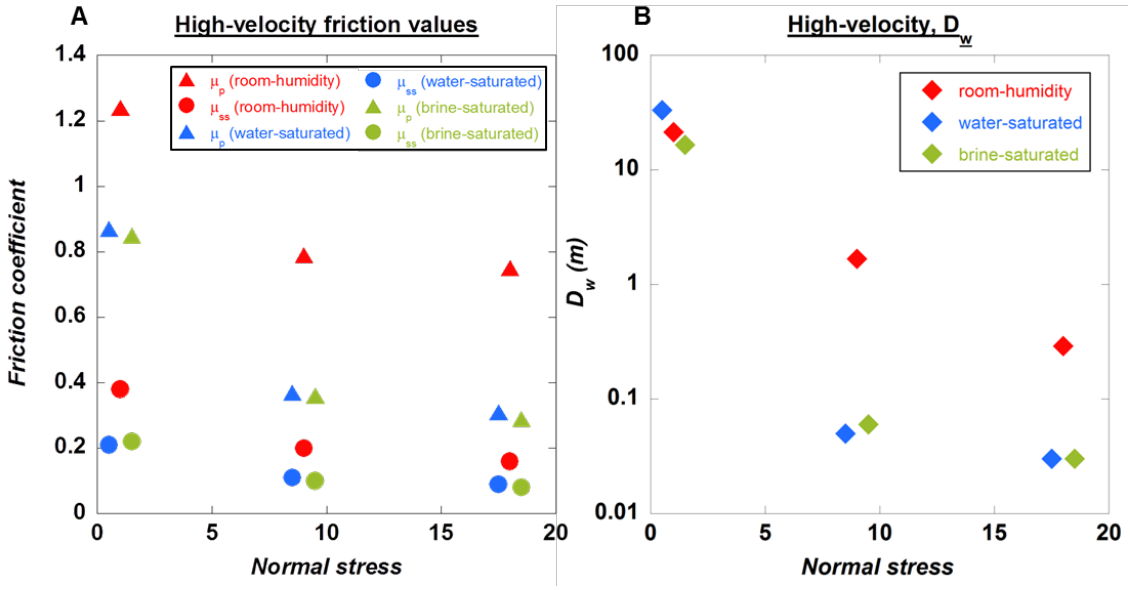

Figure 5.8 Summary of frictional parameters obtained during high-velocity friction experiments. **a)** Values of peak and steady-state friction coefficient for all gouges tested, plotted as a function of normal stress. **b)** Values of the slip-weakening distance for all gouges tested, plotted on a logarithmic scale, as a function of normal stress.

initial friction value, or yield strength, of the gouge. We obtained slip-weakening distances of 0.05 m and 0.06 m for the water-saturated and brine-saturated gouges deformed at 9 MPa, respectively, and 0.03 m for both the water-saturated and brine-saturated gouges deformed at 18 MPa. It could be argued that it is not necessary to assign a slip-weakening distance to these fluid-saturated gouges, as their initial friction values are all <<0.4, which is significantly lower than Byerlee friction (Byerlee, 1978), and so they are weak from the outset and would be unlikely to present much resistance to frictional sliding. All frictional parameters are very similar for the fluid-saturated gouges deformed at 9 and 18 MPa, although those deformed at 18 MPa are slightly weaker. The compaction curves obtained at 9 and 18 MPa may be obscured somewhat by loss of material during shearing (Figs. 5.7d and f). However, we do not observe any evidence for dilation in the gouges as observed at 1 MPa. A summary of all frictional parameters obtained during the high-velocity experiments at all normal loads is shown in Fig. 5.8.

5.3.2 *Microstructures*

5.3.2.1 *Un-sheared gouge (post-compaction) microstructures*

5.3.2.1.1 *1 MPa*

In the room-humidity gouge subjected to 1 MPa normal load, the material derived from clay-rich laminae of the Lisan sediment remains as discrete agglomerates within a matrix of aragonite crystals, i.e. there is no mixing between the clays and the material derived from purely aragonite laminae (Fig. 5.9a-b). The clay-rich agglomerates are elongated in an orientation perpendicular to the applied load (Fig. 5.9-b). The microstructures of the un-sheared water- and brine-saturated gouges are very similar. The clay-rich agglomerates are more spread out and elongated compared to in the room-humidity gouge, although mixing between clay-rich material and aragonite is still limited (Fig. 5.9c). The gouges have a lower porosity than the room-humidity gouge, although the high porosity observed in the room-humidity gouge may be a result of material loss during sample preparation, as the room-humidity gouge is very incohesive. The aragonite crystals in both the room-humidity and fluid-saturated gouge layers have retained their acicular shapes and rosette-type structures, and grain size within the gouge layer resembles that of the starting material (Figs. 5.9b and d), suggesting that very little, if any, damage, in terms of intragranular fracturing, is incurred when subject to a normal load of 1 MPa. In both cases, aragonite crystals are randomly oriented (Fig. 5.9a-d).

5.3.2.1.2 *18 MPa*

In the room-humidity gouge at 18 MPa, the material derived from clay-rich laminae is again distributed as discrete agglomerates, and sometimes as dispersed fine particles, within a matrix of aragonite crystals (Fig. 5.10a). The agglomerates are again elongated perpendicular to the orientation of the applied load (Fig. 5.10a). Acicular aragonite crystals and rosette structures are still preserved even at 18 MPa (Fig. 5.10b) and the acicular crystals often display a shape-preferred orientation with their long axes sub-perpendicular to the applied load (Fig. 5.10a). The porosity of the gouge is lower than that of its 1 MPa equivalent (compare Figs. 5.10a-b and 5.9a-b). Again, the water-saturated and brine-saturated gouges display very similar initial microstructures. The clay agglomerates are much more spread out then in the room-humidity gouge, often forming through-going clay-rich bands in the gouge (Fig. 5.10c). The through-going nature of the clay-rich bands suggests that adjacent clay-rich agglomerates have spread to the extent that they have merged with one another. However, there is a still a clear segregation between clay-dominated and aragonite-

dominated material in the gouge (Fig. 5.10c-d); mixing between the two compositions may be limited by the low permeability of the ultrafine-grained material. Acicular aragonite crystals and their radial arrangements again show little evidence for fracturing and display a very strong shape-preferred orientation (Fig. 5.10c-d).

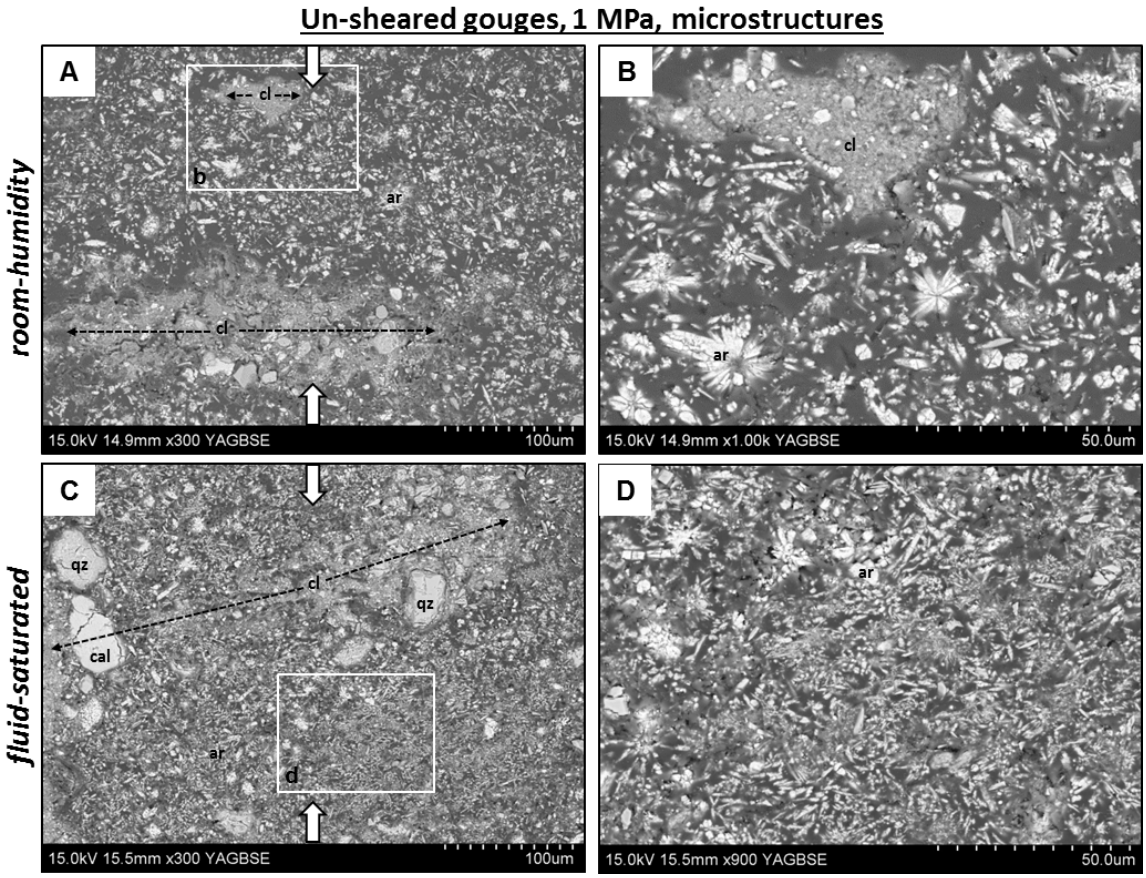

Figure 5.9 Un-sheared microstructures (post-compaction) of gouges subjected to 1 MPa normal load. See text for full description. Certain clasts are labelled to aid mineral identification: ar = aragonite; cal = calcite; cl = clay-rich clastic material; qz = quartz. The orientation of the applied normal load is indicated by vertical white arrows; the elongation of clay-rich agglomerates sub-perpendicular to the applied normal load is indicated by dashed black arrows. **a)** Room-humidity gouge. **b)** Higher magnification image of the boxed area in fig. **a**. Note the preservation of acicular aragonite crystals and their radial arrangements. **c)** Fluid-saturated gouge (in this case it is the brine-saturated gouge). **d)** Higher magnification image of the boxed area in fig. **c**. Again, note the preservation of acicular aragonite crystals, although difficulties associated with sample impregnation and subsequent thin section preparation have resulted in the slightly damaged appearance of the some of the aragonite crystals.

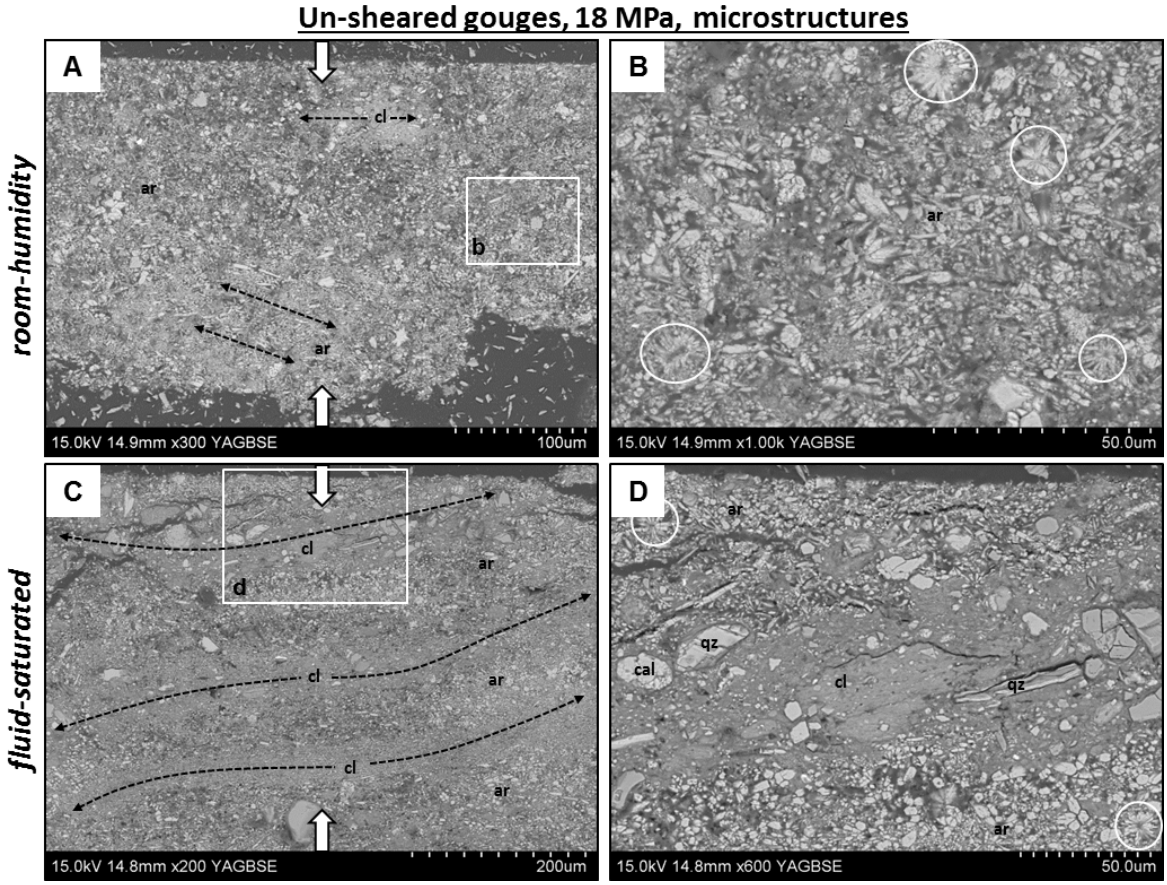

Figure 5.10 Un-sheared microstructures (post-compaction) of gouges subjected to 18 MPa normal load. See text for full description. Clast labelling applies as in Fig. 5.9. The orientation of the applied normal load is indicated by vertical white arrows; the elongation of clay-rich agglomerates and alignment of acicular aragonite crystals sub-perpendicular to the applied normal load is indicated by dashed black arrows. **a)** Room-humidity gouge. **b)** Higher magnification image of the boxed area in fig. **a**. Note the preservation of acicular aragonite crystals and their radial arrangements, examples of which are circled. **c)** Fluid-saturated gouge (in this case it is the water-saturated gouge). Note the strong alignment of through-going, clay-rich bands and acicular aragonite crystals. **d)** Higher magnification image of the boxed area in fig. **c**. Examples of preserved radial arrangements of acicular aragonite crystals are circled.

5.3.2.2 Sheared gouge microstructures

5.3.2.2.1 *Low-velocity experiments*

5.3.2.2.1.1 *1 MPa*

The *room-humidity gouge* deformed at 1 MPa split along a localized, slickensided shear plane when unloaded from the apparatus. We refer to this as the boundary shear, or B-shear (Fig. 5.11a). The deformed gouge has a well-developed fabric characterized predominantly by R_1-shears, but

also some P-shears (Fig. 5.11a), which are identified as discontinuities within the gouge layer. In addition, a through-going Y-shear is located ~50 μm below the shear plane along which the sample split (Fig. 5.11a). Some mixing has occurred between material in the gouge derived from clay-dominated host-rock laminae and that derived from aragonite-dominated laminae, so that sometimes the aragonite crystals are set within a matrix of clay particles. In other places, however, these two main gouge components remain un-mixed. Clast size throughout the majority of the gouge layer averages 1-15 μm, resembling that of the starting material and indicating that very limited cataclasis and grain size reduction has occurred. Where a fine-grained matrix is present, it is composed of the clay fraction of the gouge, rather than being a result of comminution of the clasts. In addition, some large quartz clasts up to 75 μm in diameter still exist (Fig. 5.11a). Clasts are angular and aragonite crystals have retained their acicular habits (Fig. 5.11b), although the radial arrangements of aragonite crystals are only rarely preserved. Acicular aragonite crystals often show a weak shape-preferred orientation adjacent to shear planes (e.g. Fig. 5.11b), but elsewhere they are randomly oriented. Adjacent to the B- and Y-shears at the top of the sample, the clasts are much finer, with ~70% of grains being sub-micron in size, suggesting that some cataclasis has occurred locally here (Fig. 5.11b). The elevated intensity of deformation in this region suggests that a shear zone has localized here. Despite this, clasts located along these shear planes do not appear to be sharply truncated, and consequently the shear planes are not particularly smooth, as they are constantly punctuated by clasts of varying size, shape and orientation (Fig. 5.11b). This applies also to the R- and P-shear planes in the gouge. However, it is not possible to determine whether this is an original feature of the deformed gouge, or whether, given the poor consolidation of material that has been subject to a normal load of only 1 MPa, clasts could have impinged upon the shear planes as the sample relaxed on removal of the normal load. We infer that the dominant deformation mechanism in the gouge is disaggregation of the aragonite rosettes and distributed particulate flow (Borradaile, 1981), which involves grain rotation and translation via grain-boundary sliding, without any fracturing taking place (Borradaile, 1981; Fossen et al., 2007). Cataclasis occurs only locally in narrow zones along or adjacent to the B- and Y-shears in the sample.

As with the room-humidity gouge, the *water-saturated gouge* deformed at 1 MPa possesses a slickenlined boundary shear plane (Fig. 5.11c), although the sample did not split cleanly along this plane. This may simply be because the water-saturated gouge was more cohesive. Within the gouge layer there is a fabric comprising R_1- and P-shears, plus incipient Y-shears (Fig. 5.11c), again identified as discontinuities within the gouge layer. However, this fabric is not as pervasively developed as in the room-humidity gouge. As in the room-humidity gouge, shear planes are rough

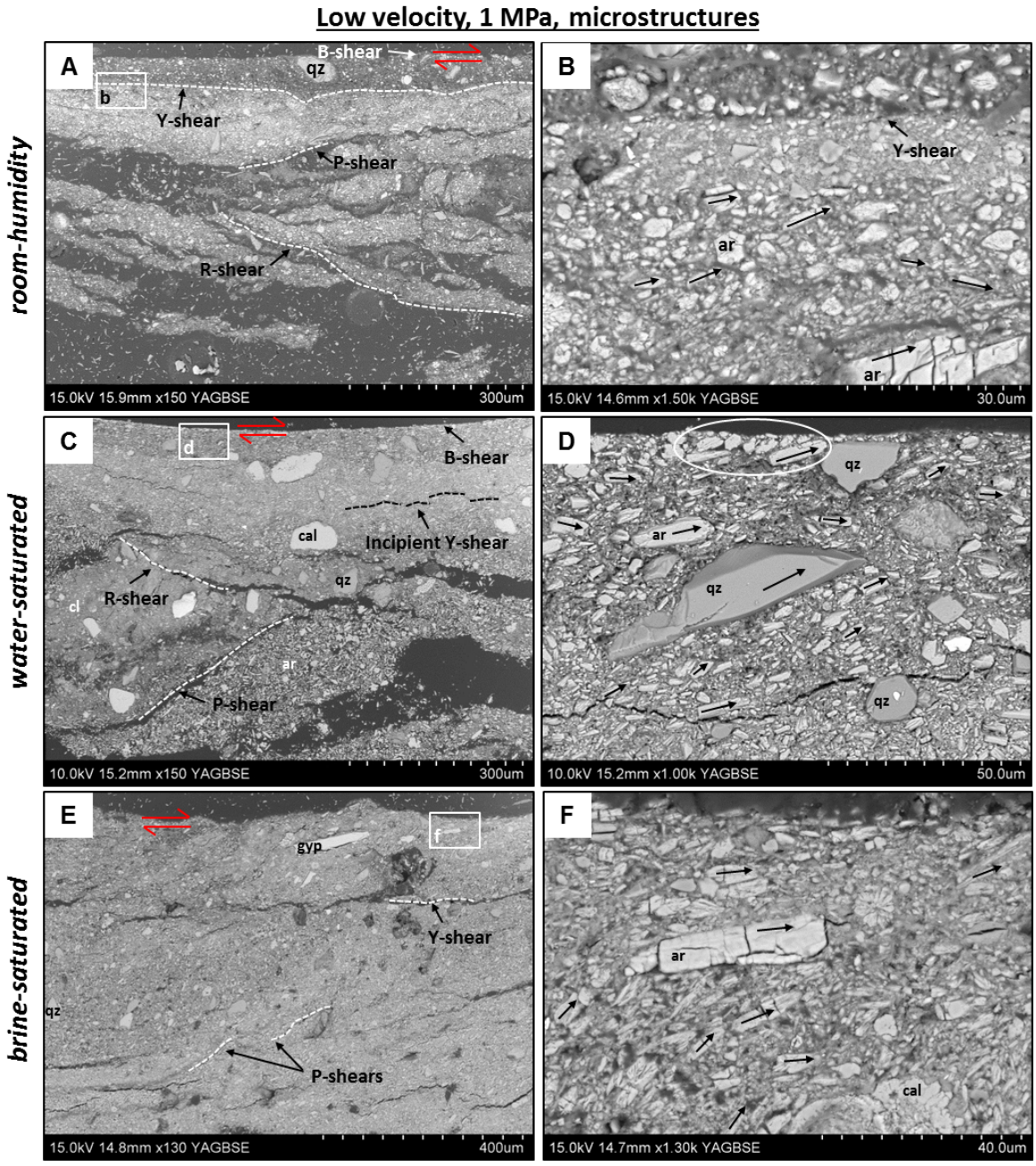

Figure 5.11 Microstructures of gouges deformed at sub-seismic slip rate under 1 MPa normal load. See main text for full descriptions. Larger clasts are labelled to aid mineral identification: cal = calcite, gyp = gypsum qz = quartz. The majority of clasts within the gouge layer are aragonite (ar) crystals, which can be easily identified due to their tabular/acicular shapes or hexagonal cross-sections. **a)** Room-humidity gouge (experiment 508, d = 0.34 m). **b)** High magnification image of the boxed area in fig. **a**. Note the shape-preferred orientation of acicular aragonite crystals (examples highlighted by arrows) sub-parallel to the Y-shear. Also note the ~10 μm wide zone of densely packed ultrafine-grained material immediately below the Y-shear. **c)** Water-saturated gouge (experiment 607, d = 0.35 m). The material in the upper half of the gouge layer is well mixed, but in the central part of the gouge layer (where the labelled R-shear cuts through) it is dominated by clay-rich material (cl) and in the lower part of the sample (to the right of the labelled P-shear) it is dominated by aragonite (ar) – continued overleaf.

d) High magnification image of the boxed area in fig. **c**. There is a strong shape-preferred orientation of clasts (examples highlighted by arrows) sub-parallel to the boundary shear at the top of the sample. A set of imbricated clasts are circled. **e)** Brine-saturated gouge (experiment 518, d = 0.36 m). **f)** High magnification image of the boxed area in fig. **e**. Although there is a moderately strong shape-preferred orientation of clasts here, adjacent to the boundary shear, this fabric is not particularly strong elsewhere in the gouge.

and punctuated by clasts (Fig. 5.11c-d), rather than sharply cutting through clasts. Again, mixing of materials within the gouge layer is variable, and typically is greatest towards the upper part of the sample where the boundary shear is located (Fig. 5.11c). Clast size distribution is even across the gouge layer, i.e. clasts do not decrease in size adjacent to shear planes (Fig. 5.11d). Again clasts average 1-15 μm in size, plus a few larger quartz clasts up to 100 μm diameter, indicating that little or no cataclasis has occurred (Fig. 5.11c-d). Clasts are angular and aragonite crystals retain their acicular shapes (Fig. 5.11d); the preservation of radial arrangements of aragonite crystals is more common than in the room-humidity gouge. Clasts show a much stronger shape-preferred orientation than in the room-humidity gouge and this fabric is much more widespread throughout the gouge layer, rather than occurring only adjacent to shear planes (compare Fig. 5.11d with 5.11b); the orientation of the clasts is sub-parallel to the orientation of the most proximal shear plane. Clasts are often imbricated (Fig. 5.11d), providing a useful indication of the shear-sense, and suggesting a significant component of flow in the gouge. We infer again that the dominant deformation mechanism is distributed particulate flow.

On the *brine-saturated gouge* sample, a slickenlined boundary shear plane could be observed when it was removed from the apparatus, but, similar to the water-saturated sample, it did not split along this surface. In addition, the exact location of the boundary shear is not well defined in thin section (Fig. 5.11e). The brine-saturated gouge does not possess such a well-developed fabric as observed in the water-saturated (or room-humidity) gouge, although a number of incipient P- and Y-shears are present, identified as discontinuities within the gouge layer (Fig. 5.11e). It then follows that there is not such a pervasive shape-preferred orientation of clasts within the gouge layer, as there are fewer planes for the clasts to align towards. Apart from this, the microstructure of the brine-saturated gouge is quite similar to that of the water-saturated gouge, for example, the distribution of grain size across the gouge layer is the same, and imbrication of clasts adjacent to shear planes is a striking feature (Fig. 5.11f). Evidence for cataclasis is once again absent and we again infer that deformation occurred predominantly by distributed particulate flow.

5.3.2.2.1.2 *18 MPa*

The microstructure of the *room-humidity gouge* deformed at 18 MPa is characterized by a strong fabric comprising R_1-, P- and Y-shears, but it is the Y-shears which dominate (Fig. 5.12a). At low magnification (Fig. 5.12a), the Y-shears are identified as through-going sub-horizontal cracks along which the sample has separated during sample recovery/preparation. These are present across the whole width of the gouge layer, with spacings of ~100 μm. Although these shear planes are very distinct, they are quite rough. At higher magnification (Fig. 5.12b), it is observed that further small-scale Y-shear development has occurred adjacent to the larger-scale through-going Y-shears. The small-scale Y-shears are observed as pervasive but discontinuous faint lines transecting the gouge matrix (Fig. 5.12b). Material in the gouge is well mixed and significant grain size reduction, by up to 3 orders of magnitude, has occurred across the whole width of the gouge layer. The gouge comprises ~70% matrix of sub-micron size material, a mixture of clay and comminuted grains (predominantly aragonite), and the remaining 30% clasts are predominantly <5 μm in size. In the regions where pervasive Y-shears are developed, grain-size reduction is even more intense (Fig. 5.12b); the gouge here often comprises >90 % matrix and clasts are ≤2 μm. Clasts are sub-rounded and there is no preservation of the original acicular habit of aragonite crystals, as observed at 1 MPa, and there is also no shape-preferred orientation of clasts. Since grain size reduction and the development of shear planes occurs across the whole width of the gouge layer, we infer that the style and mechanism of deformation is distributed cataclasis, with shear being partitioned between a number of localized shear planes. Shear partitioning may occur simultaneously during shear, or it may be that shear migrates from one plane to another as deformation progresses.

The *water-saturated gouge* deformed at 18 MPa also displays a strong shear localization fabric, although it is not quite as intense as in the room humidity gouge and it is dominated by R-, rather than Y-shears (Fig. 5.12c). Material within the gouge layer is well mixed and grain size reduction is intense (Fig. 5.12c-d). The gouge comprises only ~20% clasts, which have an average size of 1-5 μm (Fig. 5.12d), although some quartz clasts up to 80 μm diameter remain in the gouge layer, appearing relatively undeformed (Fig. 5.12c). The remainder of the gouge comprises a compact matrix of sub-micron sized grains, derived predominantly from aragonite crystals (Fig. 5.12d). This indicates that a significant amount of cataclasis and grain-size reduction, by up to 3 orders of magnitude, in the gouge has occurred. Clast size distribution is fairly even across the gouge layer, but there is a slight reduction towards shear planes, where material is predominantly of sub-micron grain size (Fig. 5.12d). Clasts are sub-rounded and, as in the room-humidity gouge, there is no preservation of acicular aragonite crystals (Fig. 5.12d). These observations suggest that the

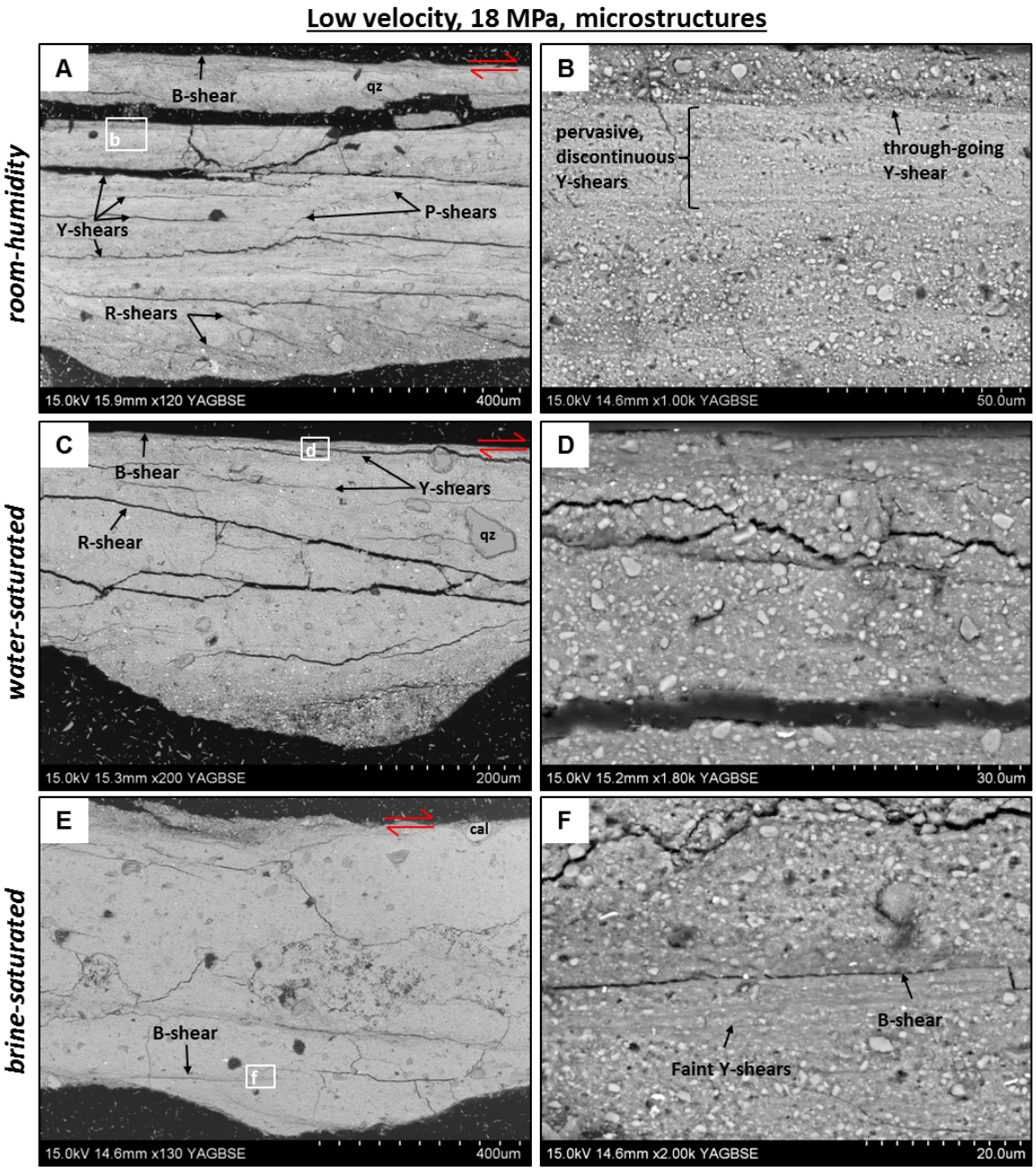

Figure 5.12 Microstructures of gouges deformed at sub-seismic slip rate under 18 MPa normal load. See main text for full descriptions. Larger clasts are labelled to aid mineral identification: cal = calcite, qz = quartz. The majority of clasts within the gouge layer are comminuted aragonite crystals. **a)** Room-humidity gouge (experiment 608, d = 0.38 m). **b)** High magnification image of the boxed area in fig. **a**. Note how the grain size is finest in the region of pervasive Y-shear development. **c)** Water-saturated gouge (experiment 611, d = 0.42 m). Note how the labelled Y-shear at the top right hand side of the image is deflected around a large quartz grain. **d)** High magnification image of the boxed area in fig. **c**. Note the jagged nature of the labelled shear planes, and also the increased reduction in grain size towards the B-shear at the top of the sample. **e)** Brine-saturated gouge (experiment 522, d = 0.41 m). **f)** High magnification image of the boxed area in fig. **e**. Note how grain-size reduction is most intense adjacent to the B-shear and in the region of Y-shears.

dominant deformation mechanism is once again distributed cataclasis, as in the room-humidity gouge, with shear partitioned between a number of localized shear planes.

The *brine-saturated gouge* deformed at 18 MPa does not have a strong or pervasive shear localization fabric as observed in the room-humidity and water-saturated gouges. At low magnification, only one localized shear plane is observed (Fig. 5.12e); this is a boundary shear located at the bottom of the gouge layer, which was observed as a dark grey, slickensided surface on removal from the apparatus. Fig. 5.12e shows that this B-shear is not continuous along the length of the gouge layer. At higher magnification, the B-shear is seen to be quite straight and smooth and is accompanied by a number of Y-shears, which are also very straight and smooth, but are faint and discontinuous (Fig. 5.12f). Clast size distribution is fairly even across the gouge layer; the gouge comprises ~80% matrix of sub-micron sized grains, derived predominantly from aragonite crystals, and the remaining 20% of clasts are typically <<5 μm, with the exception of a few quartz clasts of up to 40 μm diameter. Also, as observed in the other gouges, grain-size reduction is more intense adjacent to the aforementioned boundary and Y-shears (Fig. 5.12f). Clasts range from sub-angular to sub-rounded and once again, there is no preservation of acicular aragonite crystals (Fig. 5.12f). As in the room-humidity and water-saturated gouges, the dominant deformation mechanism is inferred to be distributed cataclasis, but with only the incipient development of localized shear planes.

5.3.2.2.2 *High-velocity experiments*

5.3.2.2.2.1 *1 MPa*

The *room humidity gouge* deformed at 1 MPa at seismic slip velocity split along a localized, slickenlined slip surface, which is dark grey in colour compared to the pale white colour of the starting material. Following the terminology adopted for the gouges deformed at sub-seismic slip velocity, we refer to this as a boundary shear (B-shear; Fig. 5.13a). This surface is straight and smooth (Fig. 5.13b), much more so than in the equivalent gouge deformed at sub-seismic slip velocity (Fig. 5.13b). Occasional incipient R- and Y-shears are present, identified as discontinuities in the gouge layer (Fig. 5.13a), but they are not as pervasive as those observed in the equivalent gouge deformed at sub-seismic slip velocity (Fig. 5.11a). Clay-rich and aragonite-rich material in the gouge appears well mixed. The gouge comprises ~30% matrix composed predominantly of clay and comminuted sub-micron size aragonite grains. The remaining 70% comprises clasts, again predominantly of aragonite, with an average size of 1-10 μm, plus several clasts of quartz and dolomite and clay aggregates which are up to 40 μm in size (Fig. 5.13b). Clast shape ranges from sub-angular to sub-rounded; typically it is the smaller clasts which are more rounded (Fig. 5.13b).

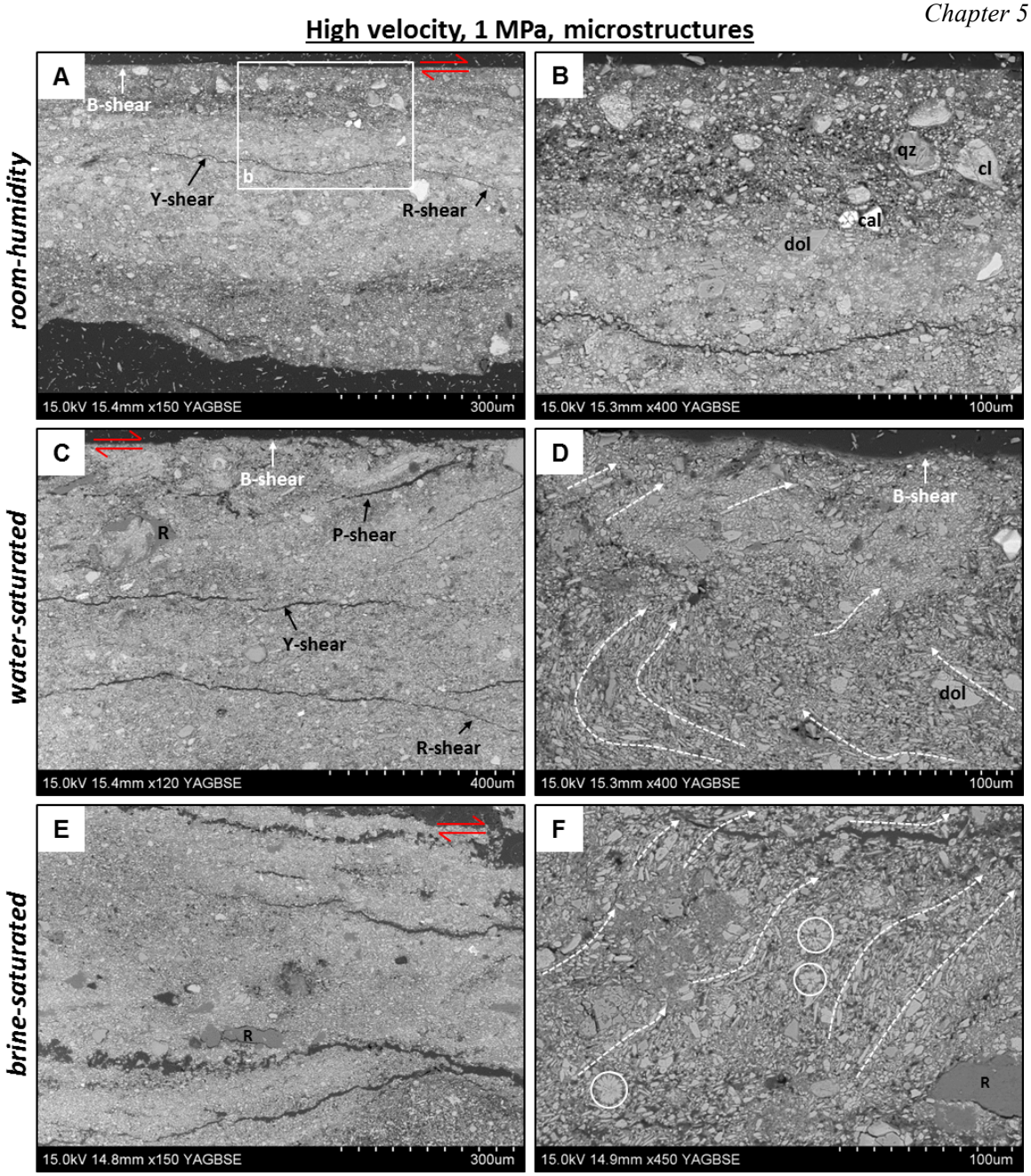

Figure 5.13 Microstructures of gouges deformed at seismic slip velocity under 1 MPa normal load. See main text for full descriptions. Larger clasts are labelled to aid mineral identification: cal = calcite, cl = clay-rich aggregate, dol = dolomite, qz = quartz. The majority of clasts within the gouge layer are aragonite (ar) crystals, which can often be easily identified due to their tabular/acicular shapes or hexagonal cross-sections. Areas labelled 'R' are resin. **a)** Room-humidity gouge (experiment 532, d = 36.77 m). **b)** High magnification image of the boxed area in fig. **a**. **c)** Water-saturated gouge (experiment 534, d = 39.03). **d)** Higher magnification image of the water-saturated gouge, showing an example of a flow-perturbation fold in the bottom left corner. Dominant flow directions in the gouge are highlighted. **e)** Brine-saturated gouge (experiment 535, d = 33.35 m). The sub-horizontal cracks are likely to be Y-shears, which have been exploited as planes of weakness during sample preparation. **f)** Higher magnification image the brine-saturated gouge, showing an example of turbulent flow structures. Dominant flow directions are highlighted by arrows. Examples of relatively intact radial arrangements of aragonite crystals are labelled.

Some aragonite crystals have retained their tabular shape, but this is much less common than in the low-velocity experiments (e.g. compare with Fig. 5.13b with 5.11b). There does not appear to be a systematic orientation of clasts within the gouge. These observations indicate that some degree of fracturing and cataclasis has occurred, although the 1-10 μm average grain size suggests that cataclasis is not particularly intense, reducing grain size typically by only 1 order of magnitude. The distribution of clast sizes is even across the layer, i.e. clast size does not decrease systematically adjacent to shear planes. Cataclasis therefore appears to be distributed across the whole width of the gouge layer. Given the moderate nature of cataclasis in the gouge, we infer that deformation occurred via a mixture of cataclasis and particulate flow, both of which are fairly evenly distributed across the gouge layer.

The *water-saturated gouge* deformed at 1 MPa also splits along a localized, slickenlined boundary shear. When viewed in thin section (Fig. 5.13c), however, this B-shear is not as straight or smooth as in the room-humidity gouge. Incipient R-, P- and Y-shears are also present in some, but not all parts of the gouge (Fig. 5.13c). Material in the gouge is well mixed. The gouge comprises <20% matrix, which is composed of clay particles. The remaining 80% comprises clasts, predominantly of aragonite, averaging 1-15 μm in size, with a few clasts of dolomite and quartz which are up to 90 μm. Clast shape is mostly angular, as most of the aragonite crystals have retained their acicular shapes (Fig. 5.13d). Radial arrangements of crystals are present, although not common. It is therefore apparent that relatively little cataclasis has occurred during deformation. Clasts have a strong preferred orientation throughout the gouge; they are imbricated and aligned sub-parallel to shear planes. Sometimes, groups of aligned clasts are over-turned in the direction of shear (Fig. 5.13d). We refer to these structures as 'flow-perturbation folds' (e.g. Alsop and Holdsworth, 2007). They are typically quite open structures and formed on scales spanning ~50-100 μm (based on maximum distance between opposing limbs). These characteristics are consistent across the whole width of the gouge layer and suggest that deformation occurred predominantly by distributed particulate flow.

The *brine-saturated gouge* deformed at 1 MPa did not split along a localized surface, and there is no obvious boundary shear observed in thin section (Fig. 5.13e). However, sub-horizontal cracks in the thin section may correspond to locations where incipient Y-shears were developed within the gouge (Fig. 5.13e). Once again, the material in the gouge is well mixed. The gouge comprises up to 30% matrix, which is composed of clay particles, and the remaining 70% comprises clasts, predominantly of aragonite, averaging 1-15 μm size, with a few quartz and dolomite clasts up to 50 μm size. Similar to the water-saturated gouge, the majority of clasts are intact, angular, acicular aragonite crystals, or their hexagonal to circular cross sections (Fig. 5.13f). In addition, radial

arrangements of these crystals are sometimes present (Fig. 5.13f). Thus it is again evident that little or no cataclasis has occurred and that the dominant deformation mechanism is distributed particulate flow. Also in similar fashion to the water-saturated gouge, there is a strong shape-preferred orientation of clasts. The angle of orientation can be quite variable (Fig. 5.13f), suggesting again that flow-perturbation folding may have occurred during shearing.

5.3.2.2.2.2 *9 MPa*

The frictional behaviour of the gouges deformed at 9 and 18 MPa is almost identical, and we therefore consider the microstructures produced at 9 MPa to be representative of those produced at 18 MPa. The *room-humidity gouge* split along a black, mirrored, slickenlined boundary shear upon removal from the apparatus. In thin section, this is presented as a straight surface at the top of the sample, which is extensively cracked at high angles to the shear plane (Fig. 5.14a-b). There is a pervasive development of R- and Y-shears in the sample, as well as several sub-vertical tensile fractures emanating from the boundary shear (Fig. 5.14a). In the lower part of the gouge layer, material is not well mixed. Clasts here are predominantly angular and aragonite crystals have retained their acicular shapes and radial arrangements. Average clast size is 1-10 μm, with occasional clasts up to 60 μm, and these are set within a matrix which comprises up to 40% of the gouge, but which is composed predominantly of clay particles, rather than comminuted material. Within the upper 250 μm of the gouge layer, however, material becomes much more thoroughly mixed and grain size starts to reduce dramatically, by up to 3 orders of magnitude as the intensity of deformation increases towards the boundary shear (Fig. 5.14a-b). The gouge now comprises ~70% matrix, which contains a mixture of clay particles and comminuted aragonite. The remaining 30% clasts here are sub-rounded and <5 μm in size. Within the top 20 μm of the gouge layer, directly underlying the boundary shear, the gouge comprises over 95% matrix (Fig. 5.14b). This matrix comprises nanoparticle-sized material, which is dotted with bubbles (Fig. 5.14b). From these observations, we infer that the dominant deformation mechanism in the sample as a whole is cataclasis, which is most localized along the boundary shear (which could also be referred to as a principal slip surface) at the top of the sample. This would explain the progressive increase in the intensity of cataclasis towards this surface, and also the bubbles present just below this surface, which are likely due to the decarbonation of aragonite, which requires local temperatures to be >~720°C (Sharp et al., 2003), during localized frictional heating. The cracking of the boundary shear and adjacent region may then be due to contraction of the sample upon cooling. These observations are very similar to those made by Bullock et al. (2015) (Chapter 3), who performed experiments under the same conditions on gouges containing mixtures of calcite and clay.

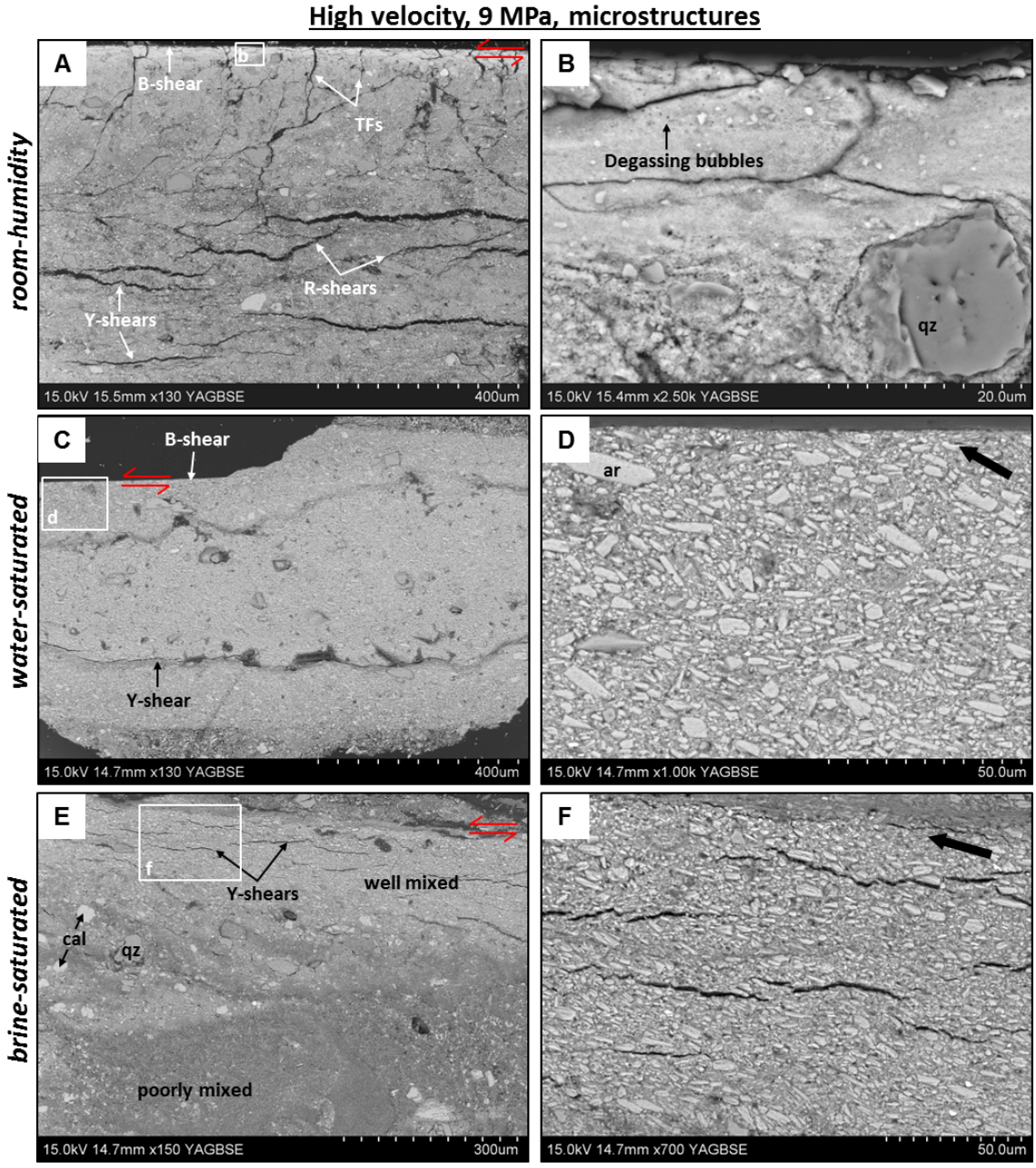

Figure 5.14 Microstructures of gouges deformed at seismic slip velocity under 9 MPa normal load. See main text for full descriptions. Clast labelling applies as in previous figures. **a)** Room-humidity gouge (experiment 624, d = 4.6 m). TFs = tensile fractures. **b)** High magnification image of the boxed area in fig. **a**. **c)** Water-saturated gouge (experiment 625, d = 2.12 m). **d)** Higher magnification image of the water-saturated gouge. Arrow indicates the dominant orientation in which clasts are aligned. **e)** Brine-saturated gouge (experiment 627, d = 1.07 m). Material in the upper part of the gouge is well mixed, comprising a mixture of aragonite and clay, whereas the material in the lower part of the gouge is poorly mixed, e.g., where the 'poorly mixed' label is, the gouge is composed predominantly of aragonite. **f)** Higher magnification image of the brine-saturated gouge. Arrow indicates the dominant orientation in which clasts are aligned.

The *water-saturated gouge* deformed at 9 MPa produced a slickenlined boundary shear, although the sample did not split cleanly along this surface. In thin section, this is observed as a smooth, straight surface (Fig. 5.14c-d). In places where the sample did not split cleanly along the boundary shear, the location of the boundary shear is not discernible (e.g. right hand side of Fig. 5.14c), as the shear plane does not appear to cut through and truncate clasts, and the nature of the material on either side of the shear plane is identical. The development of shear planes within the gouge is much less pervasive compared to in the room-humidity gouge, although a through-going Y-shear is developed in the lower half of the gouge layer (Fig. 5.14c). The intensity of deformation, and thus clast size distribution, is even across the gouge layer. Material within the gouge is well mixed and comprises up to 40% matrix, which is composed predominantly of clay particles. The remaining 60% clasts (predominantly aragonite) have an average size of 1-15 μm, suggesting that little grain size reduction has occurred from that of the starting material. In addition, aragonite crystals have retained their acicular shapes; clasts are therefore predominantly angular (Fig. 5.14d). The aragonite crystals are also imbricated and display a very strong shape-preferred orientation towards the direction of shear (Fig. 5.14d). We infer that the dominant deformation mechanism was distributed particulate flow. The microstructure is in fact very similar to that of the water-saturated gouge deformed at seismic slip velocity under 1 MPa normal load (Fig. 5.13c-d), the only difference being that the orientation of clasts in the gouge deformed at 9 MPa is much more consistent than in the gouge deformed at 1 MPa, where flow in the gouge layer appears to have been much more perturbed (Fig. 5.13d). The distributed style of deformation and lack of cataclasis in the water-saturated gouges can again be compared to observations made by Bullock et al. (2015) (Chapter 3).

The *brine-saturated gouge* sample deformed at 9 MPa does not produce an obvious slickenlined boundary shear. Some incipient Y-shears, identified as discontinuities in the gouge layer, are developed close to the top of the sample (Fig. 5.14e). Material in the lower part of the gouge is poorly mixed, but in the upper part of the gouge, where the Y-shears are located, the material appears more mixed (Fig. 5.14f).This suggests that maybe deformation is concentrated towards the upper part of the gouge layer, resulting in greater re-organization of material. The nature of the material in this upper part of the gouge layer is similar to that observed in the water-saturated gouge (Fig. 5.14d). It comprises ~25% matrix, which is composed predominantly of clay particles. The remaining 75% of clasts comprise angular, acicular aragonite clasts averaging 1-15 μm in size. As in the water-saturated gouge, the aragonite clasts are imbricated and aligned with their long-axes inclined towards the direction of shear (Fig. 5.14f). We infer again that, as in the water-saturated gouge, the dominant deformation mechanism is particulate flow.

5.4. *Discussion*

5.4.1 *Frictional behaviour at sub-seismic slip velocities*

There is a clear difference in frictional behaviour between the room-humidity and fluid-saturated gouges deformed at 1 MPa normal load (Fig. 5.5a). The room-humidity gouge starts off as velocity-strengthening at low displacement, but quickly evolves towards a velocity-neutral behaviour. The water-saturated and brine-saturated gouges, on the other hand, start off velocity-strengthening and remain velocity-strengthening for the duration of the experiments. These contrasting frictional behaviours are accompanied by contrasting microstructures (Fig. 5.11). All of the gouges possess a slickenlined boundary shear, plus variably developed Riedel shear structures within the gouge layer. However, the room-humidity gouge is the only one to contain a through-going Y-shear within the gouge layer (Fig. 5.11a). Adjacent to this Y-shear, there is a demonstrable reduction in grain size (Fig. 5.11b), which is not evident elsewhere in the gouge. Thus, although the dominant deformation mechanism within the gouge layer can be inferred to be distributed particulate flow, there is an element of localized cataclasis. Deformation in the fluid-saturated gouges, on the other hand, appears to occur almost exclusively by distributed particulate flow (Fig. 5.11c-f). Particulate flow is typically favoured over cataclasis at low confining pressure as this enables dilation within the gouge layer, which promotes grain rotation and sliding, rather than grain fracturing and comminution (Borradaile, 1981; Scuderi et al., 2013). It also presumably facilitates shear-induced disaggregation of the aragonite rosettes.

Transitions from velocity-strengthening to velocity-weakening behaviour are often attributed to a transition from distributed to localized deformation (e.g. Beeler et al., 1996; Collettini et al., 2011; Ikari et al., 2011; Logan et al., 1992; Scuderi et al., 2013). We therefore attribute the velocity-strengthening behaviour of the fluid-saturated gouges at 1 MPa, to the distributed style of deformation in these gouges, whilst the evolution of the room-humidity gouge towards a velocity-neutral behaviour can be attributed to the weak localization of deformation in the gouge. The localization of deformation in the room-humidity gouge could also explain why the gouge undergoes an overall strain-weakening over the course of the experiment, as opposed to the fluid-saturated gouges which undergo an overall strain-hardening, consistent with the distributed nature of deformation (e.g. Giger et al., 2008; Niemeijer et al., 2010).

The frictional stability of the gouges deformed at 18 MPa is quite different. The room-humidity gouge deformed at 18 MPa displays velocity-weakening to velocity-neutral behaviour at the start of the experiment and becomes increasingly velocity-weakening with increasing displacement (Fig. 5.5b). The microstructure developed during this experiment is dominated by through-going Y-

shears and the dominant deformation mechanism is inferred to be distributed cataclasis (Fig. 5.12a-b). The water-saturated gouge, by contrast, exhibits velocity-strengthening behaviour at the start of the experiment and shows a gradual evolution towards velocity-weakening behaviour as displacement increases (Fig. 5.5b). The transition to predominantly velocity-weakening behaviour does not occur as early as it does in the room-humidity gouge; it occurs at $d \approx 0.1$ m in the room-humidity gouge but does not occur until $d \approx 0.35$ m in the water-saturated gouge. The dominant deformation mechanism in the water-saturated gouge is again distributed cataclasis, and the microstructure comprises a strong shear localization fabric, which contains through-going R- and Y-shears, but the R-shears appear to be dominant over the Y-shears (Fig. 5.12c-d). The velocity-weakening behaviour of the water-saturated gouge at high displacement could therefore again be attributed to the development of through-going Y-shears in the gouge layer. The reason for the room-humidity gouge showing a greater tendency for velocity-weakening behaviour than the water-saturated gouge can then be attributed to the greater, more pervasive, development of through-going Y-shears.

In contrast to the room-humidity and water-saturated samples, the brine-saturated gouge is velocity-strengthening over the entire displacement range (Fig. 5.5b). The dominant deformation mechanism in the brine-saturated gouge is inferred to be distributed cataclasis based on the observed microstructures (Fig. 5.12e-f), and so is similar to the room-humidity and water-saturated gouges. However, the strong shear-localization fabric observed in the room-humidity and water-saturated gouges is not seen in the brine-saturated gouge. The gouge contains a boundary shear, plus a number of Y-shears, but none of these are continuous across the length of the gouge layer (Fig. 5.12e). We therefore infer that velocity-weakening behaviour did not occur in the brine-saturated gouge due to the absence of any through-going Y-shears for slip to localize on. It should be noted that all of the samples deformed at both 1 and 18 MPa displayed a slickenlined boundary shear on removal from the apparatus, which is evident to some extent in the thin sections. The development of such a boundary shear is clearly insufficient to establish unstable sliding behaviour in the gouges, for which the development of through-going Y-shears actually *within* the gouge layers appears to be a requisite. This observation is consistent with observations made on experimental samples by Beeler et al. (1996).

The switch from particulate flow to cataclasis as the dominant deformation mechanism from 1 MPa to 18 MPa can be explained by the fact that at 18 MPa, gouge compaction is greater, and hence porosity is lower. This inhibits the dilation necessary for particulate flow. Thus, deformation occurs most easily by fracturing of grains. Fracturing is a strain-weakening process that leads to the localization of deformation (Fossen, 2010), thus also explaining the stronger development of shear

localization fabrics in the gouges deformed at 18 MPa. These microstructural observations can again be used to explain the overall evolution of steady-state frictional strength in the gouges. The room-humidity and water-saturated gouges both undergo an overall strain-weakening, which can be attributed to the localization of slip, whilst the overall strain-hardening of the brine-saturated gouge can be attributed to the lack of slip localization (e.g. Giger et al., 2008; Niemeijer et al., 2010). The reason why slip does not localize in the brine-saturated gouge is not clear, particularly as the style and mechanism of deformation is otherwise identical to that of the room-humidity and water-saturated gouges. However, given the high healing rates observed in the brine-saturated gouges at 18 MPa, it may be that localized incipient shear planes formed in the gouge layer but annealed very rapidly due to chemical interactions between the brine and the gouge.

Frictional healing rates at 1 MPa are greatest in the water-saturated gouge, followed by the brine-saturated gouge and then the room-humidity gouge (Fig. 5.6a-c). Healing rates are typically lower at 18 MPa (Fig. 5.6d-f) than at 1 MPa, but a similar trend is observed in that the healing rates are lowest in the room-humidity gouge and greatest in the fluid-saturated gouges, although now the brine-saturated gouge displays higher healing rates than the water-saturated gouge. Under all conditions tested, there is a clear increase in the rate of frictional healing from the first set of slide-hold-slide tests to the second set, implying that the rate of healing increases with accumulated displacement on the fault and associated shear strain in the deformed gouge.

Frictional healing is thought to be associated with an increase in the contact area (Dieterich and Kilgore, 1994), or with an increase in the strength of contacts (e.g. Li et al., 2011), between grains/asperities. Typically it is observed that healing rates increase with increasing normal load, due to a resulting increase in the size of contacting asperities (Dieterich and Kilgore, 1994). Our results, however, show the opposite trend, displaying a decrease in healing rate with increasing normal stress, similar to the trend observed by (Tesei et al., 2014) for powdered calcite-rich gouges. The reason for this is unclear, but one possibility is that the gouges deformed at 1 MPa, which we have interpreted as undergoing significant dilation during shear, subsequently undergo a relatively greater amount of compaction during hold periods than the gouges deformed at 18 MPa, thus resulting in a greater increase in the number of contacting asperities during hold periods and hence higher healing rates. An alternative explanation could be related to the presence of phyllosilicates in the gouge, which at 18 MPa, may become more aligned sub-parallel to shear planes and form more pervasive interconnected networks throughout the gouge (e.g. Fig. 5.10), thus preventing the adhesive growth of aragonite grains (Tesei et al., 2012). The increase in the rate of healing with increasing displacement/bulk shear strain is likely to be due to a greater amount of comminution in the gouges, which would result in a greater number of contacting asperities, and/or

a greater amount of compaction, which would increase the size of contacting asperities. These effects would be enhanced by an increasing development of shear planes throughout the gouge with increasing displacement (Richardson and Marone, 1999).

The observation of higher healing rates in the fluid-saturated gouges is consistent with results from other works investigating the role of fluids in frictional re-strengthening (e.g. Dieterich and Conrad, 1984; Frye and Marone, 2002; Scuderi et al., 2014; Yasuhara et al., 2005) and particularly so in calcite-rich samples (Carpenter et al., 2014; Tesei et al., 2014). The presence of water may strengthen contacts via a number of processes, such as: hydrolytic weakening (i.e. water-assisted plastic deformation) of contacts (e.g. Blacic and Christie, 1984); hydrogen-bonding between asperities (e.g. Michalske and Fuller, 1985; Rice, 1975); water adsorption/desorption at contact points (Frye and Marone, 2002; Hirth and Rice, 1980); capillary bridging (e.g. Iwamatsu and Horii, 1996); pressure solution (e.g Bos and Spiers, 2002; Yasuhara et al., 2005); and sub-critical crack growth (e.g. Atkinson, 1984; Rice, 1978). Particularly in the case of brine-saturated gouges, chemical bonding of contacts is also likely to play a significant role (e.g. Li et al., 2011). The high healing rates in our fluid-saturated gouges are thus likely due to a combination of several of these processes.

We fitted all our healing data with a log-linear tend, as this trend best fits the majority of the data set, and fitting all data sets in the same manner allows for easy comparison of results. However, it is worth noting that the healing data from the experiment performed under room-humidity conditions at 1 MPa (Fig. 5.6a) would show a better fit using a power-law trend; this is also observed on the repeat run of the experiment (Appendix 2.2). Although the time-dependence of frictional healing is typically assumed to occur in log-linear fashion (e.g. Marone, 1998b; Marone et al., 1995), it is not unusual to find that the data could be better fit with a power law function (e.g. Carpenter et al., 2014; Karner et al., 1997; Yasuhara et al., 2005). However, these previous studies find that such a power law fit only becomes apparent during fluid-saturated experiments at elevated temperatures, and for hold times >1000 s, thus attributing it to the activation of pressure solution. It is therefore interesting that we should observe such behaviour in gouges deformed under conditions of room-temperature and humidity and for hold times ≤1000 s.

5.4.2 *Frictional behaviour at seismic slip velocities*

All of the gouges deformed at seismic slip rate at 1 MPa display a very similar behaviour (Fig. 5.7a). They all attain a peak in friction during the first 0.05-0.1 m of slip, followed by a sharp decrease in friction over the next ~4 m of slip and a subsequent gradual evolution towards steady-steady-state sliding over slip weakening distances of 21.3 m for the room-humidity gouge, 33.2 m

for the water-saturated gouge and 16.5 m for the brine-saturated gouge (Fig. 5.8b). The peak friction value for the room-humidity gouge is 1.23, and is somewhat lower for the water-saturated and brine-saturated gouges at 0.87 and 0.85, respectively (Fig. 5.8a). The steady-state friction value is also higher for the room-humidity gouge at 0.38, compared to values of 0.21 and 0.22 for the water-saturated and brine-saturated gouges, respectively (Fig. 5.8a). The observed frictional evolution is typical of the dynamic weakening behaviour observed during high-velocity friction experiments on a wide range of rock types, which is attributed to mechanically and thermally-activated weakening processes triggered by localized frictional sliding (Di Toro et al., 2011 and references therein). However, as we were unable to monitor changes in temperature and/or pore fluid pressure during our experiments, it is difficult to constrain which dynamic weakening mechanisms may have been operating at various stages. Based on the results of previous high-velocity friction experiments performed on calcite- and clay-rich gouges at similar normal load, the weakening is likely a result of a combination of factors: the dissociation of thermally unstable slip zone constituents (e.g. Brantut et al., 2008; De Paola et al., 2011; Han et al., 2007); thermal pressurization of pore fluids within the gouge (e.g. De Paola et al., 2011; Ferri et al., 2010); or nanoparticle lubrication (e.g. De Paola et al., 2011; Han et al., 2010; Han et al., 2007). It is also not possible to constrain what mechanisms may be responsible for the transient re-strengthening phases observed during the first 4 m of slip in the fluid-saturated gouges (Fig. 5.7a). A possible explanation is the loss of interlayer water from the smectite clay in the gouge due to frictional heating, which would cause it to collapse to a frictionally stronger illite-type structure (Saffer and Marone, 2003). Another possibility is that it is due to the development of flow-perturbation folds in the gouge layer (Fig. 5.13d and f), which would disrupt the smooth flow of the gouge layer. The lower friction values associated with the fluid-saturated gouges compared to the room-humidity gouge, are likely a result of the presence of clay minerals in the gouge, which are well known to become weaker when wet (e.g. Behnsen and Faulkner, 2012; Bullock et al., 2015; Ikari et al., 2009 and references therein).

The observed microstructures of the gouges deformed at 1 MPa suggest that deformation in the room-humidity gouge occurred via a mixture of distributed cataclasis and particulate flow (Fig. 5.13a-b). In the fluid-saturated gouges, there is little evidence of cataclasis (Fig. 5.10c-f) and so the dominant deformation mechanism is inferred to be particulate flow. As with the gouges deformed at sub-seismic velocity at 1 MPa, these observations are consistent with the fact that these gouges were deformed under very low confining pressure, which facilitates dilation and promotes particulate flow rather than cataclasis (Borradaile, 1981). The dominance of particulate flow in the fluid-saturated gouges compared to the room-humidity gouge can thus be explained by the greater

amount of dilation in the fluid-saturated gouges (Fig. 5.7b). Particulate flow in the fluid-saturated gouges would also be promoted by the presence of weak clay minerals (e.g. Behnsen and Faulkner, 2012; Bullock et al., 2015; Ikari et al., 2009) and the fluid-saturated nature of the material (Borradaile, 1981; Marques et al., 2010; Scuderi et al., 2013), both of which would facilitate sliding between grains.

The behaviours of the gouges deformed at seismic slip velocity at 9 MPa (Fig. 5.7c) and 18 MPa (Fig. 5.7e) are quite different to those observed at 1 MPa. First, the room-humidity gouge, although displaying the same trend in frictional evolution as observed at 1 MPa, i.e. an increase in friction to a peak value (= 0.79 and 0.75 at 9 and 18 MPa, respectively, Fig. 5.8a) at the onset of slip, followed by a dramatic decrease in friction to low steady-state values (= 0.17 and 0.16 at 9 and 18 MPa, respectively, Fig. 5.8a), has a much shorter slip-weakening distance of just 1.67 m at 9 MPa and 0.29 m at 18 MPa, compared to 21.3 m for the room-humidity gouge deformed at 1 MPa (Fig. 5.8b). The decrease in the slip-weakening distance with increasing normal stress is a known phenomenon across a wide range of rock types deformed at seismic slip velocity (Di Toro et al., 2011). Seeing as dynamic weakening behaviour is typically attributed to mechanically- and thermally-activated weakening mechanisms, the implication is that these processes are activated more quickly at greater confining pressure.

The fluid-saturated gouges are weaker still, in that they do not undergo any strain-hardening during the experiments and thus do not attain a peak in friction (Fig. 5.7c and e); they simply undergo weakening to steady-state sliding almost immediately at the onset of slip, at $d \leq 0.06$ m. The very small area under the slip-weakening curve in the fluid-saturated experiments means that these gouges have very low fracture energy, and thus it would be very easy for an earthquake to propagate through these materials (Cocco et al., 2006; Faulkner et al., 2011; Tinti et al., 2005). This deformation response is observed in a number of previous studies into the high-velocity frictional properties of water-saturated clay-bearing gouges (e.g. Bullock et al., 2015; Faulkner et al., 2011; Ferri et al., 2010; Ujiie et al., 2013). A number of weakening mechanisms have been proposed to explain this incredibly weak behaviour, for example pore fluid pressurization due to a combination of shear-enhanced compaction and frictional heating (e.g. Faulkner et al., 2011; Ujiie and Tsutsumi, 2010), the presence of thin, lubricating films of water bonded to the surfaces of clay grains (Ferri et al., 2010; Moore and Lockner, 2004), or sliding occurring on a film of water which is extruded from the gouge layer upon compaction (Ferri et al., 2010). Alternatively, Bullock et al. (2015) suggest that the weakness of clay-bearing gouges can be due to slip occurring on a distributed, interconnected network of inherently weak water-saturated clay minerals, which formed during axial loading compaction prior to shear. This mechanism would certainly be

plausible during our experiments, as examination of the initial microstructure (post-compaction, pre-shearing) of the fluid-saturated gouges at 9 and 18 MPa shows that in the room-humidity gouges, clays are present as discrete agglomerates or dispersed fine particles, whereas in the fluid-saturated gouges, these discrete agglomerates spread out and merge to form through-going clay-rich regions in the gouge layer (Fig. 5.10). At 1 MPa normal load, the clays do not spread and merge to the same extent (Fig. 5.9), which would explain why the fluid-saturated gouges deformed at 1 MPa are not as weak as their counterparts deformed at higher normal load, and they still attain a peak in friction.

The dominant deformation mechanism in the room-humidity gouge deformed at 9 MPa (and assumed to be the same at 18 MPa) is localized cataclasis, with microstructural evidence of frictional heating in excess of 720°C, whereas in the fluid-saturated gouges it is distributed particulate flow, with no microstructural evidence of significant frictional heating. These observations are consistent with the observed frictional behaviours, as follows. Cataclasis and wear would be required to localize slip in the room-humidity gouge, explaining the strain-hardening phase at the start of the experiment. Once slip is localized, thermally activated dynamic weakening is triggered (Bullock et al., 2015; Smith et al., 2015). In the fluid-saturated gouges, on the other hand, slip can preferentially localize within the weak, clay-rich regions of the gouge, diminishing the need for cataclasis and the associated strain-hardening phase. As the weak clays become mixed with the rest of the material in the gouge layer during shear, they will facilitate grain boundary sliding and hence promote particulate flow in preference to cataclasis as the dominant deformation mechanism. The reason for the difference in deformation mechanism and resulting microstructure between the gouges deformed at sub-seismic and seismic velocity at 9-18 MPa, may be due to greater dilation occurring at higher slip velocity (e.g. Mair and Marone, 1999; Scuderi et al., 2013), thereby permitting particulate flow to operate even at moderate normal loads.

5.4.3 *Implications for rupture propagation in the shallow crust*

The results of our low-velocity experiments at 1 MPa show that faults hosted in poorly-lithified calcite + clay sediments in the shallow-most portion of the crust (<50 m depth) behave in a frictionally stable velocity-strengthening manner, particularly if they are fluid-saturated. This suggests they have the potential to slow down or terminate earthquake ruptures before they reach the surface, as their velocity-strengthening nature will result in a negative stress drop (Marone et al., 1991). The likelihood of frictional instability, and hence rupture propagation, increases at 18 MPa (~1 km depth), particularly once displacements > ~15 cm have been acquired. The

exceptional result is the brine-saturated gouge, which maintains velocity-strengthening behaviour under all conditions tested. A summary of these results is presented in Fig. 5.15.

Whilst earthquakes typically nucleate at much greater depths (~5-15 km in the case of continental earthquakes and ~10-40 km in the case of subduction zone earthquakes (Scholz, 1998)), than those represented by our testing conditions, our results have important implications for the propagation of earthquake ruptures to the surface. First, they suggest that ruptures may become attenuated to some degree the closer they get to the Earth's surface. Second, they suggest that the attenuation effect would be enhanced if the fault gouges are saturated with brine, which is perhaps the most likely condition in the majority of upper-crustal fault zones, and particularly in subduction zone settings, where the pore fluid in accretionary wedge sediments is sea water. If the propagation of earthquake ruptures through the shallow portion of the crust is indeed attenuated to some degree, it will result in a stress perturbation in the shallow crust, which must subsequently be relaxed (Marone et al., 1991), either during future seismic events or aftershocks, or via aseismic afterslip. Typically, velocity-strengthening materials are associated with aseismic fault creep, phyllosilicate-rich fault rocks being the classic example (e.g. Carpenter et al., 2011; Lockner et al., 2011; Tesei et al., 2012). Phyllosilicates are also associated with very low, sometimes even negative, values of frictional healing (Carpenter et al., 2011; Tesei et al., 2012), which compounds the argument that they should deform predominantly aseismically by fault creep, as they are not able to accumulate elastic energy. Our results show the opposite trend, in that the gouges which exhibit the strongest

			Sub-seismic velocity →			Seismic velocity		
			Room-humidity	**Water-saturated**	**Brine-saturated**	**Room-humidity**	**Water-saturated**	**Brine-saturated**
Depth ↓	**1 MPa**	**Dominant deformation mechanism**	Particulate flow (+ localized cataclasis)	Particulate flow	Particulate flow	Particulate flow + cataclasis	Particulate flow	Particulate flow
		Style of deformation	Distributed (+ incipient localization)	Distributed	Distributed	Distributed	Distributed	Distributed
		Rupture propagation favoured?	✗	✗	✗	✗	✗	✗
	18 MPa	**Dominant deformation mechanism**	Cataclasis	Cataclasis	Cataclasis	Cataclasis	Particulate flow	Particulate flow
		Style of deformation	Distributed (but shear occurs on localized planes)	Distributed (but shear occurs on localized planes)	Distributed (+ incipient developmet of localized shear planes)	Localized	Distributed	Distributed
		Rupture propagation favoured?	✓	✓	✗	✓	✓	✓

Figure 5.15 Table summarising the dominant deformation mechanisms, style of deformation and frictional behaviour (in terms of whether rupture propagation would be favoured) for gouges deformed under room-humidity, water-saturated and brine-saturated conditions, and as a function of depth and slip rate.

velocity-strengthening behaviour are also the ones with the *highest* healing rates. This implies that if the velocity-strengthening regions of the faults in the Lisan Formation do attenuate earthquake propagation, then the generated stress perturbation is most likely to be relaxed via aftershocks rather than by aseismic afterslip, as is typically supposed (Marone and Scholz, 1988; Marone et al., 1991). The 2010 M_w 7.8 Mentawai earthquake, which ruptured the shallow portion of the megathrust up-dip from the 2007 M_w 8.5 Sumatra earthquakes, may serve as an example of such a scenario (Bilek et al., 2011; Lay et al., 2011). Indeed, the velocity-weakening behaviour at moderate displacements of the room-humidity and water-saturated gouges at 18 MPa, show that under certain conditions, it may be possible for earthquakes to nucleate at very shallow depth.

The results of our high velocity experiments also suggest that unconsolidated sediments at 1 MPa normal load should present a barrier to rupture propagation (Fig. 5.15), due to their large slip-weakening distances. Unless earthquake magnitude is especially large (~M $\geq$8.5), then fault frictional strength will remain in the Byerlee range and will not be easily overcome. However, it is again the case that frictional behaviour becomes more unstable with increasing normal stress (Fig. 5.15), because at 9 and 18 MPa, the slip-weakening distance is reduced to <1.7 m for dry gouges, and <<0.1 m for fluid-saturated gouges. Thus the potential for dynamic weakening increases with increasing normal stress, and particularly in the case of fluid-saturated gouges, where the fracture energy is negligible. The lower the amount of energy that is dissipated via fracturing, the greater the energy will be at the front of a propagating rupture tip, enabling slip to accelerate and thus facilitating rupture propagation (Kanamori, 2001). Given such circumstances, the velocity-strengthening properties of the fluid-saturated gouges at 1 MPa may be of secondary importance, because ruptures propagating through the frictionally unstable materials below may have enough energy to overcome the resistance to rupture propagation presented by a thin (potentially <50 m thick) package of velocity-strengthening sediment at the surface. Thus, the strong dynamic-weakening behaviour of (particularly fluid-saturated) gouges at normal stresses of 9-18 MPa, equivalent to a depth range of 0.5-1 km, plus their ability under certain conditions to behave in a velocity-weakening manner, will make rupture propagation to the surface more favourable (Fig. 5.15), and indeed may go some way towards explaining the surprisingly large near-surface co-seismic offsets associated with 'great' earthquake events (e.g. Lay, 2015 and references therein).

Rupture dynamics are of course dependent upon a number of factors, including the initial size of the rupture during its nucleation phase (Ellsworth and Beroza, 1995) and any compositional and geometrical heterogeneities and complexities along the fault which it may encounter during propagation (e.g. Ando and Yamashita, 2007; Biegel and Sammis, 2004; Bullock et al., 2014; Collettini et al., 2011; Tesei et al., 2013). This growing body of work highlights the need to better

constrain variations in fault zone composition and architecture, plus an assessment of fault frictional properties under conditions which span the entire seismogenic zone, if the seismic behaviour and hazard of a fault are to be properly assessed. The variation in the frictional behaviours of the water-saturated vs. brine-saturated gouges observed in this study also highlights the need to study the mechanical and frictional properties of fault rocks under a variety of fluid-saturation conditions. The majority of studies regarding the frictional properties of fluid-saturated fault rocks use distilled water as the saturating medium, which is unlikely to be representative of natural fault zone conditions, where formation fluids contain dissolved ions which have the ability to interact chemically with rock constituents and alter their mechanical properties.

5.4.4 *Implications for the identification of seismic markers in natural faults*

As well as the frictional behaviour being rather variable during our experiments, we also observe that deformation mechanisms and microstructural development are highly dependent on the experimental conditions, as summarised in Fig. 5.15. At 1 MPa, the dominant deformation mechanism is particulate flow in all of the gouges deformed at both low and high velocity, although an element of cataclasis does occur in the room humidity gouges. Seeing as the majority of faults close to the Earth's surface will be exposed to fluid infiltration, the microstructures developed in the fluid-saturated gouges are likely to be most representative of what may be found in nature. The fact that the microstructures developed in the fluid-saturated gouges at 1 MPa are almost identical, regardless of whether they were deformed at seismic or sub-seismic velocity, suggests that it is not possible to differentiate between faults in nature that have slipped seismically or aseismically at the near surface.

At higher normal loads, we observe quite a difference in microstructure between the gouges deformed at low and high velocity. All of the gouges deformed at low velocity are characterized by distributed cataclasis and, with the exception of the brine-saturated gouge, a strong shear-localization fabric. Those deformed at high-velocity are characterized by localized cataclasis, in the case of the room humidity gouge, and distributed particulate flow, in the case of the fluid-saturated gouges, and thus are highly variable depending on whether or not the gouge is saturated. If the gouge is dry (room humidity), then the localized slip results in frictional heating great enough to trigger calcite decarbonation, and thus leave seismic markers. If the gouges are fluid-saturated, however, then no seismic markers are produced, and in fact the microstructure is almost identical to that observed in the fluid-saturated gouges deformed at 1 MPa at both low and high velocity. It is therefore apparent that in the case of fluid-saturated gouges deformed in the shallow crust, again bearing in mind that faults in the upper crust will almost always contain fluids to some extent, there

is no way of determining visually (i.e. microstructurally) whether or not a fault has slipped seismically or aseismically. In these cases, a more comprehensive and multidisciplinary approach, such as that employed by Balsamo et al. (2014), would be required to discriminate seismic from aseismic slip, perhaps involving thorough analyses of variations in grain size, grain shape, porosity, permeability and mineralogy between the host rock and fault gouges within a fault zone.

5.4.5 *Implications for the behaviour of faults in the Masada fault zone*

Seeing as the Masada fault zone (MFZ), studied in Chapter 4, provided the motivation for this study, it seems appropriate to link our experimental results back to our field observations. The faults of the MFZ, which deform poorly lithified sediments belonging to the Lisan Formation, from which the synthetic aragonite + clay gouges used in this study were derived, formed at just a few metres depth, and under brine-saturated conditions. The results of our experiments performed on brine-saturated gouges at 1 MPa are therefore most relevant to our natural analogue. These gouges exhibited velocity-strengthening behaviour at sub-seismic velocity and exhibited a large slip-weakening distance of 16.5 m when deformed at seismic velocity. Therefore, the MFZ faults would be expected to present some resistance to rupture propagation. However, they are known to have hosted seismic events which ruptured the surface (Marco and Agnon, 1995). Therefore, our earlier suggestion that the frictional properties of faults in the shallowest part of the crust may be negated by the dynamics of an earthquake rupture propagating from greater depth, is supported by our observations of surface-rupturing seismogenic faults in the MFZ. The microstructures produced during the brine-saturated experiments at 1 MPa, which are characterized by distributed particulate flow at both sub-seismic and seismic velocity, are similar to those observed in the natural MFZ faults, which are also characterized by particulate flow (Fig. 5.16). Although this means that it is not possible to differentiate seismic from aseismic fault gouges in the MFZ, it is reassuring in that we can be confident that our experimentally produced microstructures, at least those produced at low normal stress, are representative of naturally deformed gouges.

5.5 *Conclusions*

We performed friction experiments on gouges at both sub-seismic and seismic slip velocities, normal stresses ranging from 1-18 MPa and under room-humidity, water-saturated and brine-saturated conditions, with the aim of improving our understanding of the factors that affect the propagation of earthquake ruptures through the shallowest portion of the crust (depths of 1km or less). Friction experiments were accompanied by microstructural analyses of the deformed gouges in order to assess also the deformation mechanisms operating in faults in the shallow crust.

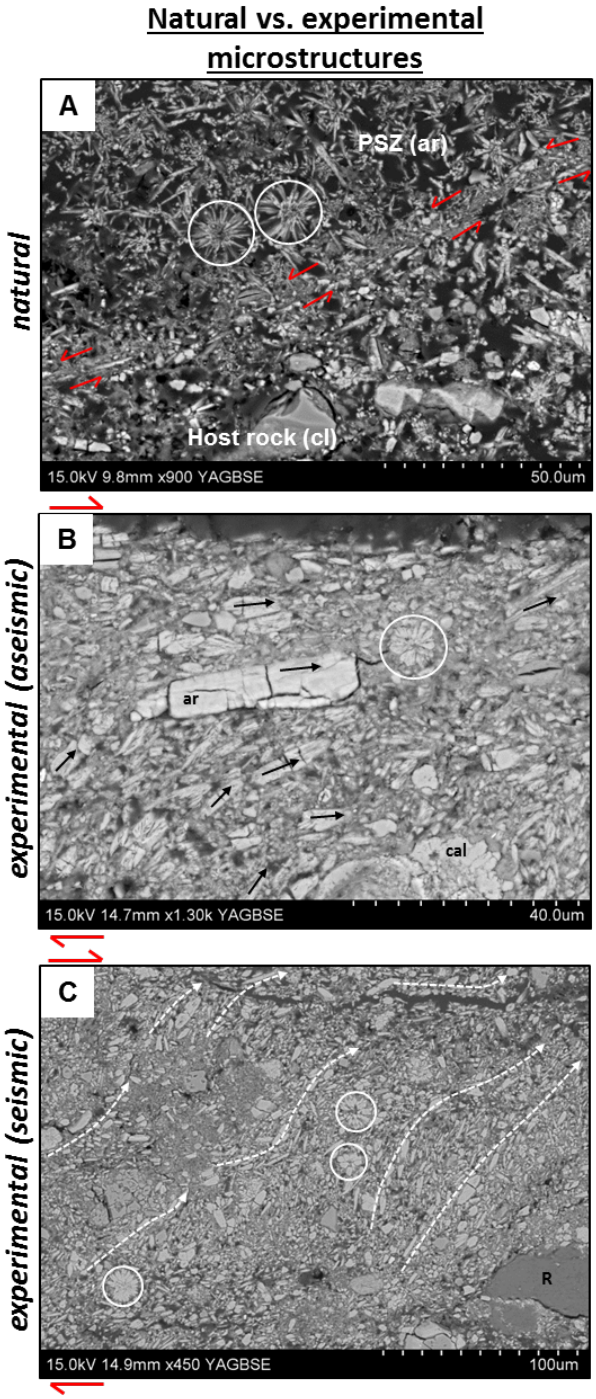

Figure 5.16 Comparison of naturally and experimentally deformed brine-saturated Lisan sediment at ~1 MPa. Labelling applies as in previous figures. **a)** Naturally produced principal slip zone (PSZ) in Lisan sediment from the MFZ. Location of principal slip surface is marked by shear-sense indicators. **b)** Experimentally produced slip zone in Lisan sediment deformed at sub-seismic slip velocity. **c)** Experimentally produced slip zone in Lisan sediment deformed at seismic slip velocity. In all cases, there is an alignment of acicular aragonite crystals towards the direction of shear (indicated by arrows), and acicular aragonite crystals and their radial arrangements are preserved (examples circled), suggesting particulate flow is the dominant deformation mechanism.

Incohesive fault gouges and poorly lithified sedimentary packages in the upper few km of the crust are often considered to act as energy sinks with the potential to act as barriers to rupture propagation. However, our results suggest that the frictional behaviour and stability of faults in poorly lithified sediments at the near surface may be very sensitive to variations in normal stress (i.e. depth of burial), fluid presence (and composition), strain rate, and fault maturity (i.e. the total amount of displacement/strain accumulated by the fault). Considering the upper few km of the earth's crust as a package with homogenous frictional properties is therefore insufficient when assessing the potential for surface rupturing and inherent seismic hazard of a fault. Our results suggest that rupture propagation to the surface is likely to be favoured by dynamic weakening processes operating at depths of just 0.5-1 km. These results go some way towards explaining the occurrence of both shallow-depth 'tsunami' earthquakes and the large near-surface co-seismic offsets associated with 'great' earthquakes. However, we suggest that future studies should look into fault frictional properties over a greater span of normal stress and fluid-saturation conditions, in order to better constrain the variations in frictional properties faced by an earthquake during its passage to the surface.

Overall, our results show that both frictional behaviour and deformation mechanisms are not simply a function of depth or strain-rate or fluid presence, but depend on complex interactions between these different environmental factors (Fig. 5.15). Therefore, linking certain microstructures in natural fault zones to a certain type of frictional behaviour should be avoided, unless environmental conditions during deformation are well constrained.

References

Alsop, G.I., Holdsworth, R.E., 2007. Flow perturbation folding in shear zones. Geological Society, London, Special Publications 272, 75-101.

Ando, R., Yamashita, T., 2007. Effects of mesoscopic-scale fault structure on dynamic earthquake ruptures: Dynamic formation of geometrical complexity of earthquake faults. Journal of Geophysical Research: Solid Earth (1978–2012) 112.

Atkinson, B.K., 1984. Subcritical crack growth in geological materials. Journal of Geophysical Research: Solid Earth (1978–2012) 89, 4077-4114.

Balsamo, F., Aldega, L., De Paola, N., Faoro, I., Storti, F., 2014. The signature and mechanics of earthquake ruptures along shallow creeping faults in poorly lithified sediments. Geology 42, 435-438.

Beeler, N., Tullis, T., Blanpied, M., Weeks, J., 1996. Frictional behavior of large displacement experimental faults. Journal of Geophysical Research 101, 8697-8715.

Behnsen, J., Faulkner, D.R., 2012. The effect of mineralogy and effective normal stress on frictional strength of sheet silicates. Journal of Structural Geology.

Biegel, R.L., Sammis, C.G., 2004. Relating fault mechanics to fault zone structure. Advances in geophysics 47, 65-111.

Bilek, S., Lay, T., 2002. Tsunami earthquakes possibly widespread manifestations of frictional conditional stability. Geophysical Research Letters 29, 18-11-18-14.

Bilek, S.L., Engdahl, E.R., DeShon, H.R., El Hariri, M., 2011. The 25 October 2010 Sumatra tsunami earthquake: Slip in a slow patch. Geophysical Research Letters 38, n/a-n/a.
Blacic, J.D., Christie, J.M., 1984. Plasticity and hydrolytic weakening of quartz single crystals. Journal of Geophysical Research: Solid Earth (1978–2012) 89, 4223-4239.
Blanpied, M.L., Marone, C.J., Lockner, D.A., Byerlee, J.D., King, D.P., 1998. Quantitative measure of the variation in fault rheology due to fluid-rock interactions. Journal of Geophysical Research: Solid Earth 103, 9691-9712.
Borradaile, G.J., 1981. Particulate flow of rock and the formation of cleavage. Tectonophysics 72, 305-321.
Bos, B., Spiers, C.J., 2002. Fluid-assisted Healing Processes in Gouge-bearing Faults: Insights from Experiments on a Rock Analogue System. pure and applied geophysics 159, 2537-2566.
Brace, W.F., Byerlee, J.D., 1966. Stick-Slip as a Mechanism for Earthquakes. Science 153, 990-992.
Brantut, N., Schubnel, A., Rouzaud, J.N., Brunet, F., Shimamoto, T., 2008. High-velocity frictional properties of a clay-bearing fault gouge and implications for earthquake mechanics. Journal of Geophysical Research 113, B10401.
Bullock, R.J., De Paola, N., Holdsworth, R.E., 2015. An experimental investigation into the role of phyllosilicate content on earthquake propagation during seismic slip in carbonate faults. Journal of Geophysical Research: Solid Earth, n/a-n/a.
Bullock, R.J., De Paola, N., Holdsworth, R.E., Trabucho-Alexandre, J., 2014. Lithological controls on the deformation mechanisms operating within carbonate-hosted faults during the seismic cycle. Journal of Structural Geology 58, 22-42.
Byerlee, J., 1978. Friction of rocks. Pure and applied Geophysics 116, 615-626.
Byerlee, J., Summers, R., 1976. A note on the effect of fault gouge thickness on fault stability. International Journal of Rock Mechanics and Mining Sciences & Geomechanics Abstracts 13, 35-36.
Carpenter, B., Marone, C., Saffer, D., 2011. Weakness of the San Andreas Fault revealed by samples from the active fault zone. Nature Geoscience 4, 251-254.
Carpenter, B.M., Scuderi, M.M., Collettini, C., Marone, C., 2014. Frictional heterogeneities on carbonate-bearing normal faults: Insights from the Monte Maggio Fault, Italy. Journal of Geophysical Research: Solid Earth 119, 9062-9076.
Cocco, M., Spudich, P., Tinti, E., 2006. On the mechanical work absorbed on faults during earthquake ruptures. Radiated Energy and the Physics of Earthquakes Faulting.
Collettini, C., Niemeijer, A., Viti, C., Smith, S.A.F., Marone, C., 2011. Fault structure, frictional properties and mixed-mode fault slip behavior. Earth and Planetary Science Letters 311, 316-327.
De Paola, N., Hirose, T., Mitchell, T., Di Toro, G., Viti, C., Shimamoto, T., 2011. Fault lubrication and earthquake propagation in thermally unstable rocks. Geology 39, 35-38.
Delouis, B., Nocquet, J.M., Vallée, M., 2010. Slip distribution of the February 27, 2010 Mw= 8.8 Maule earthquake, central Chile, from static and high-rate GPS, InSAR, and broadband teleseismic data. Geophysical Research Letters 37.
Di Toro, G., Han, R., Hirose, T., De Paola, N., Nielsen, S., Mizoguchi, K., Ferri, F., Cocco, M., Shimamoto, T., 2011. Fault lubrication during earthquakes. Nature 471, 494-498.
Dieterich, J.H., 1972. Time-dependent friction in rocks. Journal of Geophysical Research 77, 3690-3697.
Dieterich, J.H., 1979. Modeling of rock friction: 1. Experimental results and constitutive equations. Journal of Geophysical Research: Solid Earth 84, 2161-2168.
Dieterich, J.H., 1981. Constitutive properties of faults with simulated gouge. Mechanical behavior of crustal rocks: the Handin volume, 103-120.
Dieterich, J.H., Conrad, G., 1984. Effect of humidity on time-and velocity-dependent friction in rocks. Journal of Geophysical Research: Solid Earth (1978–2012) 89, 4196-4202.

Dieterich, J.H., Kilgore, B., 1996. Implications of fault constitutive properties for earthquake prediction. Proceedings of the National Academy of Sciences of the United States of America 93, 3787-3794.
Dieterich, J.H., Kilgore, B.D., 1994. Direct observation of frictional contacts: New insights for state-dependent properties. Pure and Applied Geophysics 143, 283-302.
Ellsworth, W., Beroza, G., 1995. Seismic evidence for an earthquake nucleation phase. Science 268, 851.
Engelder, J.T., Logan, J.M., Handin, J., 1975. The sliding characteristics of sandstone on quartz fault-gouge. pure and applied geophysics 113, 69-86.
Faulkner, D.R., Mitchell, T.M., Behnsen, J., Hirose, T., Shimamoto, T., 2011. Stuck in the mud? Earthquake nucleation and propagation through accretionary forearcs. Geophysical Research Letters 38, L18303.
Ferri, F., Di Toro, G., Hirose, T., Shimamoto, T., 2010. Evidence of thermal pressurization in high-velocity friction experiments on smectite-rich gouges. Terra Nova 22, 347-353.
Fossen, H., 2010. Structural geology. Cambridge University Press.
Fossen, H., Schultz, R.A., Shipton, Z.K., Mair, K., 2007. Deformation bands in sandstone: a review. Journal of the Geological Society 164, 755-769.
Frye, K.M., Marone, C., 2002. Effect of humidity on granular friction at room temperature. Journal of Geophysical Research: Solid Earth (1978–2012) 107, ETG 11-11-ETG 11-13.
Giger, S.B., Cox, S.F., Tenthorey, E., 2008. Slip localization and fault weakening as a consequence of fault gouge strengthening—Insights from laboratory experiments. Earth and Planetary Science Letters 276, 73-84.
Han, R., Hirose, T., Shimamoto, T., 2010. Strong velocity weakening and powder lubrication of simulated carbonate faults at seismic slip rates. Journal of Geophysical Research 115, B03412.
Han, R., Shimamoto, T., Hirose, T., Ree, J.H., Ando, J., 2007. Ultralow friction of carbonate faults caused by thermal decomposition. Science 316, 878-881.
Handin, J., 1969. On the Coulomb-Mohr failure criterion. Journal of Geophysical Research 74, 5343-5348.
Hirose, T., Shimamoto, T., 2005. Growth of molten zone as a mechanism of slip weakening of simulated faults in gabbro during frictional melting. Journal of Geophysical Research: Solid Earth 110, n/a-n/a.
Hirth, J.P., Rice, J., 1980. On the thermodynamics of adsorption at interfaces as it influences decohesion. Metallurgical Transactions A 11, 1501-1511.
Ide, S., Baltay, A., Beroza, G.C., 2011. Shallow Dynamic Overshoot and Energetic Deep Rupture in the 2011 Mw 9.0 Tohoku-Oki Earthquake. Science 332, 1426-1429.
Ikari, M.J., Carpenter, B.M., Kopf, A.J., Marone, C., 2014. Frictional strength, rate-dependence, and healing in DFDP-1 borehole samples from the Alpine Fault, New Zealand. Tectonophysics 630, 1-8.
Ikari, M.J., Marone, C., Saffer, D.M., 2011. On the relation between fault strength and frictional stability. Geology 39, 83-86.
Ikari, M.J., Saffer, D.M., Marone, C., 2009. Frictional and hydrologic properties of clay-rich fault gouge. Journal of Geophysical Research 114, B05409.
Iwamatsu, M., Horii, K., 1996. Capillary condensation and adhesion of two wetter surfaces. Journal of colloid and interface science 182, 400-406.
Kanamori, H., 1972. Mechanism of tsunami earthquakes. Physics of the earth and planetary interiors 6, 346-359.
Kanamori, H., 2001. Energy budget of earthquakes and seismic efficiency. Earthquake Thermodynamics and Phase Transformations in the Earth's Interior 76, 293-305.
Kanamori, H., 2014. The Diversity of Large Earthquakes and Its Implications for Hazard Mitigation. Annual Review of Earth and Planetary Sciences 42, 7-26.
Karner, S.L., Marone, C., Evans, B., 1997. Laboratory study of fault healing and lithification in simulated fault gouge under hydrothermal conditions. Tectonophysics 277, 41-55.

Lay, T., 2015. The surge of great earthquakes from 2004 to 2014. Earth and Planetary Science Letters 409, 133-146.
Lay, T., Ammon, C., Kanamori, H., Koper, K., Sufri, O., Hutko, A., 2010. Teleseismic inversion for rupture process of the 27 February 2010 Chile (Mw 8.8) earthquake. Geophysical Research Letters 37.
Lay, T., Ammon, C., Kanamori, H., Yamazaki, Y., Cheung, K., Hutko, A., 2011. The 25 October 2010 Mentawai tsunami earthquake (Mw 7.8) and the tsunami hazard presented by shallow megathrust ruptures. Geophysical Research Letters 38.
Li, Q., Tullis, T.E., Goldsby, D., Carpick, R.W., 2011. Frictional ageing from interfacial bonding and the origins of rate and state friction. Nature 480, 233-236.
Lockner, D.A., Morrow, C., Moore, D., Hickman, S., 2011. Low strength of deep San Andreas fault gouge from SAFOD core. Nature 472, 82-85.
Logan, B.W., Semeniuk, V., 1976. Dynamic metamorphism: processes and products in Devonian carbonate rocks, Canning Basin, Western Australia. Geological Society of Australia.
Logan, J., Dengo, C., Higgs, N., Wang, Z., 1992. Fabrics of experimental fault zones: Their development and relationship to mechanical behavior. International Geophysics Series 51, 33-33.
Mair, K., Marone, C., 1999. Friction of simulated fault gouge for a wide range of velocities and normal stresses. Journal of Geophysical Research: Solid Earth 104, 28899-28914.
Marco, S., Agnon, A., 1995. Prehistoric earthquake deformations near Masada, Dead Sea graben. Geology 23, 695-698.
Marone, C., 1998a. The effect of loading rate on static friction and the rate of fault healing during the earthquake cycle. Nature 391, 69-72.
Marone, C., 1998b. Laboratory-derived friction laws and their application to seismic faulting. Annual Review of Earth and Planetary Sciences 26, 643-696.
Marone, C., Raleigh, C.B., Scholz, C., 1990. Frictional behavior and constitutive modeling of simulated fault gouge. J. geophys. Res 95, 7007-7025.
Marone, C., Scholz, C., 1988. The depth of seismic faulting and the upper transition from stable to unstable slip regimes. Geophysical Research Letters 15, 621-624.
Marone, C., Vidale, J.E., Ellsworth, W.L., 1995. Fault healing inferred from time dependent variations in source properties of repeating earthquakes. Geophysical Research Letters 22, 3095-3098.
Marone, C.J., Scholtz, C., Bilham, R., 1991. On the mechanics of earthquake afterslip. Journal of Geophysical Research: Solid Earth (1978–2012) 96, 8441-8452.
Marques, F.O., Burg, J.P., Lechmann, S.M., Schmalholz, S.M., 2010. Fluid-assisted particulate flow of turbidites at very low temperature: A key to tight folding in a submarine Variscan foreland basin of SW Europe. Tectonics 29, n/a-n/a.
Michalske, T.A., Fuller, E.R., 1985. Closure and repropagation of healed cracks in silicate glass. Journal of the American Ceramic Society 68, 586-590.
Mizoguchi, K., Hirose, T., Shimamoto, T., Fukuyama, E., 2007. Reconstruction of seismic faulting by high-velocity friction experiments: An example of the 1995 Kobe earthquake. Geophysical Research Letters 34, L01308.
Moore, D.E., Lockner, D.A., 2004. Crystallographic controls on the frictional behavior of dry and water-saturated sheet structure minerals. Journal of Geophysical Research 109, B03401.
Niemeijer, A., Marone, C., Elsworth, D., 2010. Frictional strength and strain weakening in simulated fault gouge: Competition between geometrical weakening and chemical strengthening. Journal of Geophysical Research: Solid Earth (1978–2012) 115.
Noda, H., Shimamoto, T., 2009. Constitutive properties of clayey fault gouge from the Hanaore fault zone, southwest Japan. Journal of Geophysical Research: Solid Earth 114, n/a-n/a.
Reinen, L.A., Weeks, J.D., 1993. Determination of rock friction constitutive parameters using an iterative least squares inversion method. Journal of Geophysical Research: Solid Earth 98, 15937-15950.

Reznik, I.J., Gavrieli, I., Ganor, J., 2009. Kinetics of gypsum nucleation and crystal growth from Dead Sea brine. Geochimica et Cosmochimica Acta 73, 6218-6230.
Rice, J., 1978. Thermodynamics of the quasi-static growth of Griffith cracks. Journal of the Mechanics and Physics of Solids 26, 61-78.
Rice, J.R., 1975. Hydrogen and interfacial cohesion. Division of Engineering, Brown University.
Richardson, E., Marone, C., 1999. Effects of normal stress vibrations on frictional healing. Journal of Geophysical Research: Solid Earth 104, 28859-28878.
Saffer, D.M., Marone, C., 2003. Comparison of smectite-and illite-rich gouge frictional properties: application to the updip limit of the seismogenic zone along subduction megathrusts. Earth and Planetary Science Letters 215, 219-235.
Scholz, C.H., 1998. Earthquakes and friction laws. Nature 391, 37-42.
Scuderi, M.M., Carpenter, B.M., Marone, C., 2014. Physicochemical processes of frictional healing: Effects of water on stick-slip stress drop and friction of granular fault gouge. Journal of Geophysical Research: Solid Earth 119, 4090-4105.
Scuderi, M.M., Niemeijer, A.R., Collettini, C., Marone, C., 2013. Frictional properties and slip stability of active faults within carbonate–evaporite sequences: The role of dolomite and anhydrite. Earth and Planetary Science Letters 369–370, 220-232.
Sharp, Z., Papike, J., Durakiewicz, T., 2003. The effect of thermal decarbonation on stable isotope compositions of carbonates. American Mineralogist 88, 87-92.
Shimamoto, T., Tsutsumi, A., 1994. A new rotary-shear high-speed frictional testing machine: Its basic design and scope of research (in Japanese with English abstract). Journal of the Tectonic Research group of Japan 39, 65-78.
Sibson, R., 1977. Fault rocks and fault mechanisms. Journal of the Geological Society 133, 191-213.
Sibson, R.H., 1989. Earthquake faulting as a structural process. Journal of Structural Geology 11, 1-14.
Smith, S.A.F., Nielsen, S., Di Toro, G., 2015. Strain localization and the onset of dynamic weakening in calcite fault gouge. Earth and Planetary Science Letters 413, 25-36.
Tembe, S., Lockner, D.A., Wong, T.F., 2010. Effect of clay content and mineralogy on frictional sliding behavior of simulated gouges: Binary and ternary mixtures of quartz, illite, and montmorillonite. Journal of geophysical Research 115, B03416.
Tesei, T., Collettini, C., Barchi, M.R., Carpenter, B.M., Di Stefano, G., 2014. Heterogeneous strength and fault zone complexity of carbonate-bearing thrusts with possible implications for seismicity. Earth and Planetary Science Letters 408, 307-318.
Tesei, T., Collettini, C., Carpenter, B.M., Viti, C., Marone, C., 2012. Frictional strength and healing behavior of phyllosilicate-rich faults. Journal of Geophysical Research 117, B09402.
Tesei, T., Collettini, C., Viti, C., Barchi, M.R., 2013. Fault architecture and deformation mechanisms in exhumed analogues of seismogenic carbonate-bearing thrusts. Journal of Structural Geology 55, 167-181.
Tinti, E., Spudich, P., Cocco, M., 2005. Earthquake fracture energy inferred from kinematic rupture models on extended faults. Journal of Geophysical Research: Solid Earth (1978–2012) 110.
Tse, S.T., Rice, J.R., 1986. Crustal earthquake instability in relation to the depth variation of frictional slip properties. Journal of Geophysical Research: Solid Earth (1978–2012) 91, 9452-9472.
Ujiie, K., Tanaka, H., Saito, T., Tsutsumi, A., Mori, J.J., Kameda, J., Brodsky, E.E., Chester, F.M., Eguchi, N., Toczko, S., 343, E., Scientists, T., 2013. Low Coseismic Shear Stress on the Tohoku-Oki Megathrust Determined from Laboratory Experiments. Science 342, 1211-1214.
Ujiie, K., Tsutsumi, A., 2010. High-velocity frictional properties of clay-rich fault gouge in a megasplay fault zone, Nankai subduction zone. Geophysical Research Letters 37, L24310.
Yasuhara, H., Marone, C., Elsworth, D., 2005. Fault zone restrengthening and frictional healing: the role of pressure solution. Journal of geophysical research 110, B06310.

Chapter 6

Discussion and conclusions

6.1 *Introduction*

In this thesis I have presented field and microstructural observations of fault zone characteristics from two natural, shallow-crustal fault zones. Each field study was complemented by a follow-up experimental study, to better constrain the frictional behaviour of the natural fault zones. Complementary field and experimental studies also allowed the microstructures developed under experimental conditions to be compared with those observed in nature, enabling an appraisal of what can (and cannot) be inferred from natural fault rock textures in terms of deformation mechanisms and fault behaviour. A detailed discussion of results has been presented at the end of each research chapter. This final chapter serves to highlight and compare the main findings of the foregoing chapters. I will further go on to discuss the implications of the main findings for the frictional behaviour, microstructural evolution and seismic hazard assessment of shallow crustal fault zones. I will also highlight some important areas for future work. In addition, I will discuss some of the limitations associated with the work completed for this thesis, and how the results of some recently published work by other authors compliment the results of my already-published work presented in Chapters 2 and 3.

6.2 *Summary and comparison of main findings*

6.2.1 *Fault zone architecture and deformation mechanisms of natural fault zones in cohesive vs. poorly lithified sediments*

In Chapter 2 we presented observations from the Gubbio normal fault zone in the Italian Apennines, which has accumulated a maximum displacement of 3.2 km since the Miocene (Collettini et al., 2003), and along which there was an Ms = 5.2 earthquake in 1984 (Haessler et al., 1988). The fault rocks studied have been exhumed from ~2.5-3 km (Bussolotto et al., 2007), and thus give an insight into deformation processes occurring within 2.5-3 km depth along a periodically seismogenic fault. It deforms a mixture of limestone and phyllosilicate-enriched marly limestone of the Scaglia Rossa Formation, both of which are well lithified. The fault zone comprises a damage zone, up to 220 m wide, which bounds a fault core of up to 15 m wide. The fault core is sub-divided into domains with different compositional and structural characteristics. In domains derived from the limestone, deformation is characterized by pervasive fracturing, veining and brecciation. The limestone-dominated domains also host localized (≤1.5 mm wide) principal slip zones (PSZs), which are characterized by the development of cataclasites, gouges and calcite veins. These observations suggest that the dominant deformation mechanisms in the limestone-dominated parts of the fault core are fracturing and hydrofracturing, with additional cataclasis and frictional sliding occurring within the PSZs.

In domains derived from the phyllosilicate-enriched marly limestone, deformation is characterized by a pervasive S-C foliation, where the foliation is defined by phyllosilicate-rich solution seams. The dominant deformation mechanism in these domains is inferred to be pressure-solution. Slip occurs within the solution seams via pressure-solution creep and is distributed across the whole domain, rather than being accommodated within localized PSZs.

In Chapter 4 we presented observations of seismogenic faults of the Masada fault zone, part of the Dead Sea fault system in Israel. This normal fault zone deforms near-surface (the studied section has been buried to depths of <10 m), poorly-lithified, high-porosity (up to 50%), lake sediments, which were brine-saturated at the time they were deformed. The sediments comprise alternating, seasonally-controlled laminae of ultrafine-grained aragonite (summer) and clay-rich clastic detritus (winter). Individual faults have displacements of up to ~3.4 m. Studying these faults gives insights into the deformation processes occurring at burial depths of <0.05 km within a periodically seismogenic fault zone. The faults typically comprise a damage zone, up to 16 m wide, bounding a fault core of up to 30 cm wide. Fault cores are characterized by clusters of disaggregation bands (a type of deformation band (Fossen et al., 2007). However, the majority of displacement within the fault core is accommodated by a single disaggregation band, which we refer to as the PSZ. PSZs are typically up to a few mm wide. The dominant deformation mechanism in the fault cores, including within the earthquake-hosting PSZs, is thought to be particulate flow.

The gross architecture of both of the seismogenic fault zones studied conforms to the standard fault core – damage zone model that applies to many upper-crustal fault zones and is discussed in Chapters 2 (Section 2.1) and 4 (Section 4.1). It is evident from these natural examples, however, that the deformation mechanisms and the resultant deformation products within the fault core can be highly variable as a result of: 1) lithological variations within the fault core; and 2) the degree of lithification of the material (which may be considered equivalent to the depth at which deformation took place). Furthermore, the presence of phyllosilicates at Gubbio appears to promote a more distributed style of deformation, through development of a pressure-solution foliation. At Masada, on the other hand, the presence of phyllosilicates seems to promote a highly localized style of deformation, through clay smear. Phyllosilicates may therefore affect fault zone architecture in different ways, depending again on the depth at which they occur, but also on the way in which they are distributed in the protolith. For example, if the phyllosilicates are concentrated in clay-rich sedimentary layers, then clay smear is a feasible deformation mechanism. If the phyllosilicates are disseminated throughout the host-rock, on the other hand, clay-smear is perhaps less likely and pressure-solution is more likely to be important. If, however, the pressure solution leads to the concentration of phyllosilicates along a PSZ, this too may enhance shear localization.

Based on our observations, it seems that the architecture of, and dominant deformation mechanisms operating within, a particular fault zone in the upper crust may vary significantly, firstly as a function of depth, and secondly as a function of lithological heterogeneities in the protolith, which the fault may encounter, either along strike, or down-dip, as it transects the crust. Some of these heterogeneities are found in the host rocks and may be unrelated to deformation (e.g. variations in lithology) whilst others may be inherited from the earlier movement history of the fault zone concerned, e.g. due to the juxtaposition of contrasting hangingwall and footwall lithologies. The resultant spatial variation in fault zone characteristics may have significant implications, first for the fluid-flow properties of fault zones, although this is something we do not discuss in this thesis, and second for the distribution of seismicity and aseismic creep behaviours within a fault zone, which will be discussed in Section 6.3.1.

6.2.2 *Frictional behaviour of experimental faults deformed under shallow-crustal conditions*

Each of the field studies conducted during this research provided motivation for conducting experimental studies into the frictional behaviours of the earthquake-hosting PSZs. In the case of the Gubbio fault, we wanted to know what effect variable phyllosilicate content and fluid content within the PSZs would have on the frictional behaviour of the faults during earthquake propagation. We conducted experiments at seismic slip velocities (1.3 m/s), and at a normal stress of 9 MPa, on synthetic gouges containing a mixture of calcite + phyllosilicate. Experiments were performed under both room-humidity and water-saturated conditions. It was found that under water-saturated conditions, the phyllosilicate-bearing gouges were incredibly weak and exhibited little to no fracture energy. This is a result obtained also in previous similar studies performed on clay-rich gouges (Faulkner et al., 2011; Ferri et al., 2011; Ferri et al., 2010; Ujiie et al., 2013; Ujiie and Tsutsumi, 2010; Ujiie et al., 2011), but our results show for the first time that such weak behaviour is reproduced even when clay content is as low as 10-20 wt.%.

In the case of the Masada Fault zone, we wanted to better understand the processes that enable ruptures to propagate to the surface through poorly lithified sedimentary sequences. Thus we performed sub-seismic rate-and-state friction experiments, to assess the frictional stability of the Lisan faults, and seismic-velocity friction experiments, to assess the behaviour of the Lisan faults during earthquake propagation. Experiments were performed on synthetic gouges derived from disaggregated Lisan sediment, at normal stresses ranging from 1-18 MPa, and under room-humidity, water-saturated and brine-saturated conditions. During the sub-seismic velocity experiments, it was found that at 1 MPa, i.e. at near-surface conditions, the Lisan gouges were velocity-strengthening, and this behaviour was strongest in the fluid-saturated gouges. However, at

18 MPa, i.e. representative of a depth of ~1 km in the crust, the likelihood of frictional instability increased, and particularly so with increasing displacement accumulation. The exception was the brine-saturated gouge, which remained velocity-strengthening under all conditions tested. Frictional healing rates were found to be greatest in the fluid-saturated gouges and, contrary to what is typically expected (e.g. Dieterich and Kilgore, 1994), were greater at 1 MPa than at 18 MPa.

During the seismic velocity experiments performed at 1 MPa, all gouges have large slip-weakening distances on the order of tens of metres. However, frictional behaviour again becomes more unstable with increasing normal stress, as the slip-weakening distance decreases according to a power law fit, to <<1.7 m at normal stresses of 9 and 18 MPa. As with the results obtained for the water-saturated clay-bearing gouges of the Gubbio fault zone, it was observed that the fluid-saturated gouges have negligible fracture energy, suggesting that the clays within the Lisan gouges again have a significant influence on their frictional behaviour.

These results show that gouge composition (i.e. clay content), fluid presence and composition, normal stress and slip-rate can all significantly influence the frictional stability and dynamic weakening behaviour of fault gouges in the shallow crust. Future work could investigate how frictional stability changes over greater depth ranges, and also under varying fluid-saturation conditions, for example using different brine compositions and degrees of saturation.

6.2.3 *Slip zone processes in naturally vs. experimentally deformed shallow crustal fault zones*

Slip zone microstructures in natural shallow crustal fault zones can potentially reveal the deformation mechanisms operating during fault slip. For faults in low-porosity, cohesive rocks (e.g. the Gubbio fault), PSZs are up to 1.5 mm wide, although shear-localization zones <5 μm wide are also developed. The PSZs are characterized by ultracataclasites and gouges, composed of a mixture of calcite and phyllosilicate. The dominant deformation mechanism is inferred to be cataclasis, although the presence of phyllosilicate-rich stylolitic surfaces within the PSZs indicates that pressure-solution also operates in some cases. The occurrence of calcite veins within the PSZs indicates that fluids likely play an important role in faulting. In some PSZs, we also observed degassing bubbles, recrystallized calcite crystals and clay mineral transformations, all of which imply some frictional heating within the PSZ at some time in the geological past and confirming that at least some of these faults have slipped seismically.

The slip zones produced during the complementary seismic velocity experiments at 9 MPa on mixed calcite + phyllosilicate gouges (Chapter 3) are characterized as follows. The room-humidity

gouges are characterized by localized slip along a sharp, smooth PSS. Adjacent to this surface is a variably developed PSZ, within which grain size is reduced to the nanoscale, and microstructural evidence of calcite decarbonation (e.g. degassing bubbles) is present. The dominant deformation mechanism is inferred to be cataclasis, with frictional sliding occurring predominantly along the PSS. The water-saturated gouges are characterized by a more distributed style of deformation. They lack a sharp PSS or a PSZ, and although significant grain size reduction has occurred, it is not as intense as in the room-humidity gouges. Deformation is therefore inferred to occur via a mixture of cataclasis and frictional sliding on weak water-saturated phyllosilicate laminae, which are distributed throughout the gouge. There is no microstructural evidence preserved for calcite decarbonation in the water-saturated gouges, suggesting that the distributed style of deformation, and the low friction values, inhibit significant frictional heating.

It thus seems that the microstructures produced during the room-humidity experiments are most comparable to those of the natural slip zones at Gubbio. However, this contradicts field observations that suggest fluids were in frequent interaction with the natural slip zones. This may lead one to question how representative experimentally produced slip zone microstructures are of natural slip zone microstructures. One of the limitations associated with high-velocity friction experiments is that, to date, they are typically only conducted at room temperature and at normal stresses <20 MPa (Di Toro et al., 2011), representing crustal depths of <1 km. At greater depths in the crust, where ambient temperature and confining pressure are greater, the potential for frictional heating will increase. This means that even in fluid-saturated, clay-bearing gouges, cataclasis and slip-localization may occur and produce microstructures more akin to those produced in our room-humidity experiments.

For faults in high-porosity, incohesive rocks (e.g. those of the Masada fault zone), PSZs are typically up to a few mm wide. Material within the PSZs comprises a mixture of the aragonite and clay-rich clastic material derived from the host rock. Aside from some mechanical disaggregation of delicate rosettes of aragonite, the sizes and shapes of grains within the slip zone are the same as those observed in the protolith. However, there is a preferential alignment of elongate clasts towards the direction of shear. The lack of damage to grains implies that the dominant deformation mechanism is particulate flow. No seismic markers were identified within the PSZs, but the faults are known to have slipped seismically during their history, due to their close spatial associations with seismites (Agnon et al., 2006; Marco and Agnon, 1995). The absence of seismic markers is likely due to a number of reasons. First, the shallow depth of faulting, which would result in lower values of the shear stress during fault slip, compared to those at greater depth. Thus, the frictional heat generated during fault slip would be less (refer to Eq. 1, Chapter 2). Second, deformation

within the PSZs occurs via distributed particulate flow, rather than by localized cataclasis. The distributed style of deformation within the PSZs would further reduce the potential for significant frictional heating. In addition, dilation of the PSZs during fault slip would result in less grain-to-grain contact interaction, and thus also limit the potential for flash heating.

The slip zones produced during the complementary experiments performed on the Lisan sediments (Chapter 5) are quite variable depending on the conditions under which they were deformed. At 1 MPa, which is the normal stress condition most representative of the naturally deformed sediments, *all* (i.e. in the room-humidity and in the fluid-saturated gouges) of the gouges deformed, at both sub-seismic and seismic velocity, have similar microstructures. They typically contain a rough boundary-shear and sometimes a weakly developed Riedel-shear fabric within the gouge layer. Clasts are typically imbricated and aligned towards the direction of shear. A limited amount of grain size reduction occurs in the room-humidity gouges, but in the fluid-saturated gouges, grain size reduction appears to be almost absent. The dominant deformation mechanism in all of these gouges therefore appears to be particulate flow, facilitated by the low normal stress. In addition, no evidence for significant frictional heating is observed in any of the high-velocity experiments performed at 1 MPa.

Thus, in the case of the Masada fault zone, the experimentally produced microstructures at 1 MPa replicate well the natural slip zone microstructures, which were also formed under a normal load of ~1 MPa. So it seems it is possible for high-velocity friction experiments to reproduce natural fault zone processes, but only if the deformation conditions are truly representative. Indeed, the differing microstructures observed in the remainder of the experiments performed on the Lisan sediments, which were performed at 9 and 18 MPa, e.g. intense cataclasis and shear localization during the sub-seismic velocity experiments, show that deformation mechanisms and the resulting microstructures are rather sensitive to variations in normal stress.

On a similar note, the compositions of the PSZs at Gubbio and at Masada are very similar – they both contain a mixture of calcite and phyllosilicate, although the quantities and proportions of phyllosilicates may vary - and we infer that both fault zones were fluid-saturated during deformation. Therefore, one might expect to observe similar microstructures in the PSZs, but this is not the case. The differences in deformation mechanisms and resulting microstructures are again most likely due to the different depths at which they were deformed. The shallow depth at which the Lisan faults were formed, and the consequent poor lithification and high porosity of the sediment, result in dilation during shear, which facilitates the rolling and sliding of particles (Borradaile, 1981). The greater confining pressure during deformation at Gubbio, and the

consequent low porosity of the Scaglia Rossa Formation, would tend to prevent gouge dilation and subsequent particulate flow (unless perhaps transient thermal pressurization should occur within the PSZs during seismic slip), and thus strain localization is more likely to occur due to fracturing and cataclasis.

Normal stress is not the only factor controlling deformation mechanisms, however. During both experimental studies (i.e. the Gubbio-related experimental study and the Masada-related experimental study), we performed experiments at seismic slip-velocity on fluid-saturated gouges at a normal stress of 9 MPa. Seeing as gouge composition is also similar, one would expect to see similar microstructures produced. However, the microstructure produced during the Gubbio-related study was characterized by distributed cataclasis (although cataclasis was much less intense than in the room-humidity gouges), whereas in the Masada-related study, it was characterized by distributed particulate flow. These results may be considered similar so far as that in both cases deformation is more distributed and cataclasis is less intense in the fluid-saturated gouges compared to in the room-humidity gouges. However, in the Gubbio study, cataclasis is still an important deformation mechanism in the fluid-saturated gouges, whereas in the Masada study, cataclasis appears to be absent. Given the identical experimental conditions, the reason for this is presumably related to material properties. For example, the crystalline structure, size and shape of calcite/aragonite grains in the starting materials are different. The undeformed gouge used in the Gubbio experiments comprised angular calcite grains of up to 250 μm in size, whereas that used in the Lisan experiments comprised aragonite grains which were predominantly <15 μm in size and with acicular shapes. Therefore, it may be that the finer grain size facilitates particulate flow, because grains are better able to translate without locking up or abrading one another.

Although some of the microscale deformation processes occurring within the studied gouges are not well constrained, it is evident from our combined field and experimental observations that the dominant deformation mechanisms within fault slip zones are strongly affected by variations in gouge composition, fluid presence (and composition), normal stress and slip-rate. As discussed in Section 6.2.2, frictional behaviour is also found to be highly dependent on these factors. This suggests there may be a link between deformation mechanisms and frictional behaviour, although the results obtained during our Masada-related experimental study (Chapter 5), suggest that such a link is not simple. To our knowledge, no previous works have investigated how the deformation mechanisms acting within fault slip zones may affect the dynamics of a propagating rupture. For example, what is the difference in the energy required to fracture grains compared to that required for grain rolling and grain-boundary sliding? Investigating in more depth the relationship between deformation mechanisms and frictional behaviour seems an important area for future study. If we

are able to better deduce the past seismic behaviour of a natural fault zone by studying preserved microstructures, it will improve our ability to forecast future seismic behaviour.

Something we did not look into during these studies was the specific thermally-activated dynamic weakening mechanisms that operate during the room-humidity experiments performed at seismic slip velocity. Most previous studies of dynamic-weakening mechanisms at seismic slip velocity have concentrated on gouges dominated by a single mineral phase (Di Toro et al., 2011 and references therein). It would therefore be interesting to probe how dynamic weakening mechanisms vary in multi-phase gouges, such as our calcite + phyllosilicate gouges, where the phyllosilicates would thermally decompose at a lower temperature than the calcite, and the thermodynamics of this reaction would subsequently affect the thermodynamics of the calcite decomposition reaction. Such a study would be more representative of the processes occurring in a natural fault gouge, which is rarely composed of just a single mineral phase.

6.3 *Implications of main findings*

6.3.1 *Implications for the frictional behaviour and the seismic hazard posed by shallow-crustal faults*

The results of Chapter 2 suggest that lithology may play an important role in the distribution of seismicity within a fault zone. It is suggested that the limestone-dominated parts of the fault core would tend to behave predominantly in a velocity-weakening manner, whereas the phyllosilicate-rich marly limestone-dominated parts of the fault core might behave predominantly in a velocity-strengthening manner. Thus, the propagation of earthquake ruptures would be favoured in the limestone-hosted parts of the fault, whilst the marly limestone-hosted parts of the fault may act as a barrier to rupture propagation, and instead would accommodate slip aseismically by fault creep. Similar conclusions on the role of phyllosilicates in fault zones have been reached by other authors (e.g. Gratier et al., 2013; Tesei et al., 2013; Thomas et al., 2014).

The results from our experimental study in Chapter 5 suggest, however, that such models and inferences made from natural fault zones may be an oversimplification. First, despite the well-documented velocity-strengthening nature of phyllosilicates at sub-seismic slip rates, it is evident from our work presented in Chapter 3, and from the work of others (Faulkner et al., 2011; Ferri et al., 2011; Ferri et al., 2010; Ujiie et al., 2013; Ujiie and Tsutsumi, 2010; Ujiie et al., 2011), that if subject to seismic slip rates, phyllosilicates can favour rupture propagation, rather than acting as a barrier. Second, the results presented in Chapter 5 show that the frictional stability of materials in the shallow crust is very sensitive to subtle variations in normal stress (i.e. the depth of burial), the

presence and type of pore fluid, and the accumulated displacement/developed microstructure in the gouge layer. These results are consistent with those of several previous studies, which show that rate and state frictional behaviour can vary considerably according to numerous factors such as composition (e.g. Niemeijer and Vissers, 2014; Tembe et al., 2010; Tesei et al., 2014), normal stress (e.g. den Hartog et al., 2012; Ikari et al., 2007; Marone et al., 1990; Niemeijer and Vissers, 2014), fluid presence (e.g. Frye and Marone, 2002; Ikari et al., 2007; Scuderi et al., 2014), temperature (e.g. den Hartog et al., 2012; Scuderi et al., 2013; Verberne et al., 2010), slip velocity (e.g. Boulton et al., 2014; Ikari et al., 2009; Niemeijer and Vissers, 2014), grain shape/size (e.g. Anthony and Marone, 2005; Knuth and Marone, 2007; Mair et al., 2002), gouge thickness (e.g. Byerlee and Summers, 1976; Marone et al., 1990) and accumulated strain/displacement (e.g. Collettini et al., 2011; Ikari et al., 2011; Logan et al., 1992). Thus, to associate a certain rock type with a single style of frictional behaviour, without taking into account how that behaviour may vary along strike and dip due to variations in the aforementioned environmental conditions and inherited fault characteristics, will lead to over-simplified and inaccurate predictions of seismic behaviour. A large degree of caution should therefore be taken when up-scaling the results of laboratory experiments to assessing the seismic potential of a fault zone.

Another point to highlight is that, as demonstrated in Chapter 5, velocity-strengthening materials should not necessarily be associated with fault creep during all stages of the seismic cycle. Although velocity-strengthening behaviour will promote stable fault slip if the fault is subject to a velocity perturbation, low healing rates are required if a fault is going to creep during the inter-seismic period. This is a condition which is met for phyllosilicate-rich fault gouges, as phyllosilicates have been shown to exhibit both velocity-strengthening behaviour and very low, even negative, values of frictional healing (Carpenter et al., 2011; Tesei et al., 2012). However, our experiments performed on the Lisan gouges in Chapter 5 showed that the gouges which exhibited the strongest velocity-strengthening behaviour were also the ones with the highest healing rates. This implies that if the velocity-strengthening regions of the faults in the Lisan Formation were to attenuate earthquake propagation, then the generated stress perturbation would accumulate as elastic energy, resulting in greater stress drops during aftershocks or future seismic events. Thus, the presence of poorly lithified sediments with velocity-strengthening frictional properties in the shallow-most portion of the crust will not necessarily result in aseismic afterslip, as is often supposed (Marone and Scholz, 1988; Marone et al., 1991), but instead could result in damaging aftershocks. The 2010 M_w 7.8 Mentawai earthquake, which ruptured the shallow portion of the megathrust up-dip from the 2007 M_w 8.5 Sumatra earthquakes, may serve as an example of such a scenario (Lay, 2015).

It follows from the preceding discussion that, even if a large fault patch with predominantly velocity-strengthening frictional properties does exist, a propagating rupture from an adjacent velocity-weakening fault patch may still have enough energy to overcome the resistance provided by the velocity-strengthening fault patch, leading to unstable slip. At this point dynamic weakening comes into play (Noda and Lapusta, 2013). If the energy released at the front of a propagating rupture tip exceeds the energy dissipated during propagation, then slip will be able to accelerate (French et al., 2014; Griffith, 1920; Kanamori, 2001). In simple terms, the total energy dissipated during rupture propagation is a sum of the radiated energy, plus work done by frictional and fracture processes (Kanamori and Rivera, 2006). Thus, the lower the frictional strength of a fault, and the lower the fracture energy (also a function of the slip-weakening distance), the easier it will be for a rupture to propagate. The results of our high-velocity experiments in Chapters 3 and 5 show that, particularly at normal stresses in the range 9-18 MPa, where the slip-weakening distance is typically $<<1$ m, and steady-state friction values are <0.3, rupture propagation would be very likely, provided the slip associated with propagating rupture exceeds the slip-weakening distance. Rupture propagation would be even more feasible in the case of the fluid-saturated clay-bearing gouges, which weaken to steady-state friction values which are often <0.1 over slip-weakening distances of $<<0.1$ m. Using the average slip values for an earthquake of given magnitude presented by Sibson (1989), slip-weakening distances in the range 0.4-1 m, as observed for room-humidity gouges, would enable the propagation of M $\geq$6-7 earthquakes, whilst slip-weakening distances of <0.1 m, as observed for fluid-saturated clay-bearing gouges, would enable the propagation of M >5 earthquakes. These values are broadly consistent with seismological observations that only earthquakes of M $\geq$5.5 commonly rupture the surface (e.g. Bonilla et al., 1984; Wells and Coppersmith, 1994).

Although the studies presented here relate to two specific natural fault zones, the results are of relevance to fault zones in a wide range of tectonic settings. Phyllosilicates are common fault zone constituents; they are prevalent within clay-rich fault gouges of mature continental fault zones (e.g. Faulkner et al., 2003; Holdsworth, 2004; Vrolijk and van der Pluijm, 1999; Wu et al., 1975) and within accretionary wedge sediments at subducting plate interfaces (e.g. Chester et al., 2013; Ide et al., 2011; Lay et al., 2005). As shown in Chapters 2 and 4, clay smear and pressure-solution processes can also result in the concentration of phyllosilicates within narrow PSZs. Seeing as fluids are also present throughout much of the upper crust, the weakness of fluid-saturated clay-bearing gouges is therefore likely to affect the frictional behaviour of many fault zones worldwide and may go some way towards explaining surprisingly large (up to 60 m) near-surface co-seismic displacements, such as those generated during the 2010 M_w 8.8 Maule, Chile (Delouis et al., 2010;

Lay et al., 2010) and 2011 M_w 9.0 Tohoku, Japan (Ide et al., 2011) earthquakes. A pertinent on-land example of where phyllosilicate-rich gouges could generate unexpected co-seismic rupture is the San Andreas fault zone, which has a famous 'creeping' segment (Titus et al., 2006), perceived to have low seismic hazard. The creeping behaviour of the segment is attributed to the presence of smectitic phyllosilicates in fault gouges, which are frictionally weak, and exhibit velocity-strengthening behaviour, as well as low values of frictional healing (e.g. Carpenter et al., 2011; Holdsworth et al., 2011; Lockner et al., 2011). However, an earthquake propagating from an adjacent locked segment of the fault could result in an unexpected co-seismic rupturing of the entire creeping segment (French et al., 2014).

In the light of significant advances in both the realms of seismology and laboratory friction experiments over the past two decades, it is evident that the traditional conceptual model of poorly-lithified and/or phyllosilicate-rich fault gouges or sedimentary packages in the shallow crust acting as barriers to rupture propagation is vastly oversimplified, and needs to be revised. Our experimental results indicate several different conditions under which rupture propagation through such materials could be favoured. Indeed, the results of our rate-and-state experiments suggest that under certain conditions, it is even possible for earthquakes to nucleate on a fault at just 1 km depth. With this in mind, we perhaps should not be surprised by recent seismological observations of 'tsunami earthquakes', which nucleate at shallow depths of <15 km (e.g. Bilek and Lay, 2002; Kanamori, 1972; Pelayo and Wiens, 1992). The combined field and experimental observations presented in this thesis therefore call for an updated model of fault frictional behaviour based on the results of a comprehensive programme of laboratory friction experiments performed over a much wider range of slip rates and crustal conditions.

Another important topic that should be investigated further is the role that low-rigidity materials in the shallow part of the crust, such as those of the poorly lithified Lisan Formation, may play in controlling rupture velocity and ground motions. The suggestion that low-rigidity materials may be responsible for the unusual seismological characteristics of tsunami earthquakes (e.g. Bilek and Lay, 1999; Pelayo and Wiens, 1992; Satake and Tanioka, 1999) is based on theoretical reasoning, and remains to be tested by either experimental or modelling techniques. Maybe the operation of particulate flow in seismogenic faults in poorly lithified sediments could represent a viable alternative hypothesis to the low-rigidity materials hypothesis for explaining the seismological characteristics of tsunami earthquakes. Again, however, as discussed in Section 6.2.3, further work is required to link deformation mechanisms to observed seismological characteristics.

6.3.2 *Implications for the identification of seismic markers in natural fault zones*

The microstructures produced during our high-velocity friction experiments show that, only when cataclasis is the dominant deformation mechanism (which is only observed during room-humidity experiments), does slip localize onto a PSS. Cataclasis leads to the localization of slip, whereas deformation via frictional sliding on weak phyllosilicate laminae or via particulate flow (as observed during fluid-saturated experiments on clay-bearing gouges) results in a distributed style of deformation across the whole gouge layer. Localized slip is a prerequisite for significant frictional heat to be generated (Rice, 2006) and, consequently, classical seismic-slip indicators are only observed in the gouges deformed under room-humidity conditions. This is not particularly representative of upper-crustal fault zones, the majority of which will contain fluids to some degree. Further to this, during the experiments performed on the Lisan gouges at 1 MPa, almost identical microstructures were produced during deformation at both sub-seismic and seismic velocities. These observations highlight the difficulties and limitations associated with identifying faults which have slipped seismically or aseismically in natural fault zones, without even considering the added ambiguities presented by the overprinting of transient co-seismic deformations by post-seismic and inter-seismic processes and/or poor preservation. Any attempts to differentiate seismic from aseismic slip, based on microstructure alone, should therefore be approached with a high degree of caution. A thorough review of the criteria for seismic slip, and of the limitations associated with the experimental reproduction of the seismic slip indicators observed in natural fault zones, is presented in a recent review paper by Rowe and Griffith (2015).

6.4 *Limitations*

6.4.1 *Experimental procedure*

The first limitation associated with our experimental procedure relates to the sample holder used, which comprises solid cylinders of 25 mm diameter. This can produce imprecise data for two reasons: 1) as described in Chapter 1 (Section 1.4.4.3), for a given angular speed, the slip rate increases from the centre to the outer edge of the sample. The velocity gradient across the sample will also result in a variable thermal evolution across the sample and a subsequent uneven thermal dilatancy and normal stress distribution, which both affect the measured friction (Di Toro et al., 2010; Kitajima et al., 2010). The equivalent slip rate would be better constrained using a larger cylinder with a hollow centre, where there is a smaller difference between the external and internal radius, such as that used with the slow to high velocity apparatus (SHIVA) installed at INGV in Rome (e.g. Smith et al., 2013). Inconsistencies or imprecisions in our results may also have been produced by using a Teflon ring to confine the gouge. Particularly in the cases where we first cut

the Teflon ring before fitting and tightening it around the sample (as in Chapter 3), there would have been variable discrepancies in the smoothness of the ring, as a groove or step is created where the Teflon has been cut. This could be a cause of noise in some the data, and may also have increased the amount of Teflon shearing and subsequent Teflon contamination within the deformed sample. In addition, differences in the fitting and tightness of the Teflon ring likely resulted in variable gouge loss during the experiments, which may have affected the consistency of our results. An all-steel sample holder, such as that used with SHIVA, would negate the need to use a Teflon ring to confine the gouge sample, this eradicating such issues.

By using steel cylinders as the wall rock during our experiments, we were not able to simulate accurately the rheological contrast (e.g. due to differences in factors such as cohesion, grain size, porosity, permeability and mineralogy) that would occur in nature between the gouge and the host rock. Such rheological contrasts could be important for determining how slip is accommodated or localized along a fault (Rowe and Griffith, 2015). On a similar note, all of our high-velocity friction experiments were performed on synthetic gouge samples that had no pre-existing micro-structural fabric. Typically in nature, fault gouges will have acquired a deformation fabric during their history; thus in future it would be worthwhile to perform high-velocity experiments on samples that have first undergone a run-in phase at sub-seismic slip velocity in order to create a fabric that may be similar to that produced during the interseismic period in a natural fault gouge.

Another limitation of our experiments is the inability to perform experiments at normal stresses or temperatures that are representative of the seismogenic regime (~5-35 km depth, depending on the tectonic setting). The maximum normal load we were able to apply using the LHVRS at Durham University was 20 MPa, which equates to only ~1 km depth. The current maximum normal load capability of any high-velocity rotary shear apparatus worldwide is 50 MPa (SHIVA), which still only equates to ~3 km depth. Given that, in my experiments alone, a high degree of variability was observed in both frictional behaviour and microstructure over a very narrow range of normal stresses (1-18 MPa), it is evidently important to select very carefully the normal stress at which experiments are performed. With present capabilities, it is difficult to know exactly how representative our experimental results are of natural fault behaviour, but it is widely acknowledged that at higher normal loads dynamic weakening would be triggered at slower speeds and smaller slip distances (e.g. Di Toro et al., 2011).

The other major limitation associated with our experimental procedure is the inability to monitor or control pore fluid pressure during the experiments. Only very recently have technical developments been made that are helping to overcome this limitation (Violay et al., 2015; Violay et al., 2013), but

such methods are still under development. Although the axial load system used in our experiments is equipped with a high-precision air regulator to automatically correct load fluctuations during experiments, there is inevitably a time-lag between the increase/decrease in pore fluid pressure during the experiments and the adjustment of the axial load. In addition, the measured axial load is a bulk measurement across the whole sample and thus does not account for localized pockets of elevated pore fluid pressure within the gouge layer. It is possible that during certain stages of the experiment, or in certain regions of the deforming gouge layer, the effective normal stress may have been much lower than the bulk applied normal load. This possibility should be kept in mind when interpreting some of the mechanical data and microstructures.

6.4.2 *Sample recovery and thin section preparation*

Some of the materials that I have studied in this thesis were very difficult to work with. For example, the clay-rich rocks and gouges that I studied were very friable and some of them contained swelling clays, and the Lisan sediments were very poorly lithified. This made thin-section preparation rather challenging. Many samples did not survive the thin-sectioning process, and those that did were often of poor quality due to loss of material during preparation. The incohesion of many of the samples also meant that microstructures were at risk of being disturbed during sample preparation. For example, grains may have been re-arranged when samples were cut, or when they were impregnated with resin. In addition, in the experimental samples, it is possible that microstructures were altered when samples relaxed on removal of the normal load.

6.5 *Recent developments*

Considering that the work presented in this thesis on the Gubbio fault was carried out predominantly during 2011-2013, and published in early 2014, it seems appropriate to mention some recent work that has been published on a similar theme. The work of Tesei et al. (2013), which we refer to in Chapter 2, also studies the architecture and deformation mechanisms of a carbonate-bearing thrust in the Northern Apennines of Italy, which deforms rocks of similar composition to those deformed at Gubbio. Their observations are similar to ours in that where faults transect massive/competent limestones, they are highly localized and exhibit predominantly brittle deformation. Where faults transect bedded or marly limestones, on the other hand, they form wide zones of foliated rocks characterized by pervasive pressure-solution deformation. This lead them to propose a mechanical/seismogenic model analogous to that which we propose for the Gubbio fault, in which seismogenesis is concentrated in the massive limestone dominated parts of the fault core, whilst the parts of the fault core dominated by foliated marls deform predominantly aseismically. Tesei et al. followed up this work by performing rate-and-state friction experiments

on the contrasting materials from the fault zone, i.e., on the competent limestones and foliated marls (Tesei et al., 2014). Their results agree with their original seismogenic model, and with the hypothesis presented in Chapter 2 of this thesis: the competent limestone material exhibited high frictional strength and a tendency for velocity-weakening behaviour, whilst the foliated marls exhibited low frictional strength and predominantly velocity-strengthening behaviour. This work thus strengthens the reasoning behind the proposed model of fault zone behaviour presented in Chapter 2 for the Gubbio fault.

Another highly relevant piece of work by Smith et al. (2015) was published shortly after the work in Chapter 3 (Bullock et al., 2015) of this thesis was published. The study of Smith et al. (2015) aimed to determine the role of strain localization during dynamic weakening of calcite gouges deformed at seismic slip rates. This was achieved by performing two types of high-velocity friction experiment: 1) single-slide experiments and 2) slide-hold-slide experiments. In addition, certain experiments were arrested during the early stages of slip (0.01-0.35 m) to investigate the microstructural evolution of the gouges during the transition from initial strengthening to dynamic weakening. This micro-analytical approach is very similar to that adopted during the study presented in Chapter 3 of this thesis. The results of the Smith et al. study are in agreement with some of the conclusions reached in Chapter 3 (in the case of our dry calcite+clay gouges), in that: 1) they attribute the initial strain-hardening phase during high-velocity experiments to brittle fracturing and cataclasis; 2) they show that strain localization is critical to the onset of dynamic weakening.

6.6 *Conclusions*

The work set out in this thesis illustrates a range of deformation processes and behaviours present in both natural and experimentally-simulated shallow-crustal fault zones, with broad implications for the frictional behaviour, microstructural evolution and seismic hazard potential of upper-crustal fault zones. These are summarised schematically in Fig. 6.1 and described below:

- Fault frictional behaviour is likely to be highly variable along both strike and dip, as a result of variations in protolith lithology (composition, degree of lithification), fluid presence/composition, depth and fault maturity/inherited microstructure. Such factors need to be taken into careful consideration in order to produce more informed earthquake forecasting models.
- Our results show that is not generally possible to make a clear distinction between stable and unstable patches within a fault zone. It is likely that the frictional properties of fault patches

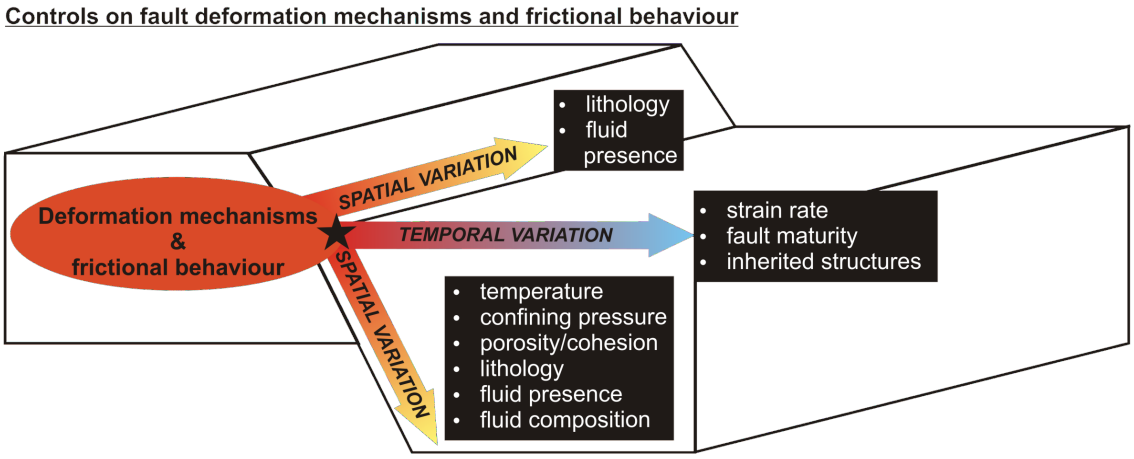

Figure 6.1 Schematic diagram showing how the deformation mechanisms and frictional behaviour at a point on a fault may vary both spatially (laterally and with depth) and temporally, due to the factors listed.

change over time as fault zone characteristics evolve, and that interactions between adjacent fault patches may produce complex fault slip behaviour.

- The dominant deformation mechanisms operating with a fault zone, which are dependent upon depth, fault rock composition, fluid presence and composition, and strain-rate, will control: 1) fault zone architecture and therefore the distribution of seismicity within a fault zone; and 2) slip zone processes, which will subsequently affect the frictional behaviour of a fault.
- Phyllosilicates can play several important and varying roles within a fault zone, even if they are only present in small amounts. The role they play depends on the way in which they are distributed throughout the fault zone, the depth of deformation, and on the presence and composition of the fluids present. First, they affect the deformation mechanisms operating within a fault zone, e.g. they promote pressure-solution during the inter-seismic period and promote particulate flow within fault slip zones during both seismic and aseismic fault slip. Subsequently, they can affect the style of deformation within a fault zone by promoting either localized (e.g. via clay-smear) or distributed (e.g. via the development of a pressure-solution foliation) deformation. Third, they have a significant effect on frictional behaviour, e.g. they may promote stable fault slip during the inter-seismic and post-seismic periods, but will promote unstable dynamic weakening behaviour during co-seismic slip.
- Fluids play an important role in determining the frictional behaviour of gouges deformed at both sub-seismic and seismic slip velocities. They also affect the dominant deformation mechanisms and resulting microstructures produced during friction experiments. Fluid

composition (i.e. water vs. brine) can also be important in determining the frictional behaviour of a fault.

- The deformation mechanisms operative during seismic slip within shallow-crustal fault zones may prevent the development of seismic markers, and therefore any attempts to identify indicators of seismic vs. aseismic slip in shallow-crustal fault zones should be approached with a high degree of caution. This is particularly true in phyllosilicate-bearing faults, where the presence of such minerals will in many circumstances lead to significant weakening across a very wide range of deformation conditions and timescales.

References

Agnon, A., Migowski, C., Marco, S., 2006. Intraclast breccias in laminated sequences reviewed: Recorders of paleo-earthquakes. Geological Society of America Special Papers 401, 195-214.

Anthony, J.L., Marone, C., 2005. Influence of particle characteristics on granular friction. Journal of Geophysical Research: Solid Earth (1978–2012) 110.

Bilek, S., Lay, T., 2002. Tsunami earthquakes possibly widespread manifestations of frictional conditional stability. Geophysical Research Letters 29, 18-11-18-14.

Bilek, S.L., Lay, T., 1999. Rigidity variations with depth along interplate megathrust faults in subduction zones. Nature 400, 443-446.

Bonilla, M.G., Mark, R.K., Lienkaemper, J.J., 1984. Statistical relations among earthquake magnitude, surface rupture length, and surface fault displacement. Bulletin of the Seismological Society of America 74, 2379-2411.

Borradaile, G.J., 1981. Particulate flow of rock and the formation of cleavage. Tectonophysics 72, 305-321.

Boulton, C., Moore, D.E., Lockner, D.A., Toy, V.G., Townend, J., Sutherland, R., 2014. Frictional properties of exhumed fault gouges in DFDP-1 cores, Alpine Fault, New Zealand. Geophysical Research Letters 41, 356-362.

Bullock, R.J., De Paola, N., Holdsworth, R.E., 2015. An experimental investigation into the role of phyllosilicate content on earthquake propagation during seismic slip in carbonate faults. Journal of Geophysical Research: Solid Earth 120, 3187-3207.

Bussolotto, M., Benedicto, A., Invernizzi, C., Micarelli, L., Plagnes, V., Deiana, G., 2007. Deformation features within an active normal fault zone in carbonate rocks: The Gubbio fault (Central Apennines, Italy). Journal of Structural Geology 29, 2017-2037.

Byerlee, J., Summers, R., 1976. A note on the effect of fault gouge thickness on fault stability. International Journal of Rock Mechanics and Mining Sciences & Geomechanics Abstracts 13, 35-36.

Carpenter, B., Marone, C., Saffer, D., 2011. Weakness of the San Andreas Fault revealed by samples from the active fault zone. Nature Geoscience 4, 251-254.

Chester, F.M., Rowe, C., Ujiie, K., Kirkpatrick, J., Regalla, C., Remitti, F., Moore, J.C., Toy, V., Wolfson-Schwehr, M., Bose, S., Kameda, J., Mori, J.J., Brodsky, E.E., Eguchi, N., Toczko, S., 343, E., Scientists, T., 2013. Structure and Composition of the Plate-Boundary Slip Zone for the 2011 Tohoku-Oki Earthquake. Science 342, 1208-1211.

Collettini, C., Barchi, M., Chiaraluce, L., Mirabella, F., Pucci, S., 2003. The Gubbio fault: can different methods give pictures of the same object? Journal of Geodynamics 36, 51-66.

Collettini, C., Niemeijer, A., Viti, C., Smith, S.A.F., Marone, C., 2011. Fault structure, frictional properties and mixed-mode fault slip behavior. Earth and Planetary Science Letters 311, 316-327.

Delouis, B., Nocquet, J.M., Vallée, M., 2010. Slip distribution of the February 27, 2010 Mw= 8.8 Maule earthquake, central Chile, from static and high-rate GPS, InSAR, and broadband teleseismic data. Geophysical Research Letters 37.
den Hartog, S.A.M., Peach, C.J., de Winter, D.A.M., Spiers, C.J., Shimamoto, T., 2012. Frictional properties of megathrust fault gouges at low sliding velocities: New data on effects of normal stress and temperature. Journal of Structural Geology 38, 156-171.
Di Toro, G., Han, R., Hirose, T., De Paola, N., Nielsen, S., Mizoguchi, K., Ferri, F., Cocco, M., Shimamoto, T., 2011. Fault lubrication during earthquakes. Nature 471, 494-498.
Di Toro, G., Niemeijer, A., Tripoli, A., Nielsen, S., Di Felice, F., Scarlato, P., Spada, G., Alessandroni, R., Romeo, G., Di Stefano, G., Smith, S., Spagnuolo, E., Mariano, S., 2010. From field geology to earthquake simulation: a new state-of-the-art tool to investigate rock friction during the seismic cycle (SHIVA). Rend. Fis. Acc. Lincei 21, 95-114.
Dieterich, J.H., Kilgore, B.D., 1994. Direct observation of frictional contacts: New insights for state-dependent properties. Pure and Applied Geophysics 143, 283-302.
Faulkner, D., Lewis, A., Rutter, E., 2003. On the internal structure and mechanics of large strike-slip fault zones: field observations of the Carboneras fault in southeastern Spain. Tectonophysics 367, 235-251.
Faulkner, D.R., Mitchell, T.M., Behnsen, J., Hirose, T., Shimamoto, T., 2011. Stuck in the mud? Earthquake nucleation and propagation through accretionary forearcs. Geophysical Research Letters 38, L18303.
Ferri, F., Di Toro, G., Hirose, T., Han, R., Noda, H., Shimamoto, T., Quaresimin, M., de Rossi, N., 2011. Low-to high-velocity frictional properties of the clay-rich gouges from the slipping zone of the 1963 Vaiont slide, northern Italy. Journal of Geophysical Research: Solid Earth (1978–2012) 116.
Ferri, F., Di Toro, G., Hirose, T., Shimamoto, T., 2010. Evidence of thermal pressurization in high-velocity friction experiments on smectite-rich gouges. Terra Nova 22, 347-353.
Fossen, H., Schultz, R.A., Shipton, Z.K., Mair, K., 2007. Deformation bands in sandstone: a review. Journal of the Geological Society 164, 755-769.
French, M.E., Kitajima, H., Chester, J.S., Chester, F.M., Hirose, T., 2014. Displacement and dynamic weakening processes in smectite-rich gouge from the Central Deforming Zone of the San Andreas Fault. Journal of Geophysical Research: Solid Earth 119, 1777-1802.
Frye, K.M., Marone, C., 2002. Effect of humidity on granular friction at room temperature. Journal of Geophysical Research: Solid Earth (1978–2012) 107, ETG 11-11-ETG 11-13.
Gratier, J.P., Thouvenot, F., Jenatton, L., Tourette, A., Doan, M.L., Renard, F., 2013. Geological control of the partitioning between seismic and aseismic sliding behaviours in active faults: Evidence from the Western Alps, France. Tectonophysics 600, 226-242.
Griffith, A.A., 1920. The phenomena of rupture and flow in solids. Philosophical transactions of the royal society of london. Series A, containing papers of a mathematical or physical character, 163-198.
Haessler, H., Gaulon, R., Rivera, L., Console, R., Frogneux, M., Gasparini, G., Martel, L., Patau, G., Siciliano, M., Cisternas, A., 1988. The Perugia (Italy) earthquake of 29, April 1984: a microearthquake survey. Bulletin of the Seismological Society of America 78, 1948-1964.
Holdsworth, R., Van Diggelen, E., Spiers, C., De Bresser, J., Walker, R., Bowen, L., 2011. Fault rocks from the SAFOD core samples: Implications for weakening at shallow depths along the San Andreas Fault, California. Journal of Structural Geology 33, 132-144.
Holdsworth, R.E., 2004. Weak Faults--Rotten Cores. Science 303, 181-182.
Ide, S., Baltay, A., Beroza, G.C., 2011. Shallow Dynamic Overshoot and Energetic Deep Rupture in the 2011 Mw 9.0 Tohoku-Oki Earthquake. Science 332, 1426-1429.
Ikari, M.J., Marone, C., Saffer, D.M., 2011. On the relation between fault strength and frictional stability. Geology 39, 83-86.
Ikari, M.J., Saffer, D.M., Marone, C., 2007. Effect of hydration state on the frictional properties of montmorillonite-based fault gouge. Journal of geophysical research 112, B06423.

Ikari, M.J., Saffer, D.M., Marone, C., 2009. Frictional and hydrologic properties of clay-rich fault gouge. Journal of Geophysical Research 114, B05409.
Kanamori, H., 1972. Mechanism of tsunami earthquakes. Physics of the earth and planetary interiors 6, 346-359.
Kanamori, H., 2001. Energy budget of earthquakes and seismic efficiency. Earthquake Thermodynamics and Phase Transformations in the Earth's Interior 76, 293-305.
Kanamori, H., Rivera, L., 2006. Energy partitioning during an earthquake. Earthquakes: Radiated Energy and the Physics of Faulting, 3-13.
Kitajima, H., Chester, J.S., Chester, F.M., Shimamoto, T., 2010. High-speed friction of disaggregated ultracataclasite in rotary shear: Characterization of frictional heating, mechanical behavior, and microstructure evolution. Journal of Geophysical Research: Solid Earth 115, n/a-n/a.
Knuth, M., Marone, C., 2007. Friction of sheared granular layers: Role of particle dimensionality, surface roughness, and material properties. Geochemistry, Geophysics, Geosystems 8.
Lay, T., 2015. The surge of great earthquakes from 2004 to 2014. Earth and Planetary Science Letters 409, 133-146.
Lay, T., Ammon, C., Kanamori, H., Koper, K., Sufri, O., Hutko, A., 2010. Teleseismic inversion for rupture process of the 27 February 2010 Chile (Mw 8.8) earthquake. Geophysical Research Letters 37.
Lay, T., Kanamori, H., Ammon, C.J., Nettles, M., Ward, S.N., Aster, R.C., Beck, S.L., Bilek, S.L., Brudzinski, M.R., Butler, R., DeShon, H.R., Ekström, G., Satake, K., Sipkin, S., 2005. The Great Sumatra-Andaman Earthquake of 26 December 2004. Science 308, 1127-1133.
Lockner, D.A., Morrow, C., Moore, D., Hickman, S., 2011. Low strength of deep San Andreas fault gouge from SAFOD core. Nature 472, 82-85.
Logan, J., Dengo, C., Higgs, N., Wang, Z., 1992. Fabrics of experimental fault zones: Their development and relationship to mechanical behavior. International Geophysics Series 51, 33-33.
Mair, K., Frye, K.M., Marone, C., 2002. Influence of grain characteristics on the friction of granular shear zones. Journal of Geophysical Research: Solid Earth (1978–2012) 107, ECV 4-1-ECV 4-9.
Marco, S., Agnon, A., 1995. Prehistoric earthquake deformations near Masada, Dead Sea graben. Geology 23, 695-698.
Marone, C., Raleigh, C.B., Scholz, C., 1990. Frictional behavior and constitutive modeling of simulated fault gouge. J. geophys. Res 95, 7007-7025.
Marone, C., Scholz, C., 1988. The depth of seismic faulting and the upper transition from stable to unstable slip regimes. Geophysical Research Letters 15, 621-624.
Marone, C.J., Scholtz, C., Bilham, R., 1991. On the mechanics of earthquake afterslip. Journal of Geophysical Research: Solid Earth (1978–2012) 96, 8441-8452.
Niemeijer, A.R., Vissers, R.L.M., 2014. Earthquake rupture propagation inferred from the spatial distribution of fault rock frictional properties. Earth and Planetary Science Letters 396, 154-164.
Noda, H., Lapusta, N., 2013. Stable creeping fault segments can become destructive as a result of dynamic weakening. Nature advance online publication.
Pelayo, A.M., Wiens, D.A., 1992. Tsunami earthquakes: Slow thrust-faulting events in the accretionary wedge. Journal of Geophysical Research: Solid Earth (1978–2012) 97, 15321-15337.
Rice, J.R., 2006. Heating and weakening of faults during earthquake slip. J. Geophys. Res. 111, B05311.
Rowe, C.D., Griffith, W.A., 2015. Do faults preserve a record of seismic slip: A second opinion. Journal of Structural Geology 78, 1-26.
Satake, K., Tanioka, Y., 1999. Sources of tsunami and tsunamigenic earthquakes in subduction zones, Seismogenic and Tsunamigenic Processes in Shallow Subduction Zones. Springer, pp. 467-483.
Scuderi, M.M., Carpenter, B.M., Marone, C., 2014. Physicochemical processes of frictional healing: Effects of water on stick-slip stress drop and friction of granular fault gouge. Journal of Geophysical Research: Solid Earth 119, 4090-4105.

Scuderi, M.M., Niemeijer, A.R., Collettini, C., Marone, C., 2013. Frictional properties and slip stability of active faults within carbonate–evaporite sequences: The role of dolomite and anhydrite. Earth and Planetary Science Letters 369–370, 220-232.
Sibson, R.H., 1989. Earthquake faulting as a structural process. Journal of Structural Geology 11, 1-14.
Smith, S., Di Toro, G., Kim, S., Ree, J.H., Nielsen, S., Billi, A., Spiess, R., 2013. Coseismic recrystallization during shallow earthquake slip. Geology 41, 63-66.
Smith, S.A.F., Nielsen, S., Di Toro, G., 2015. Strain localization and the onset of dynamic weakening in calcite fault gouge. Earth and Planetary Science Letters 413, 25-36.
Tembe, S., Lockner, D.A., Wong, T.F., 2010. Effect of clay content and mineralogy on frictional sliding behavior of simulated gouges: Binary and ternary mixtures of quartz, illite, and montmorillonite. Journal of geophysical Research 115, B03416.
Tesei, T., Collettini, C., Barchi, M.R., Carpenter, B.M., Di Stefano, G., 2014. Heterogeneous strength and fault zone complexity of carbonate-bearing thrusts with possible implications for seismicity. Earth and Planetary Science Letters 408, 307-318.
Tesei, T., Collettini, C., Carpenter, B.M., Viti, C., Marone, C., 2012. Frictional strength and healing behavior of phyllosilicate-rich faults. Journal of Geophysical Research 117, B09402.
Tesei, T., Collettini, C., Viti, C., Barchi, M.R., 2013. Fault architecture and deformation mechanisms in exhumed analogues of seismogenic carbonate-bearing thrusts. Journal of Structural Geology 55, 167-181.
Thomas, M.Y., Avouac, J.-P., Champenois, J., Lee, J.-C., Kuo, L.-C., 2014. Spatiotemporal evolution of seismic and aseismic slip on the Longitudinal Valley Fault, Taiwan. Journal of Geophysical Research: Solid Earth, n/a-n/a.
Titus, S.J., DeMets, C., Tikoff, B., 2006. Thirty-five-year creep rates for the creeping segment of the San Andreas fault and the effects of the 2004 Parkfield earthquake: constraints from alignment arrays, continuous Global Positioning System, and creepmeters. Bulletin of the Seismological Society of America 96, S250-S268.
Ujiie, K., Tanaka, H., Saito, T., Tsutsumi, A., Mori, J.J., Kameda, J., Brodsky, E.E., Chester, F.M., Eguchi, N., Toczko, S., 343, E., Scientists, T., 2013. Low Coseismic Shear Stress on the Tohoku-Oki Megathrust Determined from Laboratory Experiments. Science 342, 1211-1214.
Ujiie, K., Tsutsumi, A., 2010. High-velocity frictional properties of clay-rich fault gouge in a megasplay fault zone, Nankai subduction zone. Geophysical Research Letters 37, L24310.
Ujiie, K., Tsutsumi, A., Kameda, J., 2011. Reproduction of thermal pressurization and fluidization of clay-rich fault gouges by high-velocity friction experiments and implications for seismic slip in natural faults. Geological Society, London, Special Publications 359, 267-285.
Verberne, B.A., He, C., Spiers, C.J., 2010. Frictional properties of sedimentary rocks and natural fault gouge from the Longmen Shan fault zone, Sichuan, China. Bulletin of the Seismological Society of America 100, 2767-2790.
Violay, M., Di Toro, G., Nielsen, S., Spagnuolo, E., Burg, J.P., 2015. Thermo-mechanical pressurization of experimental faults in cohesive rocks during seismic slip. Earth and Planetary Science Letters 429, 1-10.
Violay, M., Nielsen, S., Spagnuolo, E., Cinti, D., Di Toro, G., Di Stefano, G., 2013. Pore fluid in experimental calcite-bearing faults: Abrupt weakening and geochemical signature of co-seismic processes. Earth and Planetary Science Letters 361, 74-84.
Vrolijk, P., van der Pluijm, B.A., 1999. Clay gouge. Journal of Structural Geology 21, 1039-1048.
Wells, D.L., Coppersmith, K.J., 1994. New empirical relationships among magnitude, rupture length, rupture width, rupture area, and surface displacement. Bulletin of the Seismological Society of America 84, 974-1002.
Wu, F.T., Blatter, L., Roberson, H., 1975. Clay gouges in the San Andreas Fault System and their possible implications. pure and applied geophysics 113, 87-95.